



COPYRIGHT AND USE OF THIS THESIS

This thesis must be used in accordance with the provisions of the Copyright Act 1968.

Reproduction of material protected by copyright may be an infringement of copyright and copyright owners may be entitled to take legal action against persons who infringe their copyright.

Section 51 (2) of the Copyright Act permits an authorized officer of a university library or archives to provide a copy (by communication or otherwise) of an unpublished thesis kept in the library or archives, to a person who satisfies the authorized officer that he or she requires the reproduction for the purposes of research or study.

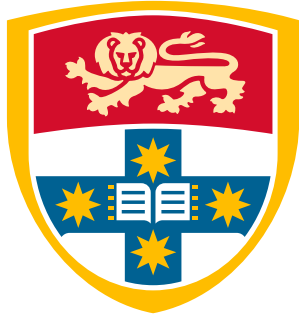
The Copyright Act grants the creator of a work a number of moral rights, specifically the right of attribution, the right against false attribution and the right of integrity.

You may infringe the author's moral rights if you:

- fail to acknowledge the author of this thesis if you quote sections from the work
- attribute this thesis to another author
- subject this thesis to derogatory treatment which may prejudice the author's reputation

For further information contact the University's Copyright Service.

sydney.edu.au/copyright



THE UNIVERSITY OF
SYDNEY

HIGH FIDELITY BIOELECTRIC MODELLING
OF THE IMPLANTED COCHLEA

Paul Chun Hymn Wong

February 2016

A thesis in conjunction with Cochlear Limited
Submitted in fulfilment of the requirements for the degree of Doctor of Philosophy
School of Aerospace, Mechanical and Mechatronic Engineering
Faculty of Engineering and Information Technologies
The University of Sydney

Declaration

I declare that the work in this thesis has not previously been submitted for a degree nor has it been submitted as part of requirements for a degree except as fully acknowledged within the text.

I also declare that the thesis has been written by me. Any help that I have received in my research work and the preparation of the thesis itself has been acknowledged. In addition, I declare that all information sources and literature used are indicated in the thesis.

Paul Chun Hymn Wong

February 2016

Abstract

Cochlear implants have been highly successful at restoring sound perception in individuals with sensorineural hearing loss. Since their inception, improvements in sound perception have largely been driven by advances in signal processing. Despite the merits of newer and more advanced processing schemes however, the level of improvement has plateaued for almost a decade, and performance in some everyday scenarios still leaves much to be desired. This suggests that there is an information bottleneck at the electrode-tissue interface, which is ultimately responsible for enacting the biophysical changes that govern neuronal recruitment during electrical stimulation.

Developing a complete understanding of the electrode-tissue interface is challenging because the cochlea is small, consists of many intricate structures, and is difficult to access. Modelling techniques, in conjunction with *in vivo* measurements, have provided useful insights into the electrical response of cochlear tissues, and recent advances in computational power have enabled spatially accurate volume conduction models for estimating the induced electric field. The predicted field can be fed into neural excitation models to predict the neuronal response. However, the models depend on a number of assumptions, some of which have yet to be tested, and despite their sophistication, many models are unable to predict patient outcomes consistently.

ABSTRACT

The present thesis aims to improve the reliability of volume conduction models by creating new, high fidelity reconstructions of the inner ear and critically assessing some of the hitherto untested modelling assumptions. Firstly, the lack of consensus around boundary conditions for monopolar simulations is addressed. The evidence suggests that the unmodelled return path should be accounted for, perhaps by applying a voltage offset at a boundary surface some distance from the cochlea itself. Secondly, the role of the cochlear vasculature, which has been ignored despite early calls for investigation, is examined. The models show that the large modiolar vessels, particularly the vein of the scala tympani, can have a strong local effect on current flow and neural excitation near the stimulating electrode. Thirdly, a time-dependent simulation is performed in response to questions about the validity of the oft-cited quasi-static assumption. It appears that the assumption is not valid due to the relatively high permittivity of neural tissue.

By demonstrating the impact of these factors, it is hoped that the trustworthiness of all bio-electric models of the cochlea is improved, either by further validating the claims of existing models, or by prompting improvements in future studies. Developing our understanding of the physics underlying cochlear implant systems will enable more robust and efficacious implant designs in the future, ultimately paving the way for improved sound perception and quality of life in individuals with sensorineural hearing loss.

I dedicate this thesis to my good friend Mitchell Seow.

I can't believe it has almost been a decade since your life was cut short so unexpectedly. I hope that by earning this degree, I am in some small way making up for the opportunities that you missed out on.

See you on the other side.

Preface

As someone who normally does a lot of introspection, I was surprised to feel a little apprehensive upon looking back on the last four years of my life. What had I achieved? Where might I be if I had followed a different path? Was it all worth it?

I remember starting off feeling a little uncertain about the decision to pursue the PhD. Despite being at the same institution, everything felt a little foreign (spending my first week at an overseas conference may have contributed to this). The friends I had completed my undergraduate studies with were no longer on campus, and those who had stayed behind were the quiet, unassuming types who mostly kept to themselves. My initial bunker buddy, Scott Townsend, bucked this trend but possessed a tenacity that I did not have, adding to the doubts in my head. The person who helped me get through that first semester though was undoubtedly the aptly named Gabby Chan. Her frequent visits and persistent noise-making were a welcome distraction from the punishing initiation that is the literature review, so I'm glad that she was still around during that time.

Four months in, Scott and I were moved downstairs to the cubicle farm in S203, otherwise known as the domain of the tissue engineers. I felt even more out of place there, but appreciated the open space, the air conditioning, and especially the abundance of natural light. By then I had started to realise how much there was to do; Howard Lau reinforced this when he pointed out that the topics Phil and I had chosen were effectively three projects

in one. Given the incredibly niche scope of my original topic, the technical difficulties of obtaining a suitable image stack to actually begin the modelling work, and my own lack of relevant background, the limited early progress was disheartening. However, my search for data lead to me to cross paths with Ian Curthoys and Christopher Wong, who were happy to collaborate on the project and kind enough to save me the trouble of obtaining my own ethics approval.

A few months later I moved offices once again, giving up the natural light to join Phil and Andrian in Link 243. Soon enough, that office became a space we could call our own. Lights and air conditioning were installed, new furniture was procured, and over time a plethora of customisations were added. Productivity increased as we bounced ideas off each other and became more aware of the intricacies of our topics. A high resolution image stack that seemed ideal for my model was finally made available, though on the flipside, I was faced with the dauntingly tedious task of semi-manually segmenting those scans for reconstruction. In conjunction with a quarter-life crisis, 2012 was a rather dark year. Fortunately, it was capped off by a delightful trip to Langkawi, Malaysia, where I presented my research work for the first time and made a heap of great memories with some new friends from Europe.

As it turned out, 2012 was not the end of the world, and by early 2013 it became clear that I needed more balance in my life. My internal supervisor gave me the chance to gain some official lecturing experience, which I enjoyed (though part of me regrets spending too much time on teaching over the course of the PhD). I started dabbling in new experiences, most notably the plunge into digital photography. The cost of entry was particularly painful for my wallet, but has since enriched my life many times more than the initial outlay. We saw the Dalai Lama and witnessed his irrepressible mirth and optimism. I also got to travel more, presenting my research at CIAP2013 by Lake Tahoe (bookended with visits to San Francisco and New York) and Medical Bionics 2013 on Phillip Island (followed by a few days in Melbourne). My sister commented around then that I had become more introverted

since starting the PhD. In hindsight, this was probably true, but I was also still recovering from the events of the previous year.

2014 was a year of change. I began socialising more and started dating again. I established a collaboration with Shefin George at the Bionics Institute and got to supervise two undergraduate honours theses, which expanded the depth of my thesis. My sister got married, and I shed tears in front of hundreds of wedding guests. My external supervisor spent most of the year abroad, and his expertise was often sorely missed as I prepared my first manuscript for publication. Towards the end of the year, I won an award at the Student Research Conference, and started seeing the end point. . . or so I thought until feedback on my paper submission prompted me to work on additional extensions to my model.

From the start of 2015 onwards, things were a blur. Between the model/manuscript revisions, thesis writing, and another visit to CIAP (and Seattle/Vancouver), there was barely any time for socialising or sleeping.* Now that I've reached the end of this journey though, I'm glad to have compiled a thesis that I am proud to submit. I've learnt a lot over this time, not only in terms of technical knowledge but also a variety of soft skills that I didn't expect to pick up when I started. Perhaps most importantly, I have discovered that I really enjoy learning new things. And exploring the world.

To all newcomers to the PhD world, chances are you'll end up making similar mistakes as I did (and consequently learning the same lessons), so for what it's worth, I'd like to offer a few words of advice based on my own experience:

Multithread your work The first thing you should do is figure out what needs to be done using, for instance, a Gantt chart. You'll inevitably find that some tasks can be done independently of others. Use that to optimise your workflow because each task will almost certainly take longer to achieve than you have planned (such is the nature of

* This meme summarises the situation pretty well.

research). When you hit a roadblock on one task, having an alternative to move on to will help you to maintain your momentum and give your mind time to come up with a solution.

Use a productivity system You may have gotten away without using one of these before, but following one will help you to stay on top of your tasks. There are many different systems out there, so try them out early on to discover which works best for you. The better systems track your to-dos as well as what you've already done to remind you of your accomplishments. For me, HabitRPG was best for planning and tracking, while an ambient noise generator (I settled on Noisli for a mix of cafe sounds and brown noise), earbuds, and a good Pomodoro timer were a terrific combination for really knuckling down. (I later wrote my own Python script to combine these latter components into one convenient package—I called it “Paulmodoro”.) Don't be afraid to rest when you need to though—working while fatigued is usually counterproductive.

Learn to use L^AT_EX Microsoft Word is adequate, but unprofessional and prone to errors. L^AT_EX was designed precisely for writing up long documents and makes it significantly easier to keep your dissertation neat and organised, even if your source files are not. Combining L^AT_EX with AutoHotkey also makes inserting references ridiculously simple. The benefits manifest most clearly in the later stages of writing up when your image and citation counts are in the hundreds, so it's definitely worth investing some time early on to set up your editor and learn the ropes.

Find good collaborators Your PhD is a pimple on a sliver in the vastness of all human knowledge.[†] While you may be tempted to learn and do everything yourself, you'll soon realise that it's much more efficient to collaborate with someone who already has expertise in that area, especially if it's not a major component of your project. They'll make your life a lot easier, whether it's by offering skills that would take you months

[†] As depicted brilliantly and succinctly by Matt Might in *The Illustrated Guide to a Ph.D.*.

or years to master yourself, or letting you piggyback on studies that already have ethics approval. One way to meet potential collaborators is to . . .

Go to conferences Travelling (either domestically or internationally) is a wonderful and enriching experience. Apply for financial assistance and present your work to other researchers because you'll receive valuable feedback while also learning more about your field. It's not all about the technical matters though—meeting people from all over the world is a great way to make new friends and reminds you that you're not alone in the quest for knowledge.

Remember the bigger picture Your PhD may feel omnipresent and all-consuming at times, but you do (or should) have a life outside of the PhD as well. Don't neglect those things, and try to keep everything in balance as much as possible. Your relationships with those who matter most in your life are especially important. There will inevitably be times when you will stumble and fall, and those people are the ones who will help you pick yourself up again.

Finally, a closing thought:

*“Happiness does not come from doing easy work
but from the afterglow of satisfaction that comes after the achievement of a
difficult task that demanded our best.”*

— Theodore Isaac Rubin

Embrace the challenge and make sure you submit something that you are proud of because it will make this accomplishment that much more fulfilling when you look back on it in the years to come.

Acknowledgements

First and foremost, I would like to thank my supervisors: Qing Li and Paul Carter. This project would not have been possible without your combined and generous guidance. To Qing, your commitment to my personal development and unwavering support over the past four years have demonstrated to me the true value of a good mentor, and I will aspire to emulate these qualities in my future endeavours. To Paul, your unfathomable technical knowledge and first-principles understanding of all things related to cochlear implant design have inspired me since we first met as part of the Advanced Engineering program. I appreciate the opportunities that you have afforded me and hope that our friendship continues to grow in the years to come.

To Ian Curthoys, Christopher Wong, and Allan Jones, thank you for being such willing collaborators and for sharing various microCT image stacks with me over the course of this project. I have always felt humbled by your kindness and expertise, and your work has opened my eyes to research outside my field.

Thank you to Peter Santi and Jonathon Kirk. Although I have not had the chance to meet either of you in person, I am very grateful for the sTSLIM dataset that was made available for this project and hope that the model made using those images helps to showcase the importance of your own research.

ACKNOWLEDGEMENTS

To Nick Pawsey and Joe Giorgio, thank you for providing access to Amira, for generating CAD models of the electrode arrays, and for your ongoing support and discussion regarding the various modelling issues. I hope that my work here adds some value to your ongoing efforts at Cochlear.

I would also like to thank Rob Shepherd and Shefin George from the Bionics Institute in Melbourne, Australia. Rob, thank you for showing such interest in my work at CIAP2013, and for encouraging me to submit an abstract for Medical Bionics 2013. Shefin, thanks for being such an awesome collaborator and for sharing your experimental data with me. I know you're going to go far and wish you all the best in your career.

Thank you to Payal Mukherjee and Bill Gibson for allowing me to attend a cochlear implant surgery. As a biomedical engineer with a fascination for human anatomy, I have always been excited to see a procedure in person. Witnessing the clinical context first-hand has allowed me to gain a more holistic understanding of all the effort required to complete the journey of a medical implant, and for that I am very grateful.

A special shout out to my undergraduate honours students, Li Cen and Shilpitha Inguva. Your friendship and assistance during 2014 was invaluable and I hope that we can all meet up again at some point to enjoy a game of mini-pool.

To my office buddies Scott Townsend, Phillip Tran, and Andrian Sue, I have appreciated your mateship and encouragement throughout my postgraduate life more than you know. To Phil and Andrian in particular, I would not have gotten through this whole ordeal without your ongoing support. You've both taught me a lot during our time together in terms of both technical skills and more general life advice. Regardless of where our future paths take us, I know we will all look back on our many adventures during this time fondly.

I also could not have gotten through this without the encouragement of my closest friends (you know who you are). As for a few special mentions, I'd like to acknowledge Gabby Chan

ACKNOWLEDGEMENTS

for her company, especially during the early months of my PhD life. Thanks to Calla Klafas and Carina Blaker for their many hours of open conversation over the past few years. Thanks also to Lulu Tan for introducing me to Melinda Nguyen.

Lastly and most importantly, I would like to thank my family for their unconditional love and support. I feel extremely privileged to have had the opportunity to undertake study at such a high level. Thank you for being patient with me, for putting up with my bad habits, and for being there through thick and thin. I love you all dearly.

Table of Contents

Front Matter

Declaration	ii
Abstract	iii
Preface	vi
Acknowledgements	xi
List of Figures	xix
List of Tables	xxiii
List of Publications	xxv

1 Introduction

1.1 Research Motivation	1
1.1.1 The Bigger Picture	2
1.1.2 The Cochlear Implant Performance Plateau	4
1.2 Thesis Goals	6
1.2.1 Enabling Knowledge Development via Computational Modelling	6
1.2.2 Addressing Untested Assumptions in the Literature	8
1.3 Dissertation Structure	9

2 Anatomy and Physiology of the Peripheral Auditory System

2.1 Anatomy Review	11
2.1.1 Overview of the Auditory Pathway	11
2.1.2 Detailed Structure of the Cochlea	17
2.1.3 Comparison of Human and Guinea Pig Cochleae	28

TABLE OF CONTENTS

2.2	Hearing Physiology	30
2.2.1	Normal Hearing	30
2.2.2	Hearing Loss	34
2.3	Chapter Summary	35
3	Literature Review	
3.1	Cochlear Implants	37
3.1.1	Components and Function	38
3.1.2	Stimulation Mechanics	40
3.1.3	Efficacy and Unsolved Challenges	47
3.2	Bioelectric Modelling	48
3.2.1	Expected Physics	48
3.2.2	Numerical Methods	51
3.2.3	Neural Excitation	56
3.3	Electric Models of the Cochlea	62
3.3.1	Lumped-Element Models	62
3.3.2	Volume Conduction Models	71
3.4	Research Questions	91
4	Model Development	
4.1	Introduction	94
4.2	Preliminary Considerations	95
4.2.1	Modelling Workflow	95
4.2.2	Geometry and Imaging	99
4.2.3	Material Properties	106
4.2.4	Electric Loads	114
4.2.5	Boundary Conditions	115
4.2.6	Numerical Solution Type and Software	116
4.2.7	Computer Hardware	119
4.3	Proof of Concept	120
4.3.1	Introduction	120
4.3.2	Method	120

TABLE OF CONTENTS

4.3.3	Mesh Result	125
4.3.4	Discussion	126
4.4	The Guinea Pig Model	127
4.4.1	Introduction	127
4.4.2	Method	128
4.4.3	Mesh Result	138
4.4.4	Discussion	139
4.5	The Human Model	141
4.5.1	Introduction	141
4.5.2	Method	141
4.5.3	Mesh Result	146
4.5.4	Discussion	146
4.6	Chapter Summary	148
5	Boundary Conditions for Monopolar Simulations: A Preliminary Investigation	
5.1	Introduction	149
5.2	Grounding Location and Size Effects	151
5.2.1	Method	151
5.2.2	Results	153
5.3	Multiscale Simulation of the Human Head	156
5.3.1	Method	157
5.3.2	Results	158
5.4	Discussion	160
5.5	Conclusions	165
6	Validation of the Guinea Pig Model	
6.1	Introduction	166
6.2	Method	169
6.2.1	<i>In silico</i> Modelling	169
6.2.2	<i>In vivo</i> Measurements	172
6.3	Results	174
6.3.1	<i>In vivo</i> Data	174

TABLE OF CONTENTS

6.3.2	Mesh Convergence	176
6.3.3	Sensitivity of Terminal Voltage Predictions	176
6.3.4	Effect on Current Pathways	180
6.3.5	Estimated Impact on Neural Excitation	180
6.4	Discussion	184
6.4.1	Modelling Workflow	184
6.4.2	Material Properties	185
6.4.3	Boundary Conditions	187
6.4.4	Study Limitations	189
6.5	Conclusions	189
7	The Role of the Cochlear Vasculature in Volume Conduction	
7.1	Introduction	191
7.2	Method	195
7.2.1	MicroCT Imaging with Microfil	195
7.2.2	Reconstruction from sTSLIM	199
7.3	Results	201
7.3.1	Degrees of Freedom and Solution Times	201
7.3.2	Voltage along the Array	202
7.3.3	Current Pathways	202
7.3.4	Activating Function	207
7.4	Discussion	207
7.4.1	Local Effects	209
7.4.2	Global Effects	210
7.4.3	Study Limitations	211
7.5	Conclusions	212
8	Incorporating Time-Dependent Effects into Models of the Cochlea	
8.1	Introduction	213
8.2	Method	218
8.2.1	Fourier Expansion of the Stimulating Pulse	218
8.2.2	Assignment of Frequency-Dependent Material Properties	222

TABLE OF CONTENTS

8.2.3	Reconstruction of the Time-Domain Signal	224
8.2.4	Resistive Formulation	224
8.3	Results	225
8.3.1	Solution Times	225
8.3.2	Convergence of the Stimulus Waveform	225
8.3.3	Output Reconstructions	231
8.3.4	Comparison with <i>in vivo</i> Data	237
8.4	Discussion	239
8.4.1	Modelling Considerations	239
8.4.2	Implications for Neural Excitation	242
8.5	Conclusions	243
9	Conclusions	
9.1	Contributions of the Thesis	244
9.2	Future Research Directions	247
9.3	Closing Remarks	249
	Appendices	
A	MATLAB Function Licences	251
B	Streamline Seeding	253
C	Ethics Approval	257
D	Microfil Specification Sheet	261
E	Digital Files	268
	References	269

List of Figures

1.1	Projected prevalence of disabling hearing loss in Australia	3
1.2	Sentence recognition scores in quiet since 1980	5
2.1	The anatomy of the ear	13
2.2	Structures within the tympanic cavity	13
2.3	Labyrinths of the inner ear	15
2.4	Tonotopic organisation of the cochlea	18
2.5	Neural pathways to the auditory cortex	19
2.6	Directional terms in the cochlear region	20
2.7	Sectional view through one turn of the cochlea	22
2.8	The organ of Corti	22
2.9	Sketch of the cochlear vasculature	25
2.10	Schematic of the cochlear arterial supply in man	26
2.11	Cross-sectional schematic of the modiolar vessels in man	27
2.12	Radiating arterioles and collecting venules	28
2.13	Schematic of the cochlear venous drainage in man	29
2.14	Internal aspect of the tympanic bulla	31
2.15	Sound wave propagation in the cochlea	33
2.16	Effect of stereocilia movement on ion channels	34
3.1	Schematic diagram of a cochlear implant system	39
3.2	The Nucleus 6 cochlear implant system by Cochlear Limited	39
3.3	Phase-contrast x-ray image of an intracochlear electrode array <i>in situ</i>	40
3.4	Correlation between electrode location and perceived frequency	41

LIST OF FIGURES

3.5	Charge-balanced, cathodic-first biphasic pulses	43
3.6	Constant current versus constant voltage waveforms	44
3.7	Modes of stimulation	46
3.8	Uniform flux lines in a homogeneous isotropic cell	50
3.9	Distortion of flux lines in the presence of a conductor or an insulator	50
3.10	Flux lines with small electrodes	50
3.11	Comparison of FDM and FEM meshes	54
3.12	Linear finite elements by shape	55
3.13	Spread of the depolarisation wavefront	58
3.14	Equivalent circuit model for excitable membranes	59
3.15	The von Békésy model	63
3.16	The Johnstone model	64
3.17	The Streljoff model	66
3.18	The Black and Clark model	67
3.19	The Suesserman and Spelman model	68
3.20	The Kral model	70
3.21	The Vanpoucke model	71
3.22	The Girzon model	72
3.23	The Finley model	75
3.24	Evolution of the Frijns model	77
3.25	Spatially distributed spiral ganglion cell bodies by Kalkman	79
3.26	The Hanekom model	81
3.27	The Rattay model	82
3.28	The Choi model	85
3.29	The Tognola model	86
3.30	The Whiten model	88
3.31	The Saba model	90
4.1	Overview workflow schematic	96
4.2	Comparison of imaging modalities for the human cochlea	103
4.3	Comparison of imaging modalities for the guinea pig cochlea	104
4.4	Workflow for the proof of concept model	121

LIST OF FIGURES

4.5	Image data for the proof of concept model	122
4.6	Volume mesh for the proof of concept model	125
4.7	Workflow for the guinea pig model	129
4.8	Segmentation of the sTSLIM images	130
4.9	Surface reconstruction of the guinea pig model	133
4.10	Virtual insertion of the HL8 array into the scala tympani	134
4.11	Volume mesh of the guinea pig model	135
4.12	XY view of nerve fibre trajectories	137
4.13	Jagged boundaries in the volume mesh	138
4.14	MicroCT image of the human temporal bone	142
4.15	Segmentation of the microCT images	145
4.16	Surface reconstruction of the human cochlear model	145
4.17	Volume mesh of the human cochlear model	146
5.1	Tested grounding locations	152
5.2	The shape of the voltage distribution around the cochlea	153
5.3	Predicted voltage profile by boundary condition	154
5.4	Effect of grounding location on current distribution	155
5.5	Effect of size on voltage profile	156
5.6	The HEATHER model	157
5.7	Voltage distribution in the whole head simulation	159
5.8	Predicted <i>in silico</i> terminal voltages by grounding location	160
5.9	Comparison of current flow patterns	161
6.1	Surface selections for boundary conditions	171
6.2	Equivalent circuit for the entire head	172
6.3	Unrolling the neural sheet for 2D activating function plots	173
6.4	<i>In vivo</i> voltage measurements along the array	175
6.5	Mesh convergence results	175
6.6	Sensitivity of terminal voltages	178
6.7	Voltage offset required to match the mean <i>in vivo</i> results	179
6.8	Streamline plots of the current paths during stimulation at E4	181

LIST OF FIGURES

6.9	Percentage change in activating function with changes in tissue resistivity	182
6.10	Percentage change in activating function with boundary conditions	183
7.1	The composition of blood	193
7.2	Perfusion of the guinea pig cochlea using Microfil	197
7.3	Visualisation of the vascular network in the guinea pig cochlea	199
7.4	Levels of detail for the vascularised reconstruction	201
7.5	Effect of vascular detail on intrascalar voltages	203
7.6	Comparison of exit pathways	204
7.7	Comparison of current density heatmaps	204
7.8	Effect of vascular detail on current density in Rosenthal's canal	205
7.9	Effect of vascular detail on the activating function	208
8.1	Quasi-static criterion for nerve tissue	217
8.2	Schematic of the solution process for time-dependent simulations	218
8.3	The base case stimulus waveform	220
8.4	Parametric implementation of the stimulus waveform	221
8.5	Interpolation of nerve conductivity in COMSOL	223
8.6	Waveform convergence for a square-shaped stimulus	227
8.7	Waveform convergence for a ramped biphasic stimulus	228
8.8	Effect of changing the pulse rate	230
8.9	Voltage reconstructions at electrode E5	232
8.10	Current exiting the nerve trunk	232
8.11	Activating function along the neural sheet (cathodic)	234
8.12	Activating function along the neural sheet (anodic)	235
8.13	Activating function over time	236
8.14	Comparison of simulated voltage profiles against <i>in vivo</i> data	238
8.15	Representative voltage waveforms for platinum electrode designs	241
B.1	The streamline seeding problem	254
B.2	Quadrilateral mesh of the electrode surface	255

List of Tables

1.1	Classification of hearing loss	3
2.1	Composition of the inner ear fluids	16
2.2	Key dimensions of the adult human cochlea	23
2.3	Comparison of human and guinea pig cochleae	31
3.1	Surface reactions at the electrode-tissue interface	42
4.1	Data inputs required for volume conduction modelling	98
4.2	Measurements of cochlear vessel diameters in man	101
4.3	Bone resistivity values	108
4.4	Nerve resistivity values	109
4.5	Perilymph resistivity values	109
4.6	Endolymph resistivity values	110
4.7	CSF resistivity values	110
4.8	Blood resistivity values	111
4.9	Resistivity of the cochlear membranes	112
4.10	Resistivity of other soft tissues in the cochlea	113
4.11	Comparison of numerical solution methods	117
4.12	Computer hardware specifications	119
4.13	Material properties for the proof of concept model	123
4.14	Material domains in the guinea pig model	132
4.15	Material domains in the human model	143
5.1	Monopolar boundary conditions used in existing models	150

LIST OF TABLES

6.1	Sensitivity of terminal voltages to tissue resistivities	177
7.1	Degrees of freedom and solution times for the vascularised models	202
7.2	Voltages along the array	203
7.3	Current density in Rosenthal's canal	206
8.1	Quasi-static criterion values at 10 kHz and 10 MHz	216
8.2	Solution times for the time-dependent model	225

List of Publications

The following is a complete listing of published works arising from this thesis. Copies of the papers are provided in Appendix E.

Peer-reviewed Journal Papers

- P. Tran, A. Sue, **P. Wong**, Q. Li, and P. Carter, “Development of HEATHER for cochlear implant stimulation using a new modeling workflow,” *Biomedical Engineering, IEEE Transactions on*, vol. 62, no. 2, pp. 728–735, February 2015.
- **P. Wong**, S. George, P. Tran, A. Sue, P. Carter, and Q. Li, “Development and Validation of a High-Fidelity Finite-Element Model of Monopolar Stimulation in the Implanted Guinea Pig Cochlea,” *Biomedical Engineering, IEEE Transactions on*, vol. 63, no. 1, pp. 188-198, January 2016.

Peer-reviewed Full Length Conference Papers

- **P. Wong**, Q. Li, and P. Carter, “Incorporating vascular structure into electric volume conduction models of the cochlea,” in *Biomedical Engineering and Sciences (IECBES), 2012 IEEE EMBS Conference on*. IEEE, December 2012, pp. 694–699.

LIST OF PUBLICATIONS

- P. Tran, **P. Wong**, A. Sue, Q. Li, and P. Carter, “Influence of blood vessel conductivity in cochlear implant stimulation using an finite element head model,” *Engineering in Medicine and Biology Society (EMBC), 35th Annual International Conference of the IEEE*. IEEE, July 2013.
- A. Sue, P. Tran, **P. Wong**, Q. Li, and P. Carter, “Time-domain finite element models of electrochemistry in intracochlear electrodes,” *Engineering in Medicine and Biology Society (EMBC), 35th Annual International Conference of the IEEE*. IEEE, July 2013.
- C. Inguva, **P. Wong**, A. Sue, A. McEwan, and P. Carter, “Frequency-Dependent Simulation of Volume Conduction in a Linear Model of the Implanted Cochlea,” *Neural Engineering (NER), 7th International IEEE EMBS Conference on*. IEEE, April 2015.
- A. Sue, **P. Wong**, P. Tran, Q. Li, and P. Carter, “Modeling the Effects of Electrode Recessing on Electrochemical Safety in Cochlear Implant Electrodes,” *Neural Engineering (NER), 7th International IEEE EMBS Conference on*. IEEE, April 2015.

Selected as an Open Finalist at NER2015 (Inguva *et al.*).

Peer-reviewed Conference Abstracts with Posters

- **P. Wong**, P. Tran, A. Sue, Q. Li, and P. Carter, “Sensitivity of cochlear volume conduction models to boundary conditions,” *Implantable Auditory Prostheses (CIAP), 2013 Conference on*. ARO, July 2013.
- P. Tran, **P. Wong**, A. Sue, Q. Li, and P. Carter, “Determining the Boundary Conditions for Cochlear Implant Models,” *Implantable Auditory Prostheses (CIAP), 2013 Conference on*. ARO, July 2013.

LIST OF PUBLICATIONS

- **P. Wong**, A. Sue, P. Tran, Q. Li, and P. Carter, “Effect of petrous bone resistivities on volume conduction in the cochlea,” *Medical Bionics, 3rd International Conference on*. The Bionics Institute, November 2013.
- A. Sue, **P. Wong**, P. Tran, Q. Li, and P. Carter, “Modelling the Electrochemistry of Platinum Intracochlear Stimulation Electrodes,” *Medical Bionics, 3rd International Conference on*. The Bionics Institute, November 2013.
- **P. Wong**, A. Sue, P. Tran, C. Inguva, Q. Li, and P. Carter, “Time-domain simulation of volume conduction in the guinea pig cochlea,” in *Implantable Auditory Prosthesises (CIAP), 2015 Conference on*. ARO, July 2015.
- P. Tran, **P. Wong**, A. Sue, Q. Li, and P. Carter, “A multi-scale model of cochlear implant stimulation,” in *Implantable Auditory Prosthesises (CIAP), 2015 Conference on*. ARO, July 2015.
- A. Sue, P. Tran, **P. Wong**, Q. Li, and P. Carter, “Investigations of irreversible charge transfer from cochlear implant electrodes: in vitro and in silico approaches,” in *Implantable Auditory Prosthesises (CIAP), 2015 Conference on*. ARO, July 2015.

Received a Monash Vision Group prize at Medical Bionics 2013 (Wong *et al.*).

Other Presentations

- **P. Wong**, “The effect of vascular structure on volume conduction in the cochlea,” *Cochlear International R&D Symposium*. Cochlear Limited, June 2012.
- **P. Wong**, “Modelling electrical stimulation in the implanted cochlea,” *Cochlear internal modelling workshop*. Cochlear Limited, May 2014.
- **P. Wong**, “Bioelectric modelling of the implanted guinea pig cochlea,” *6th Annual Student Research Conference*. The University of Sydney, November 2014.

LIST OF PUBLICATIONS

Awarded “Best Presentation from the School of AMME” at the 2014 Student Research Conference. Smaller meetings with the computational modelling team at Cochlear Limited were also held on numerous occasions.

“ . . . it is necessary to investigate the electrical geometry of the cochlea, because only with a knowledge of the voltage and resistance patterns is it possible to form an over-all picture of the electrical situation in the cochlea.”

— Georg von Békésy, 1951

Chapter 1

Introduction

This chapter addresses the following questions:

- What is the significance of the project?
- What does the thesis aim to achieve?

1.1 Research Motivation

Hearing is a fundamental sensory ability that human beings share with many other species of the animal kingdom. The ability to perceive sound allows us to communicate with each other vocally, detect objects in our environment without being physically adjacent to them or having a direct line of sight, and appreciate the melodies and harmonies of music. These qualities have established the sense of hearing as one of our primary means of gathering information about the world around us.

1.1.1 The Bigger Picture

Unfortunately, many people suffer from impaired hearing capabilities. In 2012, the World Health Organisation (WHO) estimated that 360 million people worldwide (or 5.3% of the world's population) were afflicted with *disabling hearing loss*, defined by the WHO as more than 40 dB loss *in the better hearing ear* in adults, or 30 dB in children (see Table 1.1) [1].

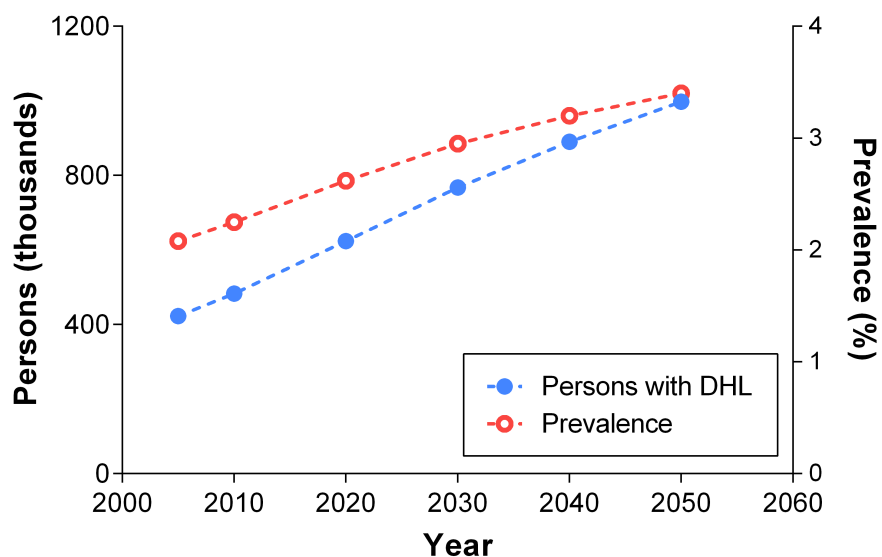
In Australia alone, over 422,000 individuals (representing 2.1% of the population) were classified as being at a similar level of hearing loss (more than 45 dB loss in adults, or 30 dB in children) in 2005 [3]. By 2050, this figure is predicted to increase to just shy of 1 million people (3.4% of Australia's projected population), as shown in Figure 1.1. (Note that these Australian numbers are underestimates relative to the WHO definition due to the more stringent criteria and earlier sample time.)

Hearing loss comes with a number of personal costs to affected individuals in addition to the reduced capacity to communicate. Quality of life is reduced through suffering and loss of leisure [3]. Participation in education, skill development, and employment are hindered, putting pressure on their consumable incomes which are, as a group, already lower than average [3]. Families, friends, and co-workers interacting with the hearing impaired person are also affected, which can cause some individuals to feel like they are a burden on those around them [4]. Social isolation is also well documented, and can lead to emotional tolls through anxiety and depression [4].

The financial costs associated with hearing loss are substantial [3]. It was estimated to cost the Australian economy about \$11.75 billion (1.4% of gross domestic product) in 2005. The largest component of this cost is productivity loss (\$6.7 billion), followed by informal carers (\$3.2 billion), deadweight losses (\$1.0 billion), and then direct health system costs (\$674 million). In addition to these numbers, the monetary value corresponding to the loss of wellbeing described in the previous paragraph was estimated to be some \$11.3 billion [3].

Table 1.1: Classification of hearing loss. (Reproduced from World Health Organisation [2].)

Grade	Loss in better ear (dB)	Description
Normal	≤ 25	No or very slight hearing problems; able to hear whispers
Mild	26–40	Able to hear and repeat words spoken in normal voice at 1 metre
Moderate	41–60	Able to hear and repeat words using raised voice at 1 metre
Severe	61–80	Able to hear some words when shouted into better ear
Profound	≥ 81	Unable to hear and understand even a shouted voice

**Figure 1.1:** Projected prevalence of disabling hearing loss (DHL) in Australia, 2005–2050. (Data from Access Economics [3].)

Considering the millions of people affected around the world, these Australian estimates only represent a small fraction of the global total. It would appear that the restoration of hearing capabilities would yield significant benefits not only for affected individuals, but also for the economy as a whole. Indeed, treatments for hearing loss are reportedly very cost-effective interventions [3].

1.1.2 The Cochlear Implant Performance Plateau

Roughly 90% of hearing loss is sensorineural in nature [5], as described in §2.2.2. For those categorised as having severe or profound *sensorineural hearing loss* (SHL), the cochlear implant (CI) is the only effective treatment. Unlike hearing aids, which simply amplify incoming sound signals, CIs work by injecting pulses of electric current into the inner ear to stimulate auditory neurons directly (§3.1). The United States Food and Drug Administration (FDA) reported that as of December 2012, approximately 324,200 people worldwide had received CIs [6], and it is expected that this number will continue to grow.

The quality of sound perception has shown marked improvements since CIs were first developed. Figure 1.2 shows the trend in sentence recognition scores in quiet environments for CI recipients using various sound processing strategies from the top device manufacturers [7]. There were (and still are) significant variations in speech performance amongst individuals [8], but innovations in the processing of speech signals [8–10] were able to produce rapid jumps in average performance over the first one and a half to two decades of CI development.

Despite the technological merits of newer schemes, however, speech performance in quiet has since plateaued [7, 11, 12]. One reason for this may be a shift in research focus towards improving other use cases—with a large portion of users experiencing adequate performance

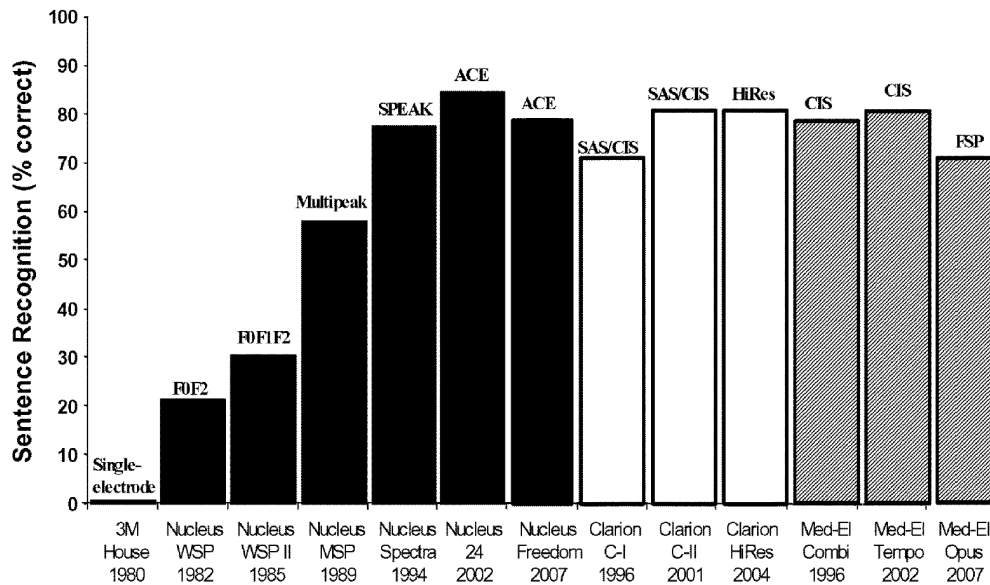


Figure 1.2: Sentence recognition scores in quiet since 1980. (Source: Zeng [7]. Copyright © 2008, IEEE.)

in quiet, researchers began working on performance in noisy environments, pitch discrimination (for music and tonal languages), and other fringe cases to make the implants more robust and relevant to the everyday lives of implant recipients.

There may however be another potential explanation. Consider that the mechanism ultimately responsible for hair cell stimulation is the *in vivo* current flow (cf. §3.1). The spatial distribution of this flow is largely dictated by three factors: the design of the intracochlear electrode array, its position within the cochlea after surgical insertion, and the electrical properties of the tissues around the implant. The design of the array is arguably the most important of these because it can affect both the intrascalar positioning of the electrode array and, at least in part, the surrounding tissue response [13–19].

CI array designs have remained relatively stagnant in comparison to speech processing techniques [20–22]. This is not to say that there has been zero progress in the area, but rather that the results of such endeavours have failed to produce comparable successes. Part of the reason for this may be a lack of impetus because early multichannel arrays were more

than sufficient to deliver the then-crude speech signals from the implant electronics. Case in point, sentence recognition scores of over 90% could be obtained in quiet with just four active channels [23,24]. As such, implants were designed with a 70 year life span [Cochlear Limited, internal communication] in anticipation that software upgrades could be relied on to improve performance.

With the sophistication of the latest algorithms corresponding to rather static speech performance metrics, it would seem that the bottleneck has shifted to other components of the system [25,26]. Whether these limitations are due to array design or biological factors is not clear since the influence of individual factors is difficult to ascertain [8], but it is most likely a combination of these. In either case, existing intracochlear array designs have reached a limit, and a lack of insight into how they might be further improved has hindered their continued development.

1.2 Thesis Goals

1.2.1 Enabling Knowledge Development via Computational Modelling

Traditional *in vivo* and *in vitro* methods for investigating biological phenomena are difficult to implement in the cochlea because it is small, contains a number of delicate structures, and is surgically inaccessible, being encased in the densest and hardest bone in the body [27,28]. For the purposes of CI design, it is of interest to determine spatially distributed field quantities [29]. This presents two main challenges to the experimentalist. Firstly, obtaining these measurements using *in vivo* or *in vitro* methods can be impractical because the probes must be physically placed at the location of the measurements [20,30], a process which inherently compromises the integrity of the cochlear structures. Most experiments therefore only involve taking measurements within the fluid chambers of the cochlea, but even then, introducing the

probes requires perforation of either the otic capsule surrounding the cochlea or the round window membrane and can damage the other soft tissue structures lying within [31] or lead to cerebrospinal fluid (CSF) contamination [32, p. 113]. Secondly, it is difficult to precisely control the positioning of the probe to obtain the large number of sample points needed for building a detailed electroanatomical map.

Over the past few decades, another method has become viable: computational modelling, also referred to as *in silico* experimentation. The progression of “Moore’s Law”, which predicts a doubling of the number of transistors in an integrated circuit every two years [33], has led to an exponential increase in processing power since the 1970s, enabling a range of numerical methods (§3.2.2) to be adapted to engineering analysis. Although the earliest *in silico* studies were relatively simple abstractions, the complexity of analyses that could be performed has increased over time, spurred by the development of more robust software that took advantage of the ever-increasing hardware capabilities.

A virtual representation of the implanted cochlea would be a useful tool for CI research [20, 21, 34] because it can provide an alternative and complementary form of investigation that is not subject to the shortcomings of traditional methods discussed above. Being able to manipulate a virtual space means that measurements can be made in hard-to-reach places (within Rosenthal’s canal, for instance) without disturbing the surrounding tissues, thereby providing a better representation of the *in vivo* situation. In addition, more intuitive visualisations of the underlying bioelectric phenomena can be produced, making the dissemination of new insights easier and more accessible to a wider audience. When used in conjunction with *in vivo* studies and bench-top testing, *in silico* studies are invaluable for obtaining a holistic understanding of medical devices [30, 35–37]. To that end, the first goal of this project is *to develop a realistic computational model of the implanted cochlea*. All of the work that went into producing the models in this thesis is documented in Chapter 4.

Existing models of the implanted cochlea have a strong focus on explaining the clinical outcomes observed in subjects, which is a significant and worthwhile objective in itself, but in doing so they provide little insight into the intermediate step of how injected current flows through the tissue both spatially and temporally. This intermediate step must be understood in order to gain insights that can be fed into the design process for next generation intracochlear electrode arrays [20,35]. It is hoped that by analysing the relationships between the stimulating pulse, the anatomy of the cochlea, and the electrophysiological response using computational techniques, a more advanced understanding of the underlying mechanisms will be developed, leading to improved intracochlear array designs that provide higher quality sound perception, greater power efficiency, and other benefits to CI recipients. To be clear, this is a longer term view for the industry. The focus for this project is to develop the groundwork, methodology, and models that would enable this future to take place.

1.2.2 Addressing Untested Assumptions in the Literature

Consider the following quote from statistician George Box:

“Essentially, all models are wrong, but some are useful.

... the approximate nature of the model must always be borne in mind.”

— George Box, 1987 [38]

All models are, by definition, simplifications of reality. Sophisticated models may approach the reality of nature, but they will never replicate it entirely; nor should they, given that the purpose of modelling is to make complexity more intuitive [Lianne Cartee, personal communication]. For practical purposes, what matters is whether or not they are representative of the system being studied.

Simply creating a model does not provide an adequate foundation for further investigation. As noted in §6.1, there is some entrenched reluctance to trust computational models in the CI research community, despite the benefits and insights that they can provide. It is suspected that this is due to the use of untested assumptions in existing models that are often not intuitive nor properly justified. Coupled with the inconsistent predictions of psychophysical outcomes from one model to the next, which are inevitable given the multiple layers of abstraction and the difficulty of representing biophysical interactions mathematically, it is understandable that these doubts exist.

Hence, the second goal of this project is *to critically evaluate some of the assumptions currently used in volume conduction models of the cochlea*. These include the impact of boundary conditions (Chapters 5 and 6), material properties (Chapter 6), vascular structure (Chapter 7), and time-dependent effects (Chapter 8). Sensitivity studies will be performed to gauge the certainty of cited input parameters, and *in vivo* measurements will be acquired and compared with the *in silico* results to provide guidance on acceptable model outputs. By addressing these outstanding issues in a thorough and logical manner, it is hoped that some of the concerns surrounding the use of *in silico* models may be alleviated. The outcome of these assessments will act to either further validate existing models, or prompt changes in future models. In either case, the profile and trustworthiness of computational models of the implanted cochlea will be improved.

1.3 Dissertation Structure

The structure of the dissertation is as follows:

Chapter 1 Explains the motivation behind the project and the goals of the thesis.

Chapter 2 Reviews the anatomy of the ear and the processes responsible for hearing.

Chapter 3 Introduces cochlear implants, examines existing work in bioelectric modelling to develop the reader's knowledge of the subject matter, and reviews the current state-of-the-art.

Chapter 4 Documents the methodology used to construct the models in the thesis.

Chapter 5 Examines the impact and accuracy of various boundary condition assumptions.

Chapter 6 Assesses the validity of the guinea pig cochlea model to ensure that input parameters and corresponding results are reasonable.

Chapter 7 Investigates the role of vascular structures in volume conduction.

Chapter 8 Evaluates the feasibility of modelling time-dependent effects and the repercussions of these dynamics.

Chapter 9 Summarises the findings of the thesis and proposes directions for future research efforts.

Chapter 2

Anatomy and Physiology of the Peripheral Auditory System

This chapter addresses the following questions:

- What structures are involved in hearing perception?
- What does the cochlea look like?
- How does normal hearing work?

2.1 Anatomy Review

2.1.1 Overview of the Auditory Pathway

The ability to hear involves a chain of anatomical structures that together form the auditory pathway. It includes the various components of the ear, which are responsible for the detection

and encoding of sound stimuli, the neural pathways that relay the encoded neural signal to the brain, and the auditory cortex, the part of the brain that processes and interprets the received signal [39].

The ear can be divided into three distinct regions: the external ear, the middle ear, and the inner ear, as illustrated in Figure 2.1. Each region is described briefly below.

The External Ear

The purpose of the external ear is to collect and direct sound waves towards the middle ear. This is primarily facilitated by the *auricle*, a cartilaginous structure making up the portion of the ear visible from outside the body. Its shape helps to funnel sound waves into the *external acoustic meatus*, a narrow tunnel that passes through the temporal bone of the skull. At the medial end of the meatus is a thin sheet of connective tissue called the *tympanic membrane*, commonly known as the eardrum.

The Middle Ear

On the other side of the tympanic membrane is a small, air-filled chamber called the *tympanic cavity* (see Figure 2.2). It opens inferiorly into the *auditory tube*, which leads to the nasopharynx. This connection allows the air pressure on both the sides of the tympanic membrane to be maintained at the external atmospheric pressure.

The key feature of the middle ear is its three tiny bones—the *malleus*, the *incus*, and the *stapes*—collectively known as the *auditory ossicles*. The malleus is attached to the tympanic membrane inferiorly and to the incus superiorly; in turn, the incus is linked to the stapes, whose footplate is fused to an opening in the bony wall of the inner ear known as the *oval*

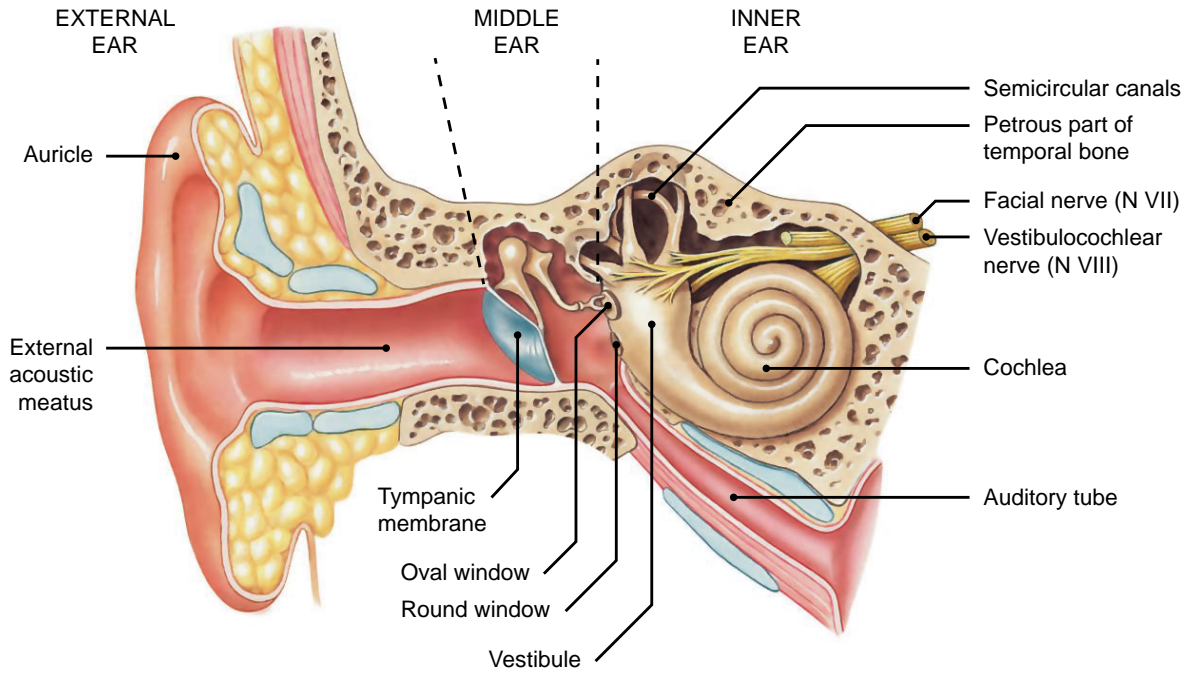


Figure 2.1: The anatomy of the ear. (Image adapted from Martini *et al.* [40]. Copyright © 2006, Daryl Fox.)

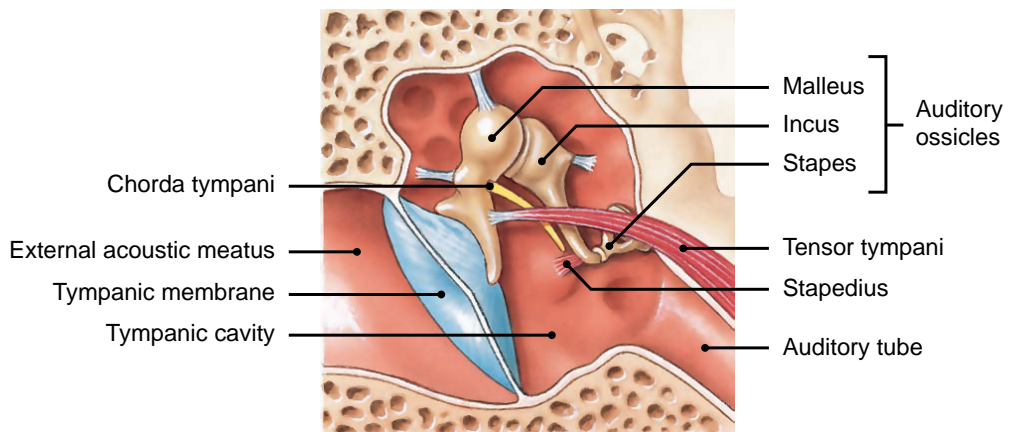


Figure 2.2: Structures within the tympanic cavity. (Image adapted from Martini *et al.* [40]. Copyright © 2006, Daryl Fox.)

window (see Figure 2.1). The ossicles conduct and amplify the vibrations of incoming sound waves from the tympanic membrane through the oval window to the inner ear.

Three other structures located in the middle ear are the *tensor tympani* and *stapedius* muscles, and the *chorda tympani* nerve. The muscles prevent excessive movement of the tympanic membrane and ossicles that would otherwise damage these delicate structures. The nerve carries taste sensations, and passes through the tympanic cavity to join with the nearby *facial nerve* (or seventh cranial nerve, N VII).

The Inner Ear

Sensory receptors for both hearing and equilibrium are housed in the chambers of the inner ear (Figure 2.3). The *membranous labyrinth*, which contains a fluid called *endolymph*, is surrounded by the *bony labyrinth* (also known as the *otic capsule* [41, p. 62]), and the space between them is filled with another fluid called *perilymph*. Endolymph and perilymph are both extracellular fluids but they have different compositions, as shown in Table 2.1. The high potassium concentration of endolymph is required for normal hearing function and makes it unique amongst bodily fluids. The composition of perilymph is similar to that of cerebrospinal fluid (CSF), likely because they are joined via the *perilymphatic duct*. There are subtle variations in composition between the two perilymphatic fluid chambers, with only the amount of protein showing a large discrepancy.

The posterolateral aspects of the inner ear, namely the *vestibule* (see Figure 2.1) and the semicircular canals, together form the *vestibular complex*. Sensations of gravity, linear acceleration and head rotation all arise from the receptors in this region. The sensation of hearing occurs in the anteromedial aspect, which is named the *cochlea* after its distinctive snail shell appearance. For both of these senses, the reception of stimuli and their transduction

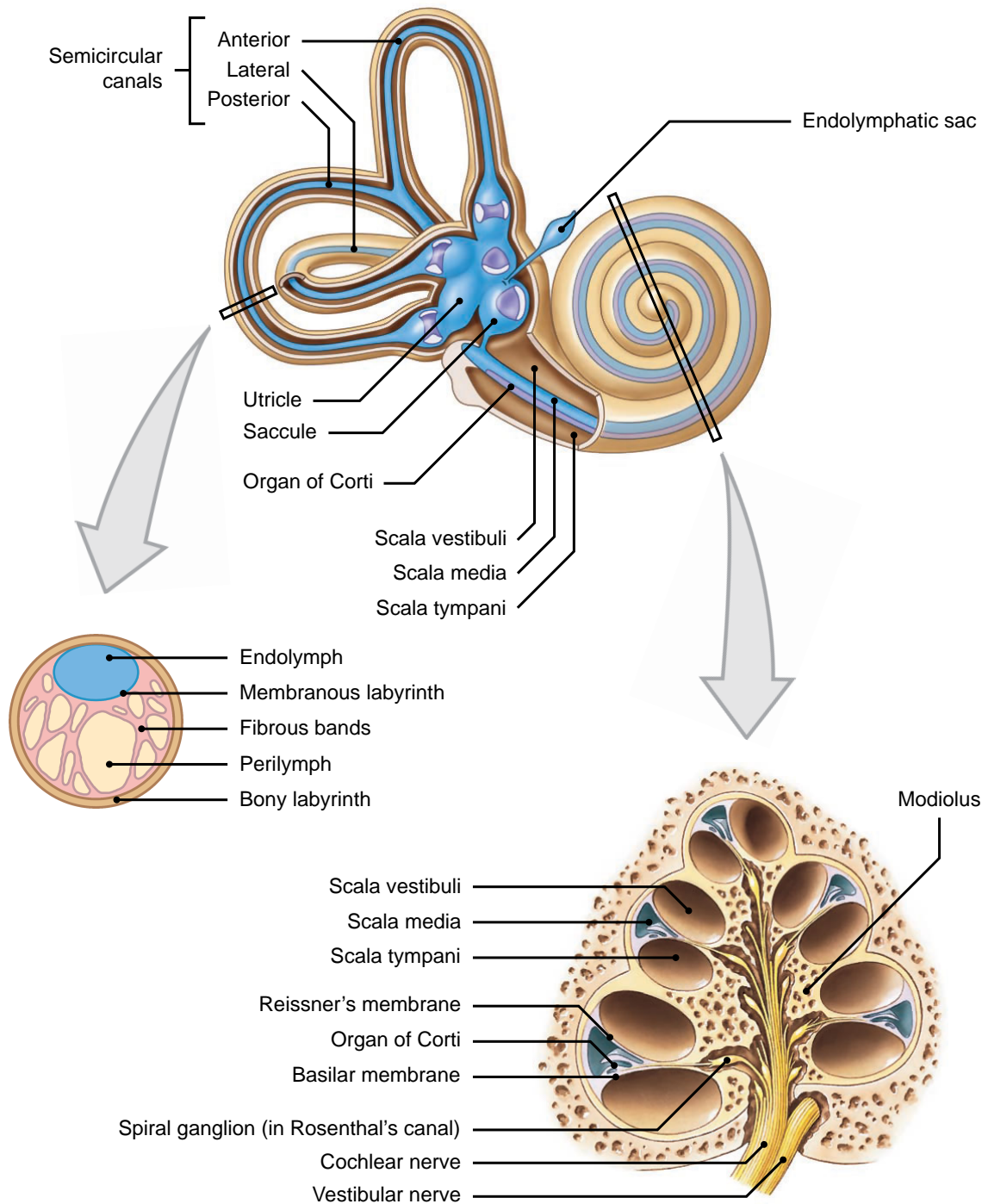


Figure 2.3: Labyrinths of the inner ear. (Image adapted from Martini *et al.* [40]. Copyright © 2006, Daryl Fox.)

Table 2.1: Composition of the inner ear fluids. All values are reported in millimolar (mM), except for protein. Measurements were obtained from various studies on guinea pigs and rodents. Not all constituents have been listed. (Data from Wangemann and Schacht [42].)

Component	Endolymph of scala media	Perilymph of scala vestibuli	Perilymph of scala tympani	Cerebrospinal fluid
Na ⁺	1.3	141	148	149
K ⁺	157	6	4.2	3.1
Ca ²⁺	0.023	0.6	1.3	1.2
Cl ⁻	132	121	119	129
HCO ₃ ⁻	31	18	21	19
Aspartate	0.015	0.003	0.002	0.003
Glutamate	0.053	0.008	0.007	0.003
Glutamine	0.054	0.645	0.625	0.45
Glycine	0.071	0.289	0.322	0.01
Alanine	0.04	0.367	0.321	0.036
Glucose	0.6	3.8	3.6	4.81
Urea	4.9	5.2	5	5.2
Protein (mg/100 ml)	38	454	178	24
pH	7.4	7.3	7.3	7.3

into neuronal signals is handled by highly specialised mechanoreceptors called *hair cells* (see inset, Figure 2.8).

The structure of the cochlea is described in more depth in §2.1.2.

Neural Pathways to the Auditory Cortex

Hair cells are monitored by the peripheral nerve endings of auditory neurons. The cell bodies of these predominantly bipolar neurons are unmyelinated in humans [43] and are clustered together in the *spiral ganglion*, housed within *Rosenthal's canal* (see Figure 2.3). Their myelinated axons combine to form the *cochlear nerve*, which exits the cochlea via its basal end and joins with the *vestibular nerve* exiting the vestibular complex to become the *vestibulocochlear nerve*, also known as the auditory nerve (or eighth cranial nerve, N VIII). These branches, shown in Figure 2.4, follow the *internal auditory meatus* through the petrous part of the temporal bone and are encased in CSF.

Upon reaching the ipsilateral *cochlear nucleus* in the medulla oblongata, second-order neurons decussate and ascend to the *inferior colliculus*, which is responsible for auditory reflexes. Connecting neurons propagate the signal to the *medial geniculate nucleus* in the thalamus, before finally reaching the *auditory cortex* in the temporal lobe of the brain. These pathways are illustrated in Figure 2.5.

2.1.2 Detailed Structure of the Cochlea

The cochlea is a biological electromechanical system with three main classes of internal structures: fluid spaces and structural support, sensory neuroanatomy, and vasculature. Each of these is comprised of different tissue types and plays a unique but interdependent role in the hearing process.

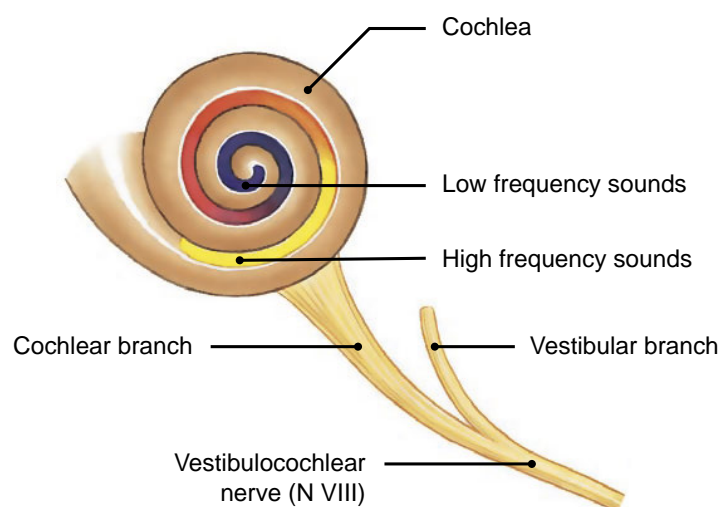


Figure 2.4: Tonotopic organisation of the cochlea. Low and high frequency receptors join together to form the cochlear branch of N VIII. The sequential frequency mapping is preserved and transferred to the auditory cortex (cf. Figure 2.5). (Image adapted from Martini *et al.* [40]. Copyright © 2006, Daryl Fox.)

Directional Terms

Due to its tapered spiral shape, directions in the cochlea are usually described relative to the *mid-modiolar axis*, i.e. the axis through the centre of the cochlea around which the labyrinth spiral (see Figure 2.6). There is also a consensus cochlear coordinate system for quantitative measurements [44]. The key terms used in this thesis are listed below:

Apical—Basal Any axis parallel to the mid-modiolar axis.

Above—Below Towards the apex/base of the cochlea. Used when describing structures in a localised region.

Radial Any axis perpendicular to the mid-modiolar axis.

Medial—Lateral, or Central—Peripheral Towards/away from the mid-modiolar axis along a radial axis. The former pair is usually used in the context of a cross-sectional slice, while the latter pair is used in reference to the three-dimensional (3D) structure.

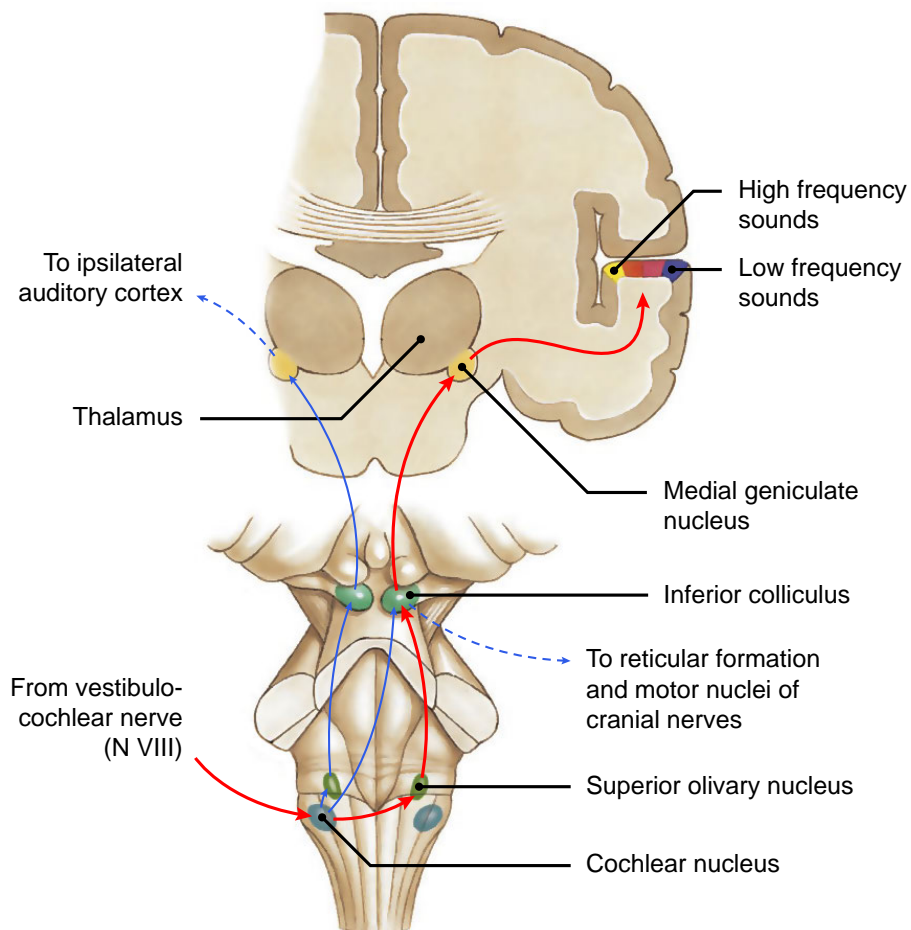


Figure 2.5: Neural pathways to the auditory cortex. The primary pathway is shown by the red arrows, while secondary connections are marked by the blue arrows. The low and high frequency regions of the auditory cortex are arranged sequentially, analogous to the tonotopic organisation of the cochlea (cf. Figure 2.4). (Image adapted from Martini *et al.* [40]. Copyright © 2006, Daryl Fox.)

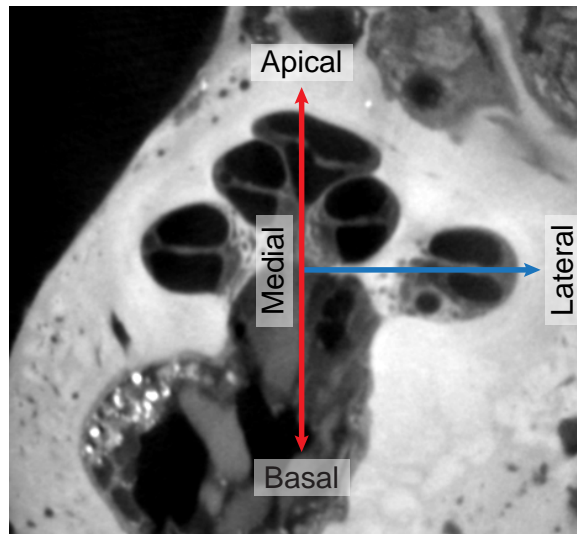


Figure 2.6: Directional terms in the cochlear region. The mid-modiolar axis is shown in red, and a radial axis in blue.

Spiral The helical path followed by the labyrinths around the mid-modiolar axis.

Turn A 360 degree segment of the cochlear spiral.

Fluid Spaces and Structural Support

At the highest level, the cochlea is dominated by the bony and membranous labyrinths. In the vestibular complex, the membranous labyrinth is attached to the bony labyrinth along one side. In the cochlea, however, the continuation of the membranous labyrinth, known as the *scala media*, is sandwiched between a pair of perilymphatic ducts, the *scala vestibuli* and the *scala tympani* (see Figure 2.7). The former leads up the spiral from the oval window, and is continuous at the *helicotrema* with the latter, which heads back down the spiral and ends at a second opening in the cochlear wall called the *round window*.

The upper and lower boundaries of the *scala media* are formed by two thin membranes—*Reissner's membrane* and the *basilar membrane*—which separate it from the *scala vestibuli*

and the scala tympani, respectively. Its lateral border is the *spiral ligament*, which is attached to the bone of the lateral wall (Figure 2.8). A capillary bed known as the *stria vascularis* forms on the upper portion of the spiral ligament at its junction with the scala media. Along with the spiral ligament and the epithelial supporting cells, the stria vascularis plays an important role in maintaining the ionic composition of the endolymphatic space [46].

The scala media only spans part of the radial distance from the lateral wall to the bony core of the cochlea, known as the *modiolus*. The remaining distance is occupied by the *spiral lamina*, a double-layer bony plate that extends outwards from the modiolus to meet the basilar membrane. The space between the plates is occupied by the auditory neurons as they pass through to the modiolus, as detailed in the next section.

All of these structures together wrap around the modiolus along the helical path of the scalae. Starting from the round window, the first four quadrants comprise the basal turn, the next four the middle turn, and the remainder the apical turn. Erixon *et al.* [47] studied 73 corrosion casts of adult human inner ears and found that an average human cochlea has 2.6 turns. The observed range of 2.2–2.9 turns indicates considerable variation between individuals. The study also revealed variations in other key dimensions; these measurements are summarised in Table 2.2.

Neural Structures

The cornerstone of the hearing mechanism is the hair cell (see inset, Figure 2.8) in that these cells are responsible for the actual transduction of physical vibrations that make up sound waves to neural impulses. They are housed within the *organ of Corti*, which is named after its discoverer, Alfonso Corti [41]. Figure 2.8 depicts the positions of the hair cells within the organ of Corti. They are embedded in epithelial supporting cells that lie on the basilar membrane and are organised into one inner row and three outer rows. *Stereocilia* protruding

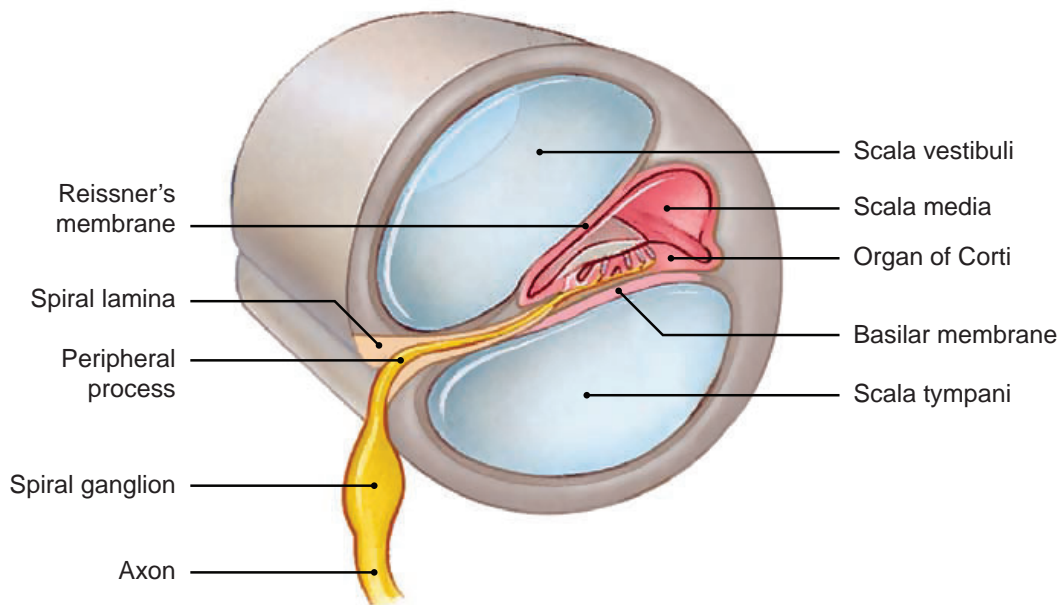


Figure 2.7: Sectional view through one turn of the cochlea. (Image adapted from Tate [45]. Copyright © 2012, McGraw Hill.)

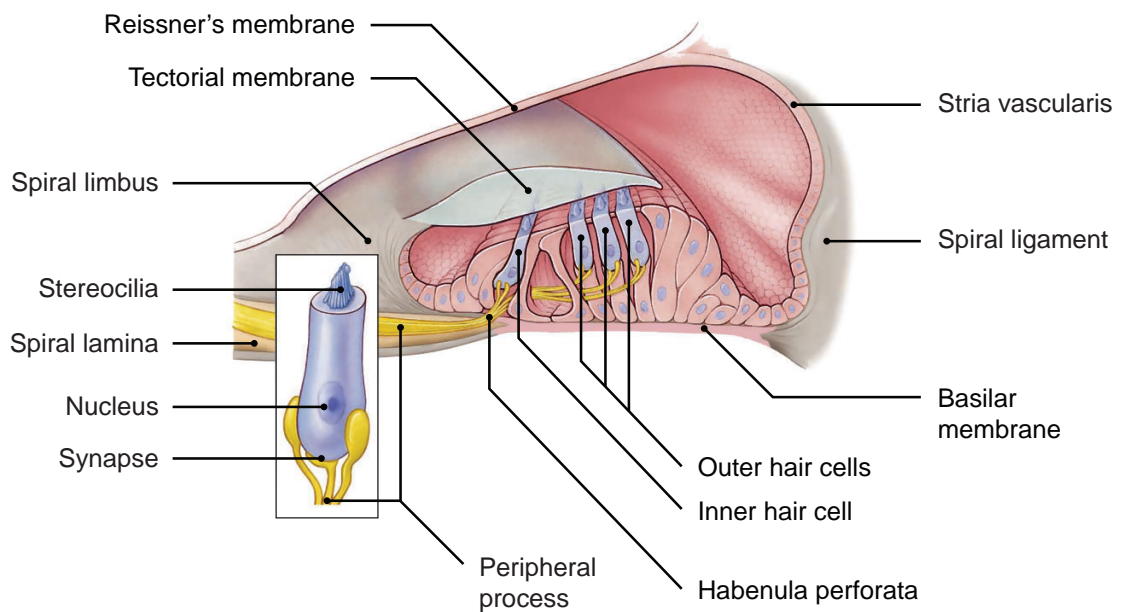


Figure 2.8: The organ of Corti within the scala media. Inset shows the basic structure of an isolated hair cell. (Image adapted from Tate [45]. Copyright © 2012, McGraw Hill.)

Table 2.2: Key dimensions of the adult human cochlea. (Data from Erixon *et al.* [47].)**(a)** Outer wall length.

Location	Mean \pm SD (mm)	Range (mm)
First turn	22.6 \pm 0.83	20.3–24.3
Second turn	12.4 \pm 0.63	10.7–13.3
Third turn	6.1 \pm 1.40	1.5–8.2
<i>Total</i>	42.0 \pm 1.96	38.6–45.6

(b) Height.

Location	Mean \pm SD (mm)	Range (mm)
First turn	2.1 \pm 0.20	1.6–2.6
Second turn	1.2 \pm 0.17	0.8–1.6
Third turn	0.6 \pm 0.18	0.3–1.1
<i>Total</i>	3.9 \pm 0.37	3.3–4.8

(c) Width.

Location	Mean \pm SD (mm)	Range (mm)
First turn	6.8 \pm 0.46	5.6–8.2
Second turn	3.8 \pm 0.25	3.3–4.3
Third turn	2.1 \pm 0.52	0.6–3.6

from the exposed surface of each hair cell are attached the overlying *tectorial membrane*, which itself is anchored to the medial wall of the scala media via the *spiral limbus*.

There are about 15,000 hair cells in the human inner ear, split into 3,000 inner hair cells and 12,000 outer hair cells [46,48]. These are monitored by the *peripheral processes* of the bipolar auditory neurons. The processes leave the organ of Corti and enter the space between the double wall of the spiral lamina via tiny openings called the *habenula perforata*. From here, they travel centrally to Rosenthal's canal, wherein the cell bodies of the neurons lie and together form the spiral ganglion. Their myelinated axons then run towards the base of the cochlea, combining to form the cochlear branch of N VIII. Most of the auditory neurons are afferent, but there are also some efferent fibres that lead back towards the hair cells to form a feedback loop.

Vascular Structures

Traditional descriptions of the cochlea have generally excluded its vasculature. The most comprehensive investigation of the cochlear vessels is a survey by Axelsson [49], which encompassed work by pioneers such as Ibsen [50] and Schwalbe [51] in the 19th century on animal specimens, as well as later studies of the human system by Eichler [52], Siebenmann [53], Nabeya [54], and Scuderi and Del Bo [55]. The information provided by these authors was at times incomplete and conflicting [49], which is not unexpected given the limitations in existing imaging technology and the complexity of the cochlear vasculature (cf. Siebenmann's illustration in Figure 2.9). Axelsson went on to unify the previous work, so the information in the remainder of this section is drawn predominantly from his account.

The origin of the cochlear blood supply can be traced back to the *brachiocephalic trunk*. From here, the arterial path typically follows the vertebral, basilar, anterior inferior cerebellar, and labyrinthine arteries in order as shown in Figure 2.10, though slight variations may exist

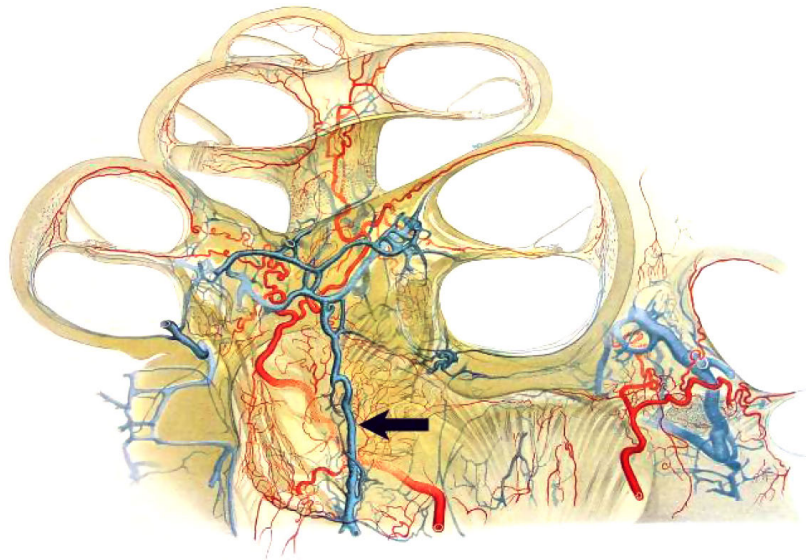


Figure 2.9: Sketch of the cochlear vasculature by Siebenmann, demonstrating the intricate structure of the blood vessel network. The black arrow indicates the “central auditory vein”, which likely refers to what is now termed the “common modiolar vein” (cf. Figure 2.13). (Source: Siebenmann [53].)

amongst individuals. In either case, the *labyrinthine artery* is usually the sole supplier of blood to the cochlea. It follows N VIII through the *internal acoustic meatus*, and branches to form the *anterior vestibular artery* (AVA) and the *common cochlear artery*. The latter then divides into the *vestibulo-cochlear artery* (VCA) and the *spiral modiolar artery* (SMA).

Each of these three terminal branches leads to a different region of the inner ear. The AVA supplies the posterior vestibule and the lateral and anterior semicircular canals [56]. The VCA enters the modiolus near the bottom of the basal turn and splits into the *vestibular branch* and the *cochlear branch*, which run basally and apically along the spiral respectively. The former supplies the basal-most end of the cochlea, the posterior semicircular canal and the vestibule, while the latter supplies about a third of the basal turn before anastomosing with the SMA. This third terminal branch supplies the remaining majority of the cochlea and is therefore the most important.

Upon entering the second quadrant of the basal turn, the SMA runs apically, spiralling around the nerve trunk until it reaches the helicotrema (see Figure 2.11). Internal and

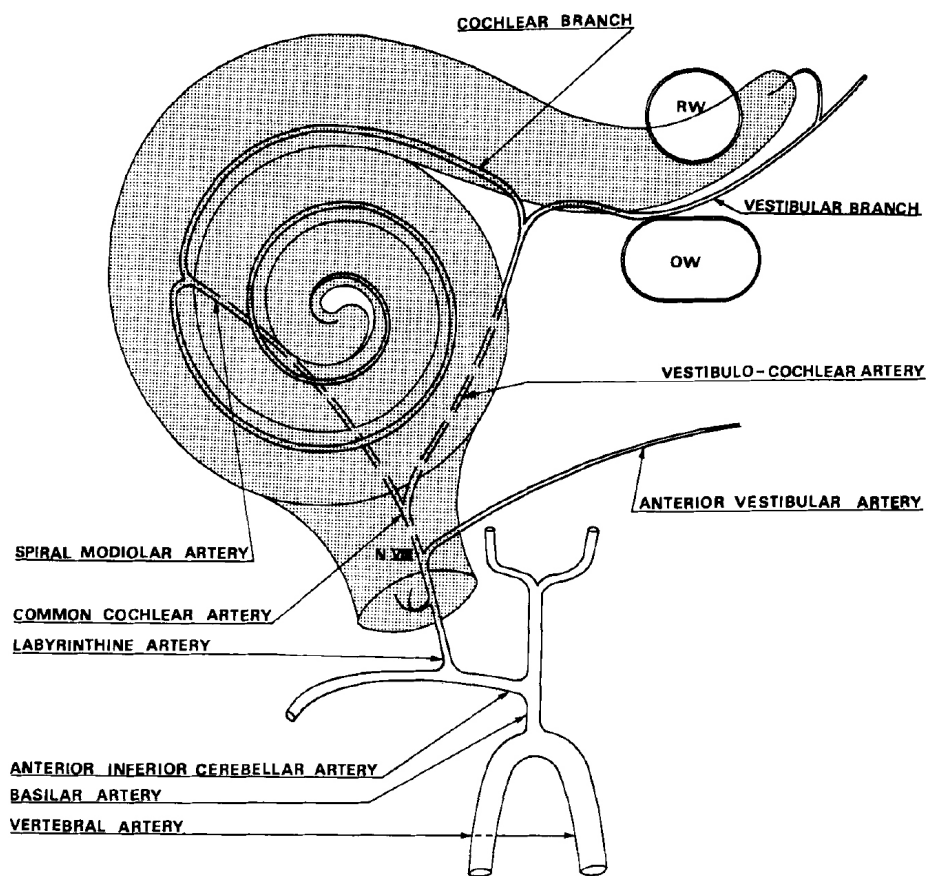


Figure 2.10: Schematic of the cochlear arterial supply in man. OW=oval window; RW=round window; N VIII=vestibulocochlear nerve. (Source: Axelsson [49]. Copyright © 1968, Taylor & Francis.)

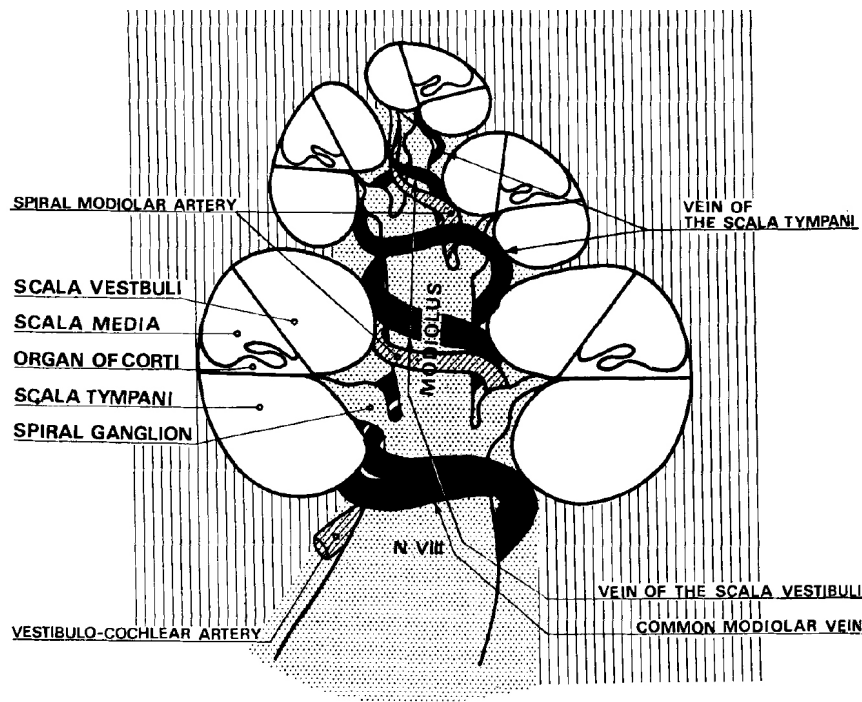


Figure 2.11: Cross-sectional schematic of the modiolar vessels in man. (Source: Axelsson [49]. Copyright © 1968, Taylor & Francis.)

external *radiating arterioles* regularly branch off normal to the helical path, feeding capillary beds in the modiolus, the spiral lamina and the external wall. The capillaries rejoin, forming *collecting venules* that drain into the cochlear veins. These radial vessels are shown in Figure 2.12.

Human cochleae exhibit a double venous system, one for the scala vestibuli and one for the scala tympani. The former is drained along with the spiral lamina by a discontinuous series of venous segments together known as the *vein of the scala vestibuli* (VSV), which is located centrally in the modiolar wall (see Figures 2.11 and 2.13). Likewise, the latter is drained with the spiral ganglion and the external wall of the scala media by the similarly-structured *vein of the scala tympani* (VST). The VSV and VST merge near the first quadrant of the basal turn to form the common modiolar vein (CMV). More basally, the *vein of the round window* (VRW) drains the associated collecting venules. Both the VRW and the CMV join with the

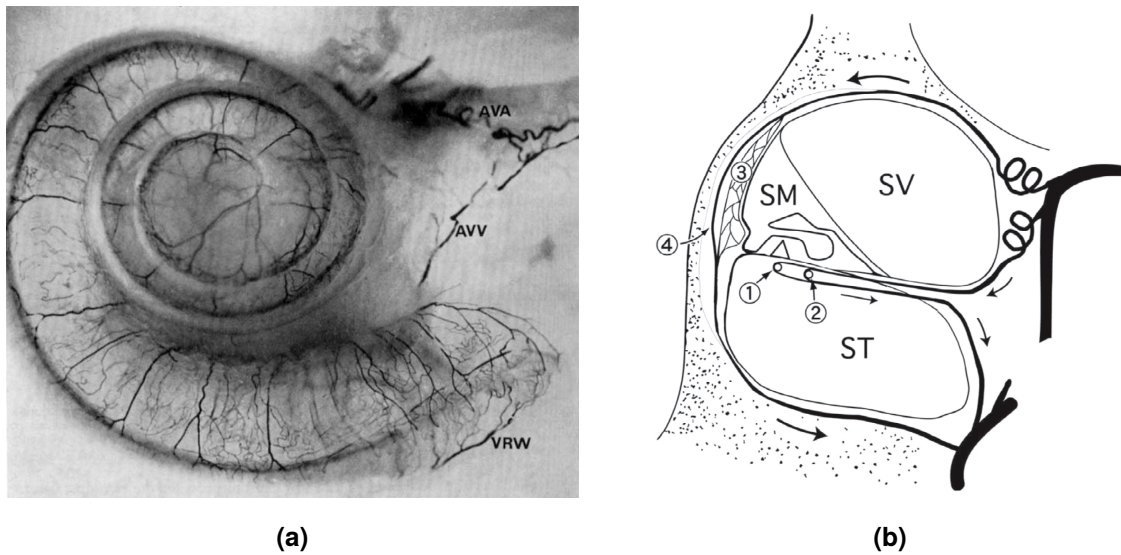


Figure 2.12: (a) Radiating arterioles (darker) and collecting venules (lighter) in the human cochlea. AVA=anterior vestibular artery; AVV=anterior vestibular vein; VRW=vein of the round window. (Source: Axelsson [49]. Copyright © 1968, Taylor & Francis.) (b) Schematic view through one turn of the cochlea. (Source: Nakashima *et al.* [57]. Copyright © 2003, Elsevier B.V.)

vestibulo-cochlear vein (VCV) to become the vein of the cochlear aqueduct (VCAQ), which leaves the cochlear region.

Reissner's membrane and some parts of the organ of Corti are avascular.

2.1.3 Comparison of Human and Guinea Pig Cochleae

Although the ultimate goal of cochlear implant (CI) research is to restore the perception of hearing in humans, the anatomical surroundings of the human cochlea make *in vivo* testing challenging. The otic capsule surrounding the cochlea is both thick and extremely dense, and its location deep within the petrous part of the temporal bone impedes surgical access. Experimental implantation and probing is unwarranted given the high ratio of risk to benefit. Cadaveric studies are one alternative, but changes in both the shape and properties of the tissues post-mortem impede the extrapolation of insights to living subjects [30,58].

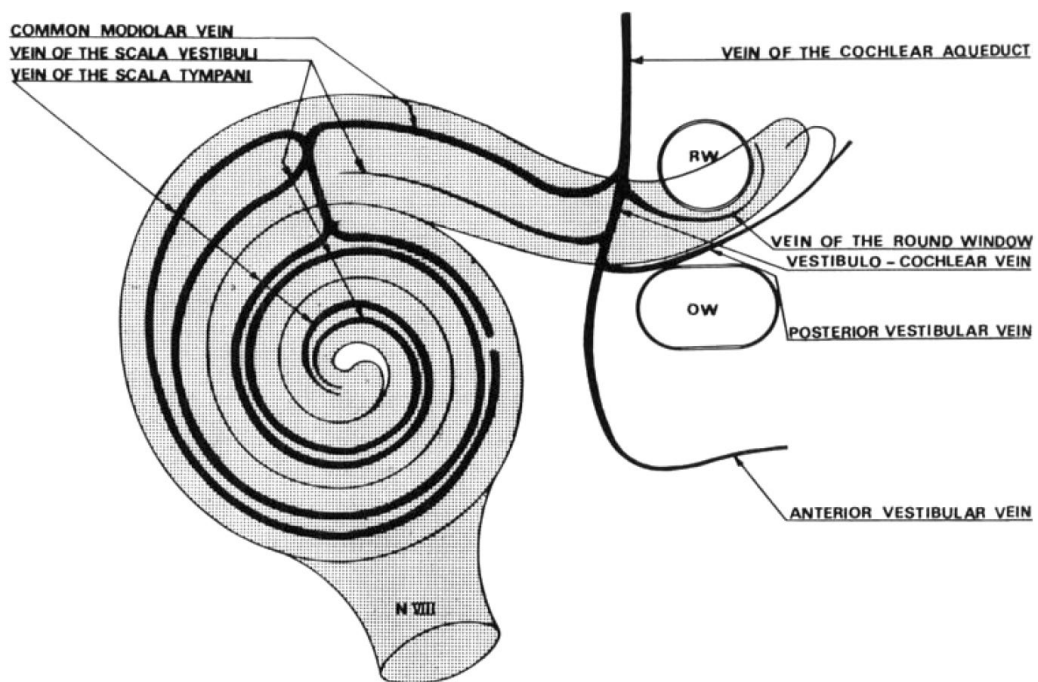


Figure 2.13: Schematic of the cochlear venous drainage in man. OW=oval window; RW=round window; N VIII=vestibulocochlear nerve. (Source: Axelsson [49]. Copyright © 1968, Taylor & Francis.)

Since the mammalian cochlea is similar in both structure and function across species, many CI studies have been performed on animals—typically cats and guinea pigs, but also mice, gerbils, rats, chinchillas, and monkeys [30,49,59,60]. The cochlea of the guinea pig is commonly used because it is relatively large [60] and, unlike the human cochlea, it is easily exposed in the tympanic bulla [61] (see Figure 2.14), allowing experimental measurements to be taken relatively easily. Miyamoto [62] noted that guinea pig cochleae serve as “an appropriate experimental animal model for. . . [electrophysiological studies] of cochlear function”.

Like other mammals, the cochleae of both humans and guinea pigs are comprised of the cross-sectional structures shown in Figures 2.7 and 2.8 spiralling around a nerve-filled modiolus. There are several notable differences relative to the human cochlea; the main ones are listed in Table 2.3.

Since the guinea pig cochlea is not embedded within the petrous part of the temporal bone, different current pathways are expected [30]. These differences mean that although the modelling results may be indicative, care must be taken when extrapolating results from one species to another [65].

2.2 Hearing Physiology

2.2.1 Normal Hearing

Normal hearing is comprised of two distinct stages: the first (sensation) occurs when a sound stimulus is detected at the biological receptor; the second (perception) occurs when a conscious awareness of the sensation is obtained [40]. Sensation is therefore clearly a prerequisite for perception, and any complications in sensing a sound stimulus flow on to impair the perception of that sound.

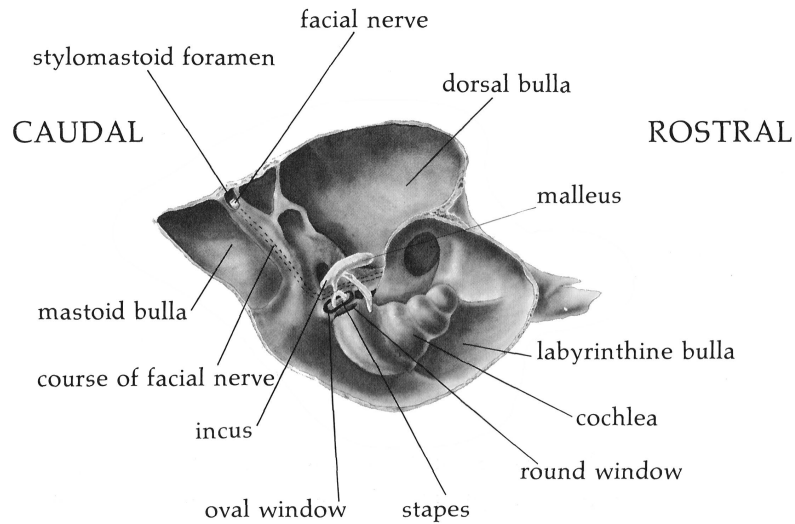


Figure 2.14: Internal aspect of the tympanic bulla in the guinea pig. Note how the lateroapical portion of the cochlea protrudes into the air space of the tympanic bulla. (Source: Cooper and Schiller [61]. Copyright © 1975, Harvard University Press.)

Table 2.3: Comparison of human and guinea pig cochleae. Data compiled from various sources [31, 43, 47, 63–65].

Attribute	Human	Guinea pig
Number of turns	2.2–2.9	3.5–4
Scalae length	26–28 mm	≈16 mm
Volume of scala tympani	29 μ L	4.8 μ L
Myelination of spiral ganglion cell bodies	Rare (<5%)	Mostly myelinated
Geometry of basal end	Follows spiral trajectory	Hooked (turns more parallel with cochlear axis)
Location within bone	Embedded except for the round and oval windows	Apex protrudes into tympanic bulla

The propagation of sound waves through the cochlea is illustrated in Figure 2.15. Sound stimuli consist of pressure waves moving through a medium, typically air or water. They are funnelled into the external acoustic meatus by the auricle and detected by the tympanic membrane, which vibrates in response. These vibrations are mechanically coupled by the auditory ossicles to the oval window, where the action of the stapes footplate induces compressional waves in the perilymph. The 20:1 area ratio between the tympanic membrane and the stapes footplate and the 1.31:1 lever ratio between the moment arms of the malleus and the incus help to minimise the loss of energy that would otherwise occur due to the large difference in acoustic impedances between air and perilymph [46].

Sound waves travel up through the scala vestibuli to the helicotrema and return via the scala tympani, generating a pressure gradient that distorts the organ of Corti and the basilar membrane (together called the *cochlear partition*). Von Békésy [66] showed that this *travelling wave* peaks at different locations along the basilar membrane due to its varying stiffness, with higher frequencies peaking at the base and progressively lower frequencies toward the apex as per Figure 2.4. As the cochlear partition is deflected by the travelling wave, relative movement between the tectorial membrane and the hair cells of the organ of Corti causes displacement of the stereocilia. Displacement toward the tallest row opens ion channels in the stereocilia, and the subsequent influx of cations depolarises the hair cell (Figure 2.16). This in turn opens the calcium channels at the base of the hair cell near the afferent nerve fibres, triggering the release of neurotransmitters across the synapse and inducing action potentials in the peripheral process of the auditory nerves. Displacement in the opposite direction leads to hyperpolarisation. Neural excitation is discussed in more detail in §3.2.3.

According to the commonly accepted *place theory* of pitch perception, hair cells only respond to the frequency component which peaks at their particular location along the basilar membrane. In this way, the cochlea can be thought of as a mechanical Fourier transformer that directly extracts a spectral representation from the sound stimulus [66]. The correlation

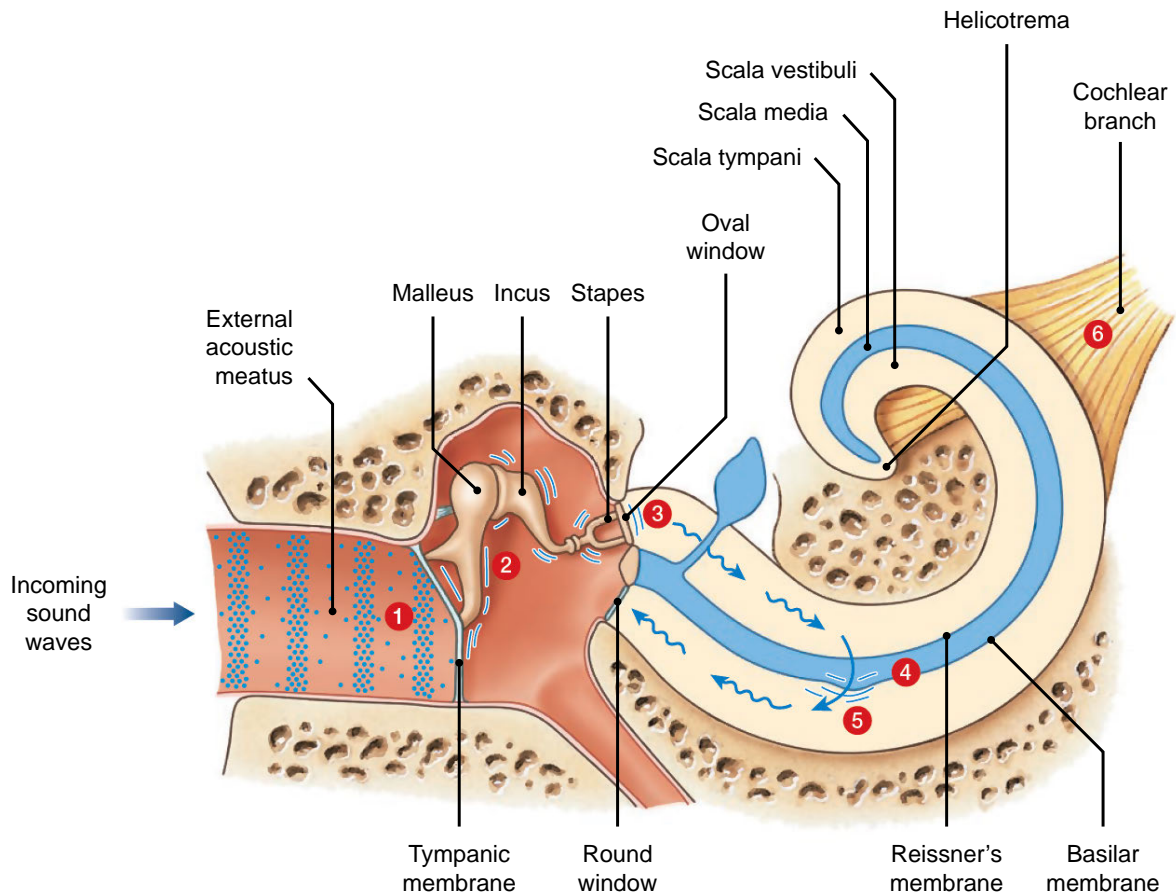


Figure 2.15: Sound wave propagation in the cochlea. Vibrations in the air are (1) received by the tympanic membrane, (2) transmitted via the ossicles to the oval window, and (3) travel up the scala vestibuli towards the helicotrema. For each frequency component, the travelling wave (4) peaks at a characteristic location along the cochlear partition and stimulates the corresponding hair cells, before (5) continuing via the scala tympani towards the round window, where the displacement is dissipated. Action potentials triggered by hair cell stimulation are (6) sent via the cochlear nerve to the auditory cortex for processing. (Image adapted from Martini *et al.* [40]. Copyright © 2006, Daryl Fox.)

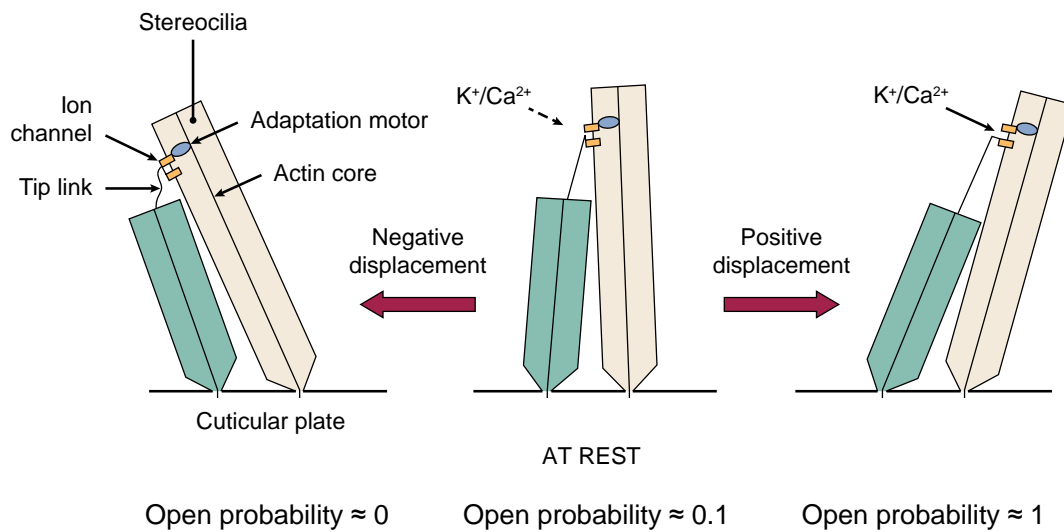


Figure 2.16: Effect of stereocilia movement on ion channels. Displacement toward the tallest row stretches the spring-link tip links, opening the cation channels and leading to depolarisation of the hair cell. (Image adapted from Flint *et al.* [46]. Copyright © 2010, Mosby.)

between characteristic frequency and location (both along the cochlear partition and in the auditory cortex) is termed the *tonotopic organisation* of the cochlea, and has been documented for several mammalian species by Greenwood [59].

In the final stage, action potentials are relayed via N VIII to the auditory cortex of the brain. It is there that the signals are decoded and interpreted, giving rise to a conscious awareness of the original stimulus (i.e. sound perception).

2.2.2 Hearing Loss

Any reduction in the ability of an individual to perceive sound naturally is known as hearing loss. There are two main categories: *conductive hearing loss* and *sensorineural hearing loss*. A small proportion of affected individuals suffer from *mixed hearing loss*, where both of these cases are exhibited.

Conductive hearing loss (CHL) occurs when there is a problem in the outer or middle ear. Such conditions prevent vibrations in the air from being mechanically transmitted through to the inner ear. Common causes of CHL include obstruction of the external auditory meatus or of the auditory tube, thickening or perforation of the tympanic membrane, bacterial or viral infections of the middle ear, and fixation or decoupling of the auditory ossicles [3, 46, 48].

Sensorineural hearing loss (SHL) occurs when there is a problem with the cochlea, the auditory nerve, or the auditory cortex. These locations are downstream in the hearing chain, so SHL can manifest in individuals with a normal outer and middle ear. The former is the most common and generally results from damage to or degeneration of the hair cells in the organ of Corti. Common causes of SHL include congenital malformations, exposure to excessive noise, hair cell attrition due to aging (known as *presbycusis*), and chemical damage from smoking or medications [3, 48]. Disorders of the inner ear vascular supply can also result in SHL [48].

In either case, the degree of impairment can vary from negligible to complete deafness. Scales are indicative but arbitrary, and can vary amongst authorities. The classification system used by the World Health Organisation is shown in Table 1.1.

2.3 Chapter Summary

The cochlea is one part of the mammalian auditory pathway. It primarily consists of three spiralling fluid chambers, known as the *scalae vestibuli*, *media*, and *tympani*. These three chambers are separated by Reissner's membrane and the cochlear partition (formed by the organ of Corti and basilar membrane) respectively, and are bordered along the peripheral side by the spiral ligament and *stria vascularis*. At the centre of the spiral path is the bony *modiolus*. The cochlear nerve enters through the base of the *modiolus* and unravels to supply

the hair cells in the organ of Corti in a tonotopic manner. The major arteries and veins of the cochlea also follow a modiolar path, with smaller radial branches and capillary beds supplying the structures within. This is all surrounded by the incredibly dense otic capsule, and is embedded in the petrous portion of the temporal bone.

The overall structure is similar between humans and guinea pigs, but naturally there are differences in geometry between species. Nonetheless, processes leading to sound perception are the same. Sound entering a normal hearing cochlea is picked up by the hair cells and transduced into a series of action potentials that are interpreted by the brain. Unfortunately, this ability is impaired in some individuals. For those with profound SHL due to hair cell damage, the only successful treatment is a hearing prosthesis known as the cochlear implant.

Chapter 3

Literature Review

This chapter addresses the following questions:

- What are cochlear implants?
- How does electrical stimulation compare to normal hearing?
- What is the state-of-the-art for bioelectric models of the cochlea?
- What are the outstanding issues that need to be addressed?

3.1 Cochlear Implants

Cochlear implants (CIs) are hearing prostheses that have been designed and successfully used to treat severe to profound sensorineural hearing loss (SHL). Although individuals with defective hair cells are unable to convert sound waves into the corresponding neural excitation patterns [10], their residual spiral ganglion cells and the corresponding neuronal axons are often still healthy and functional [67]. These tissues are therefore the target of hearing restoration efforts. By injecting electric current into the inner ear, CIs establish an

electrochemical gradient in the cochlear tissues that directly stimulates the afferent auditory nerve fibres [68, 69], bypassing the defective hair cells. The modular design of the nervous system, along with the plasticity of the brain itself, enables these artificially induced neuronal impulses to be interpreted as sound in much the same way as normal hearing [70].

3.1.1 Components and Function

As shown in Figure 3.1, most CI systems include both an external unit (Figure 3.2a), which sits on the outside of the head, and an internal unit (Figure 3.2b), which is surgically implanted under the scalp. The implant body is placed into a pocket that is drilled into the mastoid bone, and the coiled electrode array is inserted into the scala tympani of the cochlea (Figure 3.3). The two parts communicate via transcutaneous induction, enabling the battery and speech processor to be replaced or upgraded without revision surgery.

The system mimics the processes that occur during normal hearing. Sound waves are detected using a microphone on the external unit, fulfilling the role of the tympanic membrane. These signals are sent to a speech processor, which uses a combination of Fourier transformations, band-pass filters, and envelope detection algorithms to extract spectral and temporal auditory information from the waveform. In essence, the speech processor replicates the mechanical transduction of the cochlea using electronics. Over the years, many different speech processing algorithms have been developed, with the aim of extracting and presenting as many useful cues to implant recipients as possible. Louizou [8] provides a good summary of the developments in this area.

The stimulus controller then maps each frequency band to the corresponding electrode pad in the intracochlear array, adjusts each signal to meet patient-specific current thresholds that are determined during a post-operation training phase, and encodes these stimulus parameters for each channel. These signals, along with power, are sent via the induction

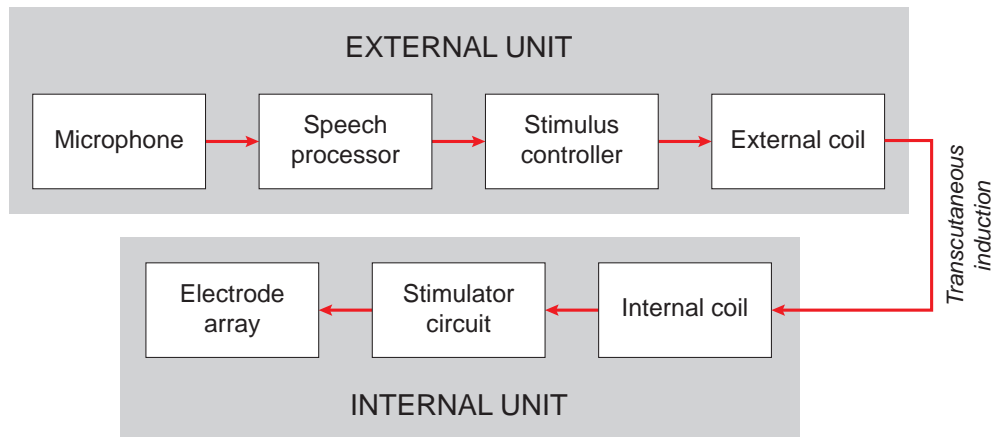


Figure 3.1: Schematic diagram of a cochlear implant system. (Adapted from Webster [71].)



Figure 3.2: The Nucleus 6 cochlear implant system by Cochlear Limited. (a) The external behind-the-ear unit, housing the battery, microphone, speech processor, and stimulus controller tethered to the external coil. (b) The cochlear implant proper, consisting of the internal coil, stimulator circuitry, return electrodes, and intracochlear electrode array. The external and internal coils are aligned using magnets. (Source: Cochlear Limited.)

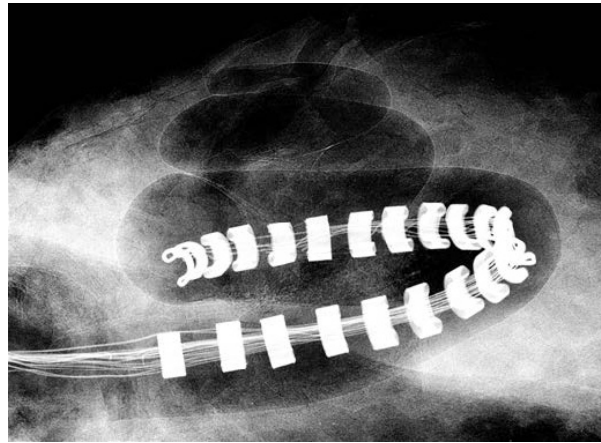


Figure 3.3: Phase-contrast x-ray image of an intracochlear electrode array *in situ*. Note how the half-banded electrode pads in this design face towards the modiolus. (Source: Xu [72]. Copyright © 2001, Wolters Kluwer.)

link to the implanted receiver-stimulator circuitry, which in turn directs the current pulses to the appropriate electrode pad along the intracochlear array [10, 71]. Since the array follows the spiral path of the cochlea, different pads inject current pulses at different locations corresponding to the tonotopic organisation of the nerve fibres (see, for example, Figure 3.4). This allows the CI to elicit percepts for a wide range of targeted frequencies as required for effective speech recognition [26, 73, 74].

3.1.2 Stimulation Mechanics

Although the process of charge injection sounds relatively straightforward, the details of actually implementing such a system are quite complex. Two aspects that are particularly relevant to this thesis are discussed briefly below.

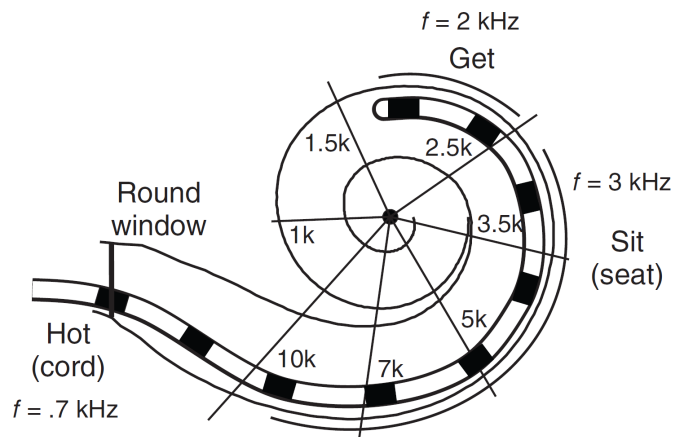


Figure 3.4: Correlation between intracochlear electrode location and perceived frequency as observed in Rodney Saunders, the first cochlear implant recipient. Note the similarities with Figure 2.4. (Source: Clark [26]. Copyright © 2013, Macmillan Publishers Limited.)

Charge Balance

Metals are *electronic conductors*, i.e. the particles responsible for carrying charge are electrons; in contrast, biological tissues are *electrolytic conductors*—the charge carriers are ions [71, 75]. Since metals contain no free ions and the inner ear fluids have no free electrons, intracochlear electrodes must transduce an electronic current into an ionic current to effect charge injection across the electrode-tissue interface. This is accomplished through chemical reactions at the interface [71].

The typical surface reactions for platinum electrodes are listed in Table 3.1. At the time of writing, platinum is the preferred material for use in intracochlear electrodes because its inertness makes it unlikely to oxidise and dissolve into the *in vivo* environment [76]—a crucial attribute for safe, long-term electrical stimulation. The chemical stability of the electrode alone is, however, not a sufficient condition for safety.

Consider electric current that is applied in a single direction, say from the electrode to the inner ear fluids. With time, this current will deliver a net charge that favours oxidation reactions, and the products of these reactions will accumulate and diffuse away from the

Table 3.1: Surface reactions at the electrode-tissue interface, in order of increasing potential. (Compiled from various sources [76, 77].)

(a) Oxidation reactions.

Reaction	Equation
Oxygen plating	$\text{Pt} + 2[\text{OH}]^- \rightleftharpoons \text{PtO} + \text{H}_2\text{O} + 2\text{e}^-$
Oxygen evolution	$4[\text{OH}]^- \rightleftharpoons \text{O}_2 + 2\text{H}_2\text{O} + 4\text{e}^-$
Oxidation of organics (example)	$\text{CH}_3\text{CH}_2\text{OH} + 2[\text{OH}]^- \rightleftharpoons \text{CH}_3\text{CHO} + 2\text{H}_2\text{O} + 2\text{e}^-$
Platinum dissolution	$\text{Pt} + 4\text{Cl}^- \rightleftharpoons [\text{PtCl}_4]^{2-} + 2\text{e}^-$
Chlorine evolution	$2\text{Cl}^- \rightleftharpoons \text{Cl}_2 + 2\text{e}^-$

(b) Reduction reactions.

Reaction	Equation
Oxygen reduction	$\frac{1}{2}\text{O}_2 + \text{H}_2\text{O} \rightleftharpoons \text{H}_2\text{O}_2$
Hydrogen plating	$\text{Pt} + \text{H}^+ + \text{e}^- \rightleftharpoons \text{PtH}$
Hydrogen evolution	$2\text{H}^+ + 2\text{e}^- \rightleftharpoons \text{H}_2$

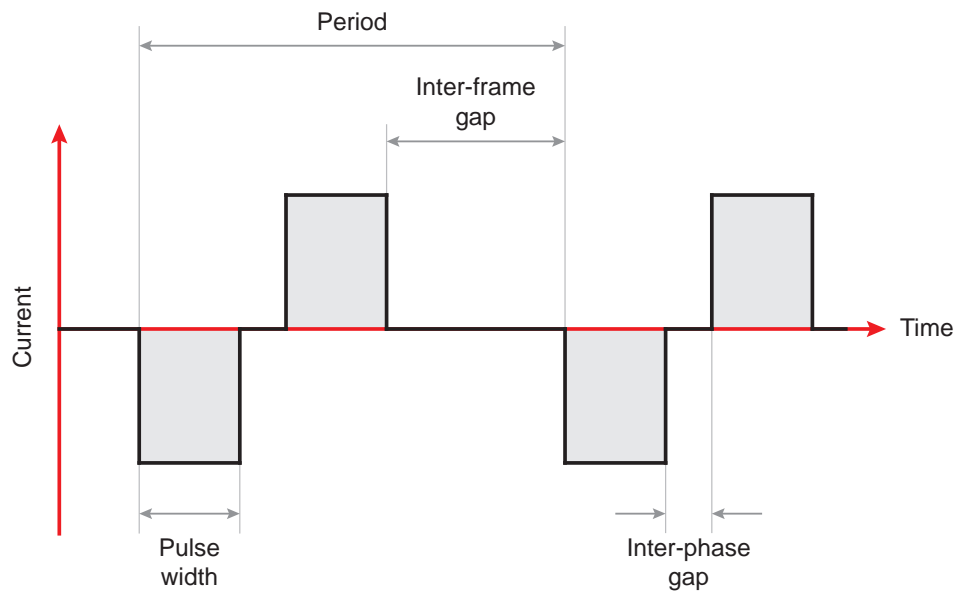


Figure 3.5: Charge-balanced, cathodic-first biphasic pulses, typically used in electrical stimulation. The overall period of a pulse can be divided into subtimings such as the pulse width, inter-phase gap, and inter-frame gap as labelled in the diagram. Charge delivered during each phase (represented by the shaded areas) should be equal.

electrode-tissue interface due to concentration gradients [75]. These products, such as the evolution of chlorine gas *in vivo* (Table 3.1a), may be harmful to the cochlear tissues [77–79].

To prevent such a situation, current is typically delivered as charge-balanced biphasic pulses [80], an example of which is illustrated in Figure 3.5. The first phase of a biphasic input is responsible for neuronal recruitment [60,81,82]. The second phase, which occurs during the refractory period of the stimulated neurons, serves to neutralise the overall charge and reverse any reactions induced during the first phase. Most electrical stimulation systems use cathodic-first pulses because cathodic stimulation produces a higher depolarisation peak than anodic stimulation [81] and therefore requires less current to reach the threshold for excitation.

CIs typically use a constant current level for each pulse to simplify the balancing of electric charge (Figure 3.6a). The phases are usually symmetric (i.e. they have the same amplitude

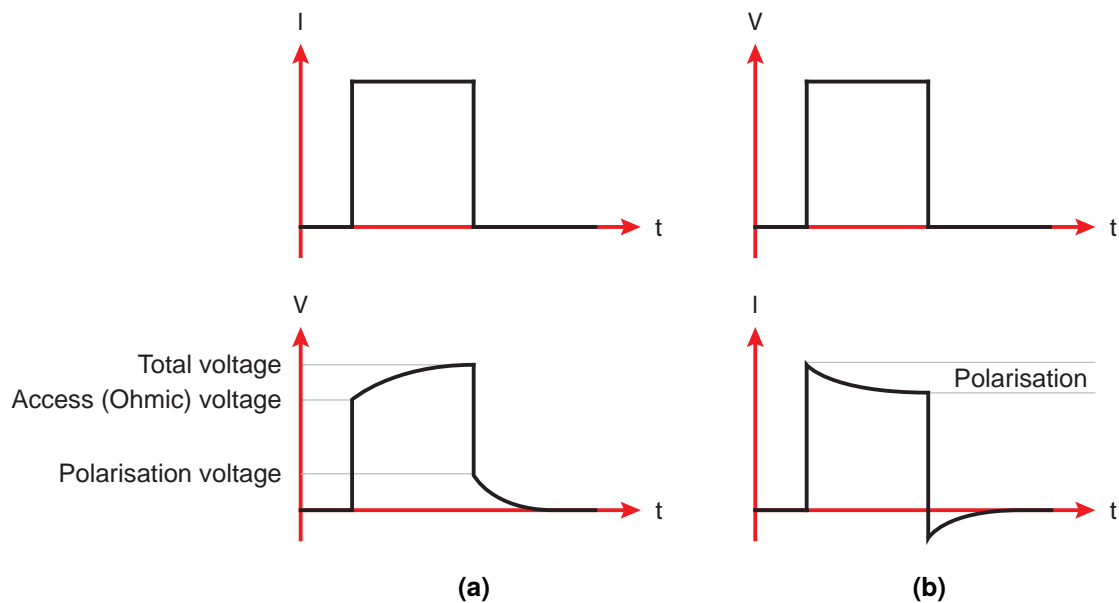


Figure 3.6: Current and voltage waveforms for (a) constant current pulses, and (b) constant voltage pulses. Constant current pulses are generally preferred because they make it easier to ensure zero net charge injection. The access voltage is the same at both the leading and trailing edges of the pulse. (Adapted from Webster [71].)

and pulse width), but it is possible to use asymmetric pulses so long as charge balance is maintained [80]. Constant voltage pulses (Figure 3.6b) may also be used, but are not common in practice. The electric potential at the stimulating electrode varies over time when constant current pulses are used due to the capacitive effects of the electric double layer at the interface [75, 83, 84]. Care must be taken to ensure that the total potential does not enter the range that induces irreversible reactions.

Electrode Configurations

Most CI systems in use today have multiple channels and up to two dozen independent electrodes [85]. Cochlear Limited's Contour Advance, for example, has 22 half-banded platinum contacts along the intracochlear array, a platinum ball-shaped electrode that is tethered to the implant unit, and the exposed titanium casing around the stimulator circuitry,

which effectively serves as a plate electrode. Since a source-sink configuration can be set up between any subset of these electrodes, there are a variety of different combinations that may be employed [74], some of which are illustrated schematically in Figure 3.7.

Monopolar (MP) stimulation is the most common configuration used in contemporary CIs. Here, current is only injected at one of the intracochlear electrodes, and returns via the bodily tissues to one or both of the extracochlear electrodes. This mode of stimulation tends to yield the lowest thresholds [74] (i.e. the minimum current level required for the CI recipient to perceive sound) because the injected current spreads out from the source electrode, but conversely, the current is also the least focused [86], stimulating neurons over a relatively wide band of frequencies in the process [12,30].

Stimulating a narrower band of neurons is an important goal because it enables finer pitch discrimination in CI recipients [12,30]. One way to achieve this is to use *common ground* (CG) stimulation, where the non-stimulating electrodes are used together as a single return path instead of the extracochlear electrode [74]. In a *bipolar* (BP) configuration, two intracochlear electrodes are used as the source and the sink. The two electrodes are typically adjacent, but may also be separated by one or two pads (known as BP+1 and BP+2, respectively). BP stimulation was often used during the early phases of multielectrode CI development because, at least in a homogeneous material, injected current would flow more or less directly between the two electrodes, limiting the spread of excitation [30,31]. A variation of BP, called *tripolar* (TP) stimulation, splits the return path between both adjacent flanking electrodes and, if desired, the extracochlear electrode, generating a more symmetric field like that of MP stimulation but with less current spread [30,74]. Recent research efforts have looked at *phased array* (PA) stimulation [12,87,88], also known as multipolar stimulation in some texts. In this mode, opposing currents are applied at all electrodes, with weightings based on the inverted transimpedance matrix along the array to yield a resultant voltage profile that is zero at all but the stimulating electrode(s) [12].

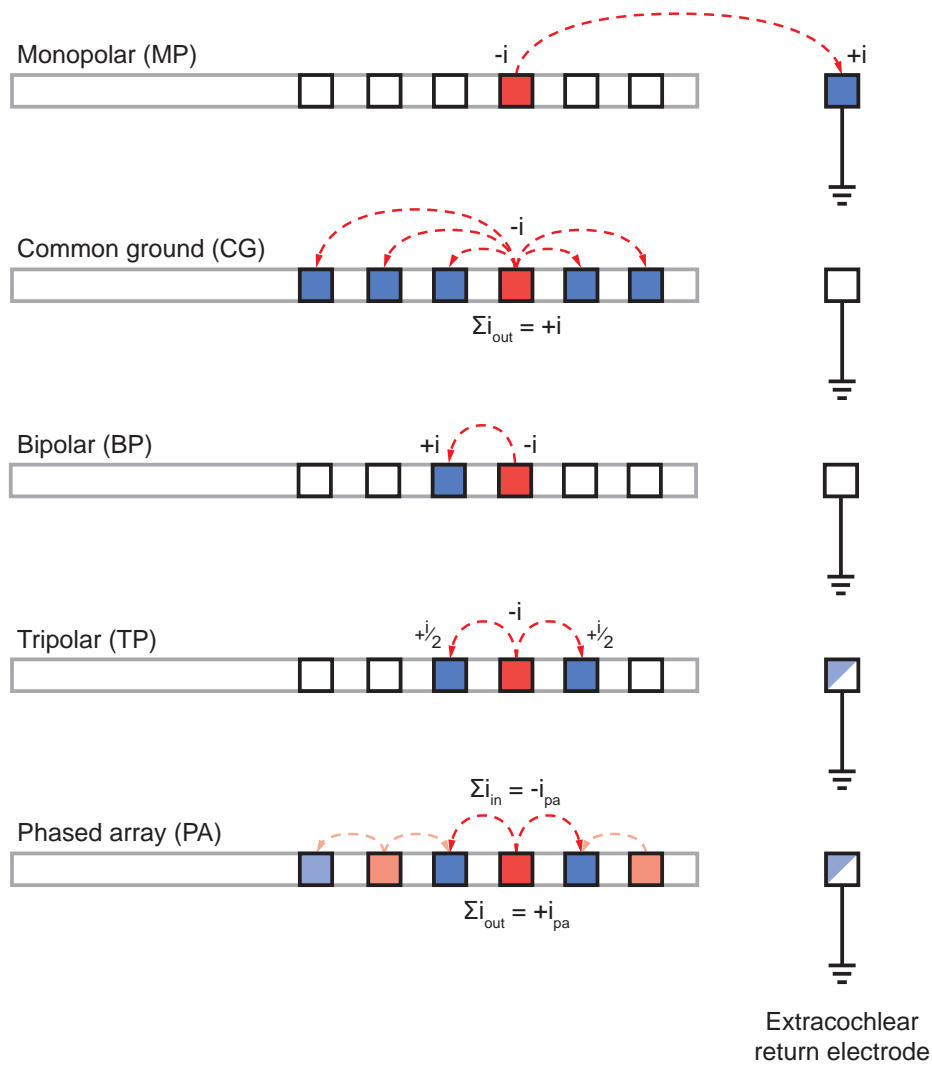


Figure 3.7: Modes of stimulation for a cochlear implant. MP stimulation is the most common mode used in implant recipients. Note that the extracochlear electrode may be used in TP and PA stimulation modes. Different configurations produce different current paths in the cochlear volume, and the resulting perception of sound can differ in many ways.

As with other design decisions, there are costs associated with the use of more focused stimulation modes. *Ceteris paribus*, the trade-off is higher power draw when generating auditory percepts at any given level of loudness [12, 37]. In addition, there may be no perceptual benefit in using more focused modes if the residual spiral ganglion cell bodies in the region of the targeted frequency band have already degenerated [67].

3.1.3 Efficacy and Unsolved Challenges

CI stimulation has come a long way since the first recipient was implanted [26, 31]. Clinical reviews, such as those by Nadol and Eddington [68] and Clark [10], have shown significant progress in the restoration of hearing perception. Economic reports [3] have also noted their benefit to the wider society due to flow on effects such as increased productivity and wellbeing in CI recipients. Indeed, the mere fact that the industry itself exists is a testament to the success of the CI in fulfilling its mandate.

Nonetheless, there are several scenarios for which CIs can still be significantly improved. Firstly, noisy environments are commonly encountered in daily life and present an ongoing challenge for CI recipients because the noise masks individual sound signals, making it difficult to isolate the desired source [89, 90]. Secondly, music perception has been found to be less enjoyable following implantation due to inadequate pitch and timbre perception [91–93]. Thirdly, although the CI is well tuned for English speakers, those who speak tonal languages miss out on a lot of semantic information [12, 94–96]. Many have called for or assumed that better speech processing techniques will overcome these challenges because most of the improvements in patient outcomes have thus far stemmed from research in that area [8, 12, 21, 97], but despite the merits of more sophisticated algorithms, updates in speech processing have not resulted in the desired level of clinical advancement for many years now [7, 11].

Considering that the mechanism ultimately responsible for auditory nerve stimulation is the *in vivo* current distribution, it would appear that the bottleneck of information transfer in CI systems lies with the implanted unit, specifically with existing designs of the intracochlear electrode array [25, 26]. Given the difficulties of obtaining and visualising such information using *in vivo* and *in vitro* experiments alone, a detailed *in silico* electroanatomical map of CI induced current flows would be valuable for furthering our understanding of the cochlea's electrical behaviour [20–22, 35, 98–101]. An accurate and well-validated model has the potential to reveal methods for achieving more precise spatial control of the electric field generated by the CI, as well as other benefits such as lower power consumption. New intracochlear electrode array designs may also be virtually prototyped and tested for efficacy before any physical assets are requested [60], reducing the overall cost of development while optimising implant design and performance.

3.2 Bioelectric Modelling

3.2.1 Expected Physics

At a fundamental level, the CI is just like any other system of electrical interactions. The flow of electric current from the stimulating electrode to the return electrode and the corresponding fields and fluxes are fully described by *Maxwell's equations* [102]. They can be written in

differential form as:

$$\nabla \cdot \vec{E} = \frac{\rho}{\epsilon_0} \quad (3.1)$$

$$\nabla \cdot \vec{B} = 0 \quad (3.2)$$

$$\nabla \times \vec{E} = -\frac{\partial \vec{B}}{\partial t} \quad (3.3)$$

$$\nabla \times \vec{B} = \mu_0 \vec{J} + \mu_0 \epsilon_0 \frac{\partial \vec{E}}{\partial t} \quad (3.4)$$

where ∇ is the gradient operator, \vec{E} is the electric field, \vec{B} is the magnetic field, ρ is electric charge density, \vec{J} is electric current density, ϵ_0 is the permittivity of free space, μ_0 is the permeability of free space, and t is time. Equations 3.1–3.4 are also known as Gauss's law for electricity, Gauss's law for magnetism, Faraday's law of induction, and Ampère's circuit law with Maxwell's addition, respectively.

In a CI system, these field quantities are determined by three main factors: the locations of the electrodes, the electric properties of the cochlear tissues, and the magnitude and shape of the injected current pulse. The current pulse is under the control of the device itself and is therefore a well-known input quantity. The other factors are more difficult to quantify, but some insight can be gained from first principles.

In a homogeneous and isotropic cell with end-plate electrodes, the induced electric field is uniformly distributed (Figure 3.8). Consider now a cell that is not homogeneous, but instead contains a second material of different resistivity to the first. In this case, the flux lines would exhibit some distortion because the newly introduced material changes the shape of the electric field [103], as shown in Figure 3.9. Relatively conductive tissues tend to funnel current flow, while those that are relatively insulating are avoided as the current seeks out the path of least resistance. The larger the difference in resistivity between the two materials, the more distortion that can be expected.

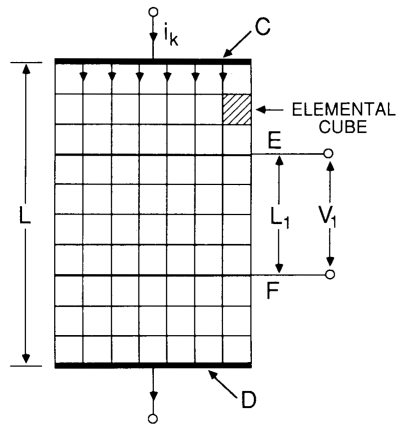


Figure 3.8: Uniform flux lines in a homogeneous isotropic cell. (Source: Baker [103]. Copyright © 1989, IEEE.)

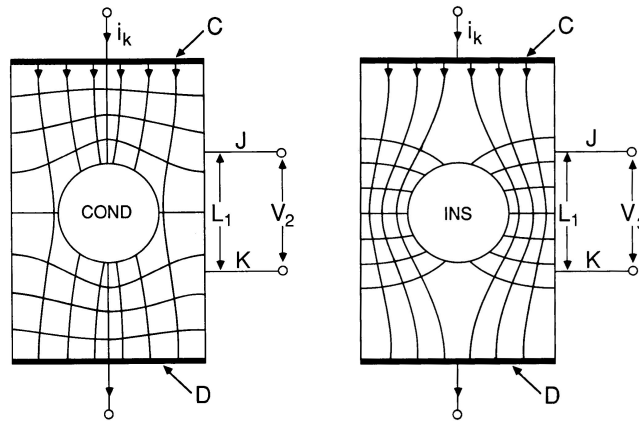


Figure 3.9: Distortion of flux lines in the presence of a conductor (left) or an insulator (right) when using end-plate electrodes. (Source: Baker [103]. Copyright © 1989, IEEE.)

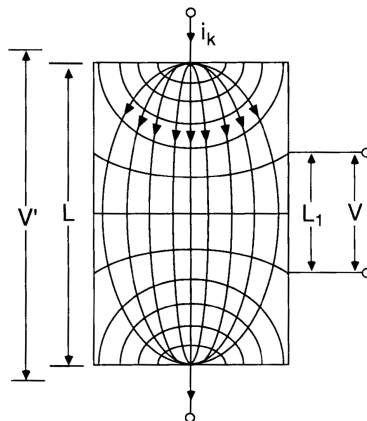


Figure 3.10: Flux lines with small electrodes. Note the non-uniform shape of the current density distribution. (Source: Baker [103]. Copyright © 1989, IEEE.)

Consider again the homogeneous cell, but this time with the end-plate electrodes replaced by much smaller ones, as per Figure 3.10). Again, the flux lines would deviate from uniformity, but here they would take on a different pattern, spreading out from the current source through the medium before reconverging at the sink. Any changes in resistivity that are introduced in this case would have more impact on the current paths if they are located near the small electrodes, since this is where the current density is highest [103].

The simulations in this thesis are expected to adhere to the same physics and thus exhibit both of these patterns. Unlike these simplistic theoretical examples though, the cochlea consists of many tissues and its three-dimensional geometry is complex, so the field patterns are not intuitive. Nevertheless, the current paths will be determined by the anatomical structures as a function of their material properties, which span a wide range due to large differences in tissue morphology, and their proximity to the stimulating electrode, which is small relative to the volume of the cochlea. Note that the cochlear models themselves are in turn small relative to the entire head, so the reconvergence of flux lines at the return electrode (as depicted in Figure 3.10) is not expected to occur within the modelled domain under MP stimulation.

3.2.2 Numerical Methods

Rationale for Computational Modelling

There are several ways these complex electric field patterns could be characterised in a spatial sense. A rudimentary method would be to measure the electric potential at numerous points throughout the cochlea of a CI recipient and then correlate these data with the Cartesian location of each sample to generate an electroanatomical map [30]. Such direct measurements could provide very realistic results since the biological aspects of the system are inherently accounted for. However, the need to physically intrude into the cochlear tissues makes this impractical for both *in vivo* and *in vitro* studies, as noted in §1.2.1.

An alternative approach would be to take measurements at fewer, more accessible locations, and make assumptions about the behaviour of the electric field at points that are not directly measured [30]. That is, in essence, the modelling process, which has become a preferred method of investigation for CI research. Early efforts used *lumped-element models* (LEMs), which attempted to represent the electric response of the implanted cochlea as an equivalent electric circuit. Key locations, such as the position of the stimulating and measuring electrodes, were connected by a network of electric circuit components (typically resistors), with each component representing the response of one or more of the biological tissues along a presumed current pathway between the connected nodes.

However, a quick comparison of the published LEMs reveals a major flaw in this approach: since the true shape of the cochlea is ignored, the selection of electrical elements and connections in these circuits is arbitrary, leading to a multitude of circuit representations for the same electroanatomical system (see §3.3.1). The models were sufficient insofar as each LEM was only related back to the corresponding experimental measurements to yield bulk impedances between two points in that circuit. LEMs are therefore useful for global insights into CI stimulation [104, 105], but better spatial representation is required for more generally applicable results. Indeed, von Békésy noted in his pioneering study that the use of more elements in the network would provide a closer approximation of the *in vivo* situation [106].

The development of integrated circuits in the 1970s was a significant milestone for modelling research because it enabled the development of numerical solution methods that were computationally intense. Although these numerical methods were originally developed for structural mechanics, they were later applied to other types of physics by discretising the appropriate governing equations; in the case of electromagnetic simulations, these are the aforementioned Maxwell's equations. Sustained increases in processing power, driven by advances in microprocessor architectures and manufacturing processes, meant that by the mid-1980s, a new class of electroanatomical model, based on numerical analysis, had become viable [107].

These models are generally referred to as *volume conduction models* (VCMs) because the geometry of the modelled domain is based on the true three-dimensional (3D) shape of the physical system. VCMs of the implanted cochlea are reviewed in §3.3.2.

Numerical methods for bioelectric volume conduction problems have been reviewed by several authors [35, 107–110]. The main differences between the mathematical formulations of the three most popular approaches—the *finite difference method* (FDM), the *finite element method* (FEM), and the *boundary element method* (BEM)—are summarised below.

Discretisation and the Finite Difference Method

All three methods involve approximating the continuous domain with a finite number of subspaces—a process known as *discretisation* or *mesh generation* [111]. The FDM is the most traditional of the three approaches and uses the differential form of Maxwell’s equations. Under the FDM, the continuous domain is discretised into a uniform orthogonal grid to yield a pointwise approximation [35]. At each point, the derivatives are expressed algebraically as differences between adjacent points in the finite difference grid. These reference the material properties representing the electric behaviour of the tissue at that point (namely conductivity and permittivity). The whole system is then evaluated by recombining the equations into a global matrix using continuity conditions and solving for the unknown dependent variable (i.e. the electric potential) at each node using a set of constraints (namely the *electrical loads* and *boundary conditions*) [107]. The numerical estimate converges to the exact solution as more subspaces are used; for the FDM, this requires a denser point cloud.

The FDM is quite simple to implement and compute, making it a good candidate for time-domain simulations [107]. It is well suited to modelling devices with man-made geometries and engineering materials, especially those with straight edges such as cantilever beams. However, geometries that are not aligned with the grid will suffer from inaccuracies due to

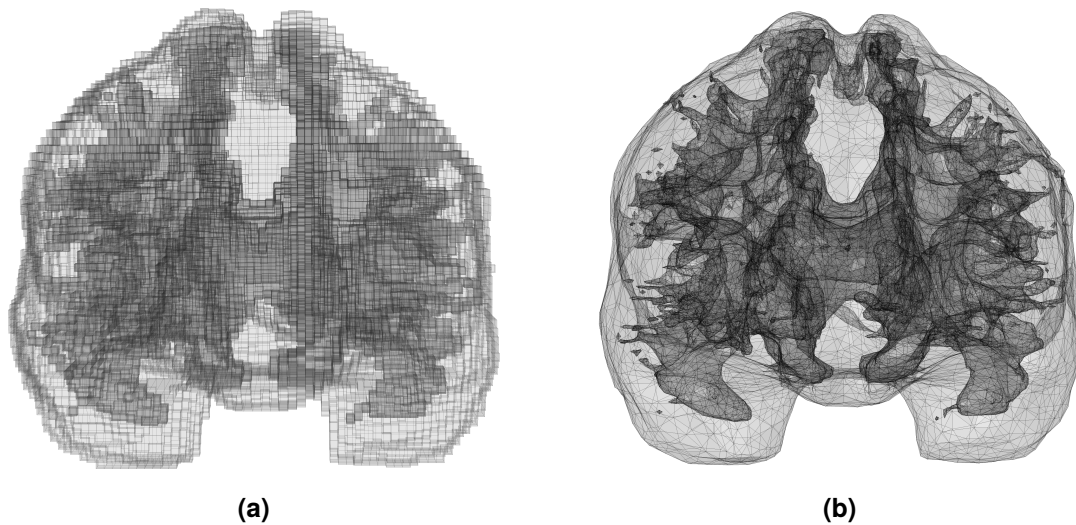


Figure 3.11: Comparison of FDM and FEM meshes for the brain of HEATHER [112]. (a) A finite difference mesh exhibits an obvious staircase effect. (b) A finite element mesh can produce smoother and more realistic boundaries with fewer elements.

the staircase effect (see Figure 3.11). This means it is unable to accurately represent the complex organic shapes encountered in anatomical structures, and faces difficulties imposing certain boundary conditions [110]. In addition, a relatively large number of equations must be solved to achieve a certain level of accuracy because discretisation using a uniform grid must account for the finest features of the geometry and the steepest concentrations in the electric field.

The Finite Element Method

Generally speaking, the FEM is the most preferred numerical method in engineering simulations. The main reason for this is its ability to handle complex geometries [107]. As with the FDM, FEM solvers use Maxwell's equations in differential form. The difference is that in the FEM, the continuous domain is discretised into an unstructured mesh.

Instead of using a uniform grid, the points (termed *nodes*) are connected to form small, discrete regions (*elements*), which have a geometrically simple (but not necessarily regular

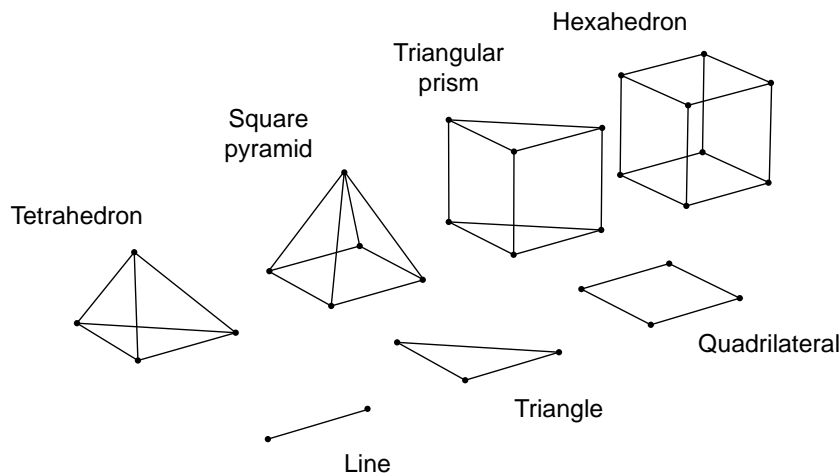


Figure 3.12: Linear finite elements by shape. Nodes are shown at each vertex. Quadratically interpolated elements also possess mid-side nodes. The final appearance of each element in the mesh is typically less regular than those shown here because the elements must conform to the geometry of the continuous domain without becoming excessively skewed. For 3D problems, the BEM uses planar elements, while the FEM uses volumetric elements. (Image adapted from Bondeson [107]. Copyright © 2005, Springer-Verlag.)

nor uniform) shape. Some typical elements are shown in Figure 3.12. In an unstructured mesh, the distribution of nodes can be non-uniform and non-orthogonal, allowing for a much smoother representation of curved geometries (cf. Figure 3.11). This flexible node arrangement also means that the mesh can be refined locally to improve the accuracy of the solution around fine geometrical details or regions with steep field gradients without resorting to a high mesh density throughout the entire domain.

The formulation of the FEM requires that the change of the dependent variable in space be defined within each element. This role is fulfilled by an interpolation function, also known as a *shape function*, which is usually a low order polynomial defined relative to the values at the nodes of the element. FEM results can thus also be refined by increasing the order of this shape function. Because the dependent variable is defined within each element and the global solution is found by evaluating these with reference to the loads and boundary conditions, the FEM solution is often described as a piecewise approximation [35].

The Boundary Element Method

The BEM (also known as the *method of moments*) takes a slightly different approach to the other two methods. In a BEM formulation, the entire volume is split into compartments by material, and as its name suggests, only the boundaries between compartments are discretised (using $(n-1)$ -dimensional elements). However, there are restrictions on the types of geometries that can be solved. To avoid ambiguity from the dimensional reduction, all compartments must form closed surfaces and they cannot intersect each other—i.e. they must be completely nested or completely independent. The material properties assigned to each compartment must also be constant within the bounding surfaces. These attributes make the BEM well suited to models that are *homogeneous* (one material only) and *isotropic* (identical properties in all directions), for *heterogeneous* models containing only a few materials with similar properties, and for unbounded problems [113].

Also note that unlike the other two methods, the BEM employs Maxwell's equations in integral form. The integrand is often decomposed into a singular part, which has an analytical solution, and a regular part, which is solved numerically. The analytical component can be an issue for certain classes of problems.

3.2.3 Neural Excitation

Calculating the electric field is only one part of the bioelectric problem. For CI (and other types of electrical) stimulation, it is also of interest to gauge the consequences of the generated electric field on the excitable tissues, in this case, the auditory nerves.

Response of the Neural Membrane

Like other electrically excitable tissues, the cell membranes of the auditory nerves contain voltage-gated ion channels (e.g. for Na^+ influx or K^+ efflux) in addition to non-gated channels (e.g. for Cl^-) [69]. The distribution of ion species across the membrane is typically uneven, with more negative charge inside the cell compared to the outside. This potential difference, known as the *resting membrane potential*, is on the order of -70 to -90 mV, and is maintained by the normal metabolic activity of the cell. If the ionic permeability of the cell membrane is changed, a local potential can develop. The cell membrane becomes *depolarised* when the potential becomes more positive, for example, when there is an influx of cations; conversely a more negative potential causes it to become *hyperpolarised*.

Only depolarisation can trigger an action potential [82]. Experiments by Hodgkin and Huxley with unmyelinated squid axons [114] and Frankenhaeuser and Huxley with myelinated toad axons [115] revealed the ionic mechanisms responsible for action potential generation. When the electric potential in one region of the membrane is depolarised to the cell's threshold level, the permeability of the cell membrane to Na^+ increases, leading to an influx of Na^+ which then further depolarises the cell [69]. This positive feedback mechanism quickly reverses the membrane potential in that region, as shown in Figure 3.13, and the subsequent transfer of charge from adjacent regions of the membrane causes the depolarisation to propagate. It is this self-propagating neural impulse that allows signals to be relayed to the brain. Other voltage-gated channels open after the Na^+ channels, allowing K^+ ions to leave the neuron and restore the resting membrane potential. The intracellular balance of cations is maintained via sodium-potassium pumps, which actively transport Na^+ and K^+ ions through the membrane against the concentration gradient.

In normal hearing listeners, depolarisation occurs due to the release of neurotransmitters by stimulated hair cells [40,69] (recall §2.2.1), so the wavefront only propagates in one direction:

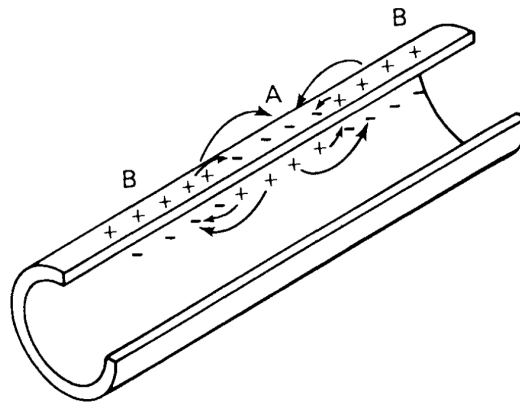


Figure 3.13: Spread of the depolarisation wavefront. When one region (A) of the neural membrane is depolarised, charge stored by the membrane capacitance is transferred from adjacent regions (B), thereby propagating depolarisation along the neuron. (Source: Reilly [82]. Copyright © 1998, Springer.)

away from the hair cell at the peripheral end. For *electrically-evoked* neural stimulation, the active electrodes set up an artificial electric field, causing voltage disturbances along the membrane which drive ions across the channels in the membrane [82]. The location of the stimulating electrodes typically induces depolarisation somewhere in the middle of the neuron, creating a bidirectional depolarisation wavefront (Figure 3.13).

Myelination of nerve fibres is a biological adaptation that permits faster conduction velocities while retaining small fibre diameters [69]. Glial cells form a non-conductive *myelin sheath* around the axon, with small gaps between adjacent sheaths known as *nodes of Ranvier*. The structure means that ionic current can only cross the membrane at the nodes, so the wavefront jumps along the axon from one node to the next instead of simply to adjacent regions of the neural membrane. This process is known as *saltatory conduction*.

Theoretical Models

Several approaches are available for explaining the membrane behaviour. Early models analysed current traversing a localised patch of neuronal membrane. However, Reilly found that “the force driving current into the membrane is the external field distribution *along the*

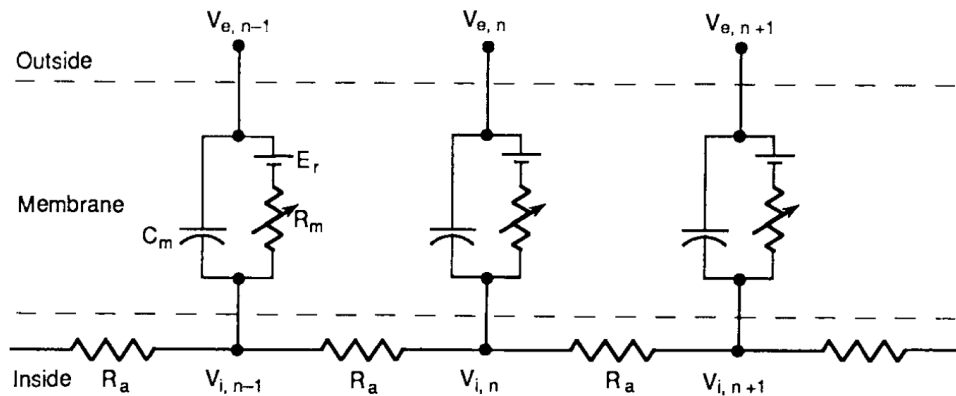


Figure 3.14: Equivalent circuit model for excitable membranes. (Source: Reilly [82]. Copyright © 1998, Springer.)

axon, which cannot be described by the current density at a single point” [82]. This suggests that the spatial and temporal interactions along the entire length of the neuron must be considered to properly represent action potential generation and propagation [82, 116–118]. On the other hand, a recent study of deep brain stimulation modelling found that activation can be approximated without coupling the finite element solution to an axon model [118]. Nonetheless, axon models are more likely to account for spatial phenomena, such as the prevention of action potential propagation by a sufficiently large “anodal surround” [81].

Many quantitative models of neural excitation have consequently been developed based on cable theory, with the neuron being modelled as a long one-dimensional cable as illustrated in Figure 3.14. McNeal’s myelinated nerve model [119] was the first to consider stimulation due to finite duration current pulses from extracellular electrodes. Here, the nodes of Ranvier were spaced at regular intervals, and the myelin sheath was assumed to be a perfect insulator. Only the central excitation node was modelled with non-linear membrane conductances, so the model was applied to subthreshold stimulation. Despite these simplifications, the McNeal model could account for a variety of electrophysiological observations.

Under this model, the membrane potential is described by:

$$\frac{dV_n}{dt} = \frac{1}{C_m} [G_a(V_{n-1} - 2V_n + V_{n+1} + V_{e,n-1} - 2V_{e,n} + V_{e,n+1}) - I_{i,n}] \quad (n \neq 0) \quad (3.5)$$

where $V_n = V_{i,n} - V_{e,n}$ is the potential difference across the membrane at the n th node along the fibre (with a positive value indicating depolarisation), t is time, C_m is the membrane capacitance of the node, $G_a = 1/R_a$ is the internodal conductance, $V_{e,n}$ is the external nodal voltage, and $I_{i,n}$ is the internal ionic current flowing in the node. The ionic current term can be modelled linearly using Ohm's law for subthreshold stimulation, or non-linearly when at or near the excited state using differential equations, such as those of Frankenhaeuser and Huxley [115], or stochastic methods [120].

In his review paper on empirical studies of electrical stimulation, Ranck found that depolarisation was primarily caused by the extracellular voltage becoming more negative (i.e. intracellular potential changes were small) [81]. He also found that current flow along the long axis of the neuron is more likely to depolarise it than transverse current. These findings were strongly supported by McNeal's theoretical model. Subsequent studies extended McNeal's basic framework. Reilly's spatially extended non-linear node (SENN) model, for instance, implemented several non-linear nodes [121] and gave further weight to the accepted tenet that stimulation occurs where neurons end or bend, or where the spatial gradient of the electric field is highest [82]. Colombo and Parkins modified the McNeal neuron geometry to match measurements by Liberman and Oliver in the cat [122], and implemented additional non-linear nodes [123]. Rattay made the framework more robust, accounting for both subthreshold and superthreshold stimulation as well as both myelinated and unmyelinated fibres [124]. He found that for electrical stimulation, "the second derivative of the external potential in the direction of the axon is responsible for all the activations inside the axon" [124]. Since it was a necessary condition for neural excitation, Rattay called this the *activating function* (AF). The AF can be expressed for both unmyelinated and myelinated

neurons respectively as:

$$AF = \frac{\partial^2 V_e}{\partial x^2} \approx \frac{V_{e,n-1} - 2V_{e,n} + V_{e,n+1}}{\Delta x^2} \quad (3.6)$$

where x is displacement along the nerve fibre. Further refinements to the model were later added to make the model more applicable to human cochlear neurons [125, 126].

Another prominent excitation model in CI research is the generalised Schwarz, Eikhof, and Frijns (GSEF) model developed by Frijns *et al.* [100], intended for use in models of the guinea pig cochlea. This model was based on earlier work by Schwarz and Eikhof with myelinated rat fibres [127] and Frijns and ten Kate's modifications of the SENN model [128]. Like Colombo and Parkins, it was based on mammalian neural kinetics, with non-uniform internodal lengths in accordance with the morphological data of Liberman and Oliver [122]. Each nerve fibre included 16 non-linear nodes. The assumption of perfectly insulating myelin sheaths was retained.

The main weakness in the majority of these models is that they mix empirical results from different animal species. This does not necessarily invalidate the model, since neural kinetics can be similar across species and the models are tuned to fit experimental data, but there is still an abstraction gap between these theoretical models and *in situ* nerve fibres. This was particularly evident in Whiten's modelling work [22] (see §3.3.2)—despite having a patient-specific model with ideal archival data for comparison, he found that the model was weakest when compared against the psychophysical data. Other aspects of the modelling methodology may have played a part in this discrepancy, suggesting that significant care and attention to detail need to be exercised throughout the reconstruction process.

More recent developments in the area of neuronal modelling have been published by a group in Melbourne, Australia. In a series of four papers [129–132], Meffin *et al.* developed a more robust model of extracellular stimulation that goes beyond the cable theory models by

incorporating the cellular composition of the neural tissue, including the effect of the confined extracellular space, as well as both longitudinal and transverse modes of stimulation. The formulation calls for parallel unmyelinated neurons, which may be applicable to the spiral ganglion, but has yet to be implemented in a VCM of the cochlea.

3.3 Electric Models of the Cochlea

Existing electric models of the cochlea fall into two categories: lumped-element models and volume conduction models. Prominent examples are described in the following sections, grouped by primary author and sorted in chronological order of appearance.

3.3.1 Lumped-Element Models

Von Békésy (1951)

Von Békésy's LEM [106] was the pioneering effort to understand the electroanatomy of the cochlea. In his experimental work with explanted guinea pig cochleae, von Békésy found that the otic capsule was a good insulator and mused that the grounding resistance must therefore lie in the modiolus. Additional measurements indicated that "the main grounding pathway of the cochlea is through the acoustic nerve to the brain" [106], and that there would be substantial cross-conduction between the turns of the cochlea because the nerves and blood vessels of the modiolus enter the cochlear partition along the entire length of the spiral. These observations gave birth to the idea that grounding the auditory nerve is a good choice for representing the cochlea's electrical behaviour.

In light of these findings, von Békésy sought to explain the attenuation of voltage along the cochlear partition by considering two extreme cases: (i) the cochlear partition is a very *poor*

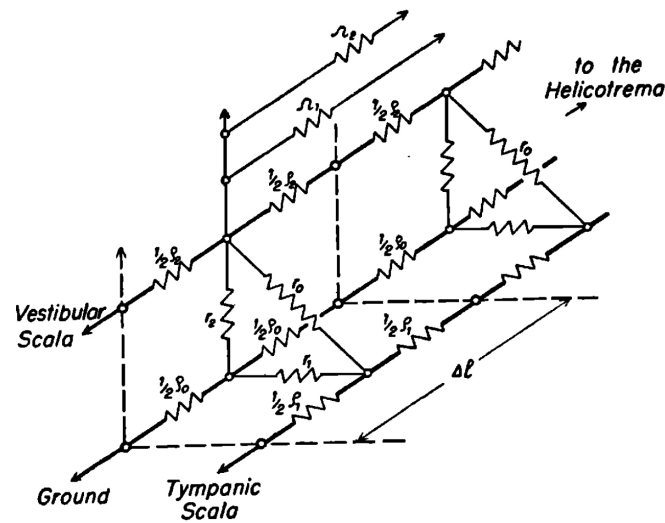


Figure 3.15: The von Békésy transmission line model, representing a small section of the cochlear tube near the basal end. (Source: von Békésy [106]. Copyright © 1951, Acoustical Society of America.)

insulator, so the intracochlear spaces would resemble a homogeneous conducting body (like a drop of fluid); and (ii) the cochlear partition is a very *good* insulator, so the cochlea was effectively a fluid-filled tube separated into two conjoined canals (analogous to a *transmission line*). He found that while neither extreme was realistic for the entirety of the cochlea, the former was more suitable at the helicotrema and the latter near the round window.

Focusing on the basal turn, he created the transmission line model in Figure 3.15. The model consisted of a 3D network of resistive elements, representing current paths along the scala vestibuli, the scala tympani, and the cochlear partition, the grounding pathway through the nerves and blood vessels in the modiolus, and additional resistances to account for cross-turn effects.

The von Békésy model was a good start to electroanatomical modelling of the cochlea, but it had several shortcomings. The model accounted for many of the possible current paths, but it failed to consider others like the scala media, the cerebrospinal fluid (CSF), and the spiral ligament. Detail was also lost where different tissue types were combined into single elements; for instance, the organ of Corti and the basilar membrane were modelled together as

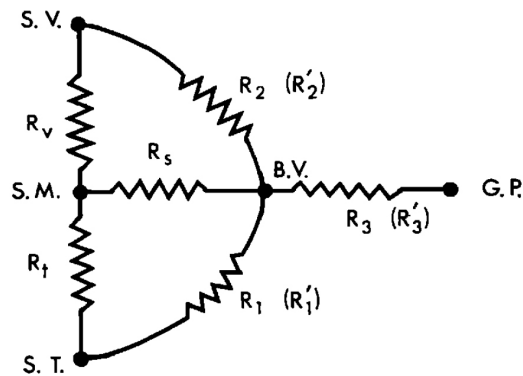


Figure 3.16: The Johnstone model. SV=scala vestibuli; SM=scala media; ST=scala tympani; BV=blood vessels; GP=guinea pig (body). (Source: Johnstone *et al.* [135]. Copyright © 1966, Acoustical Society of America.)

the cochlear partition, and the nervous and vascular pathways in the modiolus were combined into a single grounding resistance. It is impossible to determine which tissue path is preferred in these lumped regions. Von Békésy also found that capacitive effects were not important. However, the 1000 Hz stimulus signal used in these impedance measurements is well below the 10 kHz threshold typically required for such effects to manifest [133].

Johnstone *et al.* (1966)

Johnstone *et al.* were also interested in discovering more about the electrical pathways of the guinea pig cochlea, particularly the resistances of the three boundary walls of the scala media. They proposed a relatively simple LEM (Figure 3.16) that aimed to synthesise the measurements of both von Békésy and Misrahy [134] into one consistent model [135].

The Johnstone model differs from the von Békésy model in several respects. It was devised as a 2D representation of the experimental setup through one turn of the cochlea, and does not directly account for longitudinal current flow or cross-turn effects. As per the focus of this study, the main pathways considered were the boundaries of the scala media, i.e. Reissner's membrane, the organ of Corti and associated structures on the basilar membrane, and the

spiral ligament via the stria vascularis. There is a strong emphasis on the role of the cochlear blood vessels as a conductive pathway that links the scalae. Like von Békésy, Johnstone *et al.* also suggested that the grounding resistance would be through the structures of the internal auditory meatus, in conjunction with the cochlear artery. The experimental technique used also differed, with the injection of square current pulses akin to those used in contemporary CI systems, though with a significantly longer pulse width.

Overall, the Johnstone model added some extra detail around the scala media while ignoring detail from other regions of the cochlea. It still favoured a purely resistive formulation. Johnstone *et al.* admitted that the model was “the simplest measurable network”, even “oversimplified” [135], but was nonetheless able to reconcile the results of earlier studies and provide reasonable voltage predictions.

Strelioff (1973)

Another LEM was proposed by Strelioff in 1973 [116] (see Figure 3.17). It aimed to study the spatial distribution of electric potentials and currents in the guinea pig cochlea arising from acoustic stimulation.

In terms of the layout of the circuit elements, the Strelioff model was arguably more accurate than either the von Békésy or Johnstone models. It returned to a linear 3D network similar to von Békésy’s model, with a series of over 90 cross-sectional circuits connected via longitudinal resistances. Each cross-section included nodes in five different fluid-filled spaces (the scala vestibuli, scala media, and scala tympani, the tunnel of Corti, and the spiral ligament), resistances to represent the pathways between adjacent nodes, and battery elements to represent endocochlear potentials.

Weaknesses of the Strelioff model include the decision to use a linear model to represent the entire length of cochlear spiral, which ignores cross-turn effects from the true 3D geometry.

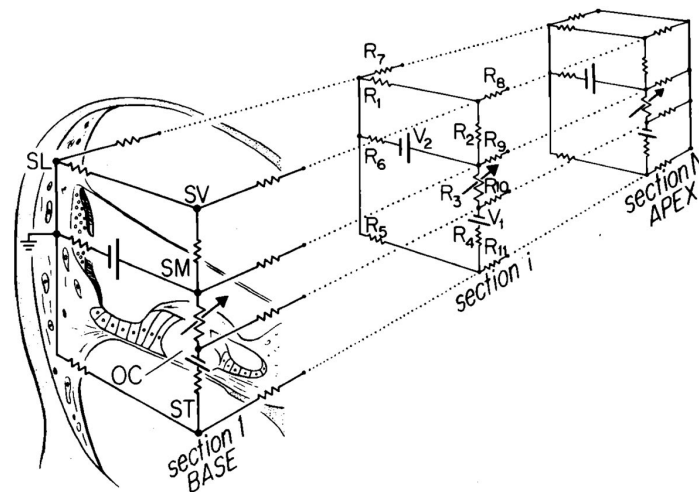


Figure 3.17: The Strelhoff model. SL=spiral ligament; SV=scala vestibuli; SM=scala media; OC=organ of Corti; ST=scala tympani. (Source: Strelhoff [116]. Copyright © 1973, Acoustical Society of America.)

Lumping the longitudinal pathways along the modiolus with those of the spiral ligament and ground is also questionable given that they lie on opposite sides of the scalae. The cochlear vasculature is not explicitly accounted for in the model, and no capacitive effects were incorporated despite an admission that they undoubtedly exist. Strelhoff also noted that the use of discrete elements could reduce accuracy, but estimated that the results were accurate to within 5% of a continuous model based on an extrapolation of some preliminary results.

Black and Clark (1980)

The Black and Clark model [31, 136], shown in Figure 3.18, was the first effort to investigate the behaviour of the cochlea during electrical stimulation for hearing restoration. The geometry of the model was based on that of Johnstone *et al.*, but extended to 16 cross-sections in the transverse direction as per the transmission line models. Resistance values were fitted to the range of published experimental measurements via scaling.

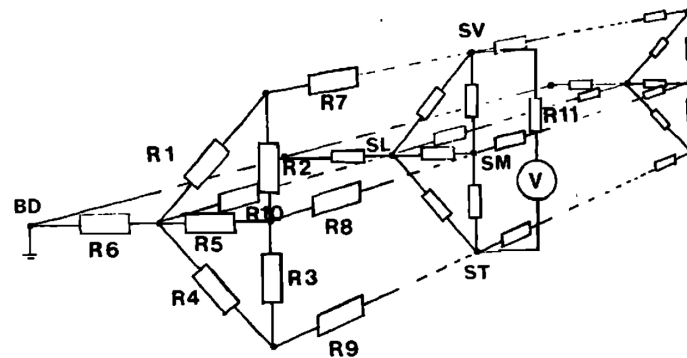


Figure 3.18: The Black and Clark model. SV=scala vestibuli; SM=scala media; ST=scala tympani; SL=spiral ligament; BD=animal body. (Source: Black and Clark [31]. Copyright © 1980, Acoustical Society of America.)

In conjunction with some additional measurements, the model revealed differences in stimulation specificity between various electrode configurations; in particular, that BP stimulation resulted in the highest specificity of the tested configurations. They also noted that the spread of current through the neural tissues may be different from the spread of potentials through the scalae, so voltage traces on their own were insufficient for inferring the effect on neural excitation.

Since they use the same circuit layout for the cross-sectional slices, this model shares some of the weaknesses of the Johnstone model. An additional concern of this study lies in the continual rescaling of model parameters to force-fit the experimental data. The authors acknowledged in the discussion that the model was too simple for some applications, such as modelling length constants under BP stimulation.

Suesserman and Spelman (1993) & Machado and Toumazou (1995)

In their studies of the cochlea, Suesserman and Spelman realised that the physical presence of the electrode array and the deterioration of cochlear structures with the onset of deafness both had an effect on the current paths, which had not been accounted for in the modelling

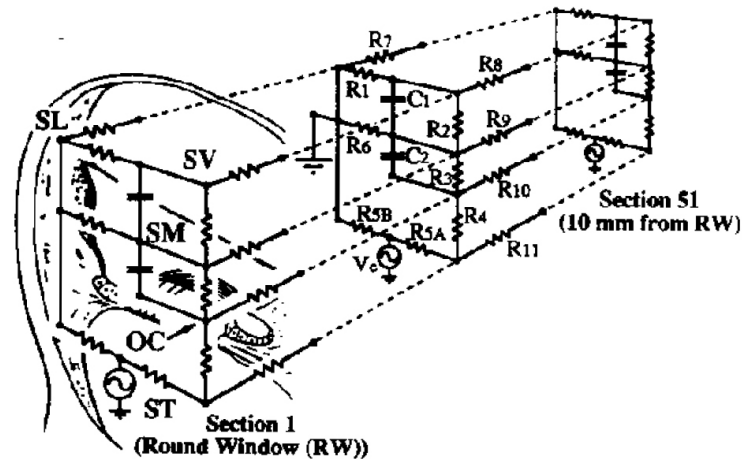


Figure 3.19: The Suesserman and Spelman model. SL=spiral ligament; SV=scala vestibuli; SM=scala media; OC=organ of Corti; ST=scala tympani. (Source: Suesserman and Spelman [99]. Copyright © 1993, IEEE.)

literature. As such, they created an extension of the Strelioff model to better match the *in vivo* electrical behaviour during electrical stimulation [99].

Their model represented the first turn of the cochlea using 51 cross-sectional slices with a thickness of 200 μm , as illustrated in Figure 3.19. It added a new node for the stimulating electrode in the scala tympani and new elements to capture the membrane capacitances ignored in previous studies. The battery elements representing endocochlear potentials were removed since the focus was on exogenous stimulation. The model parameters were adjusted to account for the increase in resistance along the scala due to the presence of the electrode array and matched to Spelman's earlier experimental work on implanted guinea pig cochleae [98].

The Suesserman and Spelman model was the most accurate LEM of the implanted cochlea. However, like prior studies, it assumed that the cochlea could be uncoiled. With the emphasis firmly on the modelling of electrical stimulation, it is important to consider that the neural structures closer to the modiolus were still not included since the uncoiling assumption becomes less applicable in this central region of the cochlea. The authors noted that induced

fields from CI stimulation would distort each other due to coupling between adjacent turns of the cochlea, but justified the exclusion of these effects in the model by saying that these distortions are quite small [20] and that psychophysical experiments had indicated minimal impact on overall sound perception [137].

In 1995, Machado and Toumazou further extended the model by deriving approximating equations for each of the model parameters [138]. These allowed the model to be used for all turns of the guinea pig cochlea, and for other species to be studied qualitatively as well. The model was heavily reliant on the earlier assumption that cross-turn effects were negligible. Machado and Toumazou went on to use their refined model to propose additional design considerations for CI system architectures [104].

Jolly also used the Suesserman and Spelman model to evaluate the feasibility of quadrupolar stimulation [139].

Kral *et al.* (1998)

A comprehensive study comparing the spatial resolution of various electrode configurations was undertaken by Kral *et al.* in 1998. It featured *in vitro*, *in vivo* (cadaveric and live cats), and *in silico* components.

The LEM featured in this study is shown in Figure 3.20. Kral *et al.* modelled the implanted scala tympani by using an axisymmetric assumption on the unrolled cochlear geometry, accounting for the change in cross-sectional area along the chamber. Material properties were sourced from prior experimental work and models, and neural excitation was modelled using a current trigger level on the elements representing the peripheral processes or the spiral ganglion. The selected threshold currents produced a good fit with the *in vivo* neuronal data. The study results showed that TP stimulation elicited the sharpest spatial tuning curves,

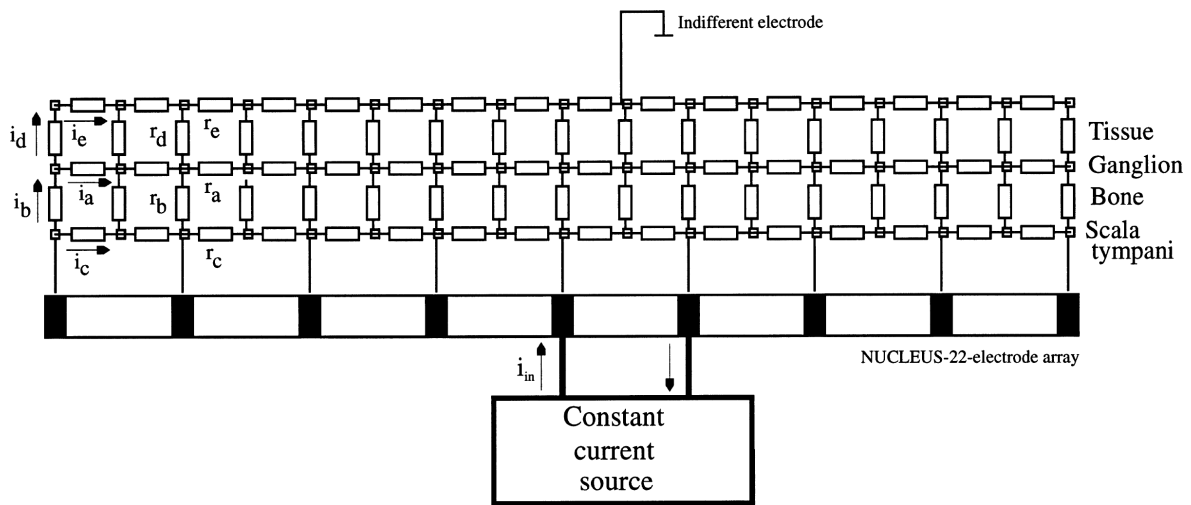


Figure 3.20: The Kral model. (Source: Kral [30]. Copyright © 1998, Elsevier B.V.)

implying focused stimulation, and that the current paths followed by injected current are important in determining spatial selectivity.

The primary limitation of the model is that it used a simplified 2D geometry, so excitable structures near the modiolar wall of the scala tympani were considered but the nerve tissue in the modiolus was poorly represented. The influence of other nearby fluid chambers (the scalae media and vestibuli) are not considered, even though the scala tympani is not perfectly insulated. In addition, it was comprised of resistive elements only and so did not consider time- and frequency-dependent effects, which are observed in *in vivo* measurements.

Vanpoucke *et al.* (2004)

Vanpoucke *et al.* created an LEM of the cochlea to help interpret data from an electrical field imaging (EFI) study [29]. EFI data were sourced because it is a simple, non-invasive, and rapid measurement technique. The complete model, shown in Figure 3.21, is roughly equivalent to the Kral model in the sense that the network was structured according to the layers of materials encountered by injected current. The circuit itself was, however, quite different. It built upon a purely resistive tissue model introduced in an earlier paper [140] and,

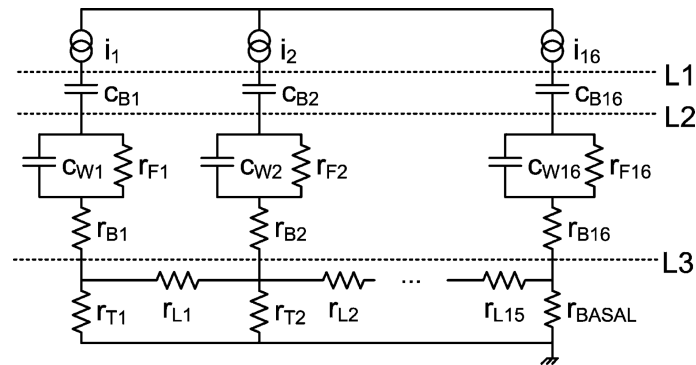


Figure 3.21: The Vanpoucke model. (Source: Vanpoucke [29]. Copyright © 2004, IEEE.)

like the Johnstone model, includes an element representing the total resistance between the cochlea and the MP reference electrode. Additional elements were introduced to represent the interface impedance for each intracochlear electrode contact. All model parameters were then calculated from experimental measurements using numerical methods.

The model provided a good match to the EFI data and was able to provide some insight into the local conductive pathways near the stimulating electrode. There was some concern about the interpretation of some unanticipated results. Simplifications made in the construction of the circuit model, such as the use of a linear tube geometry and the exclusion of the other scalar pathways, are likely weaknesses in this representation.

3.3.2 Volume Conduction Models

Girzon (1987)

Girzon was one of the first to recognise that representing gross structures as single nodes or elements was inadequate. He argued that in LEMs, the true 3D structure of the inner ear is simplified, so some current paths are ignored. The use of bulk impedance measurements between two points only reveals the *effective* impedance between them, and does not clearly demonstrate the spatial pathway traversed by injected current. In addition, the representation

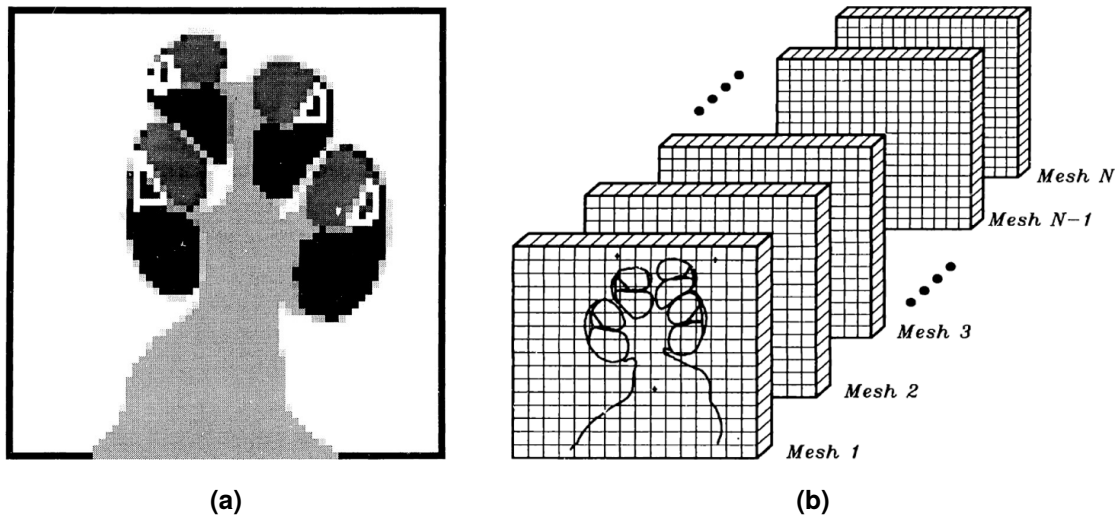


Figure 3.22: The Girzon model. (a) A downsampled mid-modiolar section was mapped onto a finite difference grid. (b) The entire model consisted of $N = 40$ slices. (Source: Girzon [20]. Copyright © 1987, MIT.)

of implanted electrodes as point sources could be inaccurate since the arrays occupy a substantial volume within the scala and have significantly different electrical properties relative to the surrounding fluids.

In order to overcome these problems a new type of model was required, leading Girzon to develop the first VCM of the cochlea (illustrated in Figure 3.22) [20]. By preserving the 3D, heterogeneous structure of the cochlea, it was hoped that the VCM would be “electro-anatomically accurate” and could uncover insights that could not be revealed using LEMs, such as the true current pathway to ground and the resultant patterns of neural excitation.

The model comprised of a volumetric geometry based on a set of serial sections of a whole human cochlea. The overall size of the domain was $9.6 \times 5.76 \times 7.4$ mm. Each section was hand-traced, vectorised, and downsampled to a $128 \times 128 \times 40$ finite difference mesh (Figure 3.22b). Tissue-specific resistivity values were used as opposed to bulk resistance measurements between arbitrary points. These were estimated from a variety of sources. Electrical loads were modelled as point sources within the scala tympani. In terms of

boundary conditions, the model was insulated on all sides (as shown by the black outline in Figure 3.22a), except for the bottom surface where the cochlear nerve exited the volume, which was grounded due to its “electrical proximity” to the MP return electrode.

Girzon’s VCM was a solid first attempt at creating a true 3D representation of the electrically stimulated cochlea. He recognised that the key advantage of this model over LEMs was that it allowed results to be interpreted in a more accurate spatial context—for instance, the magnitude and direction of field quantities could be calculated throughout the structure, and indirect current pathways linking the turns of the cochlea were demonstrated. The model was successfully used to investigate the effects of several parameters, including the distribution of electric potential in the scala tympani, the accuracy of modelling electrodes as point sources, the impact of model resolution, the effects of material models and properties, and various modes of stimulation. Validation against *in vivo* experimental measurements showed that the VCM was superior to transmission line formulations.

Girzon acknowledged that as a first attempt, the model was subject to a number of drawbacks. Regarding methodology, he suggested that the FEM would have been a better solution method since it allows for non-uniform element dimensions, but the FDM was more practical given the compromises between software and hardware capabilities at the time.

In terms of tissue modelling, the resolution was quite low due to the constraints in imaging technology. This meant that fine structures such as the cochlear vasculature could not be reconstructed despite being a highly conductive pathway. Girzon reasoned that the larger volume of the auditory nerve made it a more significant path to ground, so the effect of vasculature was likely to be small. Nonetheless, he called for further investigation of the blood vessel pathways. The electrical conductivities of several cochlear-specific tissues were probably also inaccurate since they had not been measured and were instead based on conductivities of similar tissues that had been published in the literature. Capacitive effects were ignored on the basis that the perilymph, nerve, and blood vessels, which were likely

to be the dominant current carrying pathways, had been shown to be primarily resistive at frequencies of up to 10 kHz [98, 133, 141].

Finally, Girzon acknowledged that modelling the electrodes as simple point sources was likely to have overestimated the current densities. He compared the point source with a small near-spherical volume source and did not find a large discrepancy in the voltage profile, but only after scaling to the maximum potential in each trace. The staircase effect would have added to the modelling error because the spherical current source could not be aligned to the Cartesian grid. In addition, although grounding the nerve may seem reasonable for LEMs, prescribing it in a VCM is incorrect since the spatial effects of this boundary condition are not properly considered. Girzon simply reasoned that it would be better than grounding all the model boundaries because the potential should be asymmetric and he did not want to overestimate the voltage attenuation.

Finley *et al.* (1987–1990)

Finley *et al.* improved upon the work of Girzon in a few key areas. Their models of the human cochlea were based on the FEM, and included volumetric representations of the implanted electrode array. They started with a simple two-dimensional (2D) model [142], but later extended it into a more substantial 3D model [143, 144], shown in Figure 3.23. These VCMs were used to predict the induced electric fields within the cochlea tissues, similar to Girzon's work. However, they also went a step further and coupled it with a neural model to predict the response of auditory nerve fibres, thereby providing a more complete view of the CI stimulation process.

The geometry of the Finley model is best described as being extruded. A histological image of one turn of the cochlea was segmented into various tissues and discretised, with a higher mesh density in the central regions of the cochlea. This 2D mesh was extended using

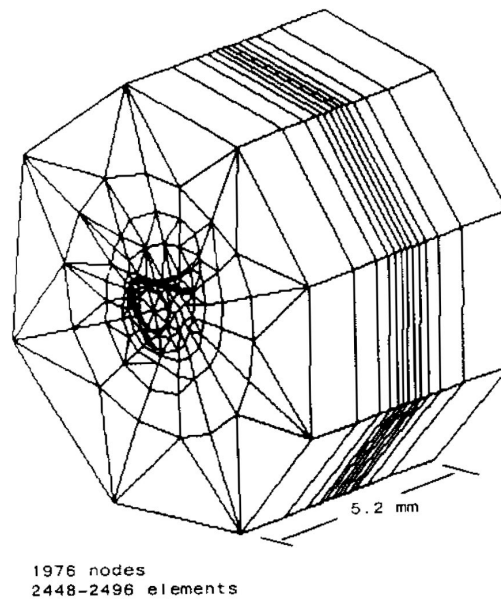


Figure 3.23: The Finley model. (Source: Finley *et al.* [144]. Copyright © 1990, Springer.)

prismatic elements to form a slab, and twelve such slabs were then put together to generate a short, straight section of the cochlear tube totalling 5.2 mm in length, resembling a short transmission line model. The slabs closer to the mid-plane of the model were thinner, so the mesh density was significantly higher in the central regions of the model than at the periphery. Purely resistive tissue properties were assigned, and a variety of bipolar electrode configurations were tested. Rattay's activating function [117, 124] was used to predict the likelihood of excitation along seven neural trajectories.

Finley *et al.* found that the model was quite useful for studying various bipolar electrode configurations. The electrical fields and neural responses were highly dependent on the arrangement of the source and sink electrodes, as well as the location of the implanted array within the scala tympani. The greater anatomical detail and improved (albeit still crude) electrode geometry, made possible through the use of the FEM and by focusing on only one turn of the cochlea, helped to increase the accuracy of the predicted electric field distribution relative to other models.

Nonetheless, omitting the curvature of the cochlea was a step backwards from the true 3D shape of the Girzon model. The authors indicated that greater anatomical detail would have been preferred, such as in the lateral wall (i.e. the spiral ligament and stria vascularis) and in the modiolus. Unlike the Girzon study though, the influence of blood vessels was not mentioned at all. The model's limited spatial domain meant that broadly spreading monopolar fields could not be considered. It also retained the use of purely resistive material models, citing Spelman's experimental results [98].

Frijns *et al.* (1995–2015)

The Frijns group is the most active in the field of cochlear modelling. They have been iterating on their model since 1995, leading to what is rightfully considered to be the most anatomically realistic representation (see Figure 3.24). The Frijns model is therefore considered to be the gold standard in this field. As per Finley *et al.*, it consists of two coupled sub-models: an electrical VCM, this time based on the BEM, and a neural excitation model (the generalised SEF model by Frijns [100]), which uses the calculated potential distribution to predict the electrically-evoked neural response.

The initial model [100,148] was based on a histological section from a guinea pig cochlea [100]. An image of the second turn was digitised, segmented and revolved to form a “rotationally symmetric” (i.e. axisymmetric) toroidal structure (see Figures 3.24a and 3.24b). The segmented tissues were embedded in a surrounding domain of bone. Due to the use of the BEM, the thicknesses of the cochlear membranes had to be increased to avoid excessive numerical errors, so their conductivities were magnified proportionally. Conductivity values for the other tissues were either sourced directly from existing literature or calculated from published resistance and morphological data. Electrodes were modelled as point sources located in one of four positions, marked as points A through D in Figure 3.24a. Only BP stimulation was modelled.

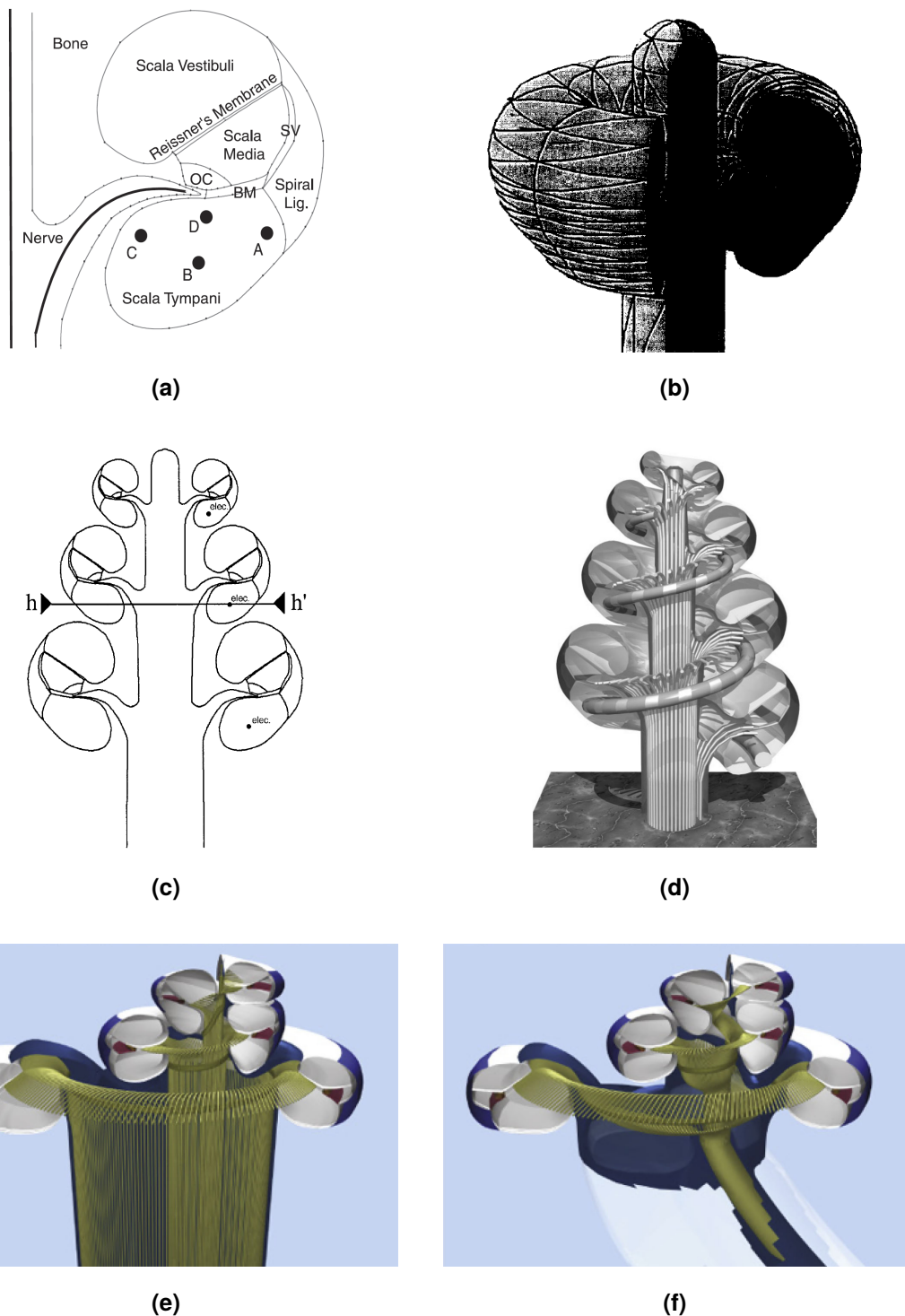


Figure 3.24: Evolution of the Frijns model over time. (a) Cross-sectional schematic showing the modelled cochlear tissues [145]; (b) the original axisymmetric model [100]; (c) the extended axisymmetric model [146]; (d) the spiral model [145]; (e) the original human model [65, 147]; (f) the refined human model [147]. (Copyright © 1995–2014, Elsevier B.V.; 2001, Wolters Kluwer.)

Frijns *et al.* went on to compare this model with existing efforts. They showed that relative to straight models, such as those of Finley *et al.* [144] and Suesserman and Spelman [99], the calculated potential fields are significantly different [100], so the assumption of an unrolled cochlear geometry was invalid. They also showed that Finley *et al.*'s omission of the spiral ligament, stria vascularis, and organ of Corti resulted in an inaccurate representation of the scala media. These three tissue boundaries act as an insulating layer and help to maintain the endocochlear potential. Further refinements to the model, including more fine detail, anisotropic conductivities, and realistic electrode shapes were also discussed.

The guinea pig model was further developed in some later papers [105, 145, 146]. The most obvious change to the model was its shape, which became tapered and spiralled up towards the apex much like a real cochlea. (The helicotrema was not modelled, however.) This helical shape is important: a comparison of results from a tapered multi-toroidal model (Figure 3.24c) and the spiral model (Figure 3.24d) showed that the latter more closely matched experimental work. This reinforced the findings of Ifukube, who had previously demonstrated the importance of the helical cochlear path on current distributions [58]. The spiral model also incorporated realistic electrode geometries based on a variety of clinical designs [145]. Differences due to factors such as electrode spacing and array positioning within the scala tympani were found. It was therefore made clear that the model geometry plays a dominant role in volume conduction problems and should ideally be modelled with the highest feasible accuracy. In terms of boundary conditions, the model was grounded at infinity [145]. No justification was given in the paper but the choice was presumably made to reflect the far-field MP return electrode.

In 2001, Frijns *et al.* began directing their efforts towards a human model [65]. Mid-modiolar sections from histological images were used to define the shape of each turn and the trajectory of the sweep path. They showed that the differences in geometry (see Figure 3.24e) and tissue properties between guinea pig and human cochleae have an impact on the modelling

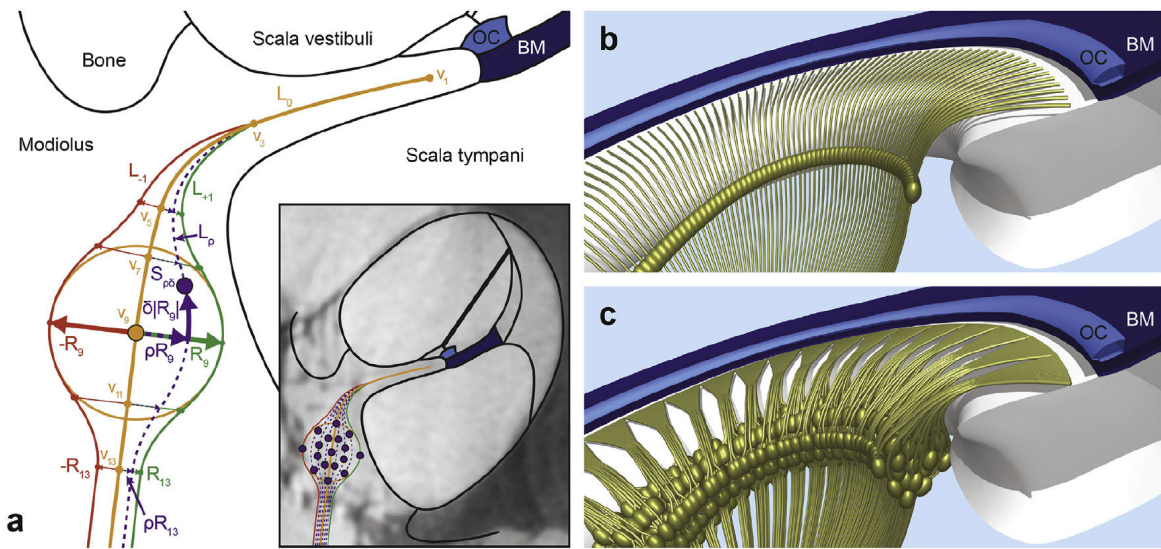


Figure 3.25: Spatially distributed spiral ganglion cell bodies by Kalkman. (a) The implementation of the distributed fibre trajectories and spiral ganglion cell body locations; (b) the spirally-aligned cell bodies as used in previous studies; (c) the updated, spatially distributed cell bodies. This enhancement to the Frijns model further improves its anatomically realistic geometry. (Source: Kalkman *et al.* [153]. Copyright © 2015, Elsevier B.V.)

predictions. As such, even though Miyamoto suggested that guinea pigs were an appropriate animal model for CI research [62], caution must be used when extrapolating *in vivo* or *in silico* experimental results to humans. Further refinements to the model have since been made to investigate specific conditions. These include solving the inverse problem to better understand the processes underlying ECAPs [149], the removal of the peripheral processes to model a degenerated physiological state [150], a comparison of time-dependent stimulation profiles [151], inclusion of the facial nerve to model ectopic stimulation [152], and an examination of PA stimulation techniques [87]. The latest revisions of the Frijns model are highly realistic and are undoubtedly the most comprehensive efforts to date, not only in terms of the geometry (see Figure 3.24f), but also the trajectory of the neuronal pathways (Figure 3.25) [147, 153].

Taken as a whole, Frijns and his co-workers have provided much insight into how variations in shape affect CI stimulation patterns. This is important because the geometry of the inner

ear differs between species and is also uniquely shaped for every individual [47, 154]. No single geometry can apply equally well to an entire population.

There are still some aspects of the model that could be further improved. For instance, it has not been shown whether the boundary conditions used in these models are truly reflective of the *in vivo* situation during MP stimulation. As with the other VCMs, the effect of the vasculature is simply assumed to be negligible, so blood vessels have been completely omitted. In addition, adjustments to both geometry and material properties for the cochlear membranes were required for accuracy reasons. These are a result of methodological limitations inherent to the BEM. The models also assume that purely resistive material models are sufficient in order to simplify the computation.

Hanekom (2001–2015)

Another FEM of the cochlea was created by Hanekom in 2001 [155]. The model is illustrated in Figure 3.26 and features an untapered 3D helical shape totalling 1.5 turns, with cross-sections based on a combination of photomicrographs from two human cochlea specimens. It incorporated both a modiolar-hugging and a peripheral track to model different intrascalar array placements, allowing a variety of bipolar and pseudo-monopolar electrode configurations to be tested. Like existing models, the cochlear tissues were embedded in bone; Hanekom opted for a cylindrical surrounding block of 5.5 mm radius and 10 mm depth oriented parallel to the mid-modiolar axis, and purely resistive material properties were used. Hanekom coupled the volume conduction model with the GSEF nerve fibre model, allowing for some comparisons with the Frijns model.

The Hanekom model was able to make conclusions regarding the asymmetry of potential distributions, as well as the effect of electrode placement on current spread, thresholds and

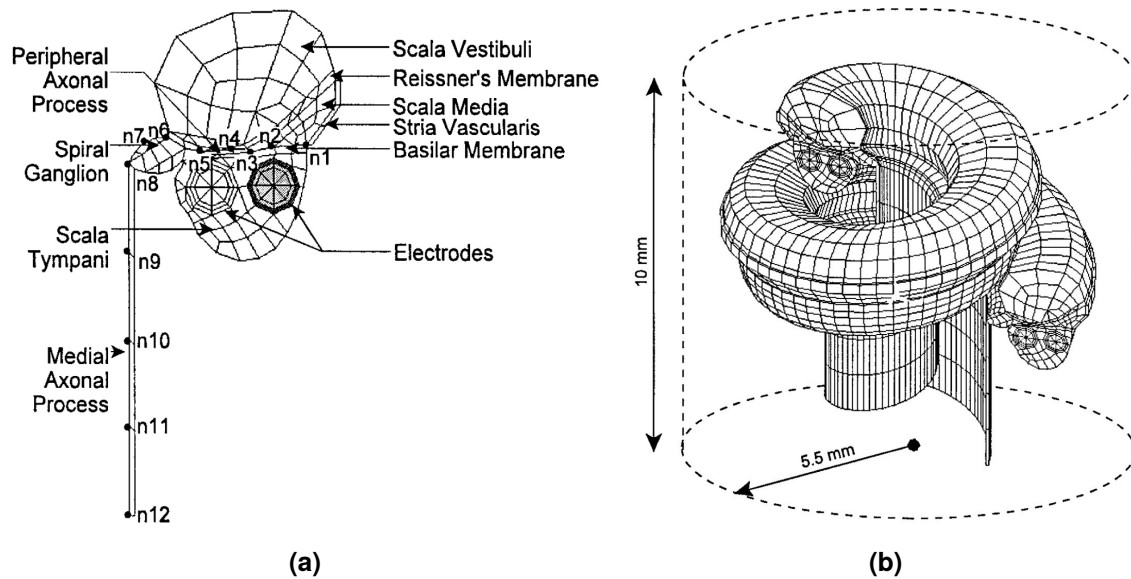


Figure 3.26: The Hanekom model. (a) Section view of a single turn in the model, with tissues as labelled; (b) 3D view of the mesh inside the cylinder of surrounding bone. (Source: Hanekom [155]. Copyright © 2001, Wolters Kluwer.)

excitation patterns (including ectopic excitation). It was later used to model the effect of encapsulation tissue around implanted electrode arrays [156].

The main weakness of the model was its geometry. It did not follow a true spiral trajectory, using instead a series of circular half-turns. The constant cross-section size was also not realistic—even though the dimensions of the scala tympani were within 6% of an average real cochlea, the overall height of the model exceeded it by some 25%. Filling and assigning the volume in the centre of the model to a nerve domain to represent the bundling of axons into N VIII ignored the other tissues that also reside in that space, and was not an accurate depiction of the shape of the nerve trunk. Some tissue thicknesses also needed to be scaled in order to obtain well-shaped elements. Finally, it did not incorporate vascular pathways or time-dependent material models.

Since then, the Hanekom group has focused on improving the model geometry by creating more realistic subject-specific models. This work began with a guinea pig cochlear

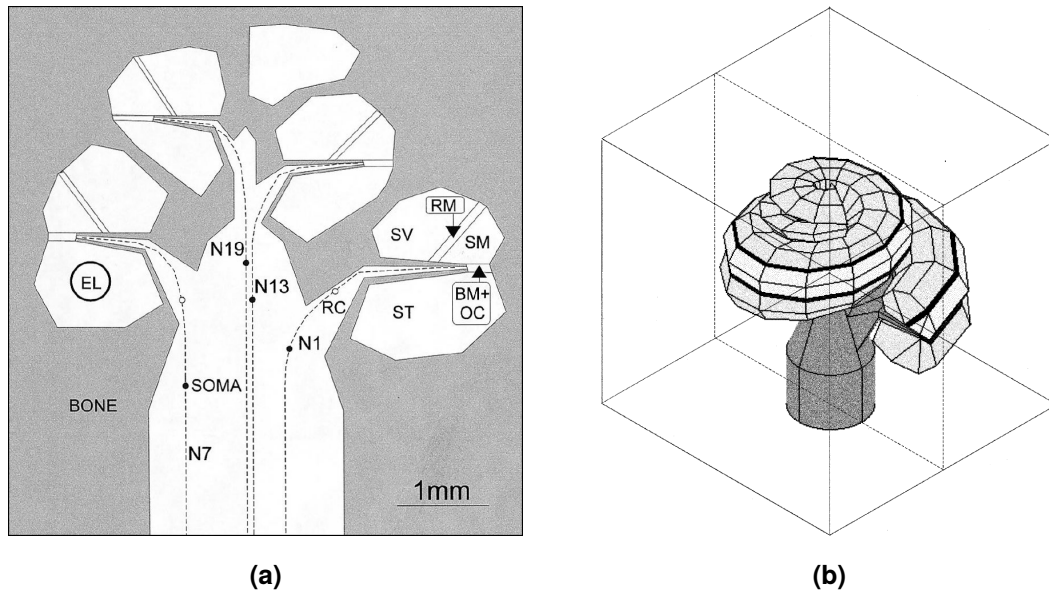


Figure 3.27: The Rattay model. (a) Section view through the mid-modiolar plane; (b) the volume mesh and surrounding bone cube. (Source: Rattay *et al.* [159]. Copyright © 2001, Elsevier B.V.)

model [157]. Human cochlear models have been developed more recently that also include a low fidelity reconstruction of the surrounding head to represent the monopolar return path [158].

Rattay *et al.* (2001)

Rattay *et al.* approached the modelling problem from the opposite end. In a companion paper on neural excitation modelling [126], they realised that they needed a potential distribution that more closely resembled the *in vivo* situation in order to properly account for effects arising from the cochlear anatomy. In response, they constructed a relatively simple FEM model of the implanted cochlea [159], which is shown in Figure 3.27.

The Rattay model was reconstructed from a single photomicrograph of a mid-modiolar section of the human cochlea. It was segmented at high resolution but significantly downsampled, with the outline of the scala tympani comprising of just seven edges (see Figure 3.27a).

Sections were extrapolated along a fitted spiral path at 30 degree intervals to form a model with 1.5 turns. An axisymmetric core representing the auditory nerve trunk was then modelled as a series of stacked cylinders and cones, and the entire structure was embedded in a cube of bone, as illustrated in Figure 3.27b. Resistivities, predominantly from Finley [144], were assigned to the corresponding tissues, and capacitive effects were omitted. 0.5 mm diameter spheres were intersected with a swept 0.4 mm diameter circular profile to approximate a banded multielectrode array. A 1 V load was placed on the stimulating electrode. All outer surfaces of the bony cube were grounded, except for the base, where a long prismatic extension of nerve tissue was used. The neural model in the companion paper [126] was then implemented on the solved VCM.

Rattay *et al.* were able to draw out several different insights. For MP simulations, it was able to predict that voltage decreased more rapidly in the basal turn due to the larger size of the scala tympani there, in line with experimental findings. It also showed that the point of maximum voltage for more apical fibres lay within the modiolus instead of at the peripheral end. Other aspects they looked at included BP and quadrupolar stimulation modes, differences in timing between neurons, and the excitation of degenerated neurons.

The authors found that the model was not particularly sensitive to the tissue resistivities used, but acknowledged some uncertainties around material properties as well as boundary conditions. Also, despite suggesting that the geometry of the VCM was sufficiently detailed, they understood that the excitation model predicted a higher probability of activation at strong curves and mused that more refinement towards the organic geometry of the neural tissue would therefore be desirable.

Choi *et al.* (2001–2014)

Choi *et al.* created several models of the cochlea to study shape and location optimisation of CI electrodes using genetic algorithms. Choi's work on virtual channels [160] also showed that several electrode design parameters had a measurable impact on the efficacy of virtual channel techniques and is a solid demonstration of how *in silico* studies can inform electrode designs.

Choi's seminal work only looked at the surface of the electrode [161], but subsequent papers also included a model of the cochlear tissues. The sectional geometry and resistivity values were the same as that of Hanekom [155, 162] (see Figure 3.28a), but the geometry was evolved over time, beginning as an extruded section [163], then becoming a semi-circular sweep [160, 164] as shown in Figure 3.28b, and finally single-turn circular and spiral models [162, 165]. Electrode shapes also changed from planar electrodes [162, 163] to more realistic banded, half-banded, and ball electrodes [160, 162, 164, 165]. A neural model was also implemented as the optimisation criterion. Initially, Rattay's AF was used [117, 163], but the most recent iteration switched over to the GSEF model [100, 165].

Choi *et al.* found that the electrode-tissue interface plays a crucial role in determining intracochlear impedances [162]. Their results suggested that a tapered geometry was important, but the spiral shape was not, in contrast to Hanekom's findings. The difference may be due to the use of a purely tetrahedral mesh, instead of Hanekom's hexahedral dominant mesh [155]. Hanekom's spiral model also included a half-turn of overlap and was coupled with a different neural model. The group's most recent work showed that ECAPs predicted by the spiral model correlated qualitatively with measurements from a CI recipient, but the *in vivo* and *in silico* results are plotted on different scales, making comparisons tricky [165].

The group also questioned some of the conductivity values used in the model, which seemed to overestimate results compared to electric field imaging. This casts some doubt on the work

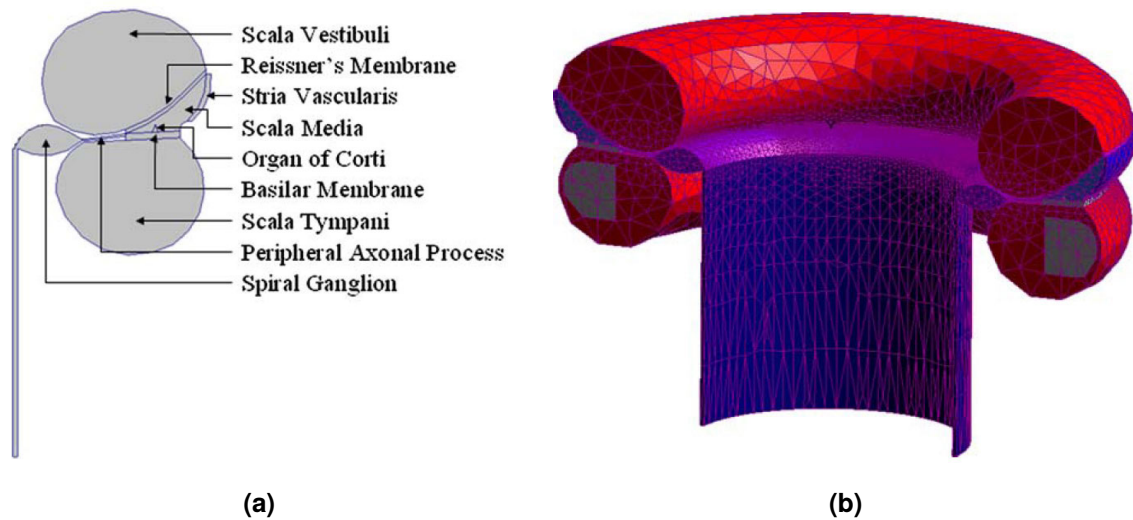


Figure 3.28: The Choi model. (a) Sectional view showing the tissue compartments; (b) the tetrahedral volume mesh. (Source: Choi *et al.* [160]. Copyright © 2009, Springer.)

by Vanpoucke [29] and Hanekom [155, 156], who had used the same values in their models. Aside from the material properties though, the glaring weakness of the Choi model is its overly simplified geometry. This was likely required in order to automate the discretisation stage for their algorithmic testing methodology.

Tognola *et al.* (2007)

Tognola *et al.* created a finite element model of the human cochlea to investigate the relationship between stimulation parameters and the electric field induced in the cochlear tissues. It highlighted some of the shortcomings inherent to *in vitro* techniques, as well as the potential promise of simulation studies for CI optimisation. Their model is illustrated in Figure 3.29.

The geometry of the Tognola model was based on the same photomicrograph as the Rattay model [159]. The cross-sectional boundaries of the tissues were not as highly simplified as in the Rattay study, but extrapolation around the spiral path was still performed in 30

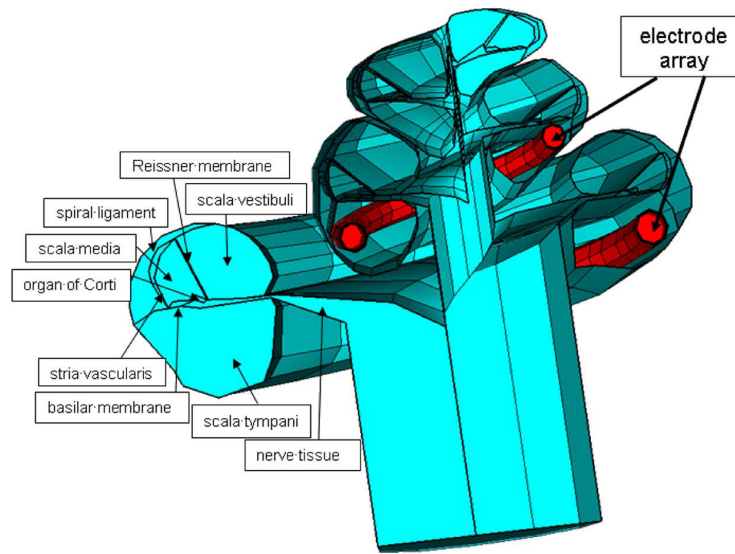


Figure 3.29: The Tognola model. (Source: Tognola [166]. Copyright © 2007, IEEE.)

degree intervals. Surrounding the cochlear tissues was a cylindrical domain of bone tissue. In addition, a full-banded CI array model based on the Nucleus CI24M was inserted into the scala tympani along an averaged insertion path. Resistivity values for both the cochlear tissues and the electrode array were sourced from previous studies [99, 116, 144, 167]. Tognola *et al.* wrote that both MP and BP stimulation modes were tested, but it was not clear what boundary conditions were imposed for the MP simulation. Finally, the simulations were compared to measurements in a water tank for validation.

Their results showed differences between the electric field patterns generated by MP and BP stimulation, with BP stimulation producing steeper gradients as expected. The *in silico* BP results also exhibited a qualitatively similar trend to the corresponding *in vitro* results. However the study was not clearly linked back to consequences for CI stimulation and offered little insight beyond what had already been demonstrated.

Whiten (2007)

The Whiten models [22] were the first attempt to reconstruct and recreate patient-specific responses to CI stimulation. Two VCMs of two different CI recipients were generated, each of which was compared to similar population data, as well as archival data (intracochlear potentials, psychophysical thresholds, and ECAP recordings) collected from each patient during life. This was crucial for properly validating the higher-level *in silico* predictions of the models.

The model geometries were reconstructed from serially-sectioned images of the implanted cochleae after death. Image resolution was $17.8 \times 17.8 \times 20 \mu\text{m}$ for the Ineraid model, and $16.8 \times 16.8 \times 40 \mu\text{m}$ for the Nucleus model. In this way, the detailed pathology of each cochlea, the locations of nearby structures in the temporal bone (namely the facial and vestibular nerves, the vestibular labyrinths, and the carotid artery, which may all be important during monopolar stimulation), and the true trajectory of the implanted electrode arrays was reflected in the digital models. The Nucleus model is shown in Figure 3.30. A generalised model was also created from one of the data sets. Purely resistive material properties were assigned to the tissues, but curiously the values used were from older papers and not specific to the human cochlea [133, 168]. The models were solved using the FDM and coupled with a modified version of McNeal's single nerve fibre model [119] to predict activation patterns. This was in turn used to predict extracellular current flow along each fibre, and finally the expected ECAP waveforms at each electrode.

Whiten used the models to investigate the effect of various parameters on current flow, neural excitation, and ECAPs, with mixed results. He found that the detailed anatomy of the cochlea and the resistivities of the materials (particularly bone and the cochlear fluids) were the primary factors driving *in silico* current flow predictions. For instance, a homogeneous model (analogous to using an analytical solution assuming a uniform resistivity) predicted a

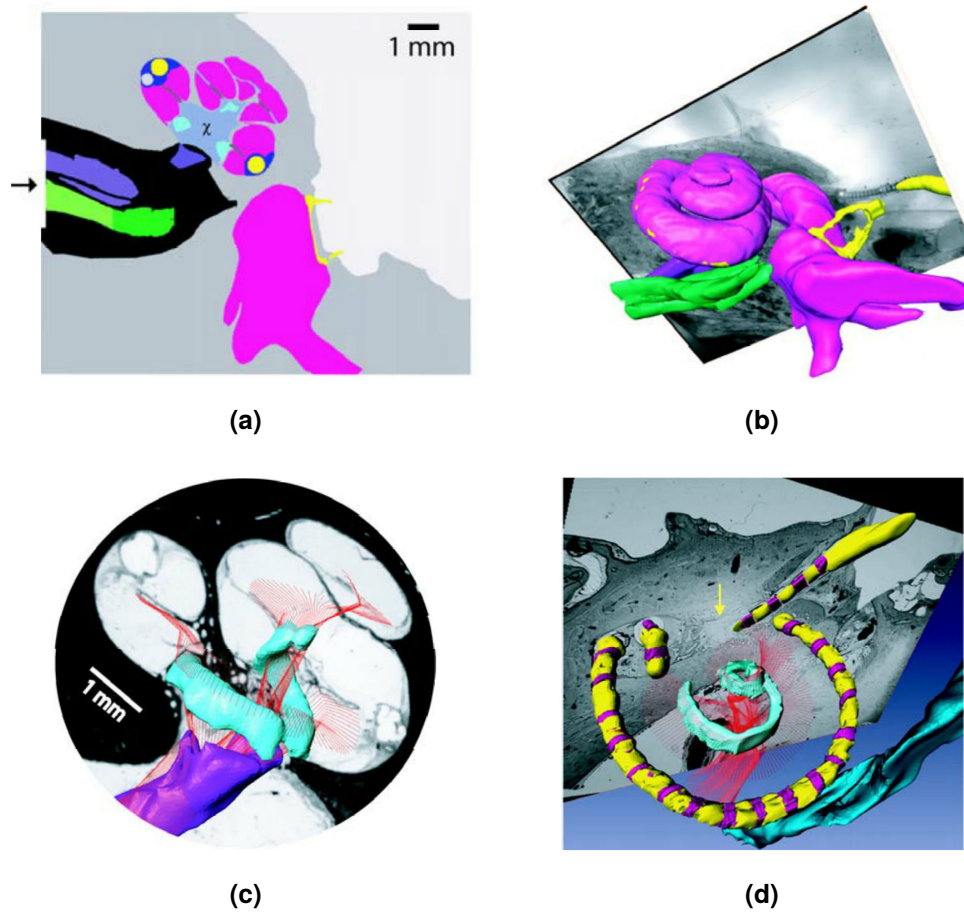


Figure 3.30: The Whiten model of an implanted Nucleus array. (a) A segmented slice of the human cochlea; (b) 3D view of the tissue surfaces; (c) a mid-modiolar view of the nerve tissue and fibre tracks; (d) the segmented electrode array. (Source: Whiten [22]. Copyright © 2007, MIT.)

vastly different pattern of current spread than the heterogeneous model, verifying the need for VCMs. Finer anatomical details also affected current flow, but the results were generally small and localised. The peripheral anatomy (namely the facial nerve and the vestibular system) is likewise expected to have minimal impact. However, encapsulation tissue is an important factor, and models of chronic CI stimulation that include this should account for the spatial distribution of the scar tissue. ECAP predictions were not perfect but the correlation with *in vivo* data was surprisingly solid. It was noted, however, that several underlying assumptions were likely to be violated, so the results are either insensitive to those assumptions or they may be falsely positive. Predictions of psychophysical data from the implant recipients were considered less successful, which might be expected considering the compounding of modelling errors through multiple layers of abstraction.

Some aspects of the Whiten study are likely candidates for improvement. The geometry is not particularly detailed, and the choice of resistivity values is questionable. Whiten also concluded that further work is required to determine appropriate boundary conditions and exit pathways under MP stimulation. Finally, the assumption of longitudinal current flow directions and measurements brings to mind the older LEM transmission line models and may not be appropriate. The promise of detailed (and in this case, patient-specific) current flow visualisation was poorly realised, though admittedly this is true for all models to date.

Saba (2012)

Saba created a few models to investigate the spread of voltage within the cochlea, the consequences of current-steering techniques, and methods for improving the power efficiency of CI devices [37]. His coiled model, shown in Figure 3.31, was based on a mid-modiolar section from Zakis and Witte [169] that was scaled to size according to dimensions from various literature sources. The 3D geometry was approximated using lofted cross-sections and guide curves in a computer-aided design (CAD) program. An electrode array model

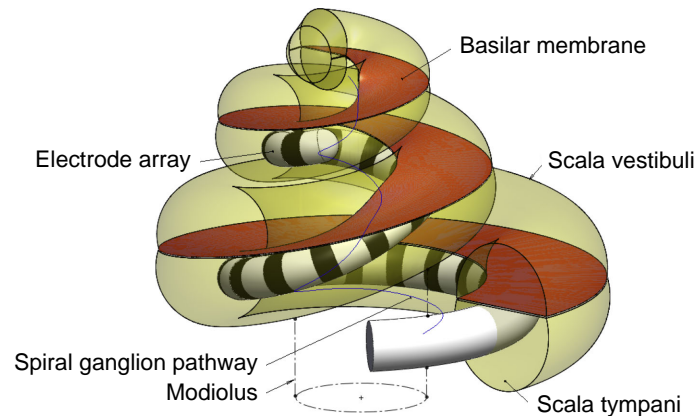


Figure 3.31: The Saba model. (Image adapted from Saba [37]. Copyright © 2012, Rami Saba.)

based on a data sheet of the Cochlear Nucleus 24 Contour and Contour Advance electrode arrays was similarly constructed for this study. Resistivity data was taken from previous modelling efforts [105, 144, 155, 159].

Once again, the spiral geometry of the cochlea was shown to be important to the voltage distribution. Saba concluded that this was a driving factor behind the inter-patient variability in CI performance. It is worth bearing in mind, however, that the geometry of the Saba model is simplified and does not include all known cochlear tissues. The modelling results also suggested that current focusing methods such as PA stimulation were less effective when considering effects at the level of the spiral ganglion, but could be optimised at a high power cost. Unfortunately, the criterion used were purely electric field quantities and were not properly tied back to neural excitation. Likewise, he found that placing a ball return electrode in the modiolus would reduce CI power consumption, but he does not consider the surgical practicality of doing so nor the effect on the auditory nerves (in terms of ectopic stimulation or electrochemical safety) near the proposed return. His final key finding was that power harvesting is not feasible for contemporary CI systems due to insufficient efficiency.

3.4 Research Questions

The state-of-the-art has advanced significantly in comparison to the pioneering studies. Nevertheless, there are some areas where *in silico* bioelectric models of the cochlea can still be improved. At the core of the problem is a hitherto incomplete investigation of the assumptions used to generate the models, which has led to a lack of consensus on some modelling issues and apprehension by CI researchers, especially those on the clinical end of the spectrum, to trust modelling predictions. These outstanding issues must be resolved because neural excitation models depend on the field distribution predicted by VCMs. If the assumptions on which VCMs are based are invalid, then the predictions of neural activity in coupled models are similarly moot.

There are three key assumptions that this thesis attempts to address. The first is how best to impose boundary conditions for models of MP stimulation. Boundary conditions are a core input parameter in modelling studies and are particularly important in MP simulations because the return path to the extracochlear electrode lies outside the physical domain of the model itself. The lack of consensus for prescribing boundary conditions is not ideal for practitioners and detracts from the appeal of models to clinicians. Different boundary conditions will affect the exit paths taken by injected current, and the significance of this impact on results in the neural structures has not yet been studied. The most accurate approach would be to create a multiscale model that includes the entire head [112], but this is not feasible in most cases. Therefore, the next best option would be to identify a boundary condition that can be applied within the model domain and that closely replicates the current flow patterns of the whole head situation.

The second assumption is that the vascular pathways in the cochlea play a negligible role in volume conduction. Early studies suspected that the low resistivity of blood and the pervasiveness of the vascular network makes them an important conductive pathway [20,

106, 135]. All VCMs to date have, however, ignored their presence despite the lack of definitive evidence for their omission. Those that discussed this issue assumed that the vessels would have minimal impact on the global current pathways because they occupy a relatively small volume, but this measure alone fails to consider the proximity of the modiolar vessels to the stimulating electrodes—which magnifies the effect on the overall current paths as shown by Baker [103]—and the trajectory of the vessels through key structures such as the modiolar bone and the nerve trunk.

Last is the quasi-static assumption on which all existing VCMs are predicated. This is perhaps their most glaring weakness because it is well known from experimental work that the *in vivo* responses—especially those in neural tissue—are time-dependent. There are several reasons VCMs have applied the quasi-static assumption. Firstly, there is a lack of data on the frequency-dependent resistivities and permittivities of cochlear-specific tissues. Secondly, at the relatively low fundamental frequency of CI input pulses, resistivity values for other bodily tissues are somewhat invariant and permittivity only plays a minor role [167]. Thirdly, voltage response measurements within the scala tympani by Spelman [98] demonstrated minimal phase lag, and this is often cited as justification for creating stationary models. However, only frequencies up to 12.5 kHz were tested, which ignores the high frequency components of clinically used square waves, and measurements in other cochlear tissues may exhibit a more pronounced effect due to higher tissue permittivities. The final reason is that model setup and solution is much simpler under quasi-static conditions, with the lower computational effort enabling substantially faster simulation times.

In addition to these, there is also a need to better visualise the underlying physics of the stimulated cochlea. Many models relate the simulation results directly to psychophysical measurements, providing no insight into the physical relationships that might be used to improve the design of electrode arrays. The models that do talk about electric current streamlines when discussing charge movement through the cochlea have not provided illustrations

of these streamlines through 3D space. An intuitive representation of these physical quantities would therefore aid in promoting a deeper understanding of the factors affecting CI stimulation in a wider audience and may lead to new and useful insights for future array designs.

Chapter 4

Model Development

This chapter addresses the following questions:

- How should the bioelectric models be created?
- What are the required inputs?
- What specific steps were followed to create the models?

4.1 Introduction

The overarching goal of this thesis is to determine how volume conduction models (VCMs) of the cochlea can be improved. An accurate VCM would allow a better spatial understanding of the cochlear implant (CI) system to be obtained, and for the research questions detailed in §3.4 to be answered. To achieve these outcomes, it was important to develop and implement a methodology that was robust, flexible, and efficient, which was not a trivial task given the challenges in model creation [22, 37, 101, 105]. Therefore, a number of solution methods, software packages, and input parameters were critically considered. The initial workflow

was progressively evolved to overcome a number of different computational issues, and to represent the data more intuitively so that implications could be inferred and conclusions easily drawn.

This chapter documents the groundwork required to prepare the models of the thesis for more in depth simulation studies. It covers the foundational work that was performed to get the models into COMSOL, such as the imaging, reconstruction and discretisation of the spatial domain, and consideration of other required inputs such as material properties, loading, and boundary conditions. The extensive documentation is intended to provide some guidance for others looking to undertake development of a cochlear VCM. Details of the actual analyses, including simulation results, are provided in the subsequent chapters.

4.2 Preliminary Considerations

4.2.1 Modelling Workflow

Generalised Pipeline

The typical flow of data when creating a VCM has been summarised by both MacLeod [170] and Lau [171]. The model development workflow used for this project was informed by these procedures and is illustrated in Figure 4.1.

The first stage of the workflow is creating the model geometry, and there are two main alternatives to achieve this. A realistic reconstruction of the cochlear anatomy can be segmented from volumetric scan data, but it is also possible to use a few cross-sectional images in conjunction with computer-aided design (CAD) software to generate a cochlea-like shape. In either case, a solid model of the cochlea is combined with an intracochlear electrode array

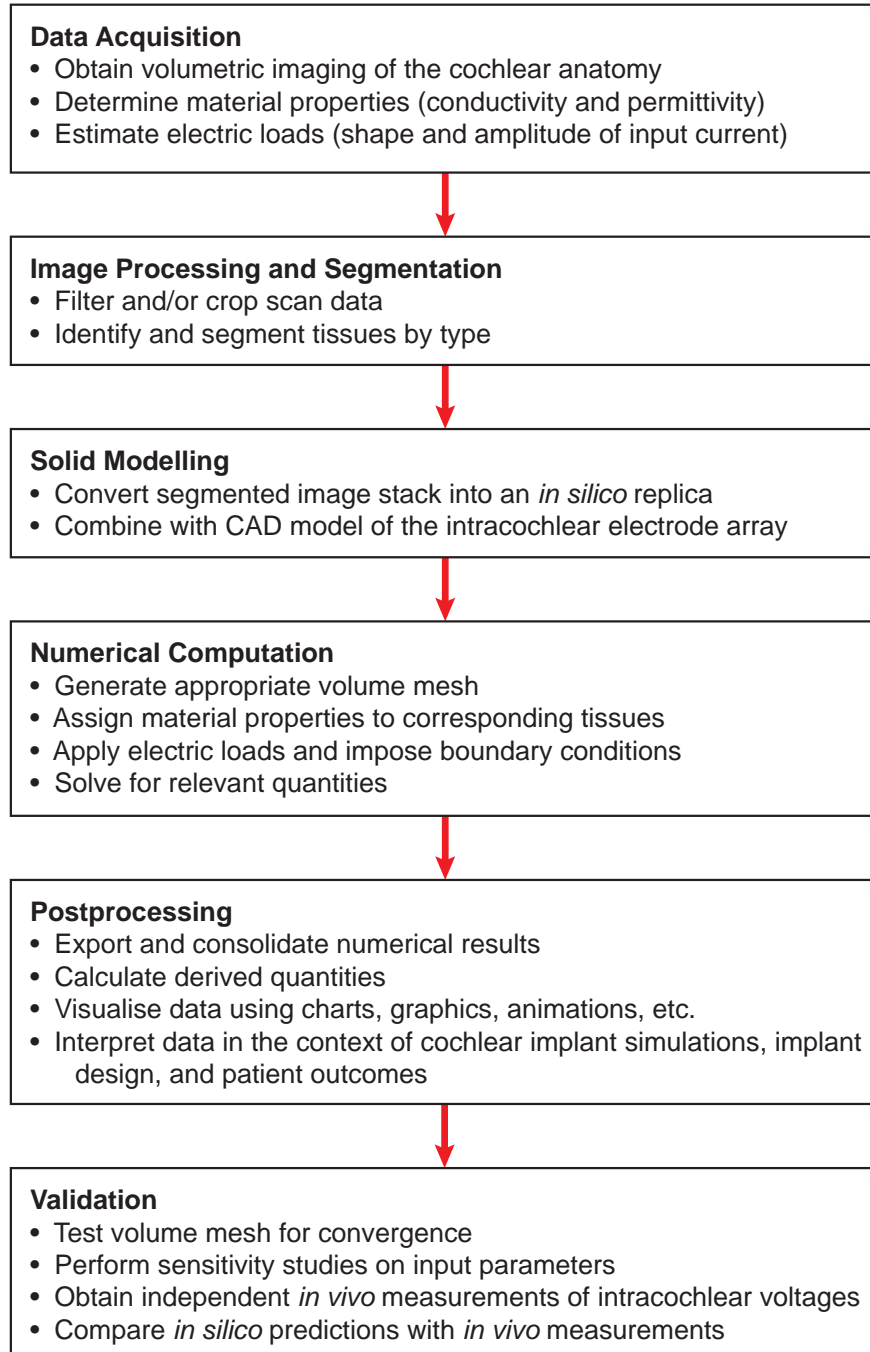


Figure 4.1: Overview workflow schematic, summarising the key objectives of each stage and the flow of data along the pipeline.

that is virtually inserted into the scala tympani. The model is then meshed and analysed using a numerical method, and various results of interest are exported, processed, and interpreted by the researcher. Finally, the *in silico* results are compared with *in vivo* validation data to demonstrate their correlation and to check whether the overall level of error is acceptable.

One of the main considerations when developing the workflow was the modularity of the pipeline. A monolithic program that encompassed the entire workflow could be ideal for ensuring format compatibility and reducing the number of programs that needed to be learned. However, it would also be useful to be able to interface with independent programs and take advantage of specific tools or functions that were more convenient or better implemented. Software-agnostic formats for the various data types along the pipeline would facilitate this flexibility and the potential for a more refined outcome. Of course, it would need to be balanced against the time and financial costs of integrating more programs—the latter could become especially prohibitive if commercial licencing agreements are required.

Effect of Uncertainties

VCMs require a number of data inputs as part of the *in silico* reconstruction. These can be classified into four categories as shown in Table 4.1. Clearly, the quality of the input data influences the accuracy of the final model, but these data are difficult to quantify accurately due to the biological nature of the system.

Of the four input types listed, only the electrical loads are well defined since these are controlled via the programming of the implant. The shape of the cochlea differs from one individual to the next, making it difficult to define an “average” or “median” cochlea. Erixon’s work with corrosion casts [47] provides a good sense of this variability. In terms of the material properties, the conductivities of the cochlear tissues have been measured experimentally, but the precision of each measurement varies and the values can also differ

Table 4.1: Data inputs required for volume conduction modelling.

Input	Description
Geometry	The shape of the structures within the region of interest
Material properties	The resistivity and permittivity of each structure due to its physical composition
Loads	The electrical forces to which the system is being subjected
Boundary conditions	The conditions for physical compatibility at the boundaries of the modelled domain

between individuals. Cochlear-specific tissue permittivities have not been measured at all. The kinetics at model boundaries, which are especially important in monopolar simulations, depend on the physical scope of the model, and to date have largely been based on assumptions with no consensus amongst practitioners. Combined with the segmentation, discretisation, and numerical errors inherent in computational modelling, these uncertainties adversely affect the reliability of modelling results. Controlling the sources of error is therefore an important consideration.

Consulting engineer David Beneke encapsulated these concerns neatly as follows:

“The art of finite element analysis is modelling

materials we do not wholly understand,

in shapes we cannot precisely form

so as to withstand forces we cannot properly assess,

in such a way that the analyst is confident in the design with the public having

no reason to suspect the extent of one’s ignorance.”

— David Beneke [172]

With this in mind, there are several avenues for inspiring trust in the *in silico* results. Firstly, a critical review of the model inputs in conjunction with sensitivity studies will reveal the degree of uncertainty; if the level of uncertainty is low or the system is insensitive to the input, then the data may be used with some confidence. Secondly, modelling errors can be minimised by using a robust workflow and by taking care during each stage of the development pipeline. Thirdly, validation of the model via comparison with independently obtained *in vivo* measurements will ensure that the *in silico* predictions are reasonable and within expected real-world limits.

The issues surrounding each input type are discussed presently.

4.2.2 Geometry and Imaging

Unlike typical engineering structures, the geometry of living organisms is incredibly complex, and very few organs exhibit true planar or rotational symmetry [109]. Defining the physical domain is therefore a significant challenge, especially given the intricate shape and inaccessible location of the cochlea. Several different aspects needed to be considered with regards to reconstructing the cochlea *in silico*.

Subject-Specific versus Generalised Modelling

The first was whether to create a subject-specific model or a generalised one. Examples of subject-specific models are those by Girzon [20], Whiten [22], and Malherbe [157, 158]. In these models, the geometry is typically obtained from volumetric scans of the region of interest for a particular individual. If the image stack is of sufficient resolution, a highly detailed and accurate reconstruction can be generated. The model would only be directly

applicable to the scanned individual, but insights may be extrapolated (with care) to a more general population, especially if the geometry does not deviate too far from the mean.

In contrast, generalised models are designed with the goal of representing an “average” or “median” cochlea without replicating any particular individual. Generalised models have been created with a variety of means; typically, a cross-sectional histological image of a real cochlea is swept along an average path that is either linear [37, 100, 144, 161, 173], circular [100, 163], or helical [37, 65, 147, 155, 159, 166] in shape. They can be easier to manipulate during the modelling phase than subject-specific models because the shape is described by a known equation, so they can be parametrised and fitted to different patients (inevitably with some degree of error). The increased tangential smoothness also makes them easier to discretise. However, they are generally less realistic, particularly at the basal and apical extremes where the shape deviates from the rest of the cochlear spiral.

A subject-specific model was deemed better for this project because of the potential for greater realism, and because the complex distribution and convoluted paths of the cochlear blood vessels would be difficult to reconstruct accurately using an equation-based model. The findings would also be more relevant to the longer-term trend in the industry towards building customised models for surgical planning and predicting patient outcomes.

Selection Criteria for Image Data

Obtaining suitable volumetric scan data for a subject-specific model was a significant challenge because the goals of the project required fine anatomical details to be part of the final model. These structures are extremely small—for instance, Reissner’s membrane, the basilar membrane, and the stria vascularis in the guinea pig are roughly 1.7 μm , 4 μm , and 40 μm thick, respectively [100]; the diameters of the smaller cochlear blood vessels are similar in scale, as shown in Table 4.2.

Table 4.2: Measurements of cochlear vessel diameters in man.

Blood vessel	Lumen diameter (μm)	Source
Radiating arterioles		
“Vascular spring-coils”	20–40	Scuderi and Del Bo [55]
Spiral lamina	30–40	Charachon [174]
Arterio-venous anastomoses	15–20	Charachon [174]
Capillaries		
Stria vascularis	7	Charachon [174]
Scala vestibuli	5–10	Charachon [174]
<i>(Unspecified)</i>	5–10	Axelsson [49]
	6–12	Mondy [175]
Vessel of the basilar membrane	10–20	Charachon [174]
Collecting venules	10–17	Charachon [174]

Visualising individual parts is relatively straightforward—the scalae can be discerned easily [101, 176], and fine structures can also be resolved provided sufficient imaging resolution [177]—but the requirements for accurate mesh generation are substantially more stringent [176]. A VCM requires that the various component structures be connected throughout the domain regardless of the complexity of the interfacing regions. Structural discontinuities (e.g. holes in the membranes, gaps between parts, or disconnected vessels) and deformations (e.g. ripples in smooth membranes, image artefacts) will adversely affect the reconstructed geometry [105, 176, 178].

The ideal dataset would therefore possess the following attributes. Firstly, given the thinness of the membranes and the small size of the vasculature, the image resolution must be of the same order as these fine structures to maximise opportunities for feature extraction. The most detailed dataset available should be used since the data could be downsampled if computational requirements are excessively high, but cannot be upsampled to provide enhanced detail of pre-existing features [35]. Technical limitations related to the specific

imaging technique and the need to maintain the entire cochlea within the field of view will enforce an upper limit on the attainable resolution for any given sensor size [176].

Secondly, the contrast and clarity of the dataset were also important. Since the model was to contain a large number of different tissue types in the final reconstruction, each tissue had to be visible and recognisable in the image stack, ideally with distinct boundaries to facilitate the segmentation process. Imaging artefacts and noise in the scans were similarly undesirable because they hinder accurate reconstruction.

Lastly, the availability of each technique was a key determinant because the scans were to be sourced from third parties with the necessary equipment and expertise. This would ensure that the image stacks from any chosen modality had the best chance of fulfilling these desired attributes.

Comparison of Imaging Modalities

Multiple options were considered for this project, namely *computed tomography* (CT), *magnetic resonance imaging* (MRI), *histological serial sectioning*, and (*laser*) *light-sheet fluorescence microscopy* (LSFM). Examples of each modality are provided in Figures 4.2 and 4.3 for human and guinea pig cochleae, respectively.

CT scans have been used to image various parts of the body for many years. Like x-ray technology on which it is based, CT images depict differences in material density based on the amount of radiation that is absorbed as the x-rays pass through the sample. Unlike x-ray however, it involves taking multiple images around the sample and correlating the luminance of each point with its position to give a three-dimensional, volumetric image stack. CT is often used to image the cochlea because the difference in density between the surrounding bone and the fluid chambers results in a high level of contrast between those two tissues.

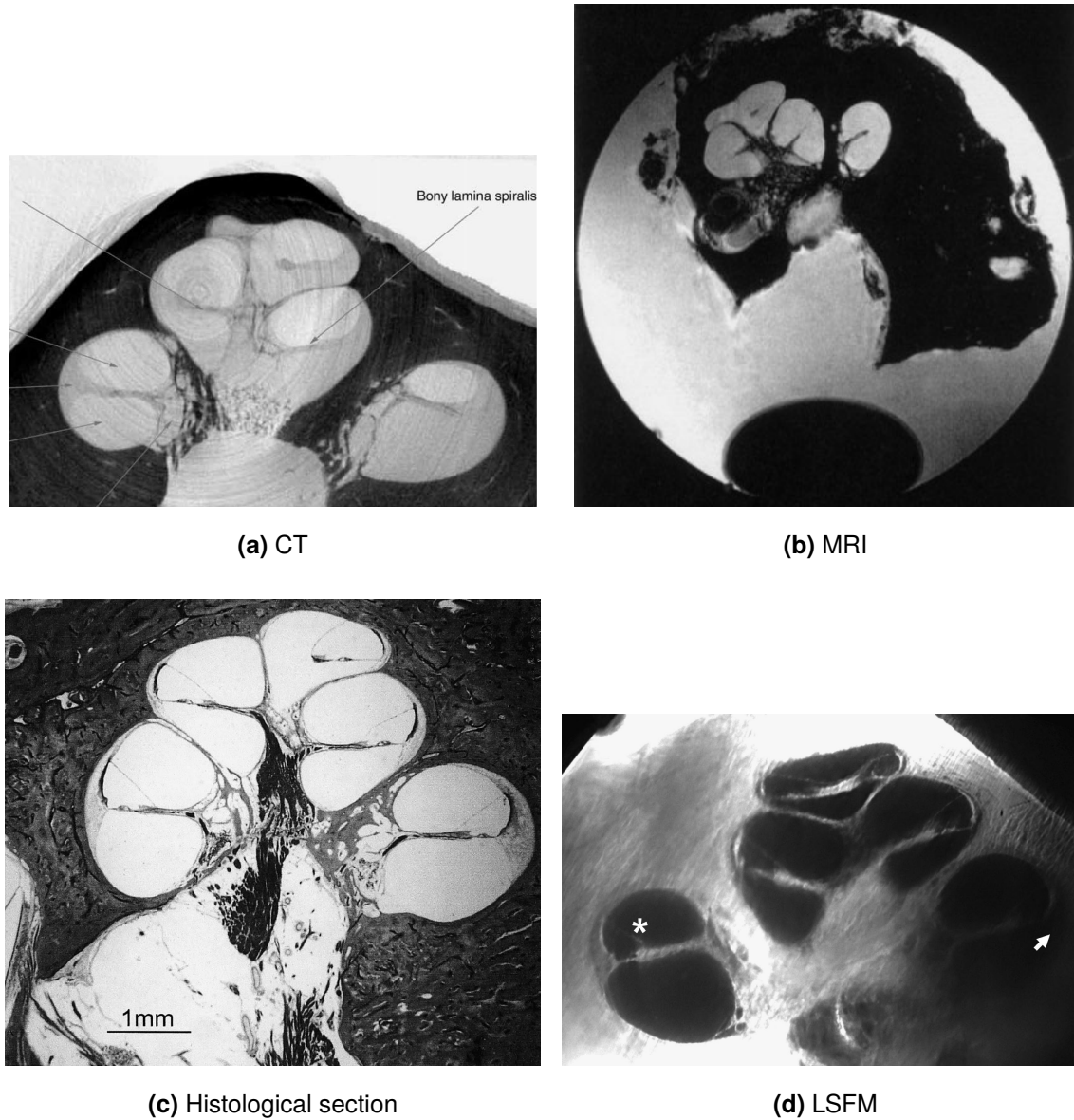


Figure 4.2: Comparison of imaging modalities for the human cochlea. MicroCT and high resolution MRI are shown here; clinical counterparts would have significantly lower resolution. Note the different types of imaging artefacts and the variations in resolution and clarity. (Sources: (a) Postnov [179], Copyright © 2006, Taylor & Francis; (b) Silver [180], Copyright © 2002, John Wiley & Sons, Inc.; (c) Rattay [159], Copyright © 2001, Elsevier B.V.; (d) Johnson [178], Copyright © 2014, Wolters Kluwer.)

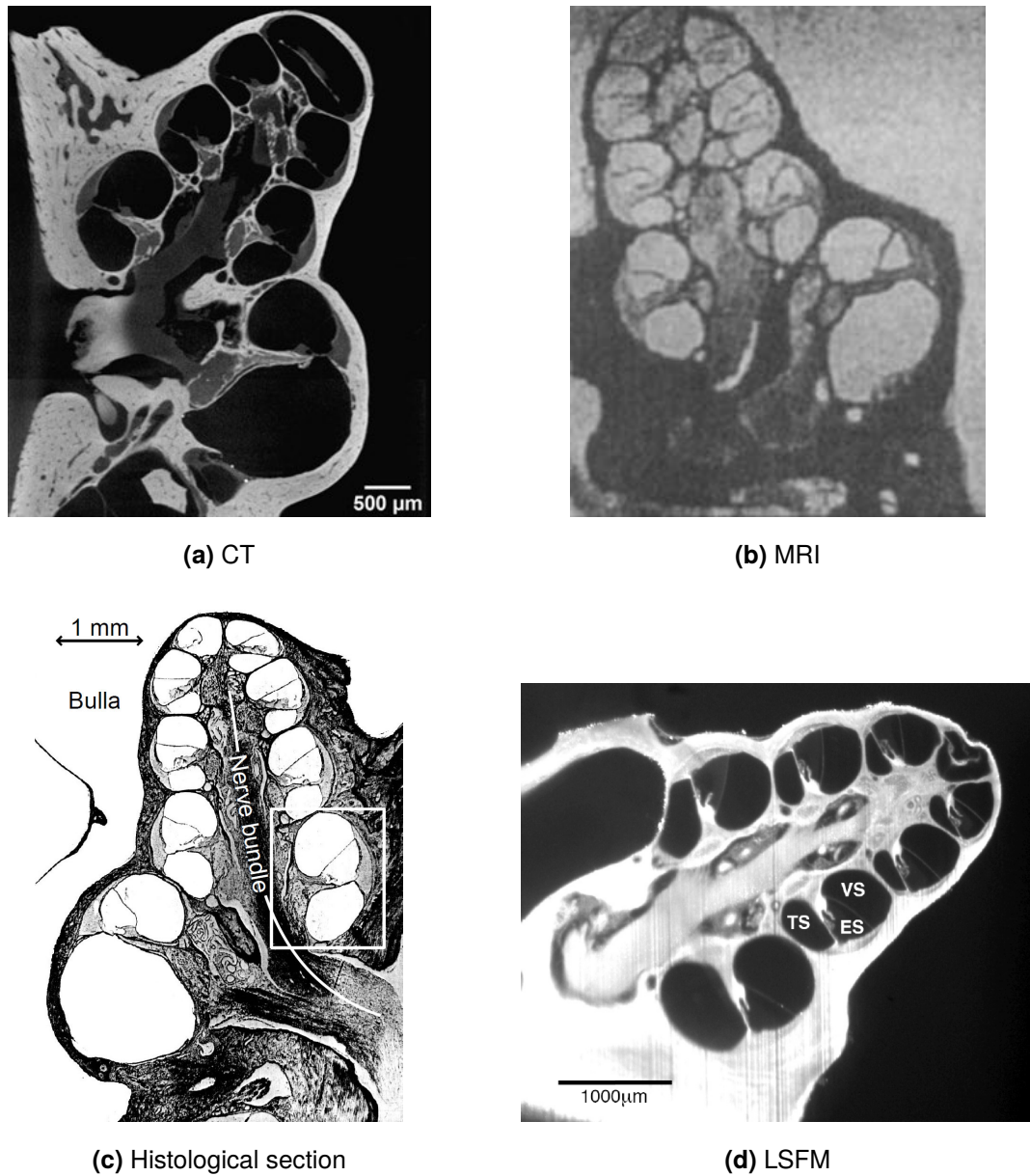


Figure 4.3: Comparison of imaging modalities for the guinea pig cochlea. Typical mid-modiolar slices were sought to show the level of detail available when the field of view includes the entire cochlea. Single turn images would provide more detail but for a much smaller region. (Sources: (a) Poznyakovskiy [176], Copyright © 2008, Elsevier B.V.; (b) Thorne [64], Copyright © 1999, John Wiley & Sons, Inc.; (c) Briaire [105], Copyright © 2000, Elsevier B.V.; (d) Hofman [181], Copyright © 2009, Rutger Hofman).

One shortcoming of this technique is resolution. Even high resolution clinical CT scans only have a resolution of about 150–300 μm , which can reveal the fluid chambers but not the constituent structures with any meaningful detail [154, 182–184]. MicroCT can do better in this respect, going down to 2–8 μm [175, 185], but requires an explanted tissue sample. Even then however, the scans often lack contrast in soft tissue regions due to the small density differences, so contrast agents are typically required to enhance the clarity of the structures of interest. CT is also susceptible to noise, though this can be mitigated to some extent by the operator via careful selection of scanning parameters prior to scanning. More exotic techniques, such as synchrotron radiation-based microCT [185], are also possible, but obtaining access to such facilities is difficult.

MRI is based on a different principle: the relaxation time of protons after excitation by an electromagnetic field. The brightness of the image corresponds to the density of protons in that region, so unlike CT, MRI is quite good at distinguishing between different types of tissue, including soft tissue. Their individual textures are often visible in scans, but most segmentation algorithms are not able to distinguish tissues in that way so the process would have to be done manually. Image resolution depends on the field of view and sensor size. Clinical MRI systems are comparable to those of CT, but typically a little worse [184]. High resolution MRI techniques offer around 25 μm voxels [180, 186], which is not sufficient to resolve the cochlear membranes.

Histological sections are the most commonly used technique for existing cochlear models. The use of light microscopy provides for a very clear image with high (sub-micron) resolution. Tissues of specific interest can be stained to enhance contrast as required. Unlike CT and MRI however, it is inherently a destructive technique. The microtome can create slicing artefacts in the final sample that result in undesirable misalignment of both gross and fine anatomical structures [181] in the reconstruction, as demonstrated in Figure 3 of Johnson [178]. This is probably why most histology-based reconstructions only use a single mid-modiolar slice. In

addition, the spacing in the slice direction is often relatively large, so even if an image stack was obtained, the voxels would be anisotropic in size.

LSFM is a more recent addition that combines the clarity and resolution benefits of histological imaging with the non-destructive nature of CT and MRI imaging [187, 188]. The technique has evolved through many variations, which were recently reviewed by Santi [184]. Studies comparing LSFM-based imaging with other forms have generally concluded that the former is superior [178, 181, 189], especially when cost is also factored in [184].

In the end, different models were produced using different imaging modalities, with the main determining factors being availability and image quality. Note however that the chosen modelling workflow is applicable to all scan types. The specific data used for each model are detailed under their corresponding methodology sections.

4.2.3 Material Properties

The cochlea, like the rest of the body, is not a homogeneous structure [75]. It contains a multitude of different tissue types, each with a unique composition, structure, and (accordingly) physical properties. The electrical properties of these component tissues can vary dramatically, so assumptions of homogeneity will lead to inaccuracies and should be avoided [170, 171]. The boundaries between most tissues are quite distinct so the overall domain can be considered as being piecewise homogeneous [109, 190], but note that tissue boundaries may be graded in reality and there can be variations in composition (and therefore properties) within a single tissue sample [28]. Properties may also vary from one person to the next [47, 171]. In addition, tissue properties are often *anisotropic* [75], i.e. they vary by direction (cf. blood vessel walls [191, 192], white matter [171, 193]), further complicating the specification process.

For electrical simulations, the material properties that govern the behaviour of a material are *resistivity* and *permittivity*, which are normalised values for the bulk properties of resistance and capacitance, respectively. Some studies use *conductivity* in place of the former; this is simply its reciprocal. Resistivity and permittivity have been measured for a multitude of biological tissue types in the literature. Most compendiums focus on general body tissues [133, 167, 194, 195], like bone, nerve, muscle, and so forth, and the reported numbers are generally accepted as good representative values. While some parts of the cochlea are comprised of such tissues, there are also specialised tissues in the cochlea that are not found elsewhere in the body. Thus, it is important to obtain values that are specific to cochlear tissues where possible.

Resistivity Values

Resistivity values can be found in the literature for all of the major cochlear tissues, but there are ongoing concerns over the accuracy of some values. The following tables list the values that have been used in previous modelling studies, as well as direct measurements where available. A range of methodologies are represented, with differences in measurement technique, stimulus frequency, and other factors. Values reported in some studies can also often be traced back to a single, often dated source [21], such as the bulk resistances measured by Strelioff [116]. This means that the reliability of those values is low, but they are used regardless due to the lack of other data points.

Permittivity Values

On the other hand, there is a severe shortage of data regarding cochlear tissue permittivities. The lack of work in this area may in part be due to Spelman's findings of minimal phase lag in voltage waveforms within the scala tympani [98]. The study is often cited in existing

Table 4.3: Resistivity values for bone from existing literature. For this and the following tables, the data are sorted first by primary investigator, then chronologically.

Source	Year	Value ($\Omega \cdot m$)	Comments
Girzon	1987	50	Temporal bone
		5	Modiolar wall
Finley	1990	6.3	
Suesserman	1992	13.73	Skull
		6.41	Lateral wall
		11.7	Modiolar wall
Frijns / Briaire	1995	6.41	From Suesserman
		5	Modiolar bone (measured using EFI)
		125	Otic capsule (assumed)
Haueisen	1995	160	Bone
		21.8	Soft bone
	1997	160	Hard bone
		25	Soft bone
Hanekom	2001	6.41	From Frijns <i>et al.</i> [100]
Rattay	2001	64	Adapted according to Kosterich <i>et al.</i> [196]
Choi / Lai	2004	6.41	From Hanekom [155]
Whiten	2007	50	Used for “normal bone”
Bai	2011	166.67	Compact bone
		35.71	Spongy bone
Saba	2012	6.41	From Frijns <i>et al.</i> [100]

Table 4.4: Resistivity values for nerve from existing literature.

Source	Year	Value ($\Omega\cdot\text{m}$)	Comments
Girzon	1987	3	Used in model
		1–4	Noted as typical values
Finley	1990	3	Axial
		15	Transverse
		3	Spiral ganglion
Frijns	1995	3.33	Reported as conductivity
Haueisen	1995–1997	3	Human brain grey matter
		7	Human brain white matter
Hanekom	2001	3	Axial
		15	Transverse
		3	Spiral ganglion
Rattay	2001	3	
Whiten	2007	3	Used for “modiolus with nerve tissue”, as well as auditory/vestibular/facial nerves
Bai	2011	3.23	Brain, except white matter
		7.14	White matter, isotropic

Table 4.5: Resistivity values for perilymph from existing literature.

Source	Year	Value ($\Omega\cdot\text{m}$)	Comments
Von Békésy	1951	0.476	Reported as conductivity
Girzon	1987	0.5	First estimate [20]
Finley	1990	0.7	
Frijns / Briaire	1995–2011	0.699	Reported as conductivity
Hanekom	2001	0.7	
Rattay	2001	0.7	
Choi / Lai	2004	0.7	
Whiten	2007	0.5	From Girzon
Saba	2012	0.7	

Table 4.6: Resistivity values for endolymph from existing literature.

Source	Year	Value ($\Omega\cdot\text{m}$)	Comments
Girzon	1987	0.5	First estimate [20]
Finley	1990	0.6	
Frijns / Briaire	1995–2011	0.599	Reported as conductivity
Hanekom	2001	0.6	
Rattay	2001	0.6	
Choi / Lai	2004	0.6	From Hanekom
Whiten	2007	0.5	From Girzon
Saba	2012	0.6	

Table 4.7: Resistivity values for CSF from existing literature.

Source	Year	Value ($\Omega\cdot\text{m}$)	Comments
Geddes	1967	0.65	
Haueisen	1995–1997	0.56	In rabbits
		0.65	In man
Gabriel	2009	0.56	At 40 Hz
		0.71	At 70 Hz
Frijns / Briaire	2009	N/A	Included in model but value was not specified
Bai	2011	0.559	Reported as conductivity

Table 4.8: Resistivity values for blood from existing literature.

Source	Year	Value ($\Omega \cdot m$)	Comments
Burger	1943	2.3	At 18°C
		1.6	Adjusted to 37°C
		0.7	At 37°C without erythrocytes
Geddes	1967	0.61–1	Plasma only
		1.31–3.63	Human at various frequencies and haematocrit
Mohapatra	1977	1.5	Standard value at normal haematocrit and body temperature
		0.68–3.95	Variations in haematocrit
Visser	1992	0.64–5.56	Variations in haematocrit
Gabriel	1996	0.7-16	
		1.23	At 40 Hz
		2.56	At 70 Hz
Haueisen	1995	1.5	
	1997	1.6	

Table 4.9: Resistivity of the cochlear membranes from existing literature.**(a)** Reissner's membrane

Source	Year	Value ($\Omega \cdot m$)	Comments
Girzon	1987	200	Listed under "scala media boundaries"
Finley	1990	604.8	Adjusted for membrane thickness
Frijns	1995	1020.4	Adjusted values from Strelhoff [116] for membrane thickness
Hanekom	2001	340.13	Adjusted for membrane thickness
Saba	2012	500	

(b) Basilar membrane

Source	Year	Value ($\Omega \cdot m$)	Comments
Girzon	1987	200	Listed under "scala media boundaries"
Finley	1990	18	Adjusted for membrane thickness
Frijns	1995	16	Adjusted values from Strelhoff [116] for membrane thickness
Hanekom	2001	4	Adjusted for membrane thickness
Saba	2012	37.5	

Table 4.10: Resistivity of other soft tissues in the cochlea from existing literature.**(a) Spiral ligament**

Source	Year	Value ($\Omega \cdot m$)	Comments
Girzon	1987	3	Used in model
		2.5	Derived from Cannon [197]
Frijns	1995	0.599	Reported as conductivity and based on endolymph

(b) Stria vascularis

Source	Year	Value ($\Omega \cdot m$)	Comments
Girzon	1987	3	
Frijns	1995	188.68	Reported as conductivity and adjusted for thickness
Hanekom	2001	125.79	Reported as conductivity and adjusted for thickness
Saba	2012	188	From Frijns <i>et al.</i> [100]

(c) Organ of Corti

Source	Year	Value ($\Omega \cdot m$)	Comments
Girzon	1987	200	Listed under "scala media boundaries"
Frijns	1995	83.33	Reported as conductivity
Hanekom	2001	83.33	From Frijns <i>et al.</i>
Saba	2012	83	Rounded from Frijns <i>et al.</i>

models to justify the use of purely resistive tissue properties throughout the cochlea, which is required to invoke the quasi-static assumption and simplify the analysis. Relative permittivity in this case can be set as unity for all tissues.

However, it is known that biological tissues are generally not purely resistive [69]. Their microstructures result in a frequency-dependent electrical response—at low frequencies the response is predominantly resistive, but at high frequencies the behaviour resembles a dielectric [20, 75, 98, 103]. Contemporary CIs operate in the 10–20 kHz range, so cochlear tissues can exhibit mild capacitive effects. (Note that this is independent of the capacitive effects arising from the double layer at the electrode surface.) The extent of these effects and the validity of the quasi-static assumption have hitherto not been investigated.

4.2.4 Electric Loads

Although the amplitude and subtimings of a typical biphasic pulse can vary from one individual to the next, the specific values used in any particular implementation are known, so the electrical load can be considered as a given input. In the simulations for this thesis, loads were defined as current sources using a Neumann boundary condition at the inner surface of the stimulating electrode:

$$n \cdot \sigma \cdot \nabla \Phi = J_n(x, y, z) \quad (4.1)$$

where n is the outward normal unit vector, σ is the conductivity of the material, Φ is the potential field, and J_n is the electrode current density [109].

The amplitudes used were chosen to represent values that are regularly seen in *in vivo* studies. Preliminary tests were performed with a 1 mA current amplitude to allow for easy scaling of results. This value was also used for the guinea pig model as it turned out to match experimental setups in that animal model. For tests in the human, 106.5 μ A was used because

this was equivalent to setting the stimulator to a current level of 100 [Cochlear Limited, internal communication].

4.2.5 Boundary Conditions

To ensure continuity at the interfaces between tissues, both the electric potential and the normal component of the current density must be compatible. For any two adjoining regions denoted by subscripts 1 and 2, this is expressed mathematically as:

$$\Phi_1 = \Phi_2 \quad (4.2)$$

$$n \cdot \sigma_1 \cdot \nabla \Phi_1 = n \cdot \sigma_2 \cdot \nabla \Phi_2 \quad (4.3)$$

at the interface, where again Φ is the potential field, n is the outward normal unit vector, and σ is the conductivity of the material [109].

The outer surfaces of the modelled domain also need appropriate boundary conditions, but this is difficult to implement for monopolar stimulation because the current flow extends beyond the reconstructed domain. This unmodelled return path is not intuitive because the global current streamlines are affected by the location and resistivities of tissues in the head that lie outside the cochlea. Reasonable assumptions can be made based on the known impedance of the system, but this has thus far led to a variety of alternative proposals with no consensus.

It is clear from the geometry, material properties, and electric loading that current injected within the scala tympani will spread out from the active electrode, and that the streamlines will only reconverge near to the return electrode [103] (recall Figure 3.10). Most models are simply grounded at an external surface to represent this outward current flow. Again however, the validity of this assumption has yet to be investigated. A preliminary study on

the impact of boundary conditions is presented in Chapter 5. This was extended as part of the validation study in Chapter 6. In these studies, external surfaces are modelled with fixed potentials using a Dirichlet boundary condition:

$$\Phi = V_0(x, y, z) \quad (4.4)$$

where V_0 is the voltage along that surface [109]. Grounded surfaces are simply set with $V_0 = 0$.

4.2.6 Numerical Solution Type and Software

Considering the types of questions that this thesis aims to answer, it is clear that an *in silico* model is required. Perhaps less clear—given the variety of existing model classes—is which numerical method is most suitable for this project. All three numerical methods have seen extensive use in bioelectric modelling, but differences in each formulation affect their suitability for different classes of problems [35, 107–110].

The relative strengths and weaknesses of the three numerical methods discussed in §3.2.2 are summarised in Table 4.11. By far the most popular method appears to be the finite element method (FEM). The boundary element method (BEM) is the next most common due to the ongoing research activities of the Frijns group. Finally, the finite difference method (FDM) has been used in a couple of different theses.

The FDM was ruled out due to its inability to handle complex geometries. The cochlea contains a number of thin membranes and blood vessels that need to be represented accurately, so the staircase effect would be an issue here. It also contains some vast fluid spaces, so if a dense point cloud was used to increase the accuracy of fine detail, the FDM would require

Table 4.11: Comparison of numerical solution methods.

Method	Advantages	Disadvantages	Notable examples
FDM	Simple to implement Easy to manipulate Efficient per-node computation	Staircase effect Inefficient refinement	Girzon [20], Whiten [22]
FEM	Unstructured mesh can handle complex geometries Per-element material properties with anisotropy	Requires discretisation of the entire volume Most difficult to implement and solve	Finley [144], Hanekom [155], Rattay [159], Choi [160], Tognola [166], Saba [37] Tran [112], Malherbe [158]
BEM	Easier to mesh than FEM Fewer nodes than FEM, so more efficient solution Good for homogeneous and unbounded problems	Restrictions on geometry Per-compartment material properties Analytical component can cause problems	Frijns [65, 100], Kalkman [153]

an extraordinarily large number of equations to be solved, eliminating its computational efficiency.

The two other approaches were better equipped to handle complex shapes, at the cost of being more difficult to implement. Discretisation is simpler and less time-consuming under the BEM, and the reduced node count meant that it would be quicker to solve than a similar FEM model. However, this advantage only holds for problems with a small surface-to-volume ratio [113], and the spiralling membranes of the cochlea mean this is unlikely to be satisfied (especially in the guinea pig, which has more turns).

Amongst practitioners, the general consensus is that the additional effort required to set up and solve a finite element model is worthwhile. The FEM is more accurate than the BEM and imposes fewer restrictions on the model geometry. For this thesis, the study on vascular effects would involve a geometry where one tissue domain penetrated many others, so the

BEM would have been suitable for this purpose. High quality FEM software was also more readily available. Given these reasons, the FEM was deemed the best method for this thesis.

Regarding selection of the FEM software itself, several candidates were considered. The first was an open source option known as SCIRun, developed at the University of Utah. The main attraction of using SCIRun was its modular framework, which encompassed the entire workflow from processing a stack of images into a virtual reconstruction through to analysis using the FEM [110, 170]. As an open source project, it could also be customised and extended as required by the user. However, it was difficult to secure reliable and knowledgeable support, and as a research-focused tool, was considered to be less proven than some commercial alternatives.

The three commercial FEM options that were available were ANSYS Classic/Workbench (ANSYS Inc., Canonsburg, PA, USA), Ansoft Maxwell (which has since been acquired by ANSYS Inc.), and COMSOL Multiphysics (COMSOL AB, Stockholm, Sweden). Unlike SCIRun, these packages focus exclusively on finite element analysis, so additional software was required for image processing, segmentation, and solid modelling. Simpleware ScanIP v4.3 (Simpleware Limited, Exeter, UK) was used for this purpose because it was readily available and is able to create and export volume meshes in a variety of compatible formats, including native ANSYS (Classic or Workbench) and COMSOL volumes, as well as the more open NASTRAN format.

ANSYS Classic was used for some early tests due to prior familiarity with the software, but the archaic user interface made it an inefficient choice for complex analyses. ANSYS Workbench and Ansoft Maxwell were also considered but encountered difficulties when importing meshes using the initial workflow. COMSOL did not suffer from the above issues. It provided similar functionality and results to the ANSYS software [112], had better data visualisation options, used more flexible Lagrangian elements (as opposed to serendipity elements) for quickly and easily changing the order of the elemental shape function, and

Table 4.12: Hardware specifications for the computers on which simulations were run. The NVIDIA Tesla K20 GPU accelerator in the workstation was not supported by COMSOL Multiphysics at the time of writing.

Component	PC (Custom-built)	Workstation Dell Precision T7600
Operating system	Microsoft Windows 7	
CPU	Intel Core i7 3930K	2 × Intel Xeon E5 2687W
Cores	6	2 × 8
Logical threads	12	32
Base clock	3.2 GHz	3.1 GHz
Turbo clock	3.8 GHz	3.8 GHz
RAM	64 GB DDR3	128 GB ECC RDIMM
Storage	256 GB solid state drive (plus various mechanical hard disks)	
GPU accelerator	N/A	5 GB NVIDIA Tesla K20

could be programmatically extended using its Java API (application programming interface). Given these advantages, COMSOL was chosen as the simulation software.

4.2.7 Computer Hardware

The majority of the simulations for this thesis were performed on a custom-built PC, but some were run on a Dell Precision T7600 workstation. Solution times reported in this thesis are for the PC. The computational resources for both machines are listed in Table 4.12.

4.3 Proof of Concept

4.3.1 Introduction

In order to provide some preliminary guidance on modelling requirements and methodologies, a simplified model was first created. This proof of concept (POC) model was based on an extruded geometry similar to that of Finley [143], but with much higher spatial resolution. An early study using this model was presented at the 2012 IEEE EMBS International Conference on Biomedical Engineering and Sciences (IECBES2012) [173]. An updated iteration of this model was also used as the basis for an undergraduate honours thesis in 2014; this was presented at the 2015 IEEE Neural Engineering Conference (NER2015) [198].

4.3.2 Method

The workflow for the POC model is shown in Figure 4.4. Only a few programs were used at this stage, namely Adobe Photoshop, Simpleware ScanIP, and COMSOL Multiphysics.

Imaging and Reconstruction

The geometry of the model was based on a histological image of a section through one turn of the human cochlea from Donkelaar and Kaga (see Figure 4.5a) [199]. Image size was 709×1091 pixels, and the relatively narrow field of view allowed the various tissue types—including the membranes and blood vessels—to be easily identified.

The histological slice was pre-processed in Adobe Photoshop. Image contrast was enhanced using the Auto Tone functionality to help distinguish the various tissues of interest. Reissner's membrane required an additional gamma boost in order to resolve the boundaries clearly.

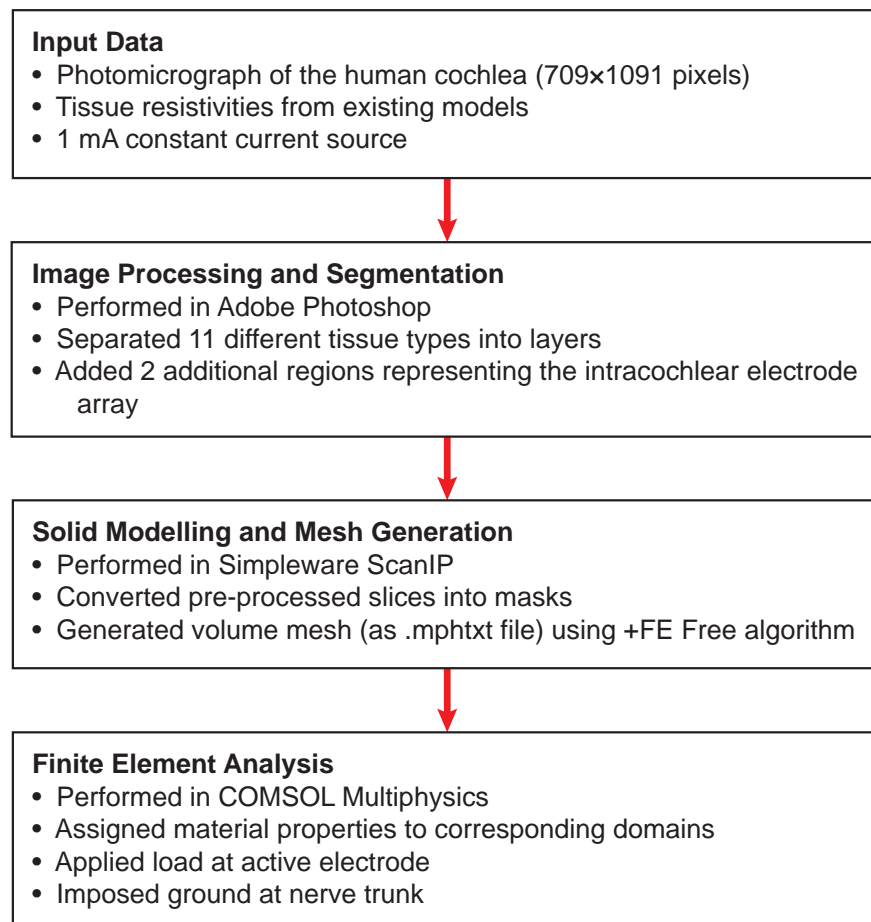


Figure 4.4: Workflow for the proof of concept model, indicating the programs used at each stage and the main tasks.

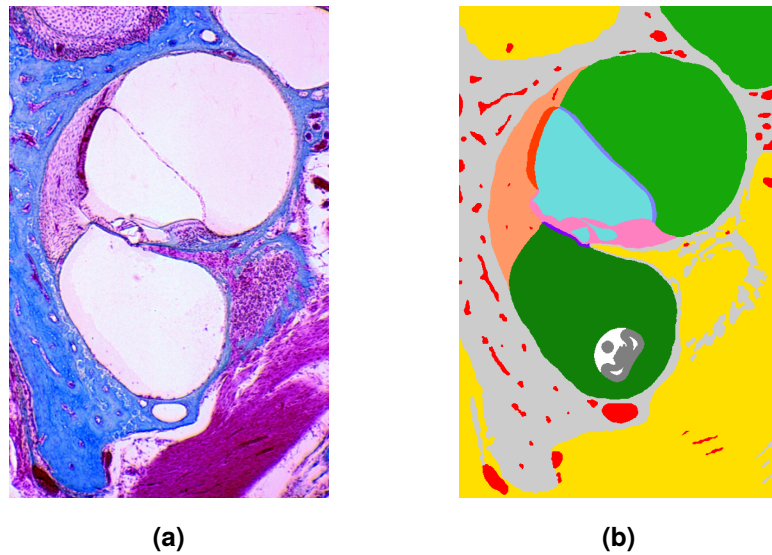


Figure 4.5: Image data for the proof of concept model. (a) Photomicrograph of the human cochlea from Donkelaar and Kaga [199]; (b) the corresponding segmentation.

Eleven different tissue types (listed under Table 4.13) were then manually segmented, with each marked in its own layer using either the hard brush tool or the lasso tool with feathering and anti-aliasing disabled to ensure accurate binarisation. Care was taken to preserve the intricate shapes of the tissue structures, especially that of the organ of Corti (note the tunnel of Corti and the tectorial membrane), the double wall of the spiral lamina, and the modiolar bone. This fine anatomical detail was important for ruling out simplifications in the model geometry as sources of error.

A Cochlear CI422 electrode array cross-section was added in the scala tympani at a position and orientation that was consistent with images from a sectioned implanted cochlea (courtesy Cochlear Limited). The final pre-processed image is shown in Figure 4.5b.

A stack of 22 copies of the pre-processed slice was then imported as a set of backgrounds in Simpleware ScanIP. The images were slightly downsampled to improve performance, and a mask for each material type was then created using threshold segmentation. For some materials, such as perilymph and blood, individual masks were created for separate structures to facilitate variation of properties during subsequent analyses. The platinum contacts were

Table 4.13: Material properties for the proof of concept model. Resistivity values for this and the subsequent models were based on values from the literature per §4.2.3 that were judged to be the most appropriate for the model.

Component	Resistivity ($\Omega\cdot\text{m}$)
Bone	6.41
Nerve	
(Axial)	3
(Transverse)	15
Perilymph	0.7
Endolymph	0.6
Blood	1.5
Reissner's membrane	10203.9
Basilar membrane	80
Organ of Corti	83.333
Spiral ligament	0.6
Stria vascularis	188.685
Fibrous tissue	6.27
Silicone	1×10^7
Platinum	1×10^{-3}

only masked on slices 5, 6, 11, 12, 17, and 18, thereby creating three evenly spaced electrode pads with realistic separation distances. Smoothing and morphological filters were applied to selected masks, taking care to patch any resultant gaps and ensure continuity throughout the volume. The image stack was then upsampled in the longitudinal direction to reduce the aspect ratio of the voxels in that direction.

Mesh Generation

All masks were then used to construct a finite element mesh. Previous FEM and BEM models have reported having difficulties meshing small structures like the cochlear membranes [37, 100, 105, 155]. As such, both of ScanIP's inbuilt meshing algorithms were tested.

The +FE Grid algorithm was quick and robust, and could easily handle the complexity of the data. However, because it worked by starting with a finite difference-style grid mesh based on the voxel size, the resultant volume mesh was much denser than it needed to be (cf. Figure 3.11). The time savings achieved through using this meshing algorithm would be easily outweighed by the increase in solution time for subsequent simulations. Given the likelihood of multiple testing scenarios during the analysis stages, a more efficient mesh was sought.

The other algorithm, +FE Free, extended upon the grid mesh by converting it into an unstructured tetrahedral mesh while largely respecting the domain boundaries. The resultant meshes contain fewer nodes and fewer elements. This was not a trivial task however, and the +FE Free algorithm took significantly longer than +FE Grid to discretise a volume. The experience with the fine anatomical detail in this model proved challenging, with the program often crashing unexpectedly despite the headroom provided by the hardware setup (ScanIP reported a peak working set of about 15 GB, which was well within the total RAM capacity of the computer). A result was therefore not guaranteed, but tweaking the meshing parameters

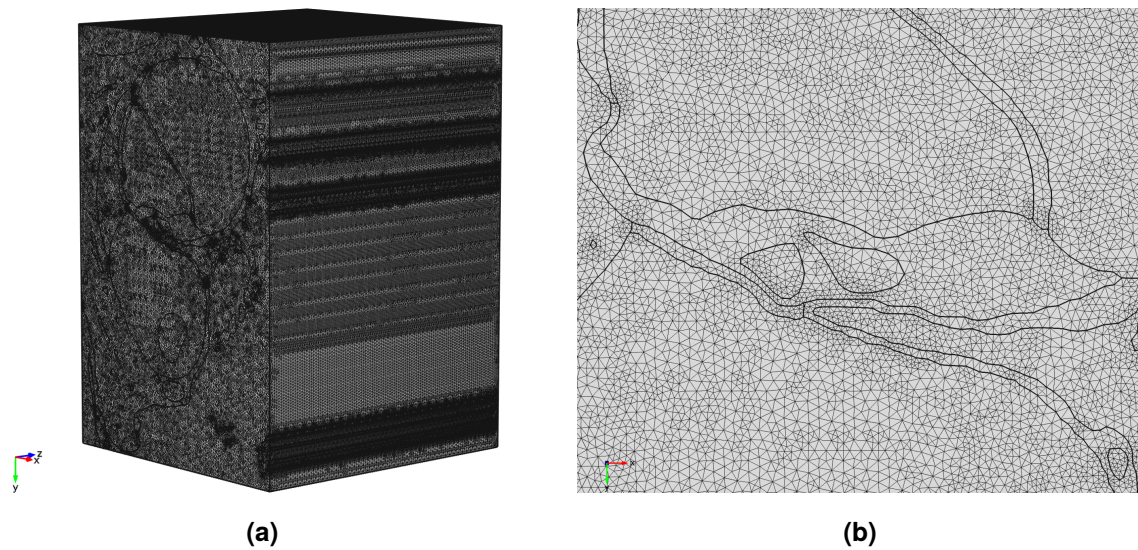


Figure 4.6: Volume mesh for the proof of concept model, generated using the +FE Free algorithm in ScanIP. (a) A global view showing the extruded direction; (b) a close up of the mesh around the organ of Corti, revealing the high element density required to discretise the fine structures.

over several iterations allowed the meshing algorithm to run to completion and create a mesh of reasonable quality.

4.3.3 Mesh Result

The successful mesh is shown in Figure 4.6. ScanIP took approximately 1 hour and 40 minutes to generate this mesh. It consisted of 10,505,119 tetrahedral elements with 1,877,712 nodes. The average element quality was 0.646, with most of the elements on the higher end of the scale as indicated by a negatively skewed element quality histogram. ScanIP was able to export the mesh in a number of different file formats. For the POC model, the volume mesh was exported directly to COMSOL using an .mphtxt file.

4.3.4 Discussion

The basic workflow established here was sufficient for converting an image of the cochlea into a functional finite element model. However, the methodology contained several limitations that could be improved in various ways.

Using a single histological image to build the model geometry allowed a high level of detail to be incorporated within a relatively short timeframe, but the true spiralling shape of the cochlea and the convoluted vascular trajectories were not captured. Since the workflow could be adapted to any type of image input, switching to a volumetric image stack would allow for a more realistic reconstruction of the cochlear anatomy.

Building the electrode array using a set of additional masks was a quick way to include a realistic array shape without the hassle of creating an extra model via CAD. A similar process was followed by Girzon [20] and Whiten [22], though in the latter case the arrays were already part of the image. Both of the inbuilt ScanIP meshing algorithms relied on the voxel grid to create the mesh though, so there was potentially a degree of discretisation error in play. The thickness of and longitudinal spacing between electrode pads could not be controlled precisely with this method since they were defined by the number of consecutive images containing or not containing the electrode pad, respectively. It is therefore suggested that future models define the electrode array using a CAD model.

Perhaps the most critical weakness of the POC method was the meshing algorithm. Although it was able to produce a high quality mesh with conformal multi-part surfaces, the coarseness parameter was not intuitively related to element size and provided limited control over the mesh. Overriding these with manually set parameters led to instability with the +FE Free algorithm that caused the program to crash on multiple occasions. The need to follow a trial-and-error process when adjusting these parameters and the high likelihood of failure were not ideal. It also appeared that the algorithm could not handle high element growth rates,

leading to a higher than necessary mesh density. This is particularly evident in Figure 4.6, where the large volumes of the scalae are filled with rather small elements. Given the direct impact of element density on solution times and the other concerns raised above, a more robust meshing workflow was sought for subsequent models.

4.4 The Guinea Pig Model

4.4.1 Introduction

Preliminary studies using the POC model [173, 198] demonstrated that unrolled linear models of the cochlea were subject to several limitations as a result of their simplified geometry. This is in line with previous findings by Frijns [100] and Choi [164]. As such, a more sophisticated model featuring the true 3D geometry was desired.

Since the goals of the thesis required that the model possess a high level of geometrical accuracy, multiple volumetric image stacks were sought. These spanned a range of different imaging modalities, and after evaluating their suitability for this project it was found that the most promising of these was a scanning thin-sheet laser imaging microscopy (sTSLIM) image stack of the guinea pig cochlea obtained by the Santi laboratory at the University of Minnesota. Most importantly, all of the structural components of the cochlea could be easily identified, including the different bone morphologies and the cochlear vasculature. This unprecedented level of detail in the images allowed for a high fidelity reconstruction, so this came to be the primary model for the investigations in this thesis.

4.4.2 Method

This section is based on the paper by Wong et al. [200], which has been published in IEEE Transactions on Biomedical Engineering.

A modular workflow based on that used by Tran *et al.* [112] was adopted in order to overcome the segmentation and meshing challenges typically encountered in electroanatomical modeling [105]. The main steps are summarised in Figure 4.7. The best features of several programs were selectively combined to create a more accurate model than would otherwise have been possible.

Imaging and Reconstruction

A high resolution ($4.625 \times 4.625 \times 5 \mu\text{m}$ voxel size) sTSLIM image stack of the guinea pig cochlea was used as the geometrical basis for the model (see Figure 4.8a). This technique combines the high resolution and clarity of optical microscopy with the non-destructive nature of computed tomography (CT) and magnetic resonance imaging (MRI), making it ideal for capturing fine anatomical details [184, 189]. The cochlea was explanted from a healthy guinea pig of unknown age, with no visible scar tissue and only minor neuronal degeneration at the basal end. Both soft and hard tissues were identifiable, and the images were predominantly free of absorption artifacts.

Fourteen different tissue types were then identified and segmented. These are illustrated in Figure 4.8b and listed in Table 4.14. Segmentation was initially performed in Photoshop as per the POC model, but it was soon discovered that this method was not ideal because alignment between slices could not be guaranteed. It was also difficult to see the outcomes of the segmentation. The open source program 3D Slicer was able to provide a 3D visualisation

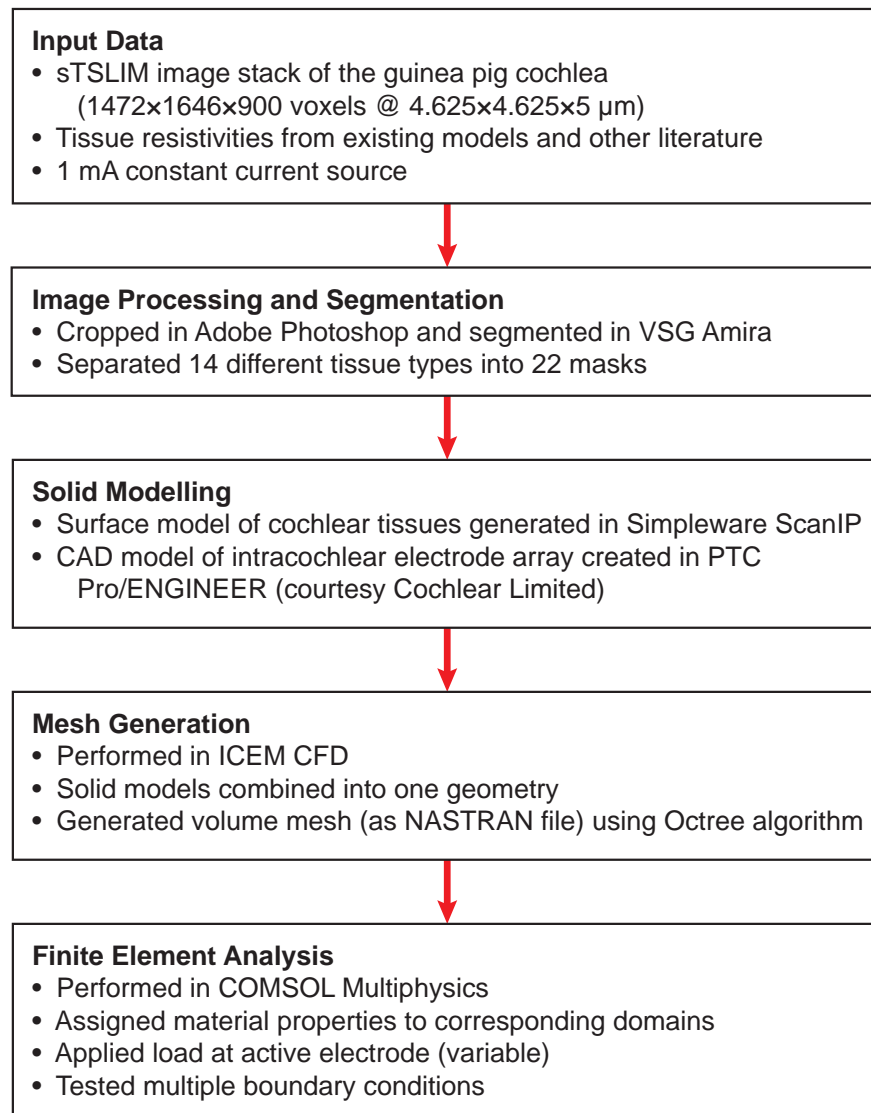


Figure 4.7: Workflow for the guinea pig model. It was extended from that of the POC model to provide more flexibility and control, and was able to overcome the problems encountered when meshing with ScanIP.

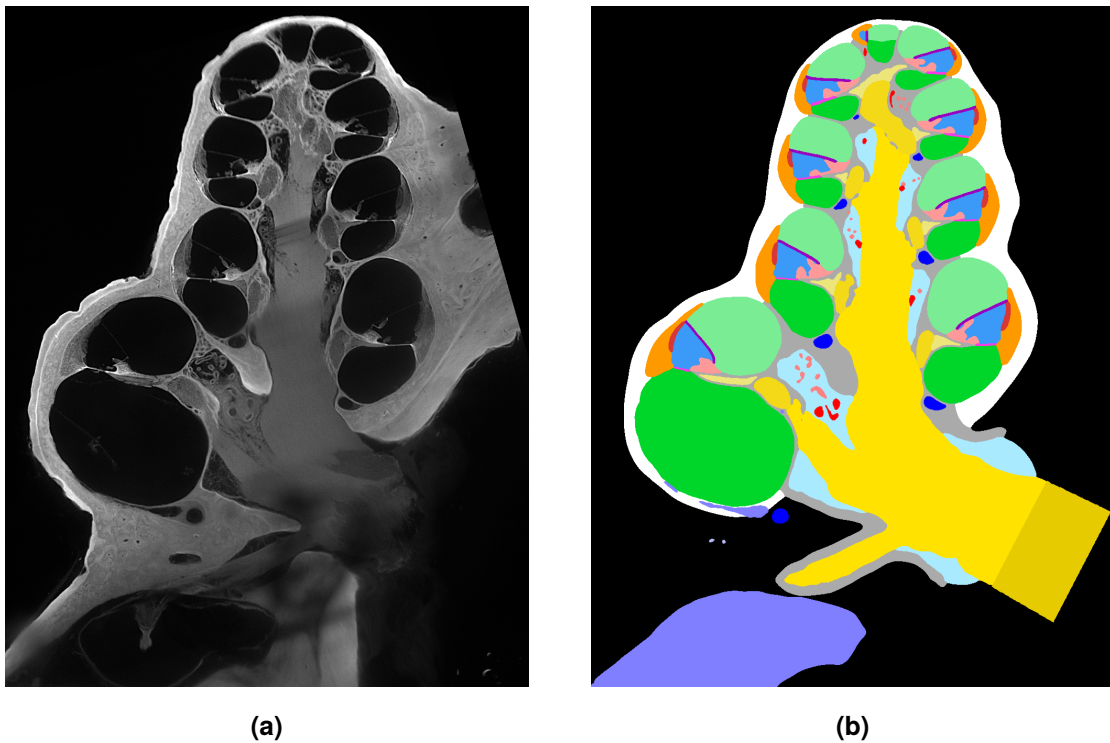


Figure 4.8: Segmentation of the sTSLIM images. (a) A mid-modiolar image from the sTSLIM stack; note the high resolution and clarity in both the soft and hard tissues. (b) 14 tissue types were identified in the voxel space; these were separated into 22 different masks to aid with visualisation and modelling. (Copyright © 2015, IEEE.)

of the segmented stack, but the cumbersome nature of using multiple programs during this stage was a drag on efficiency.

Consequently, a semi-manual process was adopted using Amira v5.4.2 (Visualization Sciences Group, Burlington MA, USA). The main advantage of this program was that it provided a 3D view of the segmented voxel space that was updated in real-time. For each tissue, a region in one image was selected with the aid of luminance thresholds. The selection was then smoothed, and the process repeated on the adjacent slice. If there was minimal variation in shape between successive slices, the next selection would be made several slices away and the volume in between was selected via interpolation. This preserved the organic appearance of the tissues while reducing the amount of data to be processed. Bone was separated by

morphology as this was found to be an important factor for model accuracy and could actually be differentiated in the sTSLIM scans [201]. Nerve, perilymph, endolymph, and blood were also categorised by anatomical structure to aid with visualisation (see Table 4.14). The thin membranes between the scala vestibuli and the vestibular complex were excluded in this reconstruction, as per other models. Finally, some additional smoothing was applied, and any remaining voxel fragments were allocated to adjacent masks using the island removal tool to ensure continuity throughout the volume in preparation for mesh generation.

The segmented domains were exported into ScanIP, and masks were created for each tissue by using the pre-segmented data mask generator on the segmented image stack. A surface model was then generated from the binarised masks in a stereolithography (STL) format. The pre-smoothing and part change options were enabled to avoid jagged surfaces, and decimation was disabled to ensure conformity between adjacent components. The resulting reconstruction is shown in Figure 4.9.

Mesh Generation

The STL files were imported into ICEM CFD v15.0 (ANSYS Incorporated, Canonsburg PA, USA) for volume meshing. A CAD model resembling the Cochlear Limited Hybrid-L8 (HL8) electrode array was inserted through the round window and into the scala tympani in a mid-scala position (see Figure 4.10). The electrodes along this array were numbered from E1 at the basal end to E8 at the apical end. Insertion depth was just over 6 mm, corresponding to an insertion angle of about 380 degrees at E8. A build topology operation was performed to ensure that the mesh respected the smooth curves of the array model.

Since orthogonal surfaces artificially draw current toward the center of each face [202], the virtually implanted cochlea was embedded in a sphere of radius 5 mm to facilitate the application of boundary conditions. This size was found to be sufficiently large for replicating

Table 4.14: Material domains in the guinea pig model.

Component	Resistivity ($\Omega \cdot m$)	Element size limits (mm)	
		Minimum	Maximum
Bone			
Modiolar bone	6.41	0.03125	0.0625
Otic capsule	70	0.0625	0.0625
Temporal bone	62.5	0.125	1
Stapes		0.0625	0.0625
Nerve			
Peripheral processes	3	0.03125	0.0625
Spiral ganglion	3	0.0625	0.125
Cochlear nerve	3	0.125	0.5
Perilymph			
Scala tympani	0.7	0.125	0.5
Scala vestibuli	0.7	0.125	0.5
Endolymph			
Scala media	0.6	0.03125	0.5
Vestibule	0.6	0.125	0.25
CSF	0.56	0.0625	0.25
Blood			
Spiral modiolar artery	1.5	0.015625	0.015625
Vein of the scala tympani	1.5	0.015625	0.03125
Reissner's membrane	10204	0.03125	0.03125
Basilar membrane	80	0.03125	0.03125
Organ of Corti	83.333	0.03125	0.03125
Spiral ligament	0.6	0.0625	0.125
Stria vascularis	188.685	0.03125	0.0625
Round window membrane	1000	0.03125	0.03125
Silicone	1×10^7	0.0625	0.0625
Platinum	1.06×10^{-7}	0.03125	0.03125

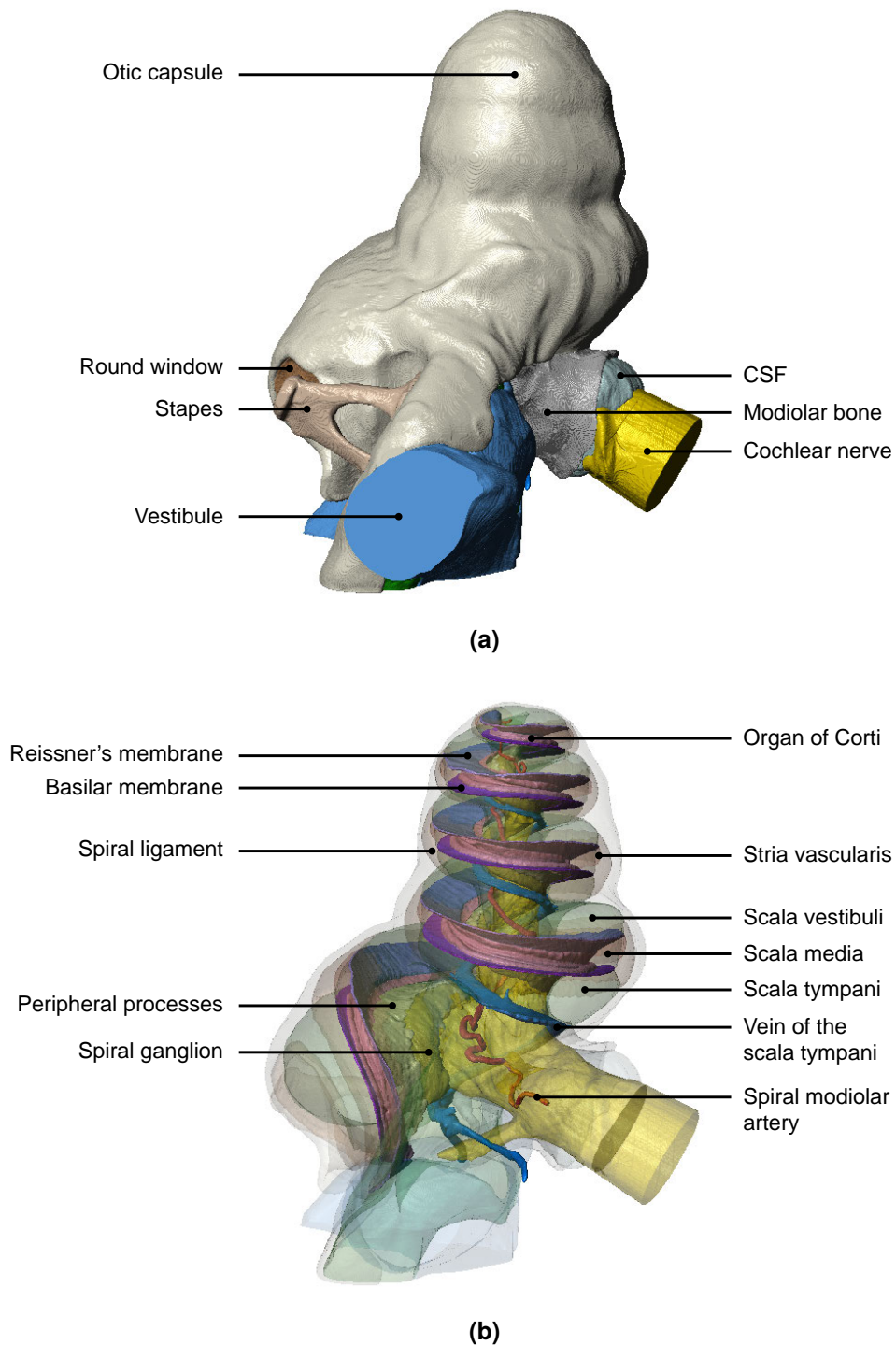


Figure 4.9: Surface reconstruction of the guinea pig model. (a) The cochlea is surrounded by the hard outer bone of the otic capsule; (b) removing the bone layers reveals the scalae, soft tissues, neural structures, and blood vessels deeper in the cochlea. (Copyright © 2015, IEEE.)

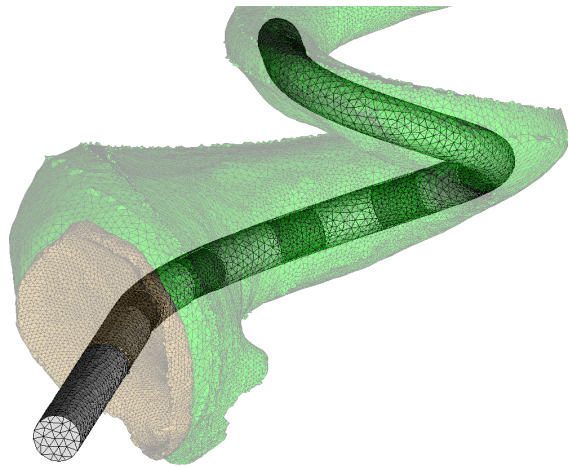


Figure 4.10: Virtual insertion of the HL8 array into the scala tympani.

far-field effects [202]. Unlike the human cochlea, which is encased within the temporal bone, the guinea pig cochlea protrudes into the tympanic bulla [61], so injected current must flow towards the temporal bone. The surrounding sphere was therefore angled such that one hemisphere extended into the tympanic bulla and the other into the surrounding temporal bone (hereafter referred to as the “temporal bone surface”; see dark grey hemisphere in Figure 4.11c), matching the bone boundary in the scans. A second concentric sphere of radius 8 mm was subsequently added to create an additional surrounding domain. This was used to define an infinite element domain for the boundary condition studies.

Element sizes for each component were established to balance node count against geometrical accuracy. A volume mesh was then generated using ICEM CFD’s top-down Octree algorithm. Finally, any small element islands resulting from the process were assigned to an adjacent domain to simplify the subsequent FEA steps. The final mesh is shown in Figure 4.11.

Estimating Neuronal Trajectories

In order to gain some insight into the simulated neural response, the activating function (AF, per Equation 3.6) was calculated because it signifies the degree to which the underlying

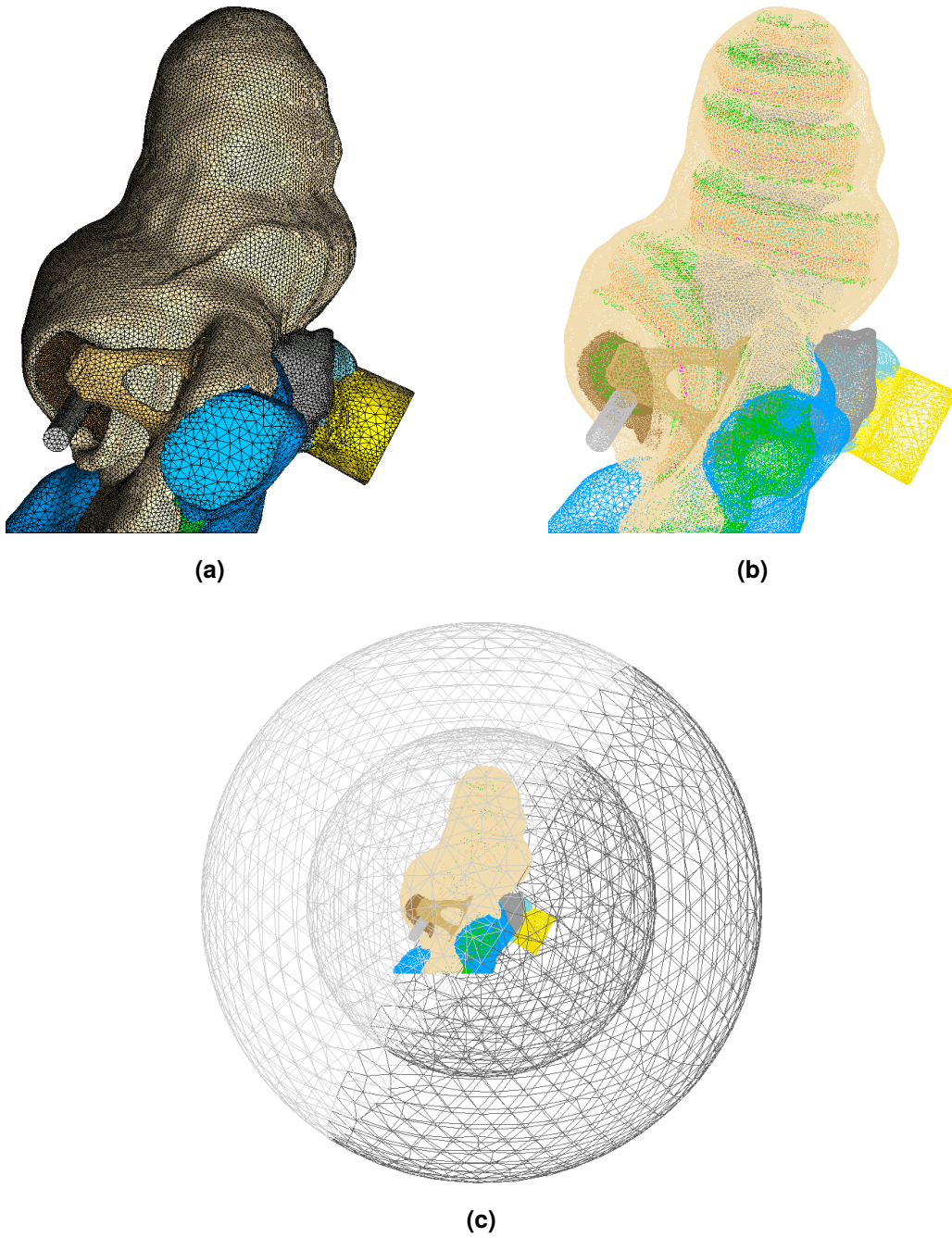


Figure 4.11: Volume mesh of the guinea pig model. (a) Solid element view of the guinea pig cochlea. (b) Outline view of the mesh, revealing the inner structures. (c) The cochlea shown within the surrounding bone spheres.

electrophysiological requirements for neural firing are met. This required finding the second derivative of the voltage scalar field *along the neuron*. Since the geometry in this model was based on an image stack, there was no simple equation-based method for fitting nerve fibre trajectories within the neural tissue [154]. Computational methods for extracting the vector field of the fibre orientations from the volumetric images (like those used by Bishop in cardiac tissue [203]) were considered, but these are difficult to implement and were not guaranteed to work with the images that had been acquired. Therefore, a semi-manual spline interpolation method was used for estimating the neuronal trajectories.

For this model, nerve fibres covering approximately the first 570 degrees of the cochlea were modelled in MATLAB (The Mathworks Inc., Natick MA, USA). This was sufficient for covering the main areas of excitation for the observed insertion depth of the HL8 array. Each fibre was assumed to run through a number of key locations: from the tip of the peripheral processes, through the centre of the spiral ganglion, then joining the auditory nerve trunk in the modiolus. This was similar to existing modelling studies, such as that shown in Figure 2b by Kalkman *et al.* [147]. The tonotopic organisation of the fibres was preserved, i.e. the more basal axons followed a path near the circumference of the nerve trunk, while progressively more apical axons spiralled inwards towards the core of the trunk.

Nodes of Ranvier were positioned along each neuron at fixed intervals from the point in Rosenthal's canal. Internodal spacing was chosen to resemble that used in the GSEF neural model [100]: 175 μm along the peripheral process and 300 μm along the axon. The node points were determined using the *interparc* and *arclength* functions published by John D'Errico on the MATLAB File Exchange (licences shown in Appendix A).

The final interpolated fibre trajectories are shown in Figure 4.12. Using these neuronal trajectories, the AF was then computed for each set of adjacent nodal triads along 100 fibers spaced equally along the cochlear spiral.

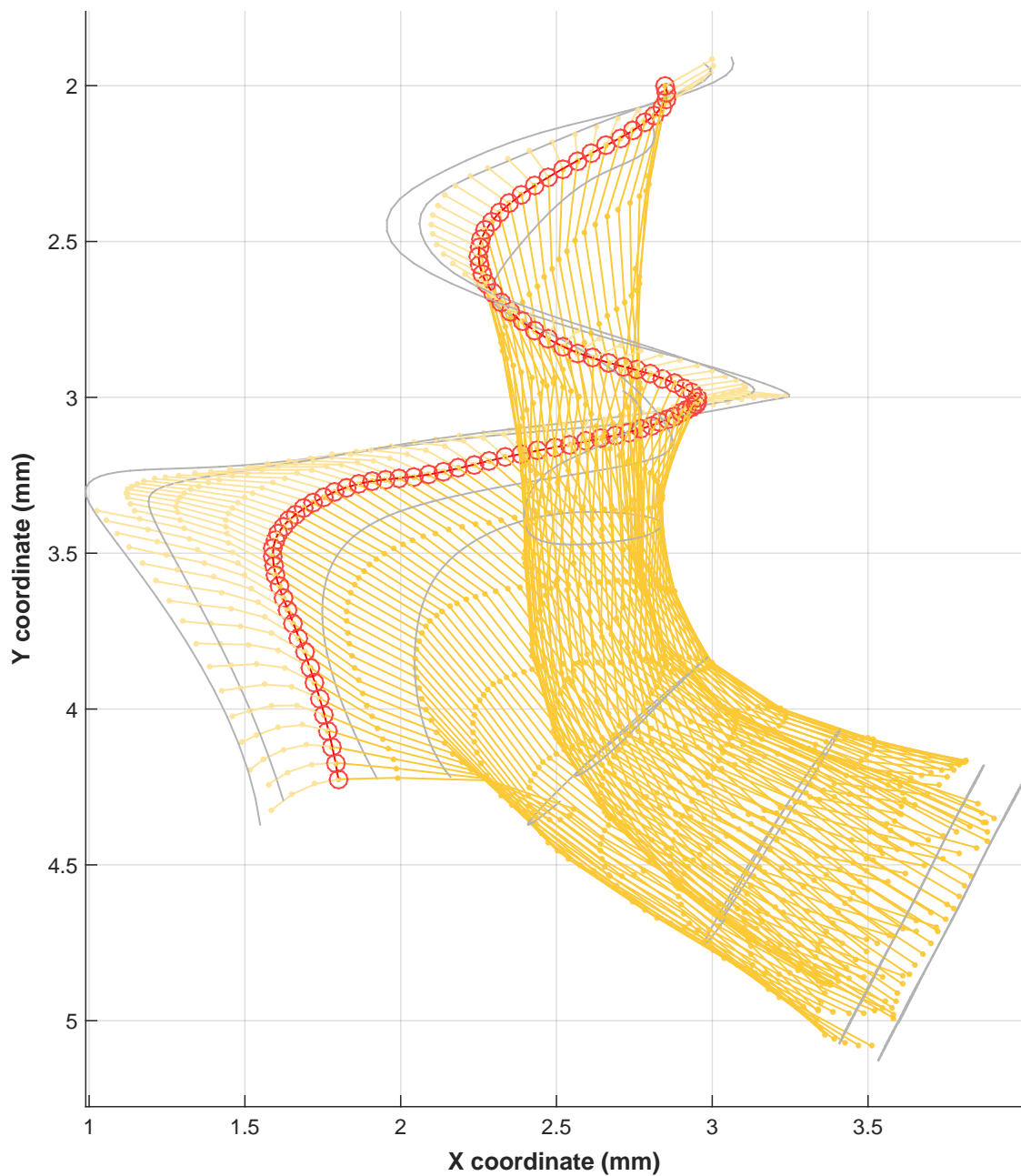


Figure 4.12: XY view of nerve fibre trajectories, estimated using MATLAB. Guide splines (grey) were determined from manually selected key points along the auditory nerve from the distal end of the peripheral process, through the centre of the spiral ganglion (marked by red circles), to the end of the modelled nerve trunk. Nodes of Ranvier were estimated along each fibre, and the electric potential at those points was used to calculate the activating function.

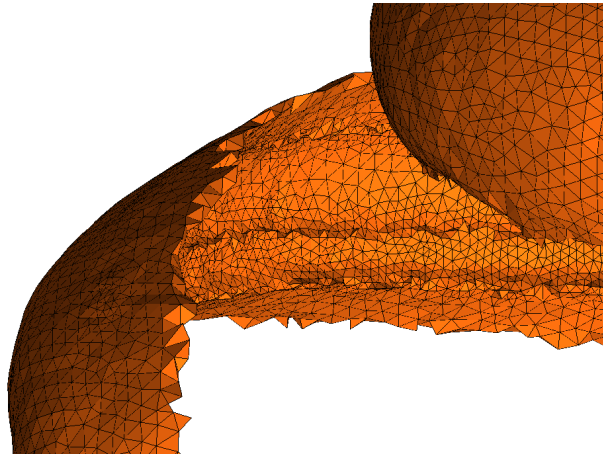


Figure 4.13: Jagged boundaries in the volume mesh due to the top-down approach of ICEM CFD. This close up shows part of the spiral ligament, which is routinely interfacing with multiple tissues.

4.4.3 Mesh Result

ScanIP took approximately 1 hour and 30 minutes to generate the surfaces, while ICEM CFD took another 1 hour and 30 minutes to generate the volume mesh. The base case volume mesh consisted of 4,684,028 tetrahedral elements with 790,653 nodes. A handful of small, spurious element islands were formed due to the way the Octree algorithm works, so some additional time was required to identify the tissues to which these elements belonged and merge them together. Following this, the mesh was successfully exported using the NASTRAN file format.

The volume mesh created here possessed a more appropriate balance between element size growth rate and quality compared with the POC model. Despite covering a much larger region of interest, it had fewer elements and a higher average element quality of 0.712. On the downside, boundaries where three or more tissues touched did not perfectly conform to the smooth input surfaces, again due to the top-down approach of the Octree algorithm. A close up view of the spiral ligament in Figure 4.13 provides some idea of the extent of this issue. The bulk of the tissue volume did not suffer from this problem.

4.4.4 Discussion

The experience of this project mirrors that of Briaire *et al.* [105] in that discretising the volume was the most difficult step. A similar conclusion was also reached by Saba [37, Appendix G] and the Hanekom group [personal communication], both of whom struggled to mesh the organic shape of the cochlea in COMSOL. This is presumably why some VCMs of the cochlea used such simplified geometries [144, 166].

The high resolution of the sTSLIM scans was a double-edged sword. It allowed for much of the fine anatomical detail to be seen and incorporated, making for a more realistic model. However, the presence of this additional detail clearly contributed to the meshing difficulties. ScanIP was unable to directly generate a working volume mesh due to the complexity of the surfaces, and ICEM CFD would sometimes crash while importing the STL files (though the reason for this was less clear and may be due to a software bug). Many of the cochlear tissues are also quite thin, which meant that a very fine mesh was required to maintain a reasonable element quality. The ability of the Octree algorithm to conform to the surfaces and transition from very small elements to significantly larger ones in the bulk regions of the scalae and surrounding bone are a testament to its robustness. A hexahedral mesh would have been preferred over the tetrahedral mesh for accuracy, but attempts to create such a mesh in ICEM CFD failed to produce a result. The Octree mesh did exhibit some discretisation error at some of the interfaces, but this is expected to have minimal impact on the results of interest because the number of affected elements is small relative to the overall volume and the measurements are taken some distance away from these boundaries.

In terms of sourcing appropriate material properties, the values are typically assumed to be similar between humans and guinea pigs. The main exception is that of bone, for which more appropriate data was available: here, the resistivities for guinea pig bone were taken from the measurements of Suesserman [204]. Like other VCMs of the cochlea though, the reliability

of the tissue resistivities is a potential weakness due to the low number of independent data sources. A sensitivity analysis was therefore performed as part of the validation study in Chapter 6.

Sources of error for the neuronal component were threefold. Firstly, the trajectories could be further improved: nerve fibre density is not uniform throughout the cochlear turns [205,206], and the bunching of peripheral processes and the curved trajectory towards the apex [207] was not reflected in the model. Secondly, the internodal spacing used in the GSEF model is based on measurements in the cat by Liberman [122]. These may not be suitable for the guinea pig. The additional simplification of constant length intervals would also have a bearing on the AF results. It is worth noting at this point that neural degeneration and demyelination can occur with deafness, altering current distribution and neural excitation predictions respectively near the damaged regions. Since the guinea pig model was compared with acute experimental data from implanted but otherwise healthy animals in this thesis, these factors were not incorporated. Finally, the use of the AF instead of a more complete model of neural kinetics limits the current iteration of this model in that thresholds cannot be predicted. Given the focus of this thesis on the physics that underpin volume conduction in the cochlea and the inconsistencies of existing excitation models, it was decided that the AF would suffice for demonstrating the likelihood of excitation and that neural kinetics would best be left to future extensions of this project. For reference though, the early guinea pig models by Frijns *et al.* predicted excitation thresholds for bipolar configurations at a stimulus current of around 1 mA [145, 146], while *in vivo* measurements by Huang *et al.* found thresholds of around 0.35 mA [208]. Threshold currents for monopolar configurations are expected to be lower than these values, as discussed in §3.1.2.

Despite these limitations, the model should be able to elucidate insightful spatial trends along the cochlear spiral.

4.5 The Human Model

4.5.1 Introduction

The third model that was made for this project was a subject-specific human cochlea. Its main aims were to test the feasibility of the methodology on a different image dataset, demonstrate the differences in geometry between human and guinea pig cochleae, and be incorporated with a detailed model of the human head from a parallel project [112] for a multiscale simulation. The initial development of this human cochlear model formed the basis for a second undergraduate honours thesis in 2014. The following section describes some of the work performed as part of that project as well as the additional work to create a more accurate iteration.

4.5.2 Method

The workflow used for the human model was essentially the same as that used for the guinea pig model (Figure 4.7), but with some of the segmentation performed algorithmically in ScanIP. Learning efficiencies obtained while working with the earlier models were put into practice during this implementation, speeding up model creation.

Imaging and Reconstruction

The human model was based on a microCT dataset of a preserved human temporal bone containing a previously implanted cochlea. Preparation and scanning of the specimen were performed by Ian Curthoys from the School of Psychology and Christopher Wong from the Australian Centre for Microscopy and Microanalysis (ACMM), both at the University of

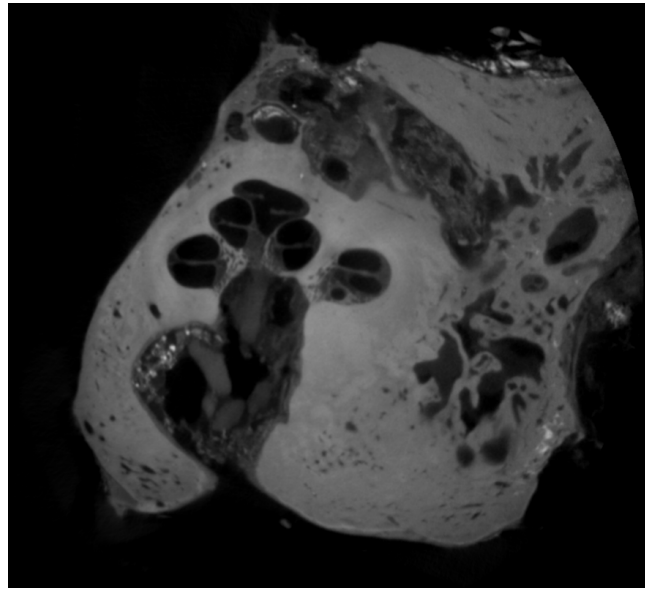


Figure 4.14: MicroCT image of the human temporal bone.

Sydney. The images obtained (see Figure 4.14) were both clean and detailed, with a field of view that was wide enough to include the semicircular canals. The $1479 \times 1501 \times 1114$ voxel space had an isotropic resolution of $27 \mu\text{m}$, so the microCT scans were not as detailed as the sTSLIM images of the guinea pig but still provided sufficient resolution to construct a reasonably accurate model.

The main improvements of this model over the preliminary iteration were the inclusion of additional tissue masks (for the otic capsule, modiolar bone, CSF, and vestibular nerves) and refinement of existing masks, most notably those for the facial nerve and the spiral ganglion. A complete list of segmented tissues is provided in Table 4.15. For most of these tissues, segmentation was performed semi-manually as per the guinea pig model. A greater focus was placed on using the interpolation functionality of Amira as this enabled the organic smoothness of the anatomy to be preserved. The vestibular structures of the inner ear were included in this model since they were within the field of view of the scans, and there is evidence to suggest that the largest fraction of injected current leaves the cochlea via the nearby basal end [29, 106].

Table 4.15: Material domains in the human model.

Component	Resistivity ($\Omega \cdot m$)	Element size limits (mm)	
		Minimum	Maximum
Bone			
Modiolar bone	5	0.0625	0.25
Otic capsule	70	0.25	1
Temporal bone	62.5	1	4
Nerve			
Spiral ganglion	3	0.0625	0.125
Cochlear nerve	3	0.25	0.5
Vestibular nerve	3	0.25	0.5
Facial nerve	3	0.25	0.5
Perilymph			
Scala tympani	0.7	0.5	1
Scala vestibuli	0.7	0.5	1
Semicircular canals	0.7	0.25	0.5
CSF	0.56	0.5	1
Cochlear partition	80	0.0625	0.0625
Spiral ligament	0.6	0.0625	0.125
Silicone	1×10^7	0.0625	0.0625
Platinum	1.06×10^{-7}	0.03125	0.0625

The otic capsule around both the cochlea and the semicircular canals required special treatment. A preliminary outline was created by dilating a mask of the corresponding fluid chambers in ScanIP into the regions occupied by the dense bone immediately surrounding the inner ear (as depicted by the lack of voids in the microCT data). This mask was then reimported into Amira for further refinement and integration with the other segmented tissues (see Figure 4.15). The otic capsule mask slightly exceeded the scanned specimen in the region of the semicircular canals because the lateral aspect of one of the canals was cut into slightly during the original extraction of the temporal bone sample.

After all tissue masks were finalised, the pre-processed image stack was again imported into ScanIP for surface reconstruction, resulting in the surface model shown in Figure 4.16.

Mesh Generation

As per the guinea pig model, the human model was discretised using ICEM CFD. The surfaces generated in ScanIP were imported into ICEM as faceted STL geometries, along with a CAD model of an intracochlear electrode array with 22 contacts, which was inserted along a mid-scalar path. A build topology operation was performed on the array to ensure that node placement conformed to the smooth edges defined in the CAD model, as per the guinea pig model.

Various meshing parameters were set up in a similar manner to that used previously. Maximum and minimum element sizes that provided a good balance between geometrical accuracy and node count were determined. The final element size limits used for this model are listed in Table 4.15. The Octree algorithm was used once again for the actual discretisation step, and the successful mesh was exported as a NASTRAN file.

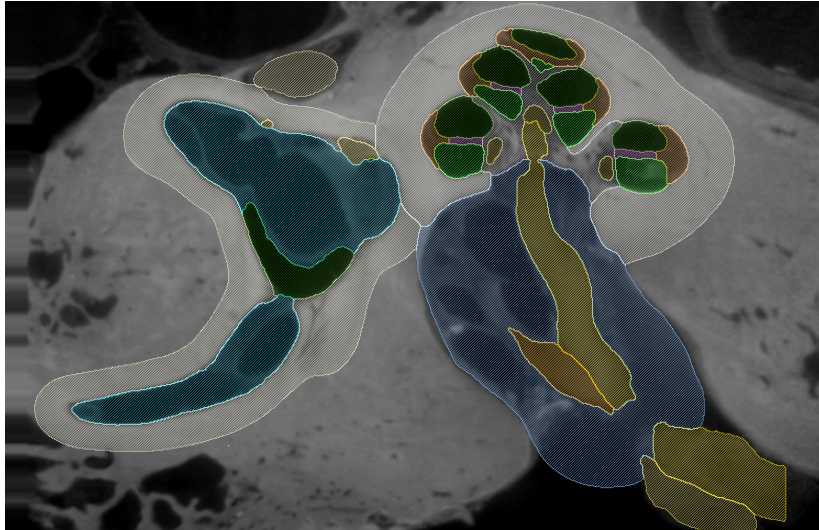


Figure 4.15: Segmentation of the microCT images. Superfluous regions were cropped from the original scans to reduce RAM usage.

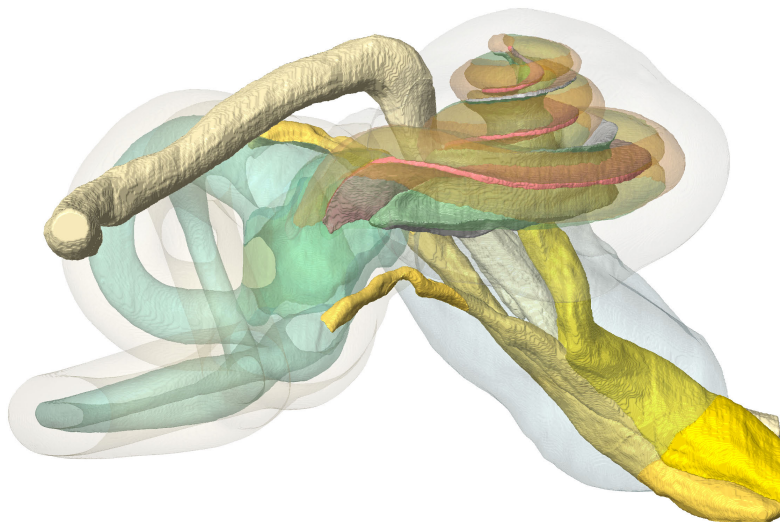


Figure 4.16: Surface reconstruction of the human cochlear model.

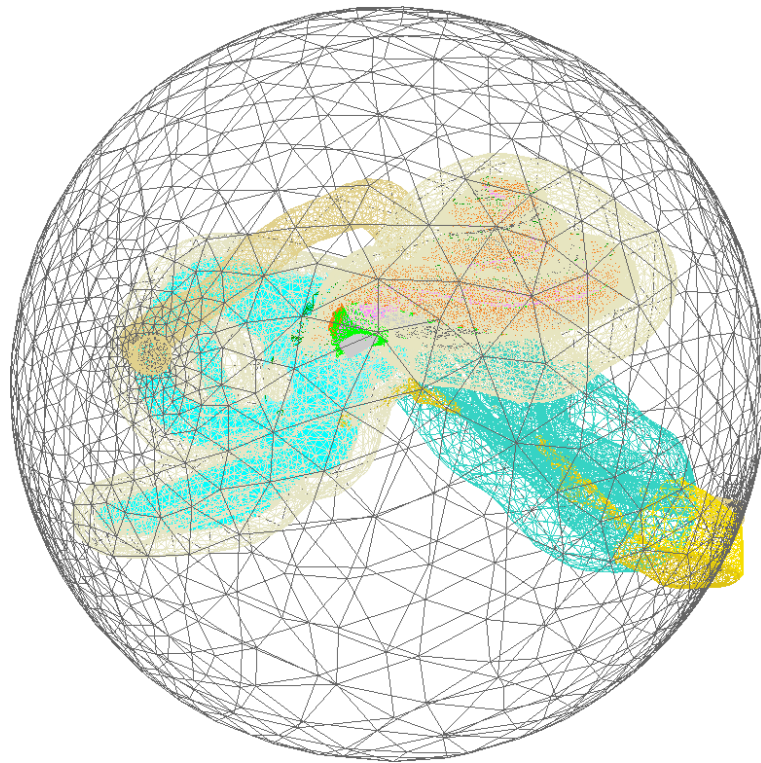


Figure 4.17: Volume mesh of the human cochlear model. The size of the surrounding sphere was deliberately chosen such that the ends of N VII and N VIII protruded slightly. The Octree algorithm would automatically identify the intersecting surface, facilitating the application of traditional boundary conditions.

4.5.3 Mesh Result

The final volume mesh for the human cochlear model is shown in Figure 4.17. Due to its relative simplicity, it only took about 15 minutes to compute. It consisted of 1,877,793 tetrahedral elements and 318,236 nodes. The average element quality was 0.712, similar to that of the guinea pig mesh.

4.5.4 Discussion

The robustness of the methodology was clearly demonstrated by the successful creation of another complex mesh. Given that it was a second attempt at implementing the workflow,

learning efficiencies significantly sped up the model creation process. Subsequent reconstructions can be expected to be even faster, perhaps even reaching a six week turnaround between scanning and the finalised reconstruction.

Another factor that reduced the required modelling time was the use of a lower resolution dataset. The smaller voxel space of the microCT data meant that less data needed to be processed to create the human model than was required for the sTSLIM data used for the guinea pig model. However, it also meant that some of the finer anatomical details were not visible and thus could not be incorporated into the model. The most notable omissions were the soft tissue structures, which were difficult to identify given the larger voxel size and the scanning technique used. The cochlear partition needed to be modelled as a single part because it was impossible to distinguish the spiral lamina, peripheral processes, organ of Corti, and basilar membrane, and the inability to resolve Reissner's membrane meant that the scala media could not be modelled. The cochlear blood vessels could not be segmented for similar reasons.

One way this might be offset in future studies is to divide the volume into smaller regions, scan each of them individually, and finally realign them to produce a larger voxel space. This would introduce a number of extra challenges, such as correct realignment of the subsections, and could be cost prohibitive, but would yield a much higher resolution reconstruction. Better image data may also be obtained as sTSLIM techniques for human specimens become more refined. If such paths were pursued, the additional computational cost required at each stage of the pipeline would also need to be taken into account to ensure feasibility. Additional pre-processing steps, such as adding an anisotropic diffusion filter to the image data prior to segmentation [176], could make the reconstruction easier to manage in that case, but care would be required to ensure that the anatomical structures do not become too distorted.

Looking further ahead, the main challenge left to address in the workflow is improving the reliability of the discretisation step. Noticeably fewer element islands were produced in

the human model, likely a by-product of the simpler segmentation, but they could not be completely and consistently eliminated. This meant that manual inspection of the mesh was always required, a step which was extremely time-consuming because the complexity of the surfaces caused the graphics subsystem to lag during all interactions with the user interface. Alternative meshing programs may yield better results in this respect.

4.6 Chapter Summary

A robust modelling workflow was established by combining the best aspects of several different programs. The various types of data required as input to the workflow were each critically considered. In the end, three different finite element models of the cochlea were produced: (i) a simply extruded proof of concept model, which was used to evaluate the basic workflow requirements, (ii) a highly detailed guinea pig model that became the primary model for subsequent investigations, and (iii) a human model, for comparison with the guinea pig model and integration with a human whole head model. High quality meshes were produced for all three models. These were imported into COMSOL Multiphysics for running further analyses. The insights gained from these studies are documented in the following chapters and aim to shed some light on the issues raised under §3.4.

Chapter 5

Boundary Conditions for Monopolar Simulations: A Preliminary Investigation

This chapter addresses the following questions:

- How does the prescribed boundary condition affect current flow?
- How accurate are the boundary conditions cited in literature?
- How do these compare to a whole head simulation?

5.1 Introduction

As mentioned in Table 4.1, boundary conditions (BCs) are a key input for volume conduction models (VCMs). If both the source and sink electrodes are contained within the modelled domain, the BCs are easy to prescribe. Previous models of bipolar stimulation fall under this category [100, 144, 155, 163]. For models of monopolar (MP) stimulation though, the

Table 5.1: Monopolar boundary conditions used in existing models. For models of the cochlear region alone, there appears to be little consensus as to which alternative should be used.

Boundary condition	Key examples
Grounded at nerve trunk	Girzon [20], Whiten [22]
Pseudo-monopolar return	Hanekom [155]
Grounded boundary box	Rattay [159], Saba [37]
Grounded at infinity	Frijns [145]
Whole head simulation	Tran [112], Malherbe [158]

return electrode lies outside the model itself, primarily due to restrictions in the field of view during imaging. Since MP stimulation is by far the most commonly used stimulation mode amongst contemporary cochlear implant (CI) recipients, it is important to prescribe boundary conditions that reflect the *in vivo* situation with a reasonable level of accuracy.

Preliminary tests using the proof of concept model demonstrated that the restricted scope and extruded geometry of unrolled models are not ideal for simulating MP current flow [173]. Here, the medial edge along the base of the auditory nerve trunk was grounded because earlier studies had identified this as a likely exit pathway [20, 106]. However, imposing a ground in the nerve trunk itself forces *all* of the injected current to flow to that point, which is unrealistic because the electrode configuration for MP stimulation implies that current does not reconverge in the nerve [103]. As such, focus was shifted towards the guinea pig and human models. Looking at the existing literature, it was discovered that a few different boundary conditions were in use, with little to no consensus amongst research groups (see Table 5.1). This raised the need for a deeper investigation into appropriate BCs.

Ideally, the BCs imposed on a cochlear model would perfectly replicate the *in vivo* current flow. Unfortunately, it is difficult to measure the volumetric flow of current in the head during CI stimulation using traditional experimental techniques. Previous whole head simulations of CI stimulation used crude geometries and did not focus on volumetric current flow [209].

Only recently (through a parallel project) has there been progress in this area, with the whole head model of Tran *et al.* [112, 210–212] revealing the monopolar current paths.

The aims of this study were twofold: to examine how the model was affected by changing the BCs, and to compare the predicted current flow patterns with those from a whole head simulation. This knowledge would help to eliminate potentially inappropriate boundary conditions from the large set of existing alternatives.

5.2 Grounding Location and Size Effects

This section is based on work that was presented at CIAP2013 [202, 211]. The simulations in Wong et al. [202] were from an early iteration of the guinea pig model; these were rerun using the finalised model for the study in this chapter.

The first part of the investigation focused on how various BCs affected the physics of the system, in particular, the intracochlear voltage profiles and current pathways. It was hypothesised that both the location/shape and size of the imposed BCs could affect the simulation results, but the sensitivity of the model to these factors was unknown.

5.2.1 Method

Several different BCs were established as test cases for this study. These included grounding at the following surfaces, as shown in Figure 5.1:

The end of the *nerve trunk* The truncated end leading toward the brain was used here. This was similar to the Girzon and Whiten studies, and the rationale can be traced back to measurements by von Békésy [66].

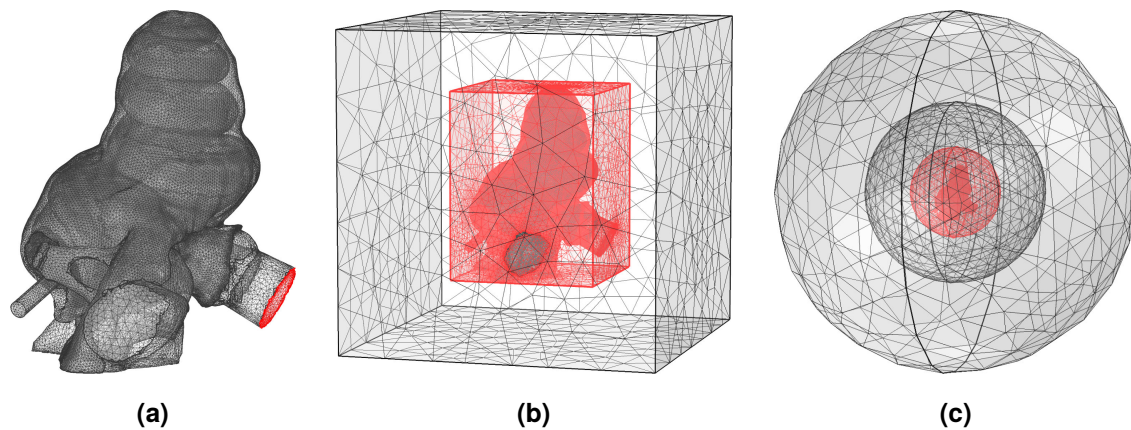


Figure 5.1: Tested grounding locations highlighted on the mesh. (a) The end of the nerve trunk (surrounding bone not shown). (b) The boundary box; the surrounding cube is also visible. (c) The surrounding spheres; the highlighted sphere has a radius of 5 mm and is circumscribed by the surrounding cube in (b). The larger spheres have radii of 10 mm and 20 mm.

The *boundary box* surrounding the cochlea Represents what might be used if the model was reconstructed using the image stack alone.

A *surrounding sphere* A new proposal inspired by Hanekom’s use of a surrounding bone block [155] and insights from the Tran whole head model [211], which revealed that the voltage distribution around the cochlea assumes a mostly convex shape (see Figure 5.2b). The length of the longest diagonal in the boundary box was 8.70 mm, so to ensure that none of the cochlear tissues were cut off, a sphere of diameter 10 mm was used. Two larger concentric spheres with diameters of 20 and 40 mm were also tested.

A *surrounding cube* Similar to that used by Rattay and Saba. An edge length of 10 mm was used, such that the surrounding cube inscribed the surrounding sphere. This allowed for a more direct comparison against the spherical BC.

To facilitate the application of these BCs, two volume meshes of the guinea pig cochlea were created, both of which included all the cochlear tissues and an electrode array based on the Cochlear Hybrid-L8 (HL8) as described in §4.4.2. One mesh included the boundary box and

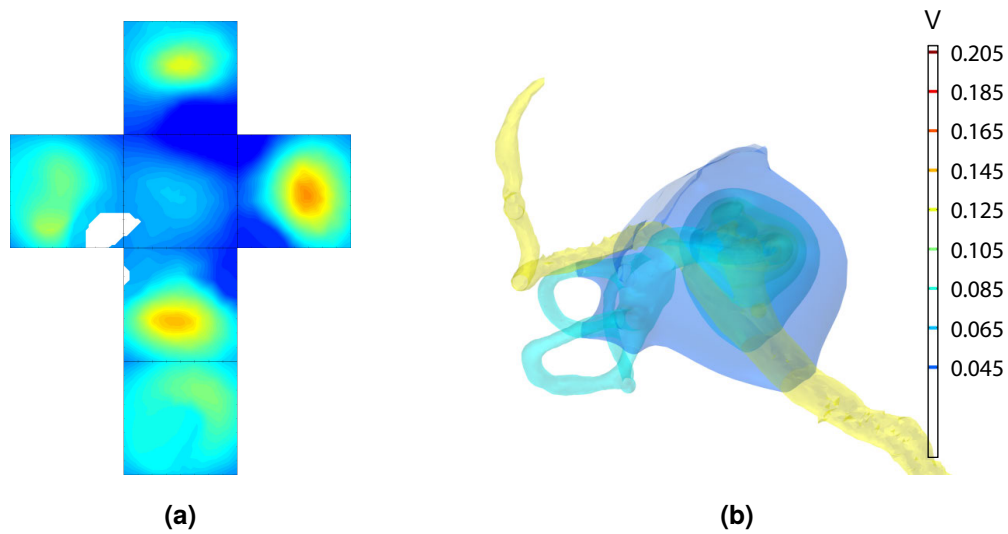


Figure 5.2: The shape of the voltage distribution around the cochlea from a whole head simulation. (a) Voltage along the surfaces of a surrounding cube; (b) voltage isosurfaces around the cochlea take on a mostly convex shape, but is distorted in accordance with the modelled tissues.

surrounding cube, whereas the other included the surrounding spheres. This separation was required to avoid distortions in the mesh where the same sized surrounding sphere and cube were tangential to each other. The meshes were then imported into COMSOL for analysis. Only results for current injection at electrode E4 are presented because the trends were largely independent of the stimulating electrode.

5.2.2 Results

Grounding Location

As shown in Figure 5.3, grounding at different locations did not seem to have a large effect on the shape of the voltage profile. This suggests that the voltage drop off is driven by other factors, likely the geometry and tissue properties. There was, however, a large discrepancy in the overall magnitude. Grounding the boundary box yielded the lowest voltages, and the

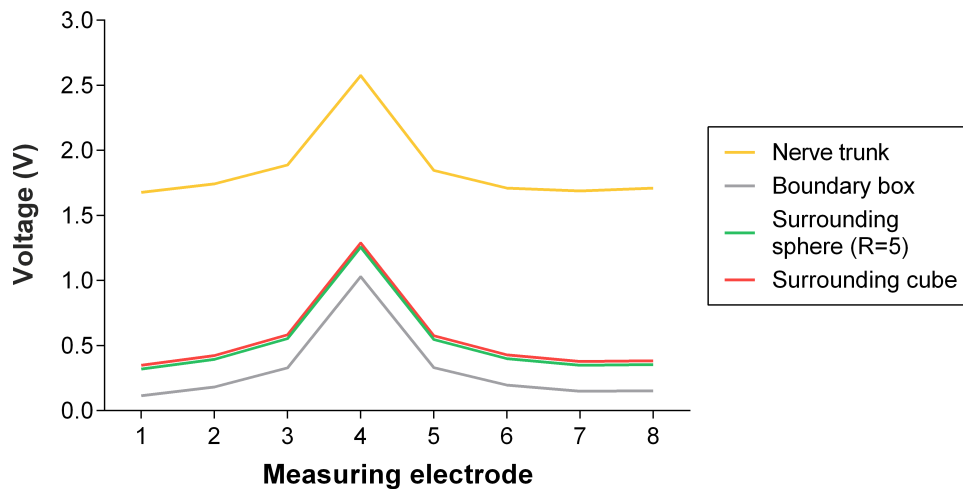


Figure 5.3: Predicted voltage profile by boundary condition for the guinea pig model.

surrounding sphere and cube were slightly higher but similar to each other. In contrast, the nerve trunk profile was significantly higher.

The resultant streamline plots (Figure 5.4) revealed that the current pathways were quite different. Grounding the end of the nerve trunk generated the most distinct flux pattern, with the current reconverging at the grounded surface and strongly increasing the current density in the surrounding neural tissue. Using a boundary box constrained the possible exit pathways, mainly to where the fluid chambers were closest to the centre of each face of the box. The surrounding sphere and cube were similar except in the far field, where current was artificially attracted towards the centre of each face in the cube in a similar manner to the boundary box condition. This phenomenon is a result of the shorter distance to ground in these regions.

Size

Increasing the size of the surrounding sphere did not have a large impact on current pathways. Streamlines inside the cochlea barely changed, while those extending out into the surrounding

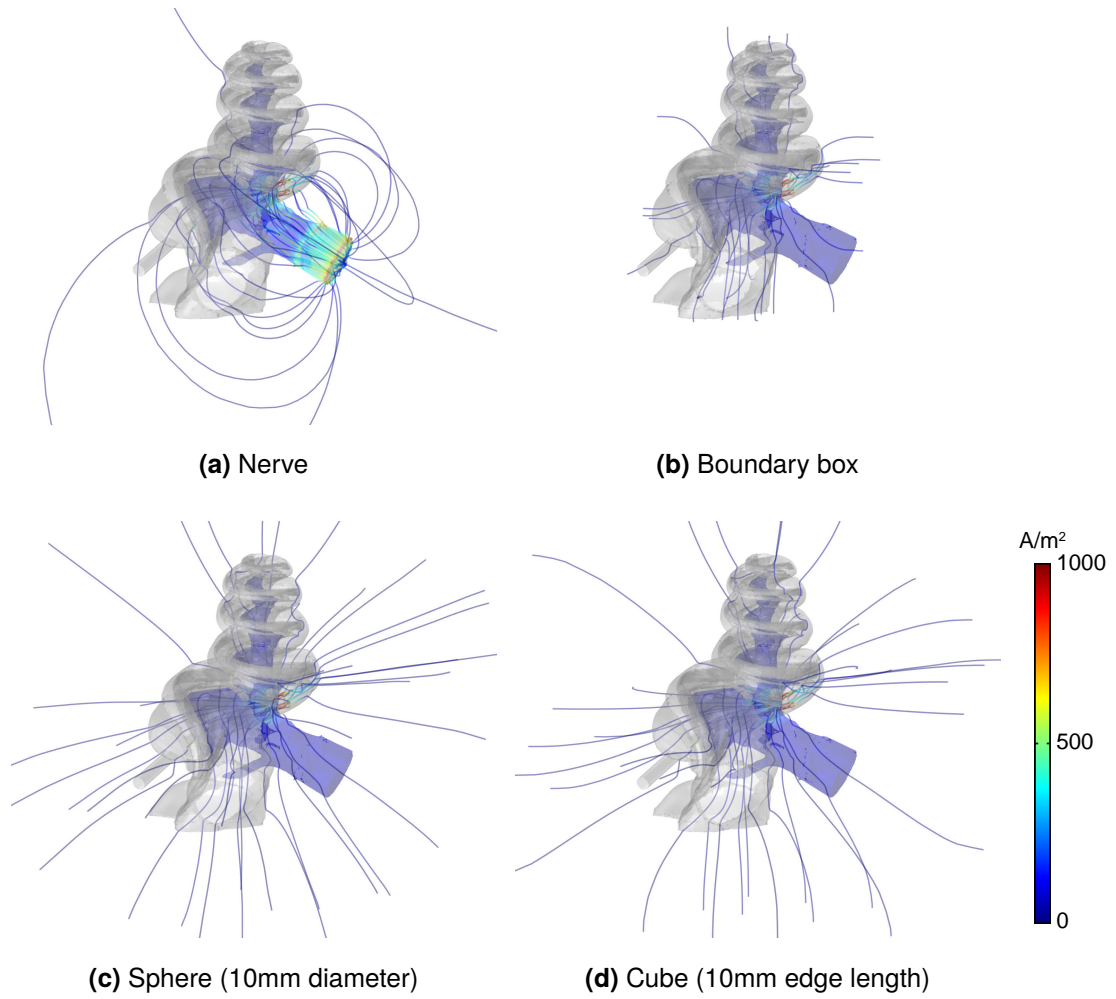


Figure 5.4: Effect of grounding location on current distribution. Scale measured current density in the neural tissue.

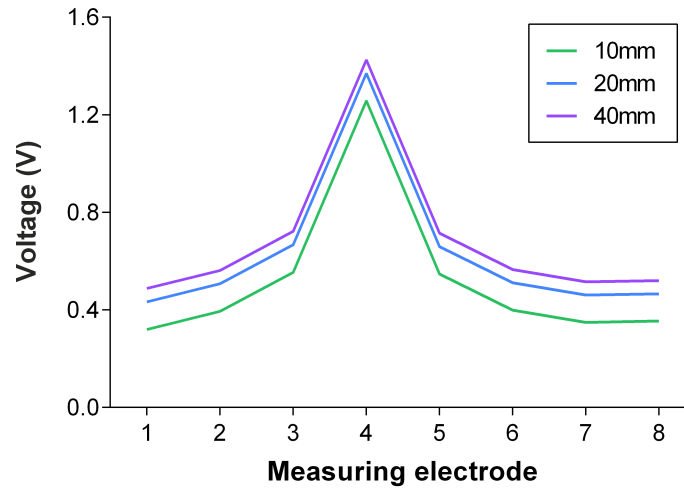


Figure 5.5: Effect of size on voltage profile. Increasing the diameter of the surrounding sphere also increased the measured voltages, due to the increase in resistance to ground. The marginal change appears to diminish with size.

bone followed an almost perfectly radial path. Differences were observed in the voltage profiles though, with larger sizes shifting the curve upwards (Figure 5.5). The marginal increase appeared to diminish with size, suggesting that a reasonable upper bound might be proposed by using an infinitely large surrounding sphere.

5.3 Multiscale Simulation of the Human Head

The second part of this investigation aimed to compare voltage and current predictions between standalone models of the cochlea and a multiscale model. It was hoped that by including reconstructions of both the cochlea and the surrounding head with realistic return electrodes, a truer sense of the *in vivo* current distribution would be acquired. Generating an accurate guinea pig head model was not feasible for this project. Instead, a human multiscale model was produced in collaboration with a parallel project. This study was presented at CIAP2015 [212].

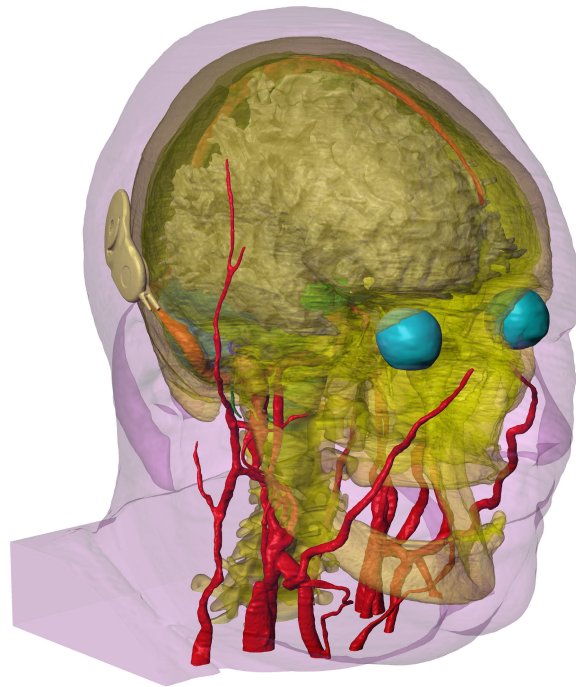


Figure 5.6: The HEATHER (Human ElectroAnatomical Total HEad Reconstruction) model [112]. (Copyright © 2014, IEEE.)

5.3.1 Method

The model of the human inner ear described in §4.5 was used for this study. It was combined with a model of the human head, dubbed HEATHER (Human ElectroAnatomical Total HEad Reconstruction), which was produced using anatomical images from female dataset of the Visible Human Project (U.S. National Library of Medicine, National Institutes of Health) [213]. Details of the human head reconstruction can be found in the paper by Tran *et al.* [112]. An image of HEATHER is provided in Figure 5.6.

The two models were combined using a process similar to that used previously. Here, the surfaces extracted from ScanIP for both the inner ear and the head were imported into ICEM CFD. HEATHER already included a low resolution reconstruction of the inner ear fluid chambers, serving as a guide for translating and rotating the reconstruction from this thesis into a near identical position. The original fluid chambers and facial nerve in HEATHER

were then removed. Computer-aided design (CAD) models of an intracochlear electrode array with 22 half-banded platinum contacts and a CI implant body were also included in realistic positions, and a surrounding sphere was added around the cochlear region to facilitate the comparison of BCs. The radius of the sphere was 11.5 mm, just sufficient to encompass all of the modelled tissues. Finally, the entire domain was discretised using the Octree algorithm, and the resultant NASTRAN mesh was imported into COMSOL for analysis.

In terms of loading, a 106.5 μA current source was applied at electrode E11, corresponding to a clinical current level of 100 [Cochlear Limited, internal communication]. Voltage and current patterns were compared for the following grounding locations:

- The end of the nerve trunk;
- The surrounding sphere;
- The ball electrode (MP1);
- The exposed plate on the implant body (MP2).

5.3.2 Results

Model Size and Solution Time

The combined human model consisted of 10,361,280 tetrahedral elements with an average element quality of 0.706. Using linear discretisation resulted in a total of 1,767,281 degrees of freedom (DOFs), which took about 4.5 minutes to solve.

Voltage Distribution

The voltage distribution under MP1, which is typically used in clinical practice, is shown in Figure 5.7. A maximum of 0.159 V was found at the stimulating electrode, corresponding

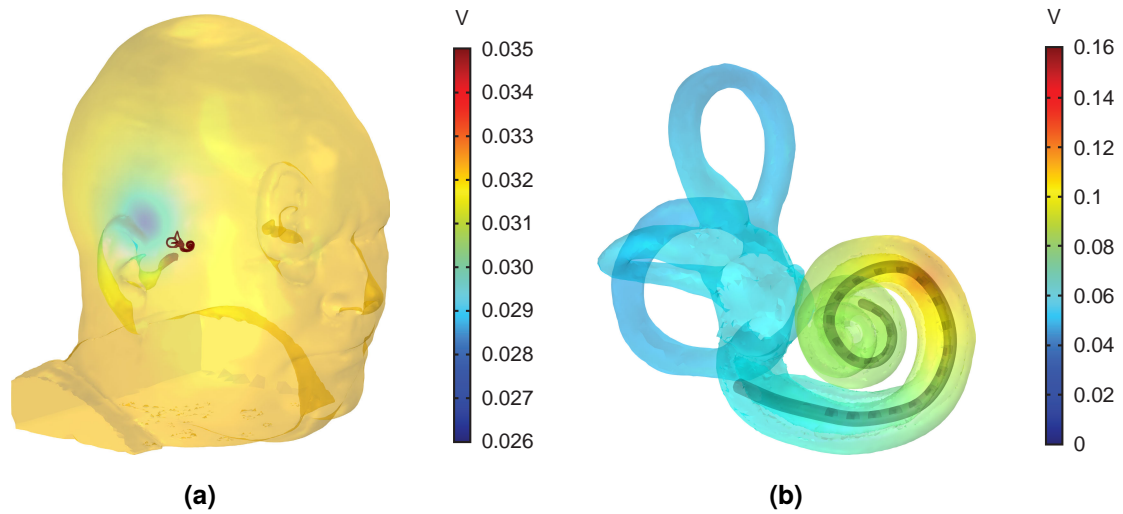


Figure 5.7: Voltage distribution in the whole head simulation under MP1 conditions. (a) The entire head; (b) the right cochlea only.

to an impedance of 1.49 k Ω . Figure 5.7 shows that the electric potential drops with distance from the stimulating electrode, but it does not fall all the way to zero near the cochlea itself. This is because the monopolar ground is located some distance away, just under the scalp.

Voltages along the electrode array under the different grounding locations are plotted in Figure 5.8. The trends here were similar to that shown in Figure 5.3 for the guinea pig model, with little change in the shape of the profile but large shifts in overall magnitude. MP1 and MP2 produced very similar voltage profiles and represent the best estimate of the true *in vivo* situation. In comparison to these values, grounding the nerve trunk overestimated terminal voltages, while grounding the surrounding sphere underestimated the voltage profile.

Current Pathways

The streamlines also varied between the different cases (Figure 5.9). There appeared to be three main exit pathways: (i) to the spiral ganglion cells next to the stimulating electrode, then to the nerve trunk, (ii) to the basal end of the cochlea via the scala tympani, then to the

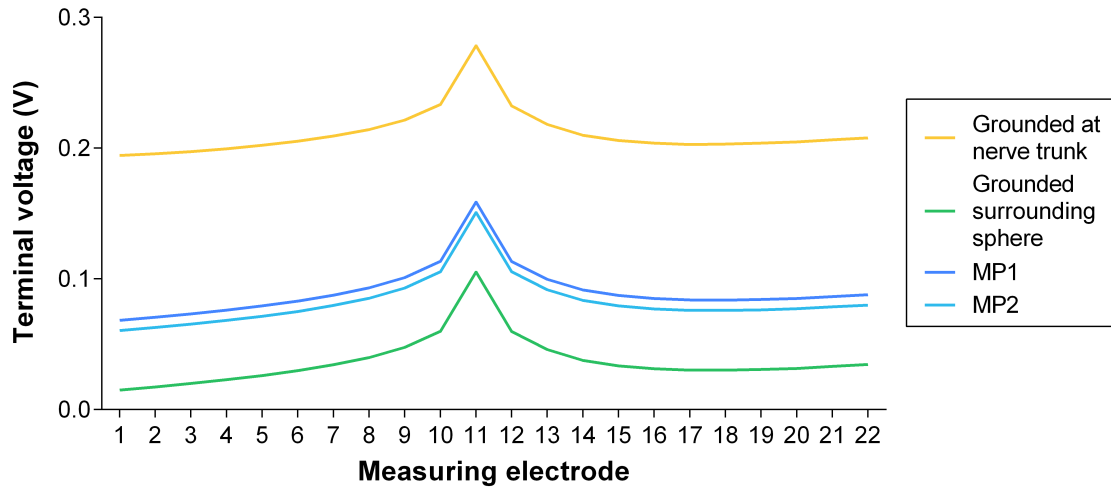


Figure 5.8: Predicted *in silico* terminal voltages by grounding location for the multiscale model.

semicircular canals, and (iii) through the cochlear walls and on to the tissues of the head. This is consistent with the findings of Micco [21].

When grounding at the nerve trunk, most of the current travelled through the cerebrospinal fluid (CSF) surrounding the nerve before converging on the truncated end surface. Grounding a surrounding sphere produced a weaker sense of directionality; most of the current still appeared to follow the CSF path, but there was more flowing via the basal end to the semicircular canals as well as through the otic capsule towards the cranial cavity and jugular vein. Current distributions under MP1 and MP2 were even more uniform, and there was very little difference between these two distant returns.

5.4 Discussion

The robustness of the workflow was once again proven by its ability to successfully create a sophisticated multiscale mesh for finite element (FE) analysis. The ability to maintain

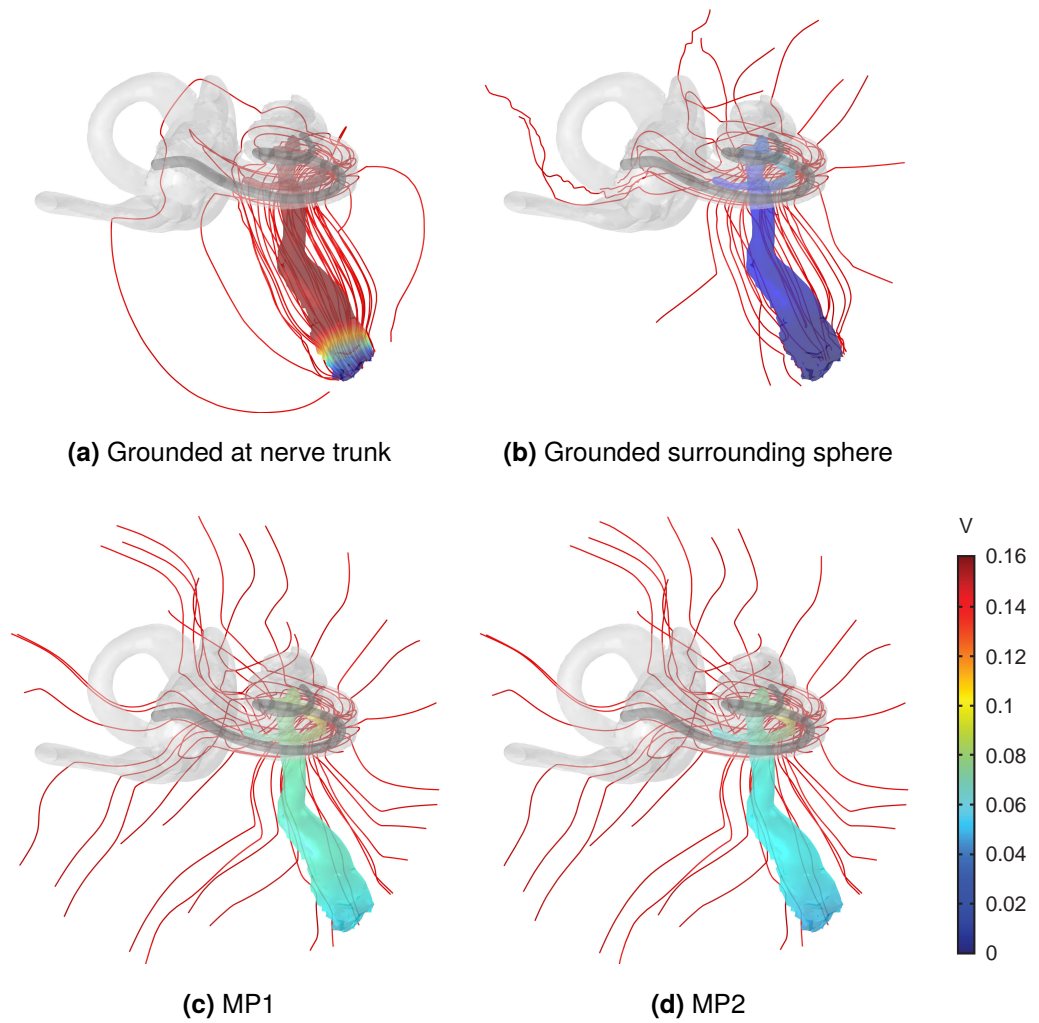


Figure 5.9: Comparison of current flow patterns for boundary conditions in man. Scale measures the electric potential in the neural tissue.

anatomical detail both locally in the cochlear region as well as throughout the important structures of the head was key to revealing insights into the expected current flow patterns.

There were several important findings in this study. Perhaps the most pertinent was that current flows out of the cochlea in all directions, as demonstrated by the MP1 and MP2 simulations in the multiscale model. There was little difference between these far-field returns, in line with findings by Miyamoto [62]. Current did not flow via the air in the tympanic cavity however. Considering that the guinea pig cochlea protrudes into the tympanic bulla (Figure 2.14), it is almost certain that the current is forced to flow towards the temporal bone in that animal. Unfortunately, this could not be confirmed in this study due to the lack of a whole head model of the guinea pig. As such, while guinea pigs might be a good animal model for studying the cochlea [62], simulations of guinea pig cochleae would likely require the application of BCs that are different from that for human models. Saba's work indicates that a sense of directionality can indeed be imposed by using asymmetric boundary conditions where required [37].

The two most traditional BCs—grounding the auditory nerve or the surrounding bone—exhibited different voltage and current patterns that have hitherto not been thoroughly examined in the literature. According to these simulations, neither of them appeared to represent the *in vivo* situation very well. Grounding the nerve forced current to follow a relatively direct path to the truncated nerve end, mostly along the highly conductive CSF encasing the auditory nerve. However, the reconvergence of streamlines seen in Figures 5.4a and 5.9a is not realistic because it is only expected to occur at the lone MP return electrode [103], which for MP stimulation is located in the far field and not in the auditory nerve itself. Even if the cochlear nerve was the *main* exit pathway, as stipulated by traditional experiments and lumped-element models, it is incorrect to force *all* of the current through it, as per Girzon [20]

and Whiten [22]. The relatively high intracochlear voltages in such implementations (Figures 5.3 and 5.8) are a result of the small area of the grounded surface, which increases the overall resistance.

On a related note, the preferential flow through the CSF jacket around the auditory nerve suggested that the nerve itself would not be the main exit path, but the CSF. This makes sense considering the higher conductivity of the CSF and its connections to other exit pathways through the head [112]. This CSF pathway may have been overlooked during early animal experiments because severing the auditory nerve during extraction of the samples would necessarily have drained the CSF.

Grounding the bone around the cochlea predicted a more dispersed streamline pattern than grounding at the nerve. The use of orthogonal bounds (i.e. along the boundary box or a surrounding cube à la Rattay [159] and Saba [37]) seemed to be less than ideal because current was artificially attracted towards the centre of each face (see Figure 5.4). This was simply because the surrounding domain was modelled as a homogeneous medium. Since the current source was closer to the centres than the corners, the lowest resistance path lay along those trajectories. Using a spherical surrounding surface prevented these artefacts, while producing similar intracochlear current paths and voltage predictions. However, the voltages in the scala tympani were still lower than expected *in vivo*. Figures 5.2 and 5.7 suggest that this is because the electric potential should not be zero at the truncated model boundary; after all, the electric potential at that location must be some finite amount in order to drive the current through the remainder of the head tissues to ground.

The voltage predictions were also affected by the size of the surrounding sphere. As alluded to in the point above, resistance increases with path length, explaining why the larger shells induced higher voltages. An infinitely large surrounding sphere per Frijns *et al.* [145] would treat the system as a true monopole and induce even higher voltages, but of course the head is not infinitely large so this may be inappropriate.

Another factor to consider is the resistivity of the surrounding bone domain, since this would also increase the overall resistance. Previous models of the human cochlea have assumed a bone to perilymph resistivity ratio of 100:1 in order to match the predicted potentials [22, 147, 209]. However, changing this value arbitrarily to fit the data is not ideal because tissue resistivities can be measured accurately [204]. Setting a value that is too far from the real resistivity can also change the current paths inside the scalae [201]. For instance, overestimating bone resistivity would predict an excessive amount of current flowing along the spiral instead of penetrating the bone. Therefore, it would be better to use accurately measured values for the tissues in the domain and explain the remaining voltage difference in terms of the incomplete drop-off arising from the unmodelled return path through the head to the true MP return.

The head is not homogeneous either though. Figure 5.2 showed that the tissues immediately surrounding the cochlea distort the electric field and therefore the resultant current patterns, so ideally this contextual information should also be incorporated. There are a few ways this might be done. The first would be to replicate the voltage isosurface from a whole head model around the standalone cochlear model prior to meshing and apply the corresponding voltage magnitude over the entire surface in the FE software. This would be difficult to accomplish due to the complex shape of the isosurface. An alternative would therefore be to map a non-uniform voltage field onto a bounding surface whose shape is simple to model, preferably a sphere. The main challenge in this case would be in getting the locations of the nodes to match [202]. For both of these options, the voltage values would also depend on the magnitude of the stimulus. This could be mitigated by using a distributed resistance to ground, where the voltage at each node on the bounding surface is normalised by the normal current density at that point.

Despite these suggestions, it should be noted that the impact on the neural response was not tested here. It may be insensitive to these changes in the current distribution because

quantities nearer to the current source may be less affected, and if that were the case then the added complexity of these alternatives above would not be worth the effort required to implement them [107]. The model should also be compared to experimental measurements to validate the predictions. Both of these issues are addressed in the next chapter.

5.5 Conclusions

Boundary conditions are a key determinant of both intrascalar voltages and current pathways through the cochlea. It was found that the BCs typically imposed on cochlear VCMs—grounding either the nerve or the surrounding bone—induced markedly different voltage profiles and current flow patterns. A multiscale human model of monopolar CI stimulation was successfully produced for the first time and demonstrated that neither of these boundary conditions were robust representations of the expected *in vivo* situation—nerve grounding appeared to be inappropriate for both guinea pig and human models due to unrealistic predictions of current flow; grounding a spherical shell around the cochlea produced more realistic streamlines, but the voltage magnitudes were lower than expected. Alternative explanations for these differences are explored in Chapter 6.

Chapter 6

Validation of the Guinea Pig Model

This chapter addresses the following questions:

- How realistic are the model predictions?
- How sensitive is the model to various input parameters?
- What is the set of ideal inputs?

6.1 Introduction

This chapter is based on the paper by Wong et al. [200], which has been published in IEEE Transactions on Biomedical Engineering.

Experimental verification of a model is always necessary [35, 109]. Computational models capture the physics of the system from a theoretical, bottom-up approach, so there are a number of simplifying assumptions and potential errors inherent to the modelling process that can affect the accuracy of the *in silico* results. In the cochlear implant (CI) research community,

there is already a reluctance to trust the findings from existing computational models. This is probably due to a range of factors, including the crude geometry of some existing volume conduction models (VCMs), unfamiliarity with computational methods, insufficient justification of assumptions, and the limited ability of models to predict psychophysical outcomes with consistent accuracy. Validation is therefore an essential step to pursue before the model is used for any further investigations.

The primary goal of this chapter is to compare the *in silico* predictions of the guinea pig model against similar *in vivo* voltage tomography data obtained independently at the Bionics Institute in Melbourne, Australia by Shefin George (under the supervision of James Fallon). This will help to determine whether or not the model outputs are reasonable. If a good correlation between the *in silico* and *in vivo* results is found, confidence in the model will be established, and some of the concerns surrounding the use of VCMs may be alleviated.

The correlation is expected to be strong because the new model includes several improvements over previous models. Existing VCMs typically use histological sections traced and swept along a spiral path, or a simplified computer-aided design (CAD) geometry. This model was reconstructed from a stack of scanning thin-sheet laser imaging microscopy (sTSLIM) images [184], so the geometry is considerably more realistic: the hook region is accurately represented and includes the round window membrane and the stapes; the scala tympani and scala vestibuli are truly continuous at the helicotrema; the major blood vessels and cerebrospinal fluid (CSF) in the modiolus were incorporated—unique for VCMs of the cochlea. Furthermore, bone was not treated as a homogeneous material, but instead separated into the modiolar bone, the otic capsule, and the temporal bone. These have markedly different microstructures and hence different electrical resistivities, so they should be treated as separate material domains [21, 201, 204, 214].

The secondary goal of this chapter is to evaluate the validity of long-held assumptions on material properties and boundary conditions. These two factors are important in determining

the *in silico* results for any particular geometry. An updated set of boundary conditions was tested relative to Chapter 5, and the basic neural response was also considered using the activating function (AF) [124].

Like previous studies, this model assumes that the cochlear tissues are purely resistive, based on the evidence provided by Spelman [98]. Resistivity values from the literature (Table 4.14) are used as base values. There are no measurements in the literature for the round window membrane, which is being incorporated into a VCM for the first time. To determine the impact of any measurement uncertainties, as well as natural variations in properties between individuals, the sensitivity of the model to each tissue resistivity value was evaluated.

Boundary conditions are modeling constraints necessary for solving the field problem [110] and should ideally replicate the physics at the boundary of the modelled domain accurately. This is problematic for VCMs of the cochlea simulating monopolar (MP) stimulation because the return electrode lies outside the physical domain of the model. Existing models deal with this issue by assuming that the end of the auditory nerve is grounded [20,22], that the ground is infinitely far away [145], or that boundary box surfaces are grounded [37,159]—none of these perfectly match the *in vivo* situation. Alternatively, they avoid the MP situation altogether and focus on pseudo-monopolar or bipolar stimulation [100,144,155,163]. Although the simulation results in these cases are indicative, they are less clinically relevant given the widespread use of MP stimulation in CI recipients. To clarify how the boundary condition assumption affects simulation results, several different cases, reflecting the range of existing choices as well as more realistic alternatives, are compared to provide some guidance for future modeling efforts.

6.2 Method

The following sections cover the procedures specific to performing the validation study. For details about how the model was reconstructed from the raw image stack and meshed, refer to §4.4.2.

6.2.1 *In silico* Modelling

A base case was first defined as a reference for comparison of the *in silico* results. All tissue domains were configured with isotropic resistivities as in Table 4.14. A 1 mA constant current source was placed at the inner surface of the stimulating electrode, identical to that used for the *in vivo* measurements. The external surface of the round window membrane was insulated to prohibit current flow from the scala tympani into the non-conductive middle ear air space, as expected *in vivo*. Lastly, the temporal bone surface was grounded to represent the expected MP current sink.

A convergence test was then performed to ensure sufficient discretisation. Five meshes were generated by varying the element size limits described in §4.4.2, then imported into COMSOL Multiphysics using the NASTRAN file format. Both the PARDISO (direct) and Conjugate Gradient (iterative) solvers were tested, with no observed difference in numerical results. PARDISO just exceeded the computer's RAM capacity when solving quadratically discretised meshes, so the Conjugate Gradient solver was used to prevent writing to disk.

Using the converged mesh, both material properties and boundary conditions were altered *ceteris paribus* from the base case. For the sensitivity analysis on material properties, individual tissue resistivities were set to either double or half of the base value (à la Finley [143] and Rattay [159]), or the highest or lowest values from literature, whichever deviated more from the base value. Since there was no data for the round window membrane, its resistivity

was assumed to be 1000 $\Omega\cdot\text{m}$ based on the geometric average of Reissner's membrane and the basilar membrane (see Table 4.14), and an order of magnitude variation was tested to account for the additional uncertainty.

For the boundary condition tests, the base case rerun with each of the following boundary conditions:

1. Ground the auditory nerve trunk only;
2. Ground the caudal aspect of the temporal bone surface;
3. Ground the entire temporal bone surface;
4. Apply a voltage offset on the temporal bone surface;
5. Ground the entire outer surface of the surrounding sphere;
6. Ground at an infinite large surrounding sphere.

The corresponding boundary surfaces are shown in Figure 6.1. Boundary conditions 2–5 were applied on a surrounding sphere of radius 5 mm because this size was found to be sufficiently large for replicating far-field effects [202]. For grounding at infinity, a second shell of radius 8 mm was added and configured as an infinite element domain in COMSOL, with resistivity set to that of the guinea pig skull [204].

The voltage offset boundary condition is a novel proposal. In a real CI recipient, the stimulating current must pass through the cochlear tissues as well as the rest of the head in order to reach the return electrode under MP stimulation (see Figure 6.2). If the resistance of the head is not accounted for in the model, the total resistance will be underestimated. The circuit is also a voltage divider, so given the non-zero resistance of the head, the electric potential at the model boundary should also be non-zero (i.e. not grounded). The offset value for these simulations was determined as the average difference in terminal voltages between grounding at the temporal bone surface and the mean *in vivo* profile.

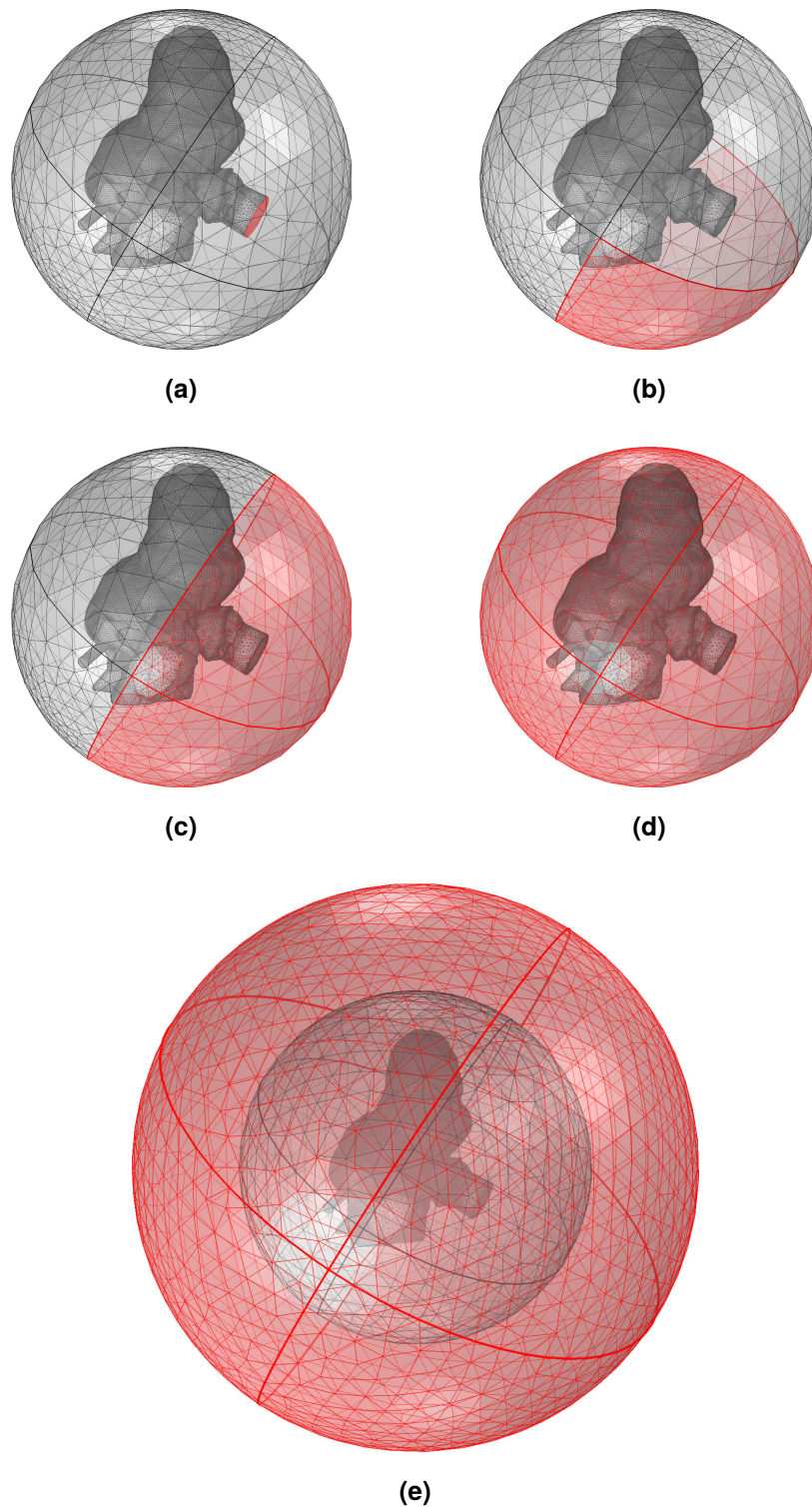


Figure 6.1: Surface selections for boundary conditions: (a) the end of the auditory nerve trunk; (b) caudal aspect of the temporal bone surface; (c) the temporal bone surface; (d) the surrounding sphere; (e) at infinity. The outermost domain in (e) is configured as an infinite element domain.

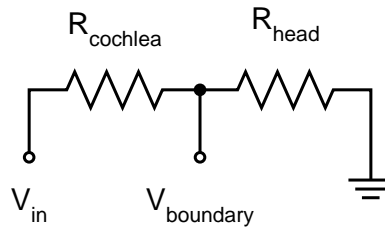


Figure 6.2: The modelled domain only includes the resistance inside the cochlea. For monopolar stimulation, injected current must also overcome the resistance of the head in order to reach the ground electrode. This acts like a voltage divider, so the electric potential at the model boundary should be non-zero. (Copyright © 2015, IEEE.)

The primary model output was the average voltage at each electrode, because this could be directly compared with the *in vivo* results. The magnitude and direction of current flow were depicted using streamline plots of current density seeded on a regular quadratic grid over the surface of the active electrode (see Appendix B). Neuron trajectories covering the first 570 degrees of the cochlea were modelled in MATLAB by connecting key points from the tips of the peripheral processes, through the cross-sectional center of the spiral ganglion, and down along the cochlear nerve trunk (see Figure 4.12), similar to Kalkman *et al.* [147]. For each neuron, nodes of Ranvier were placed at fixed intervals from the point in Rosenthal's canal. Spacing resembled that used in the GSEF neural model [100]: 175 μm along the peripheral process and 300 μm along the axon. The AF, i.e. the discrete second derivative of electric potential with respect to distance along the fiber [82], was computed for each set of adjacent nodal triads along 100 equally spaced fibers, then plotted along the unrolled neural sheet (Figure 6.3). This signifies the degree to which the underlying electrophysiological requirements for neural firing are met.

6.2.2 *In vivo* Measurements

Voltage tomography measurements were collected from eight (N=8) adult pigmented guinea pigs (500–800 g) for comparison with the *in silico* results. All procedures were approved by

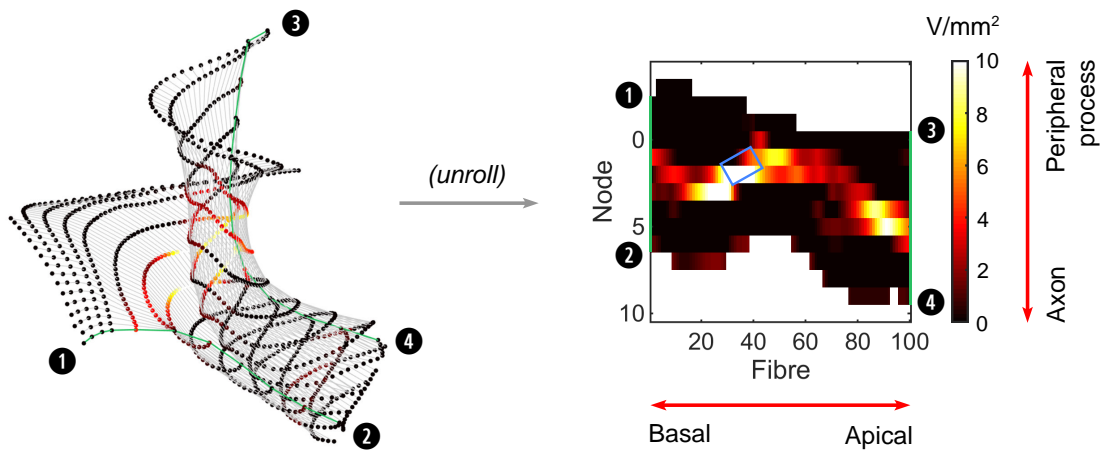


Figure 6.3: Unrolling the neural sheet for 2D activating function plots. The data shown here are for the base case scenario. The coordinate system follows that of Kalkman *et al.* [147], but here Rosenthal's canal is always at node 0. Fibres 1 and 100 are traced in green, and the blue box in the 2D plot marks the approximate location of the stimulating electrode (E4). (Copyright © 2015, IEEE.)

the Royal Victorian Eye and Ear Hospital Animal Research and Ethics Committee (project number 12/250AB, granted 28 February 2012; see Appendix C) and were in accordance with the Australian Code of Practice for the Care and Use of Animals for Scientific Purposes. All procedures were performed in an electrically isolated Faraday room.

The animals were anaesthetised using isoflurane (1.5–2%) and oxygen (1 L/min). Respiration rate (normal levels: 15–25 breaths/min) and end-tidal CO₂ levels (normal levels: 1–3%) were monitored over the duration of the experiment (2–3 hours). Core body temperature was maintained at $37.0 \pm 1^\circ\text{C}$. A post-auricular incision was made and the left cochlea was surgically exposed. Each animal was implanted with a Hybrid-L8 (HL8) array, containing eight intracochlear platinum half-band electrodes on a silicone carrier. The electrode array was inserted approximately 6 mm through the round window into the scala tympani, typically placing 7–8 electrodes within the scala. A platinum ball electrode placed in the neck muscles served as the MP return and reference electrode.

For each intracochlear electrode, a monopolar cathodic-first biphasic pulse (25 μs per phase and 8 μs inter-phase gap) was delivered with an amplitude of 1 mA. The voltage at each of the non-stimulating electrodes was measured with respect to the reference electrode at the end of the cathodic phase. The voltage at the stimulating electrode was estimated as the maximum among the values extrapolated from all available adjacent pairs, as adapted from van den Honert and Kelsall [12], to ensure that the sharpness of the current spread function was not underestimated.

6.3 Results

6.3.1 *In vivo* Data

The raw measurements for all eight guinea pigs during stimulation at E4 are shown in Figure 6.4. (Only results at E4 are presented for brevity.) Differences between guinea pigs were observed, presumably due to the unique geometry of each cochlea and its surrounding tissues, variations in the surgical insertion of the implants and the resistivity of the tissues, and other subject-specific factors. Most of the profiles clustered around the average, so a mean profile was calculated to serve as a benchmark for comparison with the *in silico* results. The minimum to maximum voltage range over all specimens was also found and is shaded in Figure 6.4.

The apical electrode (E8) was excluded from the comparisons because measurements from that electrode could not be obtained in four of the eight guinea pigs. This was likely due to the electrode tip folding over during insertion.

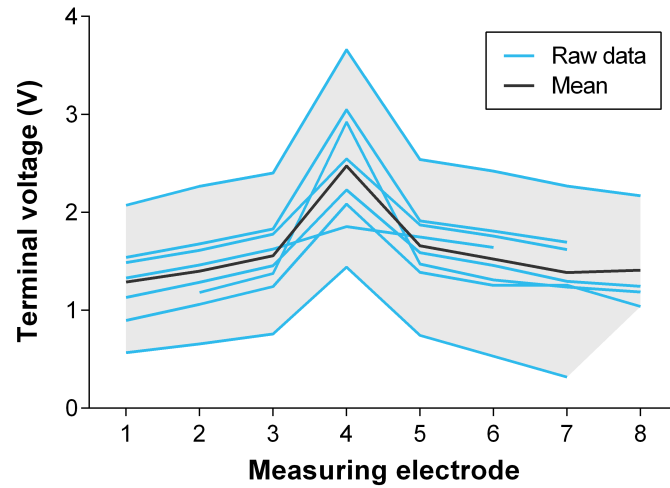


Figure 6.4: *In vivo* voltage measurements (N=8) along the array during E4 stimulation. Shortened traces are likely due to tip fold-over or incomplete insertion. The shaded area represents the spread of *in vivo* results. (Copyright © 2015, IEEE.)

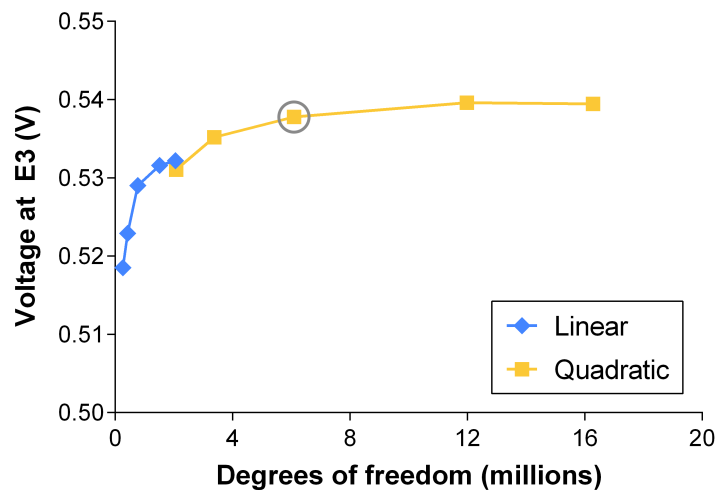


Figure 6.5: Mesh convergence results for terminal voltage at E3 during stimulation at E4. The selected mesh exhibits only 0.3% difference relative to the densest quadratic mesh (far right). (Copyright © 2015, IEEE.)

6.3.2 Mesh Convergence

Each mesh was solved using both linear and quadratic elements. The coarsest linear mesh had 262,620 degrees of freedom (DOFs) and the finest quadratic mesh had 16,278,789 DOFs. Solution times ranged from 12 seconds to 2 hours per simulation.

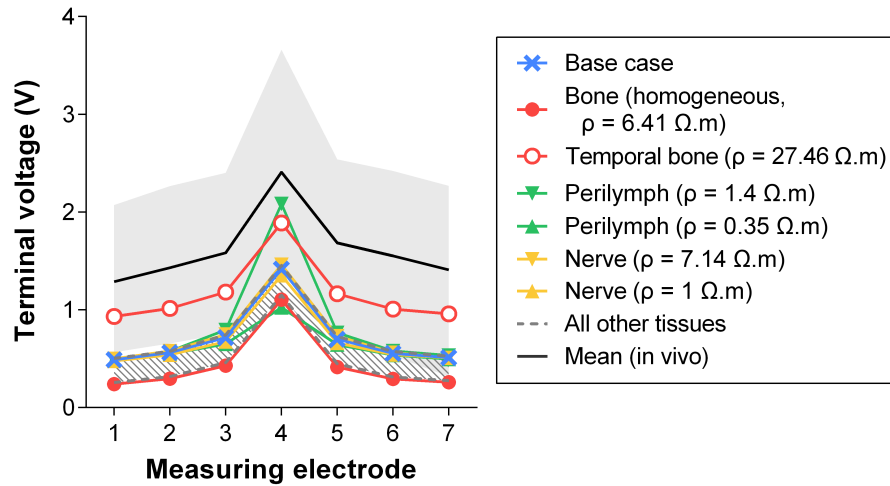
Figure 6.5 indicates that the mesh with 6,092,537 DOFs is well converged, with only 0.3% difference relative to the densest quadratic mesh that was tested. Solution time was about 30 minutes, striking a good balance between accuracy and computational cost. All of the linearly discretised meshes exhibited greater than 5% difference. This suggests that linear shape functions were not sufficient for capturing the electric field behavior in this model (cf. Frijns *et al.* [100]).

6.3.3 Sensitivity of Terminal Voltage Predictions

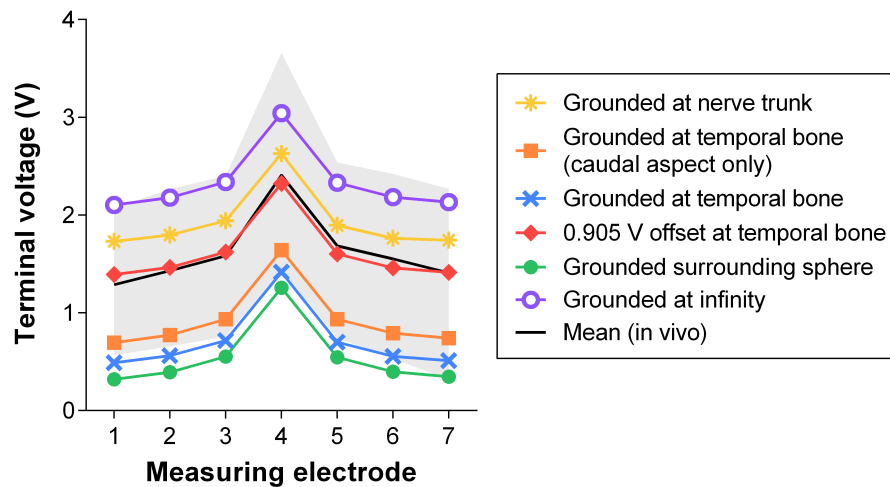
Table 6.1 shows the percentage impact of tissue properties on terminal voltage predictions. These values were calculated relative to the base case and classified as either negligible (less than 1% difference), weak (1–5%), or strong (more than 5%), again based on the 5% sufficiency criteria of Frijns *et al.* [100]. For this model, the resistivities of most tissues had either a negligible or weak effect on terminal voltages. The exceptions were bone, perilymph, and nerve. Temporal bone resistivity was the most sensitive, with differences of up to 90.8% relative to the base case. At extreme literature values for otic capsule resistivity [215,216], up to 59% difference was observed. Treating bone with a homogeneous resistivity of 6.41 $\Omega\cdot\text{m}$ underestimated terminal voltages relative to the base case (see Figure 6.6a). Perilymph had a particularly strong effect at the stimulating electrode and was notably the only tissue to change the shape of the profile. Nerve resistivity had up to 5.79% impact on terminal voltages.

Table 6.1: Sensitivity of terminal voltages to tissue resistivities. Deltas were calculated relative to the base case. Weak (+) and strong (++) impact tissues are indicated. ^aResistivity changed from base value by a factor of two. ^bUpper and lower resistivity limits based on extreme values from literature, as indicated. ^cResistivity changed from base value by a factor of ten.

Tissue	Deviation from base case (%)		Impact
	Mean	Max	
Bone (homogeneous, $\rho=6.41 \Omega \cdot m$)	43.2	51.0	++
Modiolar bone ^a	1.76	3.60	+
Otic capsule ^b ($\rho=1.5\text{--}350 \Omega \cdot m$)	50.7	59.0	++
Temporal bone ^a	73.9	90.8	++
Perilymph ^a	10.3	47.2	++
Endolymph ^a	0.51	0.65	
Nerve ^b ($\rho=1\text{--}7.14 \Omega \cdot m$)	3.18	5.79	++
CSF ^a	0.83	1.06	+
Blood ^b ($\rho=0.61\text{--}5.56 \Omega \cdot m$)	0.18	0.61	
Spiral ligament ^b ($\rho_U=2.5 \Omega \cdot m$)	2.03	2.99	+
Stria vascularis ^b ($\rho_L=3 \Omega \cdot m$)	0.28	0.42	
Organ of Corti ^a	0.08	0.14	
Basilar membrane ^a	0.03	0.06	
Reissner's membrane ^a	0.02	0.04	
Round window membrane ^c	0.02	0.05	



(a) Sensitivity to tissue resistivities



(b) Sensitivity to boundary conditions

Figure 6.6: Sensitivity of terminal voltages to key model inputs. Base case values are marked with blue crosses. The light grey areas represent the range of *in vivo* voltage measurements from Figure 6.4. (a) Most tissues had little impact on the *in silico* predictions, and almost all data points fell outside the *in vivo* range. (b) Boundary conditions had virtually no effect on the shape of the profile, but strongly affected the voltage magnitudes. (Copyright © 2015, IEEE.)

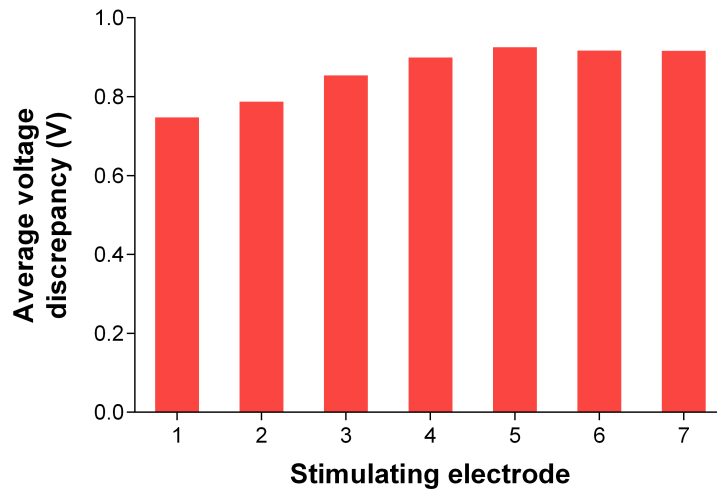


Figure 6.7: Voltage offset required to match the mean *in vivo* results changed with the location of current injection. Offset values were lower for basal electrodes, and levelled off between E4 and E7. (Copyright © 2015, IEEE.)

Figure 6.6b compares the *in silico* and *in vivo* terminal voltages for each of the tested boundary conditions. The shape of the profile was unaffected, but a wide spread of voltage magnitudes was observed. Grounding at infinity or at the nerve trunk overestimated voltages along the array, relative to the observed *in vivo* mean. In contrast, grounding the surrounding sphere or part thereof led to substantial underestimates, with smaller grounding areas corresponding to higher terminal voltages. Some of these fell outside the range of observed *in vivo* measurements.

Offset values required to match the *in vivo* average were found to vary with the location of current injection, as shown in Figure 6.7. For stimulation at E4, a 0.905 V offset on the temporal bone surface was required to match the *in vivo* measurements, equivalent to a 905 Ω of resistance to ground. This compares well with values in the literature. Von Békésy estimated the resistance between the round window and the body at 2000 Ω [66], and Johnstone *et al.* estimated total resistance to the monopolar return to be 1580 Ω [135]. Both of these are slightly higher than the *in silico* offset voltages obtained here, but this is expected

since they were measured from inside the cochlea and so include additional resistance from the cochlear tissues and some surrounding bone.

6.3.4 Effect on Current Pathways

Streamline plots revealed that current spread in the near-field was relatively insensitive to both tissue properties and boundary conditions, leading to similar gradients of voltage falloff as shown in Figure 6.6. Beyond the scala tympani however, current flow patterns were noticeably different. Figure 6.8 shows that current paths were strongly dependent on the prescribed boundary condition. Grounding the nerve (Figure 6.8a) was the most distinct, with streamlines reconverging at the grounded nerve surface and an obvious edge effect around its periphery. Grounding the entire surrounding sphere (Figure 6.8d) resulted in omnidirectional current spread beyond the cochlea, as did grounding at infinity (Figure 6.8e). Restricting the grounding surface to a quadrant (Figure 6.8b) or hemisphere (Figure 6.8c) imposed a sense of directionality on the exit pathway. Lastly, applying a voltage offset on the temporal bone surface produced virtually identical streamlines as grounding it.

6.3.5 Estimated Impact on Neural Excitation

Differences in current flow pathways in turn affected predictions of neural excitation as measured by the AF. The main regions of excitation were largely similar for any particular stimulating electrode, but localised differences along the neural sheet were also observed. Percentage differences in AF relative to the base case (Figure 6.3) are shown in Figures 6.9 and 6.10. These plots show the change in predicted AF at each node of Ranvier along the unrolled neural sheet when a single simulation parameter was varied.

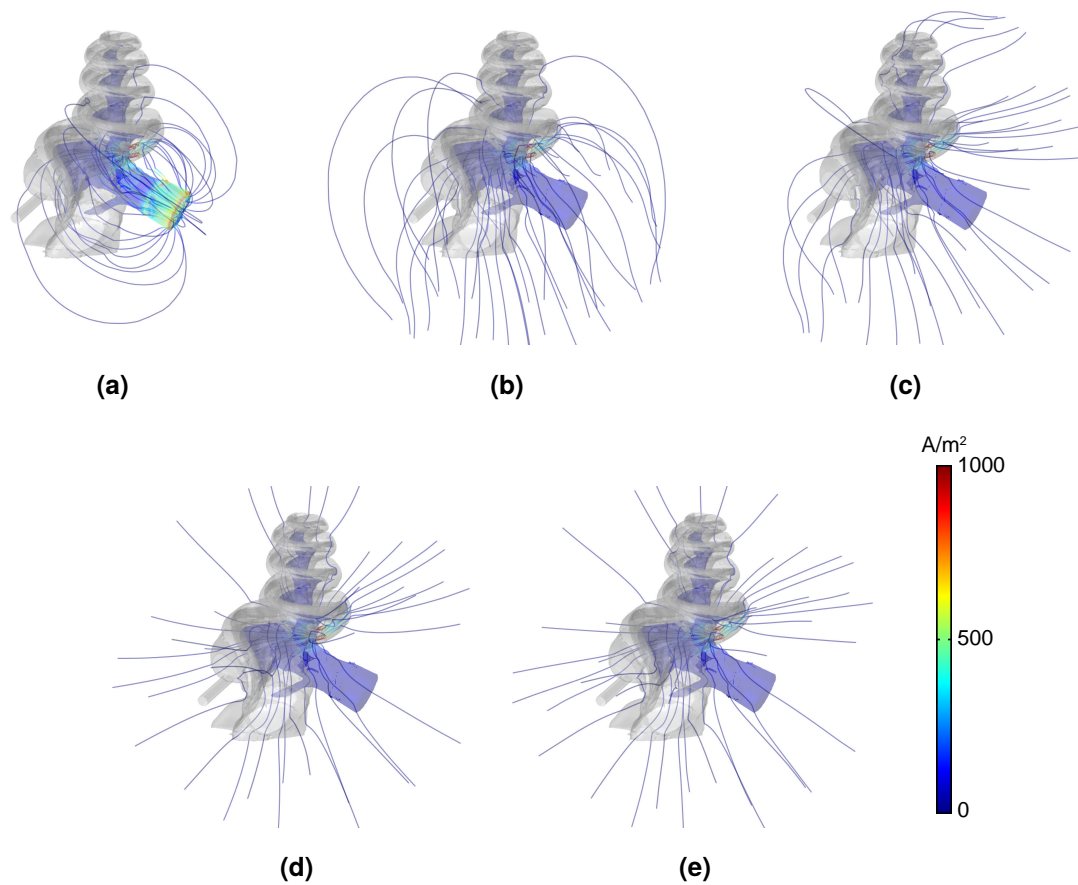


Figure 6.8: Streamline plots of the current paths during stimulation at E4 for (a) grounding the nerve trunk, (b) grounding the caudal aspect of the temporal bone surface, (c) grounding or applying a 0.905 V offset on the temporal bone surface, (d) grounding the entire surrounding sphere, and (e) grounding at infinity. These correspond to the highlighted surfaces in Figure 6.1. Scale indicates current density in the nerve tissue.

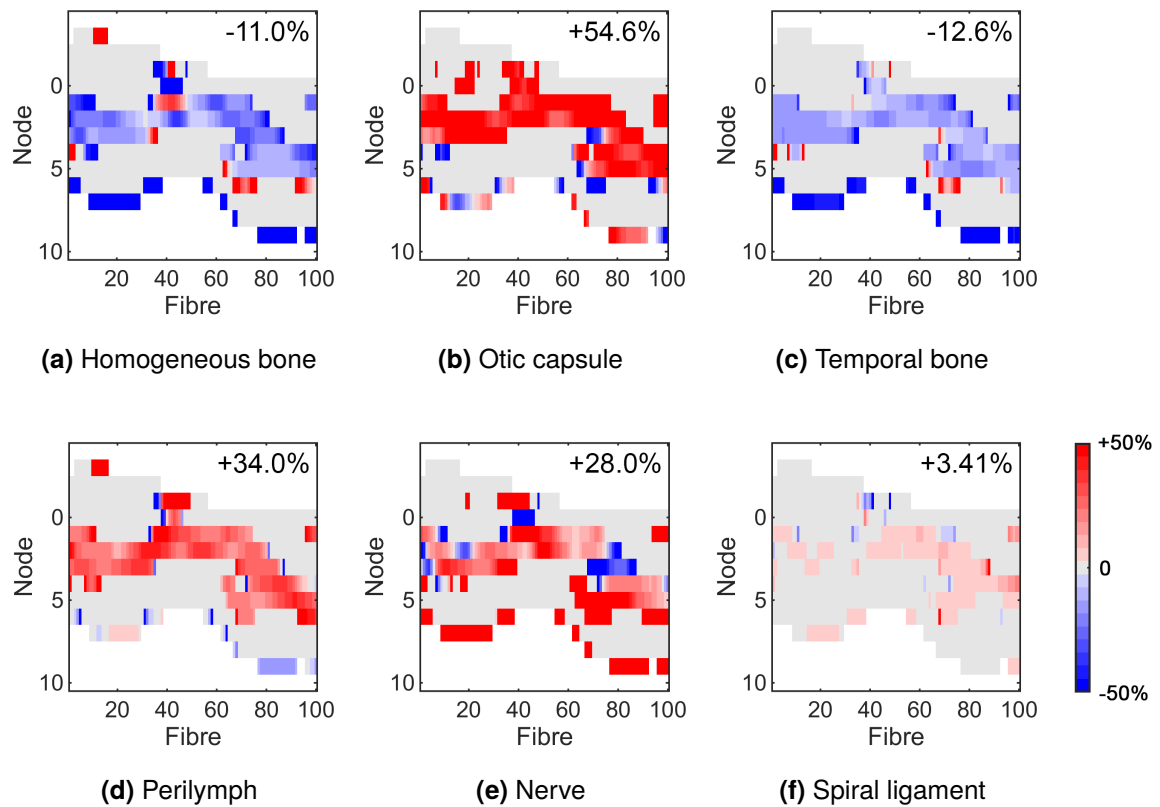


Figure 6.9: Percentage change in activating function with changes in tissue resistivity. Deltas were calculated relative to the base case. RMS deltas are shown in the top right corner. (Copyright © 2015, IEEE.)

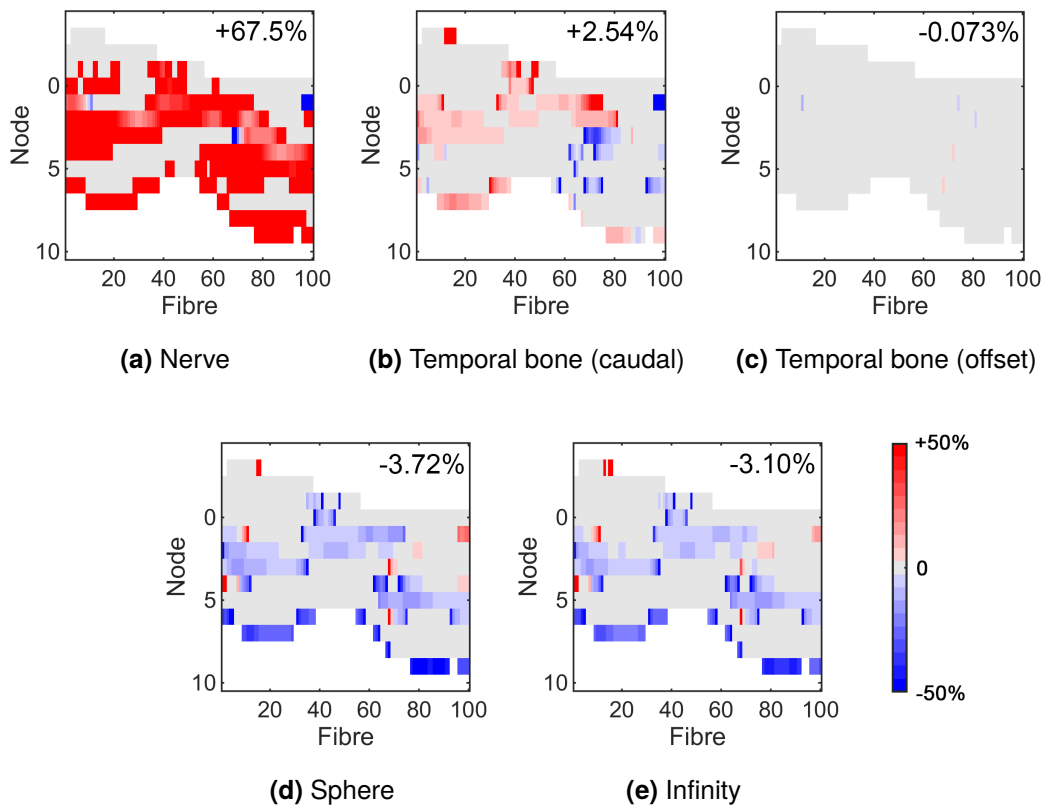


Figure 6.10: Percentage change in activating function with boundary conditions relative to the base case for (a) grounding the nerve trunk, (b) grounding the caudal aspect of the temporal bone surface, (c) applying a voltage offset to the temporal bone surface, (d) grounding the entire surrounding sphere, and (e) grounding at infinity. The voltage offset by itself had negligible effect on the AF prediction. (Copyright © 2015, IEEE.)

Figure 6.9a–6.9c show that higher bone resistivity drove more current into the nerve tissue and increased depolarisation relative to the base case, and vice versa. Likewise, higher resistivities for perilymph, nerve, or the spiral ligament led to increased axonal activity (Figure 6.9d–6.9f). The differences were not uniform and tended to be more pronounced near the main area of excitation (especially at the peripheral process) as well as at fibres one full turn away (around fibre 90).

For the boundary conditions, grounding the nerve trunk (Figure 6.10a) resulted in significantly more widespread depolarisation than in the other cases (+67.5% RMS, the largest discrepancy of all the test cases). The differences were largest near the end of the axon where the ground was imposed. Grounding the caudal temporal bone (Figure 6.10b) reflected the directionality of the corresponding streamlines. AF values for the grounded temporal bone surface and the corresponding offset case were virtually identical, which was expected given their similar current pathways. A slightly larger discrepancy was observed between the sphere grounding and infinite grounding conditions (Figures 6.10d and 6.10e). Nonetheless, boundary conditions 2–6 all produced AF patterns that were within about 5% of each other, so the model was not sensitive to this assumption.

6.4 Discussion

6.4.1 Modelling Workflow

The methodology used in this study allowed for a high fidelity reconstruction of the cochlea with an unprecedented amount of anatomical detail, but it also suffered from a few drawbacks stemming from the large size of the data set. Firstly, the time required to process the image stack was in the order of months due to the large number of tissues and the need for some

sophisticated manual segmentation. Secondly, the segmentation process required comprehensive knowledge of the anatomy in the region of interest, and consultations with anatomical experts were needed to minimise the risk of incorrect reconstruction. Algorithmic segmentation could be employed in the future to reduce the time requirements and inconsistencies due to human error, but to the extent of the authors' knowledge, existing techniques are not well suited to datasets with many tissues and are usually optimised for CT or MRI image stacks. Thirdly, although the Octree algorithm was robust enough to handle the complexity of the surfaces, it always resulted in the production of some small element islands. While smoothing the segmentation eliminated some of these islands, the requirement for manual intervention limits the potential for a fully automated process.

Overall, the capabilities of this workflow far outweighed its limitations. It can be expected to translate well to other data-sets and other organs, regardless of imaging modality.

6.4.2 Material Properties

There is some concern that the base resistivity values for cochlear-specific tissues may not be appropriate because the scaling and disregard of spatial effects necessary to derive them from bulk resistances compromises their accuracy [20,21,100,144]. Most values can also be traced back to a single source [116], so there is doubt over the reliability of the measurements.

According to the simulation results, the model is not very sensitive to most tissue resistivities. The spread of terminal voltage predictions in Figure 6.6a is smaller than the standard deviation of the *in vivo* measurements, suggesting that any uncertainties were within inter-subject variability limits. The continued use of these values in the literature also suggests that they represent the electric behavior reasonably well.

For the tissues to which the model was sensitive, some (namely CSF, endolymph, and perilymph) have resistivities that are known accurately [100,217] and can therefore be used

with confidence. The FE model in this study was based on a healthy, unimplanted guinea pig cochlea, and the validation data was obtained from acute experiments, so the base value of perilymph resistivity was suitable. In chronic implants however, the perilymph around the electrode array is displaced by a layer of fibrous encapsulation tissue [218]. Given the sensitivity of the model to perilymph resistivity, this would have a bearing on predictions of stimulation thresholds [156].

Terminal voltages were most sensitive to the bone domains because injected current must pass through them to reach ground. As such, these values were particularly crucial. The Suesserman resistivity measurements [204] used in this study are specific to the guinea pig and, given the care with which they were taken, should be quite accurate. However, it is curious that the lateral wall was reported as being less resistive than the modiolar wall because higher density bone is more resistive [216] and the otic capsule is the densest bone in the body [27]. The use of the skull value for the temporal bone and infinite domains may also be an underestimate since the temporal bone is relatively dense. Conversely, the current path through the head is likely to follow lower resistance pathways, such as through the CSF [112]. Determining the true effect on the return pathway would require a whole head model.

The resistivity of the spiral ligament should also be verified. At $0.6 \Omega\cdot\text{m}$, it is relatively low, reflecting the suspicion that perilymph can diffuse freely through it and that it is involved in ion transport [28, 219]. However, considering the known presence of various cell types and extracellular matrix material in the tissue, and that perilymph itself has a resistivity of $0.7 \Omega\cdot\text{m}$, this may be inaccurate. The only other estimate in the literature is $2.5 \Omega\cdot\text{m}$ [20]. At this higher resistivity, the scala media became more insulated, leading to differences in terminal voltages, current pathways, and AF. It may be worth investigating whether the scala media should be modelled as being insulated on all sides to represent the tight junctions between the surrounding epithelial cells that prevent ionic current flow *in vivo* [28].

The ideal resolution to these uncertainties over material properties would be to re-measure the resistivities of all the cochlear tissues using an accurate and up-to-date technique [220]. At the least, this would provide an alternative data point for comparison with the values derived from lumped-element models; at best, these values would form a new gold standard as inputs for future electroanatomical studies of the cochlea.

6.4.3 Boundary Conditions

Three criteria were considered for evaluating the boundary conditions: closeness of match to the *in vivo* terminal voltages (Figure 6.6b), the current paths exiting the cochlea (Figure 6.8), and the impact on AF values (Figures 6.9 and 6.10).

Grounding the nerve trunk seemed to make sense based on early evidence that the nerve trunk is the dominant exit pathway [66]. Using this boundary condition, simulated voltages were relatively high because current was forced to flow through a small return area. However, the otic capsule is not a perfect insulator and both the stimulating and return electrodes are small relative to the head, so injected current spreads out as it flows through the cochlear tissues and is not expected to re-converge within the domain [103, 112] as observed in Figure 6.8a. Because of this, the AF plot (Figure 6.10a) predicted substantially more widespread depolarization than the other boundary conditions. Combined with the relative proximity of this isosurface to the regions of interest within the domain, it appears that this boundary condition violates Saint-Venant's Principle of far field equivalence by not faithfully reproducing true MP loading patterns. The evidence suggests that grounding the end of the modelled nerve trunk is inappropriate, at least in the case of the guinea pig cochlea.

Simply grounding an outer surface to represent the current sink is also insufficient. It ignores the presence of the return path through the head and thus underestimates intrascalar voltages. Including the return path as an infinite domain is plausible, but tends to overestimate voltages.

Of course, this depends on the resistivity of the infinite domain, and a value could be applied that forces a match with the *in vivo* data, but that would alter the ratio of resistivities between the temporal bone and other cochlear tissues, which could result in unintended effects on the current paths within the cochlea [21, 201] and the AF (e.g. Figure 6.9b). This is not ideal because resistivities are not a variable and can be measured. The value used for the infinite element domain in this study appears to be higher than the effective resistivity of the mean guinea pig head. In any case, purely grounded boundary conditions cannot be easily matched to *in vivo* data, which may be important in future subject-specific modeling efforts.

Given that none of the above boundary conditions presented a close match to the *in vivo* data, the voltage offset was proposed and tested. This alternative explanation for the voltage drop along the unmodelled return path through the head did not seem to influence the current pathways or AF, presumably because it is cancelled out in the calculation. Its value could therefore be set arbitrarily to model different cases, as required for subject-specific models. The principle could also be applied to cochlear models from other species.

The offset would ideally be applied to a grounding surface that replicates the *in vivo* current paths. In these simulations, grounding the temporal bone surface was considered to be the most realistic because the protrusion of the guinea pig cochlea into the tympanic bulla, the low voltages exhibited during CI stimulation, and the extremely high impedance of air together suggested that injected current would flow away from the bulla (Figure 6.8c). However, there is no way to be sure without implementing a complete guinea pig head model.

Ultimately, grounding surfaces need to be sufficiently large and far from the stimulating electrode in models of MP stimulation to prevent adverse impacts on the computed AF.

6.4.4 Study Limitations

The trajectory of the electrode array within the scala tympani was unlikely to be a perfect match despite taking care to accurately replicate the insertion at the round window. HL8 arrays tend towards a more lateral position, but the exact *in vivo* positions of each electrode were not confirmed in this study. Each insertion was also slightly different, and the data for more apical stimulation suggest that the modelled insertion was slightly deeper than the *in vivo* average. This adds a little uncertainty to the *in silico* predictions, but the close fit inspires confidence in the model nonetheless.

Another concern was that the *in vivo* measurements were taken at the end of the stimulating phase. It is known that the voltage profile changes over the duration of the pulse, and there is some speculation that time-dependent effects may play a role despite Spelman's observations [98]. Until this hypothesis is tested, the purely resistive formulation of this model should only be taken as a first approximation.

Lastly, the sample size for the *in vivo* measurements was relatively small. Ideally, more measurements would be added to the comparison, not only from more animals, but also from more locations within each animal to validate the field quantities outside the scala tympani. However, this must be balanced against the financial, time, and ethical costs of obtaining these additional data points. It is hoped that if *in silico* models such as the one presented here become sufficiently accurate and trustworthy, the reliance on animal testing may be reduced in the long term.

6.5 Conclusions

The workflow used in this study successfully overcame the difficulties seen in other *in silico* modeling methodologies to enable the creation of a high fidelity FE model of the guinea pig

cochlea. Intrascalar voltages predicted by the model were more sensitive to the choice of boundary condition than to the assigned tissue resistivity values. However, the AF along the neural sheet was more sensitive to certain material properties. Grounding the nerve trunk appeared to be inappropriate for the guinea pig model; conversely, the proposed voltage offset boundary condition was able to characterise multiple facets of the *in vivo* situation realistically. In addition, the offset provides a feasible method for accommodating subject-specific differences, and may therefore be considered for use in future models of monopolar CI stimulation.

Overall, the strong correlation between the *in silico* results and the average *in vivo* measurements indicated that the model can be used to represent an average implanted guinea pig cochlea.

Chapter 7

The Role of the Cochlear Vasculature in Volume Conduction

This chapter addresses the following questions:

- What role do blood vessels play in volume conduction?
- How strongly do they affect the current pathways?
- Should vascular structures be modelled?

7.1 Introduction

The cardiovascular system plays a vital role in providing oxygen and nutrients to almost every cell in the body while also removing metabolic waste products. Oxygenated blood leaves the heart and is distributed around the body via the arteries of the systemic circuit. These branch off to supply specific regions and organs. Smaller arterial branches, known as arterioles, eventually give way to capillaries, where nutrient, gas, and waste exchange actually takes

place. The morphology then reverses, with the capillaries merging into progressively larger venules and veins until they re-enter the heart. Deoxygenated blood is then pumped through the pulmonary circuit, and the cycle begins anew.

The histological structure of each vessel type depends on its function. For instance, arteries must withstand high, cyclically-loaded intraluminal pressures, so they are elastic and have a thicker muscle layer. On the other hand, capillaries only possess thin endothelial linings, which may contain *fenestrations* (pores) to facilitate chemical exchange with surrounding cells [40, 175].

Like other organs, the cochlea is highly vascularised (recall §2.1.2). Anatomical studies of the cochlear vessels have revealed that the network of blood vessels in the inner ear is both pervasive and delicate [49, 57, 221–223]. The role of these vessels under electrical stimulation has been speculated over since the pioneering experiments of von Békésy. He observed a multitude of vessels in the bony wall of the scalae [66, p. 659], and suggested that they may be one of the main pathways from the cochlea to the rest of the body. Resistance results from the Johnstone model [135] indicated that the vascular pathways are indeed measurably more conductive than others in the model, but the simple lumped element nature of this model was unable to reveal any meaningful spatial insights. Girzon did not include any vascular structures in his volume conduction model (VCM) [20], suggesting that they were “probably represented adequately. . . by lumping the nerve tissue and blood vessels together”. He mused that nerve was the main grounding pathway due to its larger volume, but called for further investigation of the vasculature as well as the well-supplied spiral ligament. Whiten’s VCM [22] included the nearby carotid artery but none of the internal cochlear vessels. He also speculated that they do not form a substantial exit pathway, but could not rule out the possibility due to the known connectivity with larger vessels, such as the carotid artery and jugular vein.

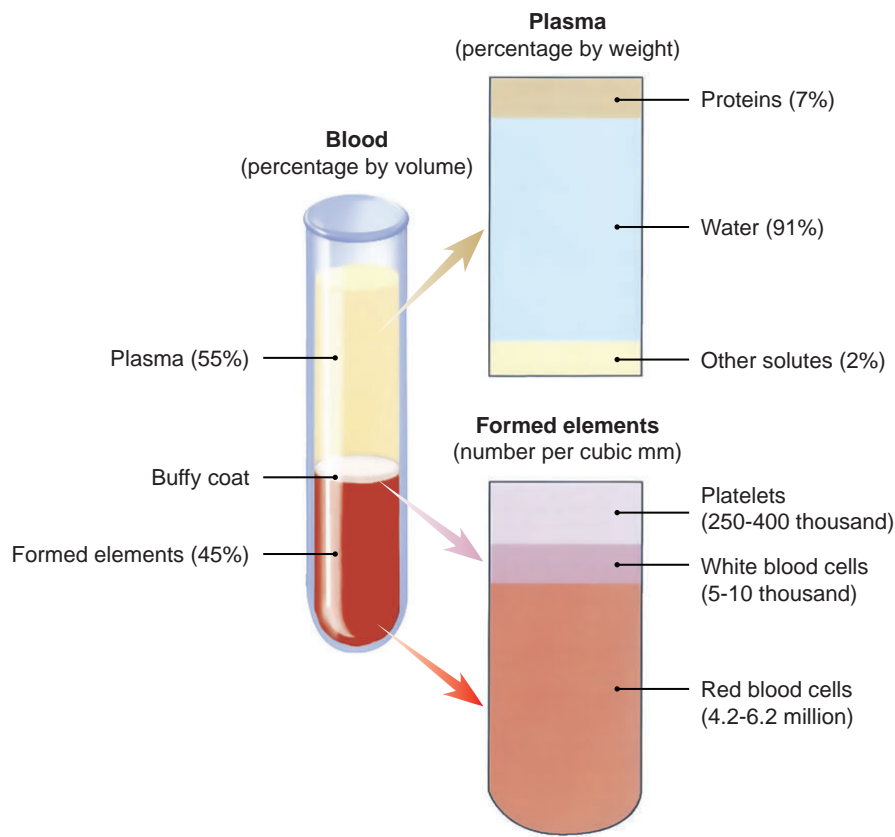


Figure 7.1: The composition of blood. (Adapted from Tate *et al.* [45]. Copyright © 2012, McGraw-Hill.)

The early calls for further investigation were never truly answered, with all other modelling efforts neglecting the vascular pathways and simply assuming that they play a negligible role despite the lack of conclusive evidence. As such, this assumption has remained untested, which is undesirable for a couple of reasons. Firstly, blood is one of the most conductive tissues in the cochlear region due to the presence of electrolytes and charged proteins in the plasma (cf. Figure 7.1 and Table 4.14) [75, 167]. The sprawling vascular network passes through almost all of the other cochlear tissues, which have quite different—and often substantially higher—electrical resistivities. Since current is known to follow the path of least resistance, these vascular shortcuts may be an important route for intracochlear currents. Preliminary studies using the proof of concept model [173] and the finding by Tran *et al.* that the jugular vein is an important extracochlear current pathway [210, 224] lend further weight to this idea.

Secondly, the major cochlear vessels—namely the spiral modiolar artery (SMA) and the vein of the scala tympani (VST)—lie very close to the modiolar wall, in between the intracochlear electrodes and the neural tissue. This proximity to the current source means that the vessels may have a more profound impact on the current pathways than sheer volume alone would suggest, as per the discussion in §3.2.1 [103]. Even if the differences are mainly localised and do not have a large bearing on the exit pathways, it would be prudent to attain a sense of the sensitivity of the model to the vasculature since it is the current distribution in this main region of excitation that determines the dominant neural response.

Imaging and reconstruction of blood vessels are possible using contemporary techniques. Studies of larger vessels, such as those in the heart [203] and lungs [225] are actually quite common. Smaller vessels and even entire capillary beds have also been reconstructed successfully [175,226–228]. However, most studies involve organs other than the cochlea, are usually on non-human species, and generate reconstructions that are suitable for visualisation but do not meet the more stringent requirements for finite element (FE) modelling.

The absence of vasculature in existing VCMs of the cochlea suggests that there may be technical barriers to incorporating them. Perhaps the foremost concern is spatial resolution because most of the vessels in the cochlea are quite narrow (see Table 4.2). The inherent trade-off between resolution and field of view during the scanning process may make it difficult to see the entire vascular tree [175,227]. This is particularly problematic for human cochleae simply because of their relatively large size [64].

Another problem is that of contrast. Müller found that even with the resolution advantages of synchrotron radiation-based microCT, the difference in absorption between the blood vessels and their surrounding tissues was very small, so the use of appropriate contrast agents is required [227]. Associated with this is a need for a reliable staining protocol, made difficult in the cochlea by the lack of physical access to the site. Even perfusion-based methods cannot guarantee that the vessels will show up in the scans with complete connectivity [227, Fig. 5].

If these imaging challenges can be overcome, then a viable FE model of the vascularised cochlea may be possible. This would address the existing knowledge gap and provide a greater understanding of the role played by the cochlear vessels during electrical stimulation, which may in turn reveal further insights into the variability between cochlear implant (CI) recipients, or help to improve future intracochlear electrode array designs and surgical techniques.

7.2 Method

Previous investigations of the cochlear vasculature have made use of a technique known as *vascular corrosion casting* [229,230]. This involves injecting a polymer into the bloodstream, which solidifies *in vivo*. The organ of interest is then extracted from the body and the surrounding tissue is removed using a corrosive chemical, revealing the hardened polymer in the shape of the underlying blood vessel network [231]. These are then typically imaged using *scanning electron microscopy* (SEM).

Although such SEM images are great for illustrating the morphology of vascular networks, they only provide a 2D view of the anatomy. In order to create a 3D reconstruction, a volumetric dataset is more appropriate. Mondy detailed how computer models might be obtained from a vascular corrosion cast using microCT [175, 232]. Unfortunately, that methodology results in a free-standing vascular tree model, which is not integrated with the surrounding tissues and cannot therefore be used to study the volume conduction problem.

7.2.1 MicroCT Imaging with Microfil

To overcome these limitations, a new imaging protocol was developed in the hopes of obtaining a scan that was suitable for a complete reconstruction of the cochlea. A collaboration

was established with Ian Curthoys from the School of Psychology and Christopher Wong from the Australian Centre for Microscopy and Microanalysis (ACMM), both at the University of Sydney. The general idea was to fill the blood vessels of the guinea pig cochlea with a radiopaque polymer, similar to the corrosion casting methods. Instead of eroding the surrounding tissues however, the specimen would be scanned with all tissues intact.

Perfusion

The guinea pig perfusion was conducted according to the standard ethics approval (University of Sydney Animal Ethics Committee approval L29/4-2010/3/5266). The animal was deeply anaesthetised with Nembutal and perfused with 400 mL of saline containing heparin, followed by 500 mL of phosphate buffered Karnovsky's fixative (3.5% paraformaldehyde and 0.5% glutaraldehyde). This perfusion technique has been shown to cause minimal distortion to the delicate cochlear membranes at the electron microscope level [233].

At the same time, the injection compound was prepared. In this case, Microfil by Flow Tech Inc. was used. This compound was selected for its radiopacity, which allowed it to serve as a contrast agent for microCT imaging. The yellow MV-122 variant was procured as a kit and approximately 20 mL of the compound was prepared according to the standard mixing procedure (see Appendix D).

The chest of the guinea pig was opened and the heart was exposed. A cannula was inserted into the left ventricle and the descending aorta was clamped. The curing agent was then added to the mixture of MV-122 and diluent and the Microfil was injected into the cannula after ensuring that there were no air bubbles in the syringe. The animal was left in place overnight to allow the Microfil to set. After this, the temporal bone was removed (see Figure 7.2) and wrapped in parafilm with phosphate buffer solution.

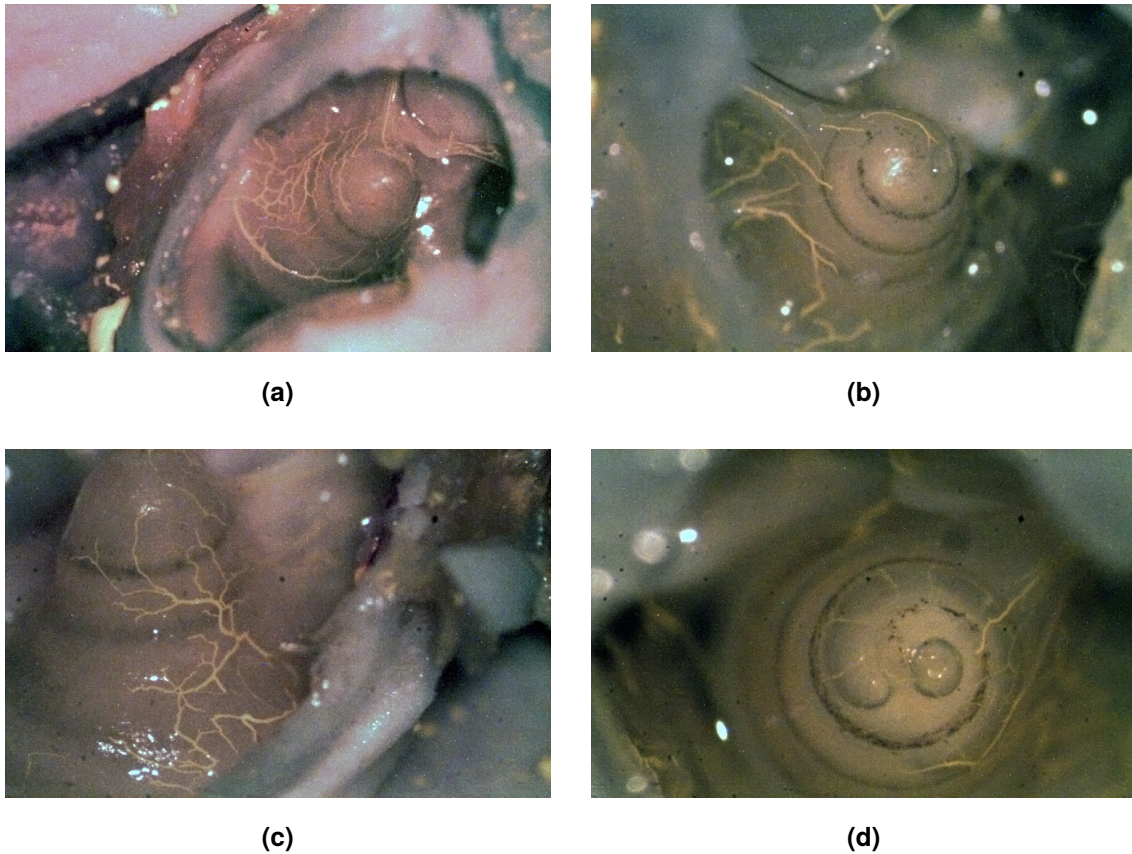


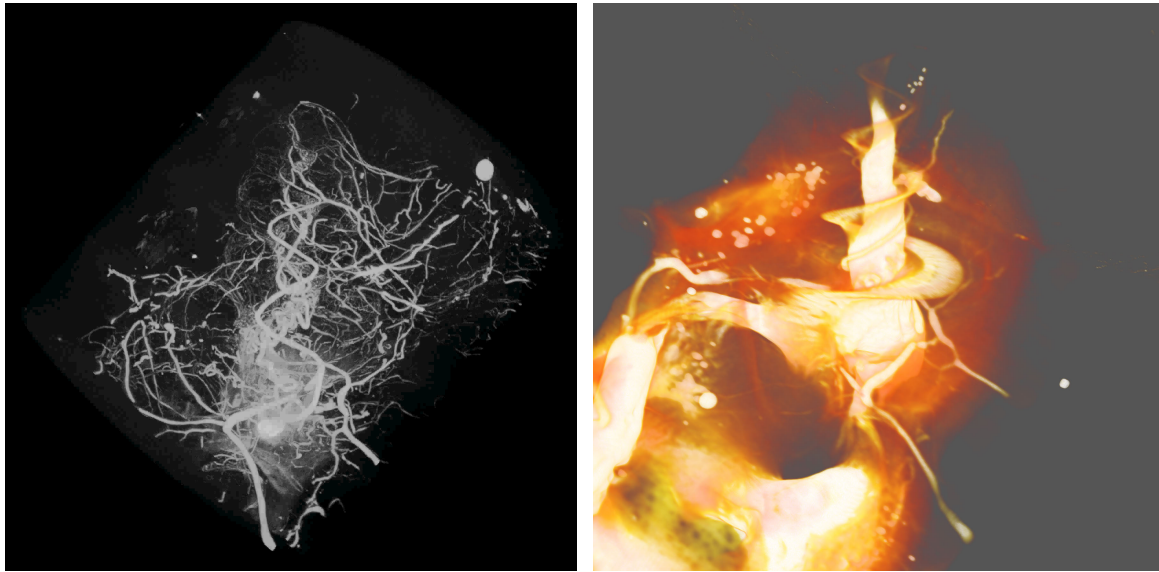
Figure 7.2: Perfusion of the guinea pig cochlea using Microfil (yellow). The compound appears to have filled most of the vessels along the surface of the bone at the very least. (a) The perfused cochlea within the exposed tympanic bulla; (b) the apex of the perfused cochlea; (c) the vessels along the outer surface of the otic capsule; (d) the radiating arterioles at the apical turn. The Microfil in the radiating arterioles suggests that the modiolar vessels were also successfully perfused.

Imaging

The wrapped specimens were attached to holders and placed within the scanning chamber of an Xradia MicroXCT-400 (Xradia, CA, USA; recently bought out by Zeiss). To ensure optimal acquisition of the images through the utilisation of maximum dynamic range, the scanning parameters for each specimen were individually optimised. For the actual acquisition of the 3D dataset, the specimens were scanned incrementally over 360 degrees in steps of approximately 0.2 degrees for a total of 1800 x-ray images. In general, the exposure time for each image was about 30–40 seconds. The tomographic dataset was then reconstructed using the local hardware-based back projection reconstruction software supplied by Xradia. This produced a 16-bit, $1024 \times 1024 \times 1024$ voxel image stack with a resolution of 11 μm in each direction.

Initial scans lacked contrast between the tissues, so additional staining was performed. Both the oval window and a semicircular canal were penetrated to facilitate diffusion of the stains through the volume. The specimens spent up to 6 days in ethylenediamine tetra-acetic acid (EDTA) for bone decalcification [234] and another 2 days in osmium tetroxide (OsO_4) to enhance the soft tissues [235]. Typical scan results are shown in Figure 7.3.

The protocol was able to produce a spectacular and insightful map of the cochlear vasculature, and the results presented here represent the first time the cochlear vasculature has been imaged in microCT with such detail *in situ*. However, a couple of shortcomings ultimately ruled out reconstruction using this dataset. Figure 7.3 shows that despite the care taken throughout the experiment, some of the vessels appeared to be disconnected, potentially due to microbubbles or clotting. The microCT images were also not as clear as the alternative sTSLIM dataset (which were received part way through this experiment) for showcasing all of the cochlear tissues. Although segmentation of the blood vessel network would have been substantially



(a) After 6 days in EDTA

(b) After another 2 days in OsO₄

Figure 7.3: Visualisation of the vascular network in the guinea pig cochlea. (a) Reconstruction of the vessels only using the Xradia software, showing that the vascular tree was extensive but not perfectly perfused. (b) Volume rendering in Amira after additional soft tissue staining shows the VST spiralling around the cochlear nerve trunk.

quicker with the Microfil data, it was judged that a better overall model could be achieved by using the sTSLIM scans.

7.2.2 Reconstruction from sTSLIM

The sTSLIM data, as discussed previously in 4.4.2, provided an ideal combination of resolution and clarity, and revealed an unprecedented amount of structural detail. However, it was difficult to ascertain the locations of the cochlear vessels from the images themselves because previous reports [49, 57] were largely schematic—they did not illustrate the vessel trajectories in the context of the surrounding tissues clearly, nor did they reveal their true (often convoluted) shape. With the microCT map of the vessels serving as a reference, the cochlear vessels could be segmented from the sTSLIM images with more certainty. In this

way, the high resolution sTSLIM images were combined with the high contrast microCT data to enable a more accurate reconstruction of the vascularised guinea pig cochlea.

In terms of practicality, two simplifications were made. The first was that only the larger blood vessels were segmented, because it was likely that the finer branches of the vascular tree, especially those further from the current source, would only have a small effect on volume conduction. In order to test this hypothesis, three levels of detail were modelled:

BV0 No blood vessels, analogous to existing VCMs.

BV1 Major vessels only, i.e. the SMA, VST, vestibulo-cochlear vein (VCV), and the vein of the cochlear aqueduct (VCAQ).

BV2 Major vessels with visible primary branches, including the “vascular spring-coils” [55] or glomeruli [236] extending from the SMA, and the vein of the round window (VRW).

These three cases are illustrated in Figure 7.4. For each case, the blood vessels were segmented independent of the other cochlear tissues (i.e. as separate layers), and only the relevant masks for each level of detail were made visible during the surface reconstruction process in ScanIP. This allowed for a *ceteris paribus* comparison of the VCM with and without blood vessels. An attempt was made at including the radiating arterioles because their trajectories could be discerned in the sTSLIM images. Unfortunately the arterioles were only a few voxels wide in the images, which made them extremely difficult to segment accurately. Given that this would have complicated the subsequent discretisation steps, it was decided not to include them in this study.

The second simplification was that the vessel walls were ignored. The main reason for this was that they could not be distinguished clearly in the sTSLIM images. Even if they could be segmented, they would be extremely difficult to discretise. Considering that the resistivity of blood vessel walls has been estimated to be about two to four times that of blood [191],

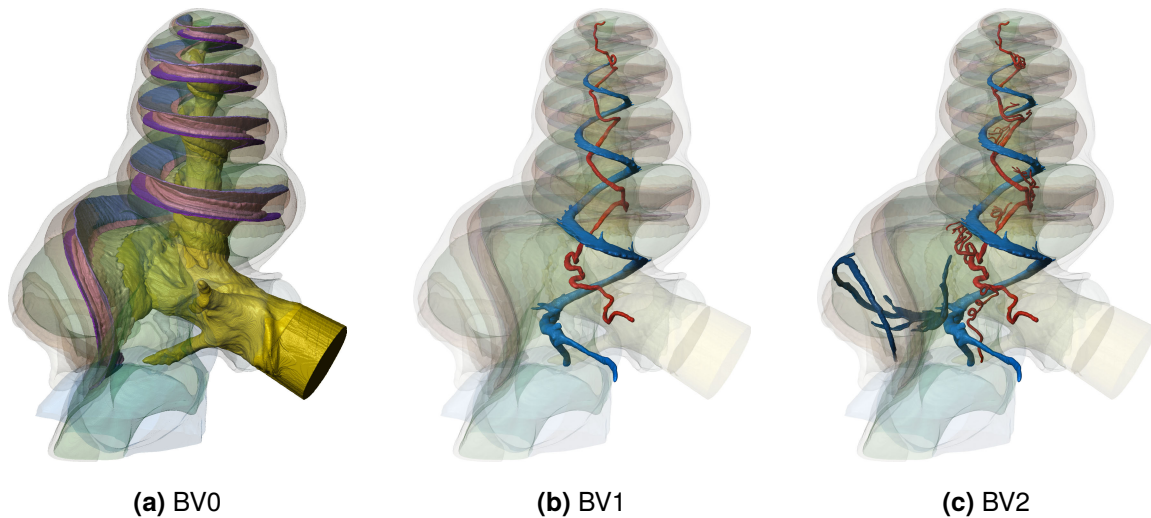


Figure 7.4: Levels of detail for the vascularised reconstruction. (a) The unvascularised model (BV0); (b) the model with major vessels only (BV1); (c) the model with major vessels in addition to some primary branches (BV2).

which would put their electrical response close to that of the surrounding tissue, and that they are thin relative to the lumen (which are already quite narrow), the vessel walls were not expected to have a large effect.

The simulations for this study were set up as in previous investigations, with material properties per Table 4.14, a 1 mA current source injected at electrode E4, and the voltage offset boundary condition applied at the temporal bone surface.

7.3 Results

7.3.1 Degrees of Freedom and Solution Times

Unsurprisingly, the number of degrees of freedom (DOFs) increased with the amount of vascular detail as shown in Table 7.1. Using quadratic discretisation, the unvascularised model resulted in just over 5 million DOFs. Adding the main vessels and additional branches

Table 7.1: Degrees of freedom and solution times for the vascularised models.

Level of detail	Degrees of freedom	Solution time
BV0	5,132,816	21 mins 54 secs
BV1	6,277,592	27 mins 23 secs
BV2	7,140,772	31 mins 17 secs

required another 1.1 million and 900,000 DOFs respectively. Solution times using the Conjugate Gradient solver were quite reasonable, with all three simulation cases completing in about 80 minutes.

7.3.2 Voltage along the Array

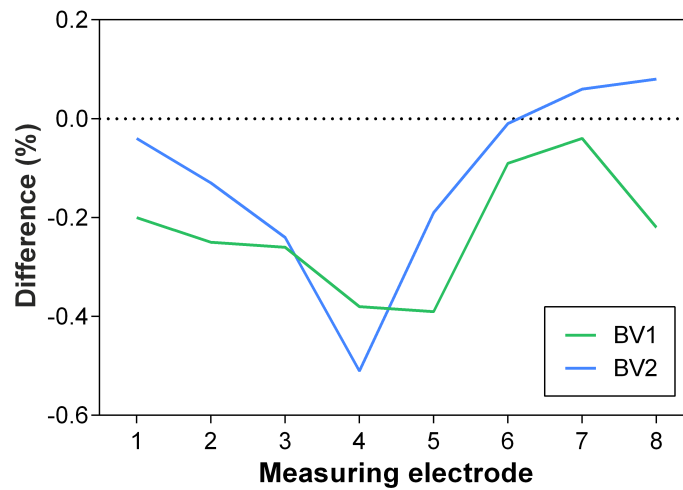
Voltages measured along the intracochlear electrode array were highly insensitive to vascular detail. A plot showed the traces as overlapping, so the data were tabulated (Table 7.2) and the deltas plotted (Figure 7.5). These show there was very little difference between the three cases, with average deltas of only -0.23% and -0.12% for BV1 and BV2 respectively relative to the unvascularised BV0 case. In fact, the largest delta at any point was only -0.51%, observed at the stimulating electrode E4 in the BV2 case, well below the Frijns sufficiency criterion [100] used previously.

7.3.3 Current Pathways

Adding vasculature to the model only appeared to have a small effect on the conduction pathways as well. The streamlines in Figure 7.6 show that the apical exit pathways moved slightly towards the modiolus when vascular pathways were included, but the overall pattern was largely similar between the BV0 and BV2 cases. This is likely because the effects

Table 7.2: Voltages along the array. Percentage differences were calculated relative to BV0.

Electrode	BV0	BV1		BV2	
	Voltage (V)	Voltage (V)	Δ (%)	Voltage (V)	Δ (%)
E1	1.3947	1.3919	-0.20	1.3941	-0.04
E2	1.4683	1.4646	-0.25	1.4664	-0.13
E3	1.6261	1.6219	-0.26	1.6222	-0.24
E4	2.3322	2.3233	-0.38	2.3203	-0.51
E5	1.6090	1.6027	-0.39	1.6060	-0.19
E6	1.4605	1.4592	-0.09	1.4603	-0.01
E7	1.4152	1.4146	-0.04	1.4161	0.06
E8	1.4261	1.4229	-0.22	1.4273	0.08
Average			-0.23		-0.12

**Figure 7.5:** Effect of vascular detail on intrascalar voltages. Percentage deltas are relative to BV0 as per Table 7.2.

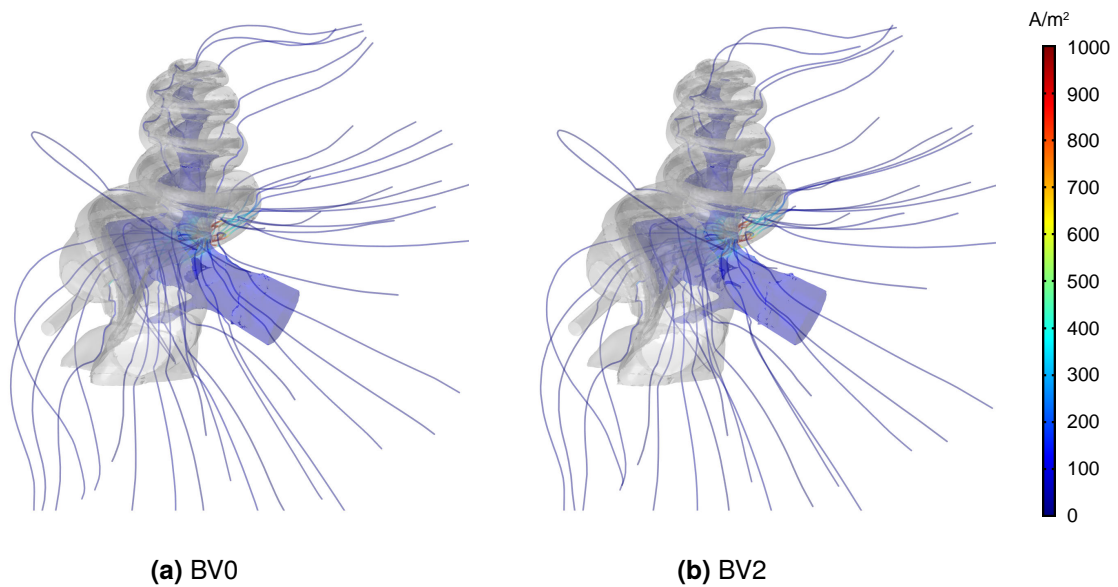


Figure 7.6: Comparison of exit pathways. There was very little difference between the two cases. Current appeared to veer slightly closer to the modiolus due to the lower resistance posed by the blood vessels, especially towards the apical end.

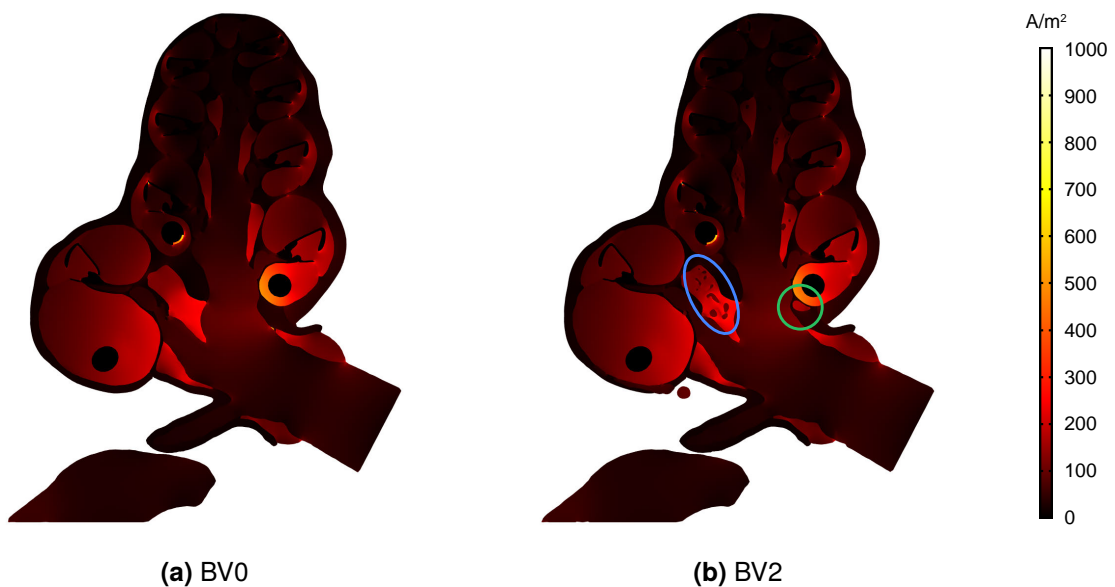


Figure 7.7: Comparison of current density heatmaps. The BV2 case shows current density that is elevated in some regions (e.g. the VST, circled in green), but lower in others (e.g. vessels in the CSF, circled in blue). Note that the current source is behind the mid-modiolar slice shown here.

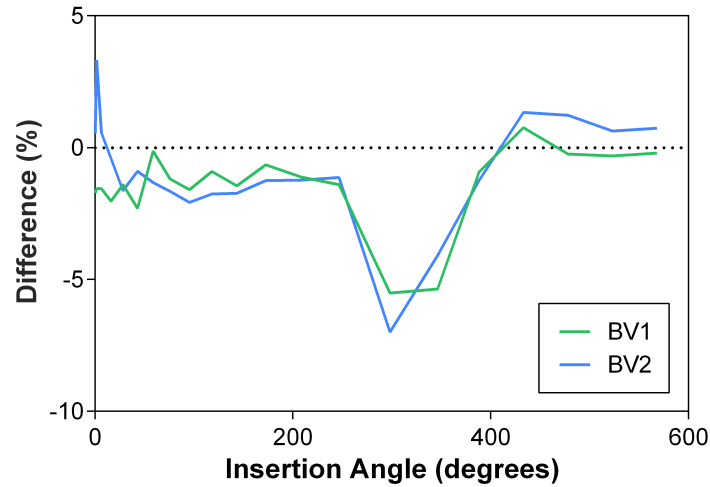


Figure 7.8: Effect of vascular detail on current density in Rosenthal's canal. Percentage deltas are relative to BV0 as per Table 7.3.

were predominantly localised to the regions near the blood vessels, as shown in Figure 7.7. Changes in the current distribution depended on the tissue surrounding the vessel. Those passing through bone saw an increase in local current density due to the lower resistivity of blood. Vessels passing through cerebrospinal fluid (CSF) experienced the opposite because the surrounding tissue was more conductive.

It was of particular interest to see how the current density in neural structures was affected. The current density in Rosenthal's canal (JRC) for the three test cases is tabulated in Table 7.3 and the deltas plotted in Figure 7.8. JRC was more sensitive to the vascular detail than suggested by the previous results for voltage profiles and exit pathways. Peak JRC values were 0.90–1.76% lower than in the unvascularised model. More dramatic changes were seen at an insertion angle of 298 degrees, half a turn deeper than the stimulating electrode, where the deltas were 5.5–7%. The average change over all sample points was less than 1.5%, indicating that the differences were quite localised. For the most part, the vascularised models predicted lower JRC values than the unvascularised model, adding weight to the view that blood vessels are a preferred pathway.

Table 7.3: Current density in Rosenthal's canal. As before, the deltas were calculated relative to BV0.

Insertion angle (Degrees)	BV0		BV1		BV2	
	JRC (μm^2)	JRC (μm^2)	Δ (%)	JRC (μm^2)	Δ (%)	
0	56.95	55.973	-1.72	57.251	0.53	
1.5	51.781	50.971	-1.56	53.505	3.33	
6.3	46.074	45.356	-1.56	46.335	0.57	
16.2	42.43	41.57	-2.03	42.26	-0.40	
28.1	43.492	42.882	-1.40	42.783	-1.63	
42.9	60.757	59.358	-2.30	60.215	-0.89	
58.7	91.911	91.79	-0.13	90.7	-1.32	
75.9	145.66	143.94	-1.18	143.24	-1.66	
95.5	238.57	234.78	-1.59	233.62	-2.07	
118.1	288.85	286.25	-0.90	283.78	-1.76	
143.4	189.16	186.41	-1.45	185.89	-1.73	
172.5	114.18	113.44	-0.65	112.75	-1.25	
208.1	69.819	69.045	-1.11	68.961	-1.23	
246.7	38.813	38.271	-1.40	38.375	-1.13	
298.1	32.843	31.033	-5.51	30.547	-6.99	
346.4	27.583	26.105	-5.36	26.454	-4.09	
388.1	26.301	26.056	-0.93	25.972	-1.25	
433.1	31.407	31.646	0.76	31.828	1.34	
478.1	34.833	34.749	-0.24	35.26	1.23	
523.1	31.854	31.756	-0.31	32.054	0.63	
568.1	28.057	28	-0.20	28.264	0.74	
Average			-1.47		-0.91	

7.3.4 Activating Function

Variations in neural current density and current pathways were both small when measured independently. However, the likelihood of excitation as measured using the activating function (AF) was more substantial because it effectively considers both quantities in tandem. AF results for all three cases are given in Figure 7.9, and once again, there were indications of localised differences along the neural sheet. The region nearest to the stimulating electrode saw a substantial increase in depolarisation at the nodes of Ranvier immediately neighbouring the VST. The nodes slightly further out from there saw a mild reduction in depolarisation. Deeper nodes from more apical axons one turn away also experienced a large increase in AF, highlighting the importance of considering the 3D structure of the cochlea. In both of these regions, the level of depolarisation was slightly shifted towards the axonal end, as expected given the location of the VST and its effect on the local current paths.

To quantify the overall level of activity, the root mean square (RMS) value of AF was calculated for each case. Differences in these RMS values, reported in the delta plots in Figure 7.9, confirmed that the general pattern was mostly unchanged, with deltas below 1.5%. Both vascularised cases predicted a net reduction in overall depolarisation compared with the unvascularised model. The AF trend from BV0 to BV1 was slightly reversed by the additional detail of BV2, indicating that the changes are not due to volume of tissue alone. However, in the region closest to the stimulating electrode, the marginal impact of additional vasculature always increased the AF.

7.4 Discussion

Due to the historical development of cochlear models, with lumped element models (LEMs) evolving into VCMs as technology progressed, many studies have framed the question of

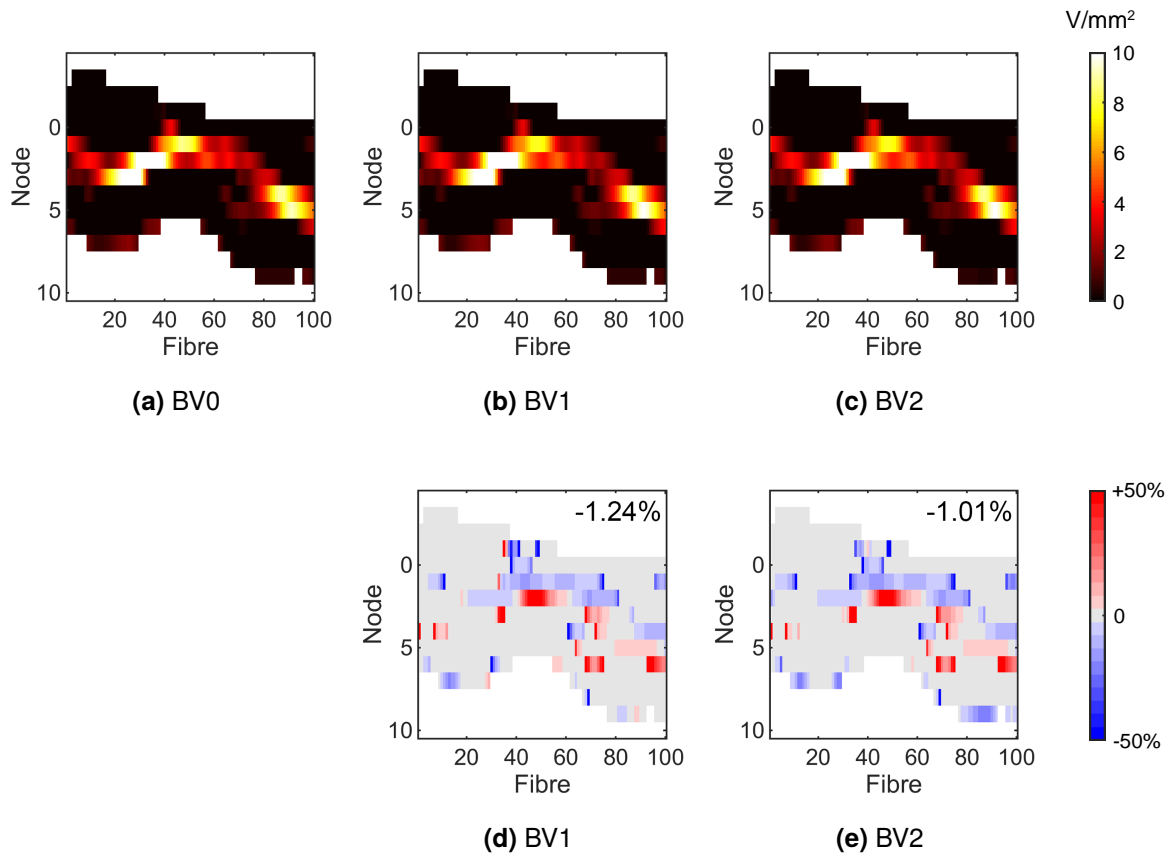


Figure 7.9: Effect of vascular detail on the activating function. Absolute value of the computed AF for (a) the unvascularised case, (b) with the main vessels, and (c) with the additional branches. Percentage differences along the neural sheet (relative to BV0) are also shown for the latter two cases in subfigures (d) and (e), with RMS deltas in the top right corner. It appears that the presence of the main modiolar vessels has a funnelling effect on nearby current, leading to more depolarisation in the neural tissue immediately surrounding it. The effect is very localised but can affect the axons of more apical neurons as they pass through the region of influence. Additional fine detail had little marginal impact in this study.

current flow through the tissues as “either/or” in nature. Unlike in an electrical circuit though, where current is restricted to flowing through wires and elements, current in the cochlea flows volumetrically and can pass in and out of tissues at any point, with the actual path determined by the overall spatial distribution of the conductive medium. As such, there is no single tissue that can be thought of as *the* exit pathway, and in determining the role of the cochlear vasculature, it is worth considering both local and global perspectives.

7.4.1 Local Effects

From the results, it was clear that the AF is more sensitive to the presence of the vasculature than suggested by the negligible changes in intrascalar voltages. The difference in resistivity between the blood and the immediately surrounding tissue was a key driver of the local current distribution. Streamlines emanating from the stimulating electrode were densest near the electrode itself, so the major vessels in the nearby modiolus had the strongest influence on the results, as predicted by Baker [103].

For insertions in the scala tympani, the vessel of primary interest was the VST, which lies in the modiolar wall where it meets the floor of the scala tympani. The presence of the VST diverted some of the current that normally flows through the spiral ganglion cells. This shift in the local pathway indicated that the blood provided a lower resistance alternative. It reduced the level of depolarisation at nodes of Ranvier nearest the spiral ganglion while elevating depolarisation at nodes further down the axon (see Figure 7.9). The differences were smaller toward the basal end but neurons from more apical turns were affected because their axons passed through the region of influence. More advanced neural excitation models may be sensitive to the changes brought on by the inclusion of the blood vessels.

A corollary of these findings is that the presence of the cochlear vasculature has a greater impact in simulations with modiolar-hugging electrode arrays than those with more lateral

designs. Current injected nearer to the modiolus is more likely to encounter and be diverted by the VST, so optimising the alignment of the platinum pads relative to the modiolus (e.g. by changing the orientations of the exposed platinum surfaces and/or ensuring that they are slightly angled towards the apex during insertion) may increase current flow and depolarisation in the spiral ganglion cells, and could potentially reduce ectopic stimulation of more apical fibres. Further simulations would need to be conducted before such effects can be confirmed.

Insertions in the scala vestibuli are less common in clinical practice and were not directly studied here. However, given the simulation results, it can be expected that the SMA and its branches would be the key vessels to consider in those cases. The impact is expected to be weaker than that observed in scala tympani insertions because although the arteries still lie between the scala and the nerve tissue, they are thinner, more distant from the scala, and are surrounded by the highly conductive CSF.

7.4.2 Global Effects

The study demonstrated that in general, the blood vessels have little bearing on the dominant patterns in the cochlea. Voltages in the scala tympani exhibited negligible change, which may have attributed to early experimental findings that the vasculature could be ignored. Both voltages and JRC were slightly lower in the vascularised models (Tables 7.2 and 7.3), which was expected because the vessels have a lower resistivity than their surrounding tissues. RMS values for the AF also did not change much beyond the regions of the neural sheet near the current source. This provides some affirmation for existing cochlear models that have omitted the vascular structures.

The only substantial changes in regions further from the stimulating electrode were almost exactly half a turn away in the apical direction (Table 7.3). This can be explained by the

current flowing in that direction encountering more of the modiolar vessels, with a cumulative effect from the localised distortions in current density. However, JRC and AF magnitudes were significantly lower there than at the peak, so the absolute deltas are not expected to result in large changes in neural excitation at those neurons. On a related note, there appeared to be a correlation between JRC and AF in these data. This provides some support for the finding by Åström *et al.* that computational neuron models may not be required for predicting excitation in certain types of investigations [118].

These findings may be relevant to other neuroprosthetic devices that involve electric current injection in close proximity to vascular structures, such as subretinal or suprachoroidal retinal prostheses [237]. *In silico* studies of those implants would be advised to include the larger vascular structures at the very least as part of the anatomical reconstruction.

7.4.3 Study Limitations

Aside from the issues mentioned previously under §6.4, the main limitation specific to this study is that of detail. Most of the vessels that were included in this study were located in the modiolus because the larger size of these vessels made them relatively easy to segment and mesh, and their proximity to both the current source and the neural structures justified the effort required to reconstruct them. However, Figures 2.9 and 7.3 illustrate that the modelled vascular tree was far from complete. With time, it may be possible to include the radiating arterioles in addition to other peripheral vessels, and perhaps also model the vessel walls using simple mask dilation techniques (only the lumen is represented in these models). However, judging from the results of this study, it would seem that the additional time and computational resources required to produce and analyse a vasculature-complete model is not warranted.

7.5 Conclusions

The addition of the cochlear vasculature did not have a large effect on the modelling outputs, with the exception of the large vessels in the modiolus where a strong local effect was observed. In particular, the vein of the scala tympani was shown to have a substantial impact on activating function in the surrounding neural tissue due to its large size and close proximity to the current source. It diverted some of the injected current away from the spiral ganglion, which caused changes in the activating function distribution along the neural sheet. In that sense, the vascular pathways offered a preferred low resistance pathway over the nerve tissue in that region.

Considering the substantial additional effort required to incorporate the vascular structures and the overall small impact on the end results, it is recommended that future models wishing to add vascular detail focus their efforts on the vein of the scala tympani only. The localised changes arising from this vessel alone may prove important for more sophisticated models of neural excitation.

Chapter 8

Incorporating Time-Dependent Effects into Models of the Cochlea

This chapter addresses the following questions:

- Are time-dependent effects important in volume conduction?
- How could these effects be modelled?
- What are the implications of these effects?

8.1 Introduction

All of the volume conduction models (VCMs) discussed in §3.3.2 are different in terms of appearance and methodology, yet they share the key assumption of *quasi-stationarity*. Quasi-static models have in fact been used in most electrophysiological studies [238], enabling the use of relatively simple stationary (i.e. time-independent) formulations. If valid, this

assumption implies that all field components in the system will be synchronous and greatly reduces computational requirements.

However, the quasi-static assumption should only be invoked if a number of conditions are met. According to Plonsey [238], these are:

- Propagation can be neglected.
- Capacitive effects can be neglected.
- Inductive effects can be neglected.
- The system is bounded by a region of zero conductivity.

The weakest of the four conditions is that capacitive effects can be neglected or, equivalently, that the conductivity of the medium dominates its behaviour [238]. This is only true if:

$$\frac{\omega\epsilon(\omega)}{\sigma(\omega)} \ll 1 \quad (8.1)$$

where $\omega = 2\pi f$ is the angular frequency of the stimulus, ϵ is the absolute permittivity of the medium, and σ is the conductivity of the medium [238]. Here, the “ \ll ” comparator is interpreted as requiring a reduction of at least one order of magnitude. It is important to note that the conductivity and permittivity of materials is a function of frequency, especially for biological tissues [141, 167, 239].

Equation 8.1 can also be written as:

$$\frac{\omega\epsilon_0\epsilon_r(\omega)}{\sigma(\omega)} \ll 1 \quad (8.2)$$

where ϵ_0 is the permittivity of free space, and ϵ_r is the relative permittivity of the medium. Equation 8.2 will henceforth be referred to as the quasi-static criterion (QSC).

Existing models of the implanted cochlea have all assumed that the cochlear tissues are purely resistive in order to satisfy the QSC. There are a few reasons for this, beginning with the fact that the fundamental frequency of the input pulses used in cochlear implant (CI) systems is relatively low, typically around 10–20 kHz [29]. At these frequencies, conductive effects are expected to dominate [75]. Early experimental work seemed to support this: von Békésy reported observing no capacitive component when measuring impedances with a 1000 Hz pure tone stimulus [106], and Spelman demonstrated minimal phase lag in his experiments with broadband (8–12,500 Hz) white noise current waveforms in the scala tympani of the guinea pig [98]. Spelman concluded that the system is primarily resistive in nature, and his paper is often cited as justification for using purely resistive material models (see, for example, Girzon [20], Finley [144], Frijns [100], and Hanekom [155]).

However, it is well known that biological tissues are not purely resistive. The presence of proteins and amino acids in the fluids of the inner ear (cf. Table 2.1) endows them with a small capacitive component [75]. The other two dominant tissues in the inner ear, bone and nerve, which have been found to be major determinants of the current pathways, both have well documented dielectric responses [69, 167, 216]. Blood is also capacitive due to the cell walls of erythrocytes and proteins in the plasma [75].

While the frequency-dependent conductivities and permittivities of more general bodily tissues have been measured, there is no permittivity data for cochlear-specific tissues, and measurements of the conductivity values have only been performed in a narrow range of frequencies. This has been the biggest barrier to performing time-dependent cochlear studies *in silico*. Data that is available for general tissues can provide some guidelines though. The IT'IS Foundation database [240] is the most comprehensive source of dielectric tissue properties at the time of writing. This database consolidates the data of Geddes and Baker [133], Gabriel *et al.* [167, 194, 195], and many others into an interactive online compendium, building upon the earlier work of Andreuccetti [241].

Table 8.1: Quasi-static criterion values for some comparable tissues at both 10 kHz and 10 MHz. The frequency-dependent tissue properties were sourced from the IT'IS Foundation database [240]. For most tissues, the criterion is not substantially less than one at the higher frequency as per Equation 8.2.

Tissue	Quasi-static criterion	
	10 kHz	10 MHz
Bone (cortical)	0.01424	0.47834
Bone (cancellous)	0.01118	0.32023
Nerve	0.46710	0.38668
CSF	0.00003	0.03032
Blood	0.00417	0.14161
Tendon / ligament	0.00770	0.14044

Table 8.1 shows the QSC calculated for some of the tissues in the database that might be applied to models of the cochlea. At a frequency of 10 kHz, the QSC values for most tissues are less than 0.015, which suggests that the quasi-static assumption is reasonable. However, the QSC for nerve tissue is not substantially less than unity. The criterion is directly proportional to frequency, and at 10 MHz the values for most tissues are much higher. At this higher frequency, only cerebrospinal fluid (CSF) satisfies the QSC.

There are two main implications of these data. The first is that higher frequency components of the stimulus may play a non-trivial role in determining the field quantities. Higher frequency components are seen in clinical practice because CIs deliver charge into the cochlea using square, biphasic, constant-current pulses (see Figure 3.5). The biphasic nature of the stimulus means it is an alternating current (AC) signal, and its square shape means that it is not a pure tone but a combination of the fundamental frequency and higher frequency harmonics, as revealed when considering its Fourier transformation. These high frequency components are important in describing the relatively sharp rising and falling edges [166, 242]. Therefore, the stimulus should not be modelled as a simple direct current (DC) signal.

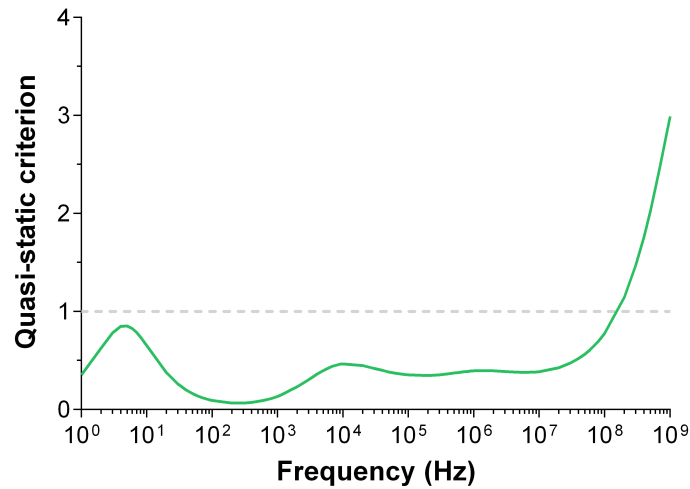


Figure 8.1: Quasi-static criterion for nerve tissue, up to 1 GHz. The values vary with frequency and are generally not significantly less than unity (dashed line).

The second implication draws from the relatively high QSC value for nerve regardless of frequency as shown in Figure 8.1, which indicates that quasi-stationary results are not valid in those regions. This is worrisome for VCMs with coupled neural models because they assume that the extracellular potential in the nerve tissue is time-invariant [119]; the high QSC value suggests that the electric field does change over time. Since neural excitation is a function of voltage differences in the nerve tissue, fluctuations in the extracellular potential may have a large impact on predictions of neural excitation, depending on the sensitivity of the model. Despite concerns from early studies that purely resistive models of the cochlea should only be considered as a first approximation [100, 144, 155], no subsequent studies have properly considered the validity of this assumption.

As such, the aim of this chapter is to address this long-standing concern by exploring the feasibility of performing time-dependent simulations of the implanted cochlea, documenting observed differences between otherwise equivalent quasi-static and time-dependent models, and extrapolating how these differences might affect the predictions in both this and other modelling efforts. Some early work on this topic, based on an updated iteration of the proof

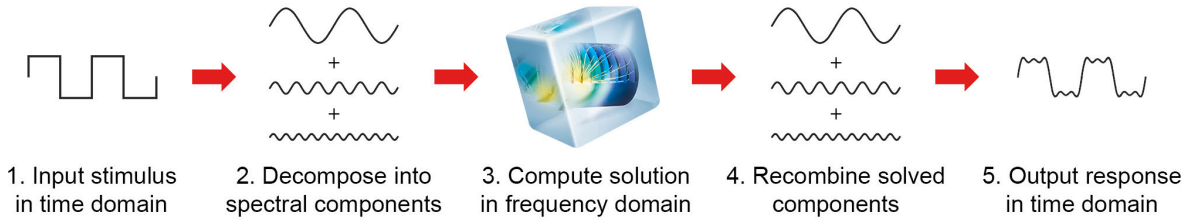


Figure 8.2: Schematic of the solution process for time-dependent simulations. The time-domain stimulus was decomposed into its spectral components via a Fourier transformation. The response at each frequency was analysed in COMSOL, and the outputs later recombined to obtain the corresponding transient response. (Copyright © 2015, IEEE.)

of concept model, was published at the IEEE Conference on Neural Engineering 2015 [198].

A refined methodology has been applied to the guinea pig model for the present study.

8.2 Method

In order to model time-dependent effects, the stimulating pulse was converted from the time domain into its equivalent frequency-domain representation via Fourier analysis (as suggested by Plonsey [238]) before the numerical solution. The model was then set up and solved across the range of frequencies in COMSOL, after which the field results were reconstructed in MATLAB to produce a time-domain signal representing the dynamics of the field interactions. This procedure is illustrated schematically in Figure 8.2.

8.2.1 Fourier Expansion of the Stimulating Pulse

Consider a periodic time-domain signal with period $2L$. This function, $F(t)$, can be decomposed into its Fourier components, given by:

$$F(t) = \sum_{n=0}^{\infty} a_n \cos n\omega t + b_n \sin n\omega t \quad (8.3)$$

$$\begin{pmatrix} a_n \\ b_n \end{pmatrix} = \frac{1}{N_n} \int_0^{2L} F(t) \begin{pmatrix} \cos n\omega t \\ \sin n\omega t \end{pmatrix} dt \quad (8.4)$$

where n is a non-negative integer, ω is the *fundamental frequency* in radians per second, given by $\omega = 2\pi/\text{period} = \pi/L$, and the normalisation factor is $N_n = L(1 + \delta_{n0})$, with δ being the Kronecker delta function [242].

If $F(t)$ is an odd function, $a_n = 0$, so the Fourier series reduces to a pure sine expansion and Equations 8.3–8.4 become:

$$F(t) = \sum_{n=1}^{\infty} b_n \sin n\omega t \quad (8.5)$$

$$b_n = \frac{1}{N_n} \int_0^{2L} F(t) \sin n\omega t dt \quad (8.6)$$

Equations 8.5–8.6 can be used to simplify the simulation. Consider a biphasic pulse train as illustrated schematically in Figure 3.5. By shifting the phase of the signal such that the midpoint of an inter-frame gap (IFG) occurs at time $t = 0$, $F(t)$ becomes an odd function. Therefore, the original time-domain signal can be approximated by using sine terms only, halving the number of simulations required to compute the solution.

The base case stimulus waveform for the following time-dependent simulations is shown in Figure 8.3. It has a period of 100 μs , giving it a fundamental frequency of 10 kHz. A 25 μs pulse width (PW) is used for both cathodic and anodic phases, separated by an inter-phase gap (IPG) of 10 μs . The amplitude of the pulse is 1 mA. The waveform was programmed into COMSOL parametrically so that the input stimulus could be modified easily. The relevant settings are shown in Figure 8.4.

Although Equations 8.3 and 8.5 stipulate the sum of an infinite number of harmonic terms, the marginal impact of an additional frequency component progressively diminishes. The series

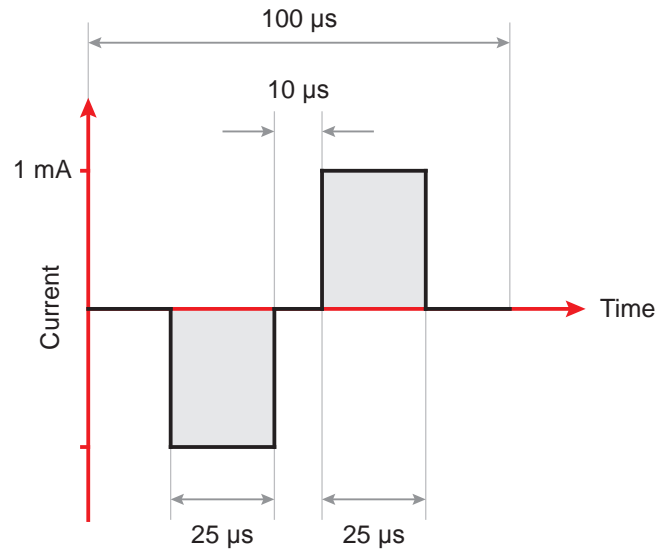


Figure 8.3: The base case stimulus waveform used for the time-dependent simulations. The inter-frame gap is driven by the other intervals, with onset of the cathodic phase occurring at the midpoint of the inter-frame gap to ensure that the function is odd.

does converge, with similar previous studies requiring in the order of 500–5000 harmonics to achieve reasonably-shaped waveforms [198, 243, 244]. However, the overshoot that appears at the discontinuities of $F(t)$ is a result of the non-uniform convergence at those points and cannot be entirely removed [242]—this is known as the *Gibbs phenomenon*. In this study, a total of 5000 harmonics was solved to test for convergence. The corresponding frequency range extended up to 50 MHz.

An analytic function describing the stimulus waveform was then applied as the input current at electrode E4. Since the simulations were performed using the guinea pig model, the overall amplitude was set to 1 mA. As the frequency sweep stepped through each harmonic in the specified range, the system was solved with the weighted input current specific to that harmonic frequency. The model was grounded at the temporal bone surface because the voltage offset boundary condition was based on a full 1 mA stimulus and thus inappropriate for lower magnitude current components.

Settings
Parameters

Parameters

Name	Expression	Value	Description
period	100e-6 [s]	1.0000E-4 s	Period of biphasic pulse
L	period/2	5.0000E-5 s	Half-period of biphasic pulse
PW	25e-6 [s]	2.5000E-5 s	Pulse width
IPG	10e-6 [s]	1.0000E-5 s	Inter-phase gap
IFG	2*L-2*PW-IPG	4.0000E-5 s	Inter-frame gap
w0	pi/L	62832 1/s	Fundamental frequency (angular)
t1	IFG/2	2.0000E-5 s	Phase 1 leading
t2	t1+PW	4.5000E-5 s	Phase 1 trailing
t3	t2+IPG	5.5000E-5 s	Phase 2 leading
t4	t3+PW	8.0000E-5 s	Phase 2 trailing
N	5000	5000	Number of harmonics

Name:
Expression:
Description:

(a)

Settings
Analytic

Plot Create Plot

Label: Analytic 1

Function name: fourier_coeff

Definition

Expression: $(\cos(w*t2) - \cos(w*t1) - \cos(w*t4) + \cos(w*t3)) / (\pi * w / w0)$

Arguments: w

Derivatives: Automatic

Periodic Extension

Units

Arguments: 1/s

Function: mA

Advanced

Plot Parameters

(b)

Settings
Frequency Domain

Compute Update Solution

Label: Frequency Domain

Study Settings

Frequency unit: Hz

Frequencies: $\text{range}(1/(2*L), 1/(2*L), N/(2*L))$ Hz

Load parameter values: Browse... Read File

Reuse solution for previous step: Yes

Results While Solving

Physics and Variables Selection

Modify physics tree and variables for study step

Physics interface	Solve for	Discretization
Electric Currents (ec) {ec}	✓	Physics settings

Values of Dependent Variables

Mesh Selection

Study Extensions

(c)

Figure 8.4: Parametric implementation of the stimulus waveform in COMSOL. (a) The parameters defining the stimulus waveform; (b) the expression for the Fourier transform; (c) the frequency sweep used in the solution. Temporal and angular frequencies were related by defining a model variable.

Note that the capacitance at the electrode-tissue interface was not incorporated here. This is because the study was more interested in quantities in the tissue, and the current delivered to the tissues would not depend on the polarisation voltage at the electrode surface due to the constant current nature of the stimulus [75]. This does however have a bearing on comparisons with *in vivo* measurements.

8.2.2 Assignment of Frequency-Dependent Material Properties

The model was formulated in the frequency domain, so it was necessary to assign frequency-dependent tissue properties. The main difficulty here was the lack of suitable, cochlear-specific tissue data. As a first venture into this area though, a rudimentary methodology would suffice. The model was previously found to be most sensitive to the resistivities of bone, perilymph, and nerve in the stationary simulations (see Chapter 6). These tissues also made up a majority of the cochlear volume, so it was plausible to assume that these were the key drivers in a time-dependent formulation. The available data for each of these was considered carefully.

For bone tissue, the IT'IS database listed separate entries for cortical and cancellous bone. In light of the morphological differences in the cochlear bone, the conductivity and permittivity of cortical bone were assigned to the denser otic capsule, while the properties of cancellous bone were assigned to the softer modiolar bone. Given that the petrous part of the temporal bone is known to be extremely hard [27, 61], the surrounding bone was also modelled as cortical bone. In a similar fashion, the model domains representing the peripheral processes, spiral ganglion, and auditory nerve trunk were modelled using the listed data for nerve tissue.

The closest candidate for perilymph was CSF. Table 2.1 documents the compositions of the two fluids and reveals that they are remarkably similar, as pointed out by Martini [40]. However, there are substantial differences in their protein content, which is known to have

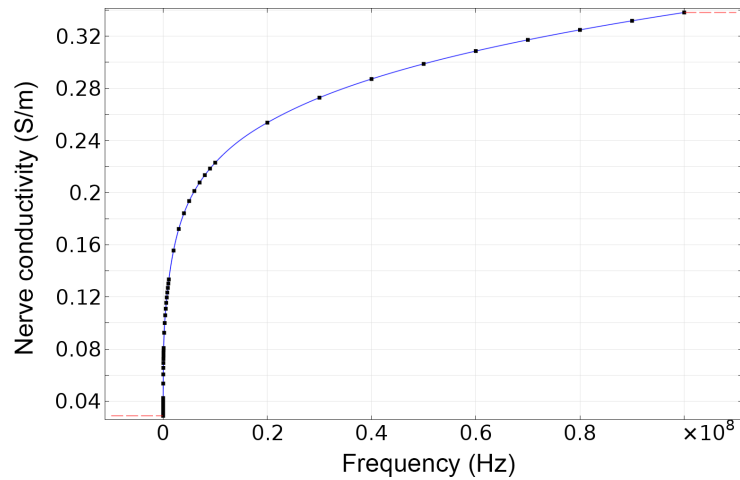


Figure 8.5: Interpolation of nerve conductivity in COMSOL. Data was sourced from the IT'IS Foundation [240].

an impact on electric properties [75]. Due to this uncertainty and the evidence of minimal phase lag in the scala tympani [98], it was decided to retain the assumption of pure resistivity for perilymph, as well as endolymph. The actual CSF in the model was of course assigned with the available material properties.

The other two tissues that were assigned frequency-dependent properties were blood and the spiral ligament. The latter used the value listed for tendon/ligament. Neither are expected to have a significant impact on the result given their comparatively low QSC values, but these values were not low enough to warrant complete omission.

For all of the tissues discussed above, the values for both conductivity and permittivity were pulled from the IT'IS database in the frequency range of 1 kHz to 100 MHz. This provided some leeway on either side of the frequency sweep range used in the model solution. Values between the data points were interpolated in COMSOL using cubic splines, an example of which is shown in Figure 8.5. All other cochlear tissues were modelled as purely resistive as per previous solutions since no better data were available.

8.2.3 Reconstruction of the Time-Domain Signal

Frequency-domain simulation outputs are represented in COMSOL as complex quantities. The quantity values for a single frequency component can be written in modulus-argument form, representing the amplitude and phase of the quantity respectively, as:

$$Z = A \text{ cis } \phi \quad (8.7)$$

where Z is the output quantity, A is the amplitude of the signal, cis is the complex exponential function, and ϕ is the phase. Reconstructing the corresponding time domain signal is simply a matter of summing each frequency component while accounting for the phase shift. Since the input signal was formulated as per Equation 8.5, only sine terms were required for the reconstruction, that is:

$$G(t) = \sum_{n=1}^N A_n \sin(n\omega t + \phi_n) \quad (8.8)$$

where $G(t)$ is the reconstructed signal and N is the total number of harmonics used. The reconstructions for this study were scripted in MATLAB.

8.2.4 Resistive Formulation

In order to provide a more direct comparison with these time-dependent results, a purely resistive counterpart was required. The stationary models from earlier chapters were not used for this because the data sources for some of the tissue properties were different. Instead, a new stationary model was created where those tissues that could be modelled with frequency-dependent values (namely bone, nerve, CSF, blood, and spiral ligament) were assigned their corresponding conductivity values at the fundamental frequency. Relative permittivities for all tissues were set to unity.

Table 8.2: Solution times for the time-dependent model. Note that the mesh was linearly discretised.

Number of harmonics	Solution time
1 (stationary)	1 min 26 secs
100	2 hrs 33 mins
5000	5 days 8 hrs

Since the calculated field quantities are synchronous with the rise and fall of the input current in a purely resistive formulation [238], the temporal waveform was identical in shape to that of the stimulus. The amplitudes were set to the corresponding solution values.

8.3 Results

8.3.1 Solution Times

Since the simulations were solved as a string of stationary analyses (one for each harmonic in the sweep), it was not surprising to find that solution times scaled in a very linear fashion. Representative solution times are listed in Table 8.2. The stationary study with linear discretisation consisted of 793,311 degrees of freedom (DOFs) and took about 1.5 minutes to compute using the PARDISO solver. For comparison, a simulation with 100 harmonics took just over 2.5 hours to complete, while 5000 harmonics took about 5 days and 8 hours.

8.3.2 Convergence of the Stimulus Waveform

Since the overall solution time increased with the number of harmonics used, it was desirable to find a balance between the two that yielded reasonable results. Too few harmonics would

lead to a poorly shaped stimulus (and consequently, poorly shaped outputs); too many would be an inefficient use of computational resources with negligible marginal benefit.

Comparison of Square and Ramped Stimuli

The first test involved reconstructing square biphasic stimuli to varying degrees of accuracy to determine how this affects the shape of the waveform. For the square-shaped biphasic stimulus shown in Figure 8.3, the accuracy of the reconstruction was noticeably improved with more harmonics, all the way up to the 5000 harmonic (50 MHz) cap for which the model was solved. The use of higher harmonics reduced the ripples in the waveform and provided better definition at the leading and trailing edges. Convergence was quite slow, with the signal requiring at least 1000 harmonics before becoming well-shaped. The Gibbs phenomenon overshoot was also shifted progressively closer to the discontinuities; as noted earlier however, the overshoot (approximately 9% in this case) could not be completely eliminated regardless of the number of harmonics used. These differences are illustrated in Figure 8.6.

Although the programming of the stimulator might stipulate distinct time points for turning the injected current on and off, a practical implementation would inevitably require a finite amount of time to reach the working amplitude from a resting state. As such, the effect of signal ramping was also investigated. Instead of a direct jump to and from the amplitude values in each phase, the level was incremented linearly over a 1 μ s interval such that the stimulus was piecewise continuous. The corresponding waveforms are plotted in Figure 8.7.

The differences in convergence speed between the two waveforms can be seen in videos in Appendix E. For a square-shaped stimulus, the full 5000 harmonics might be necessary to yield a reasonable result, yet even then the overshoots would be present. The ramped stimulus converged much faster than the square one and had the additional benefit of reducing the Gibbs overshoots; these still existed at the leading and trailing edges of each phase due to

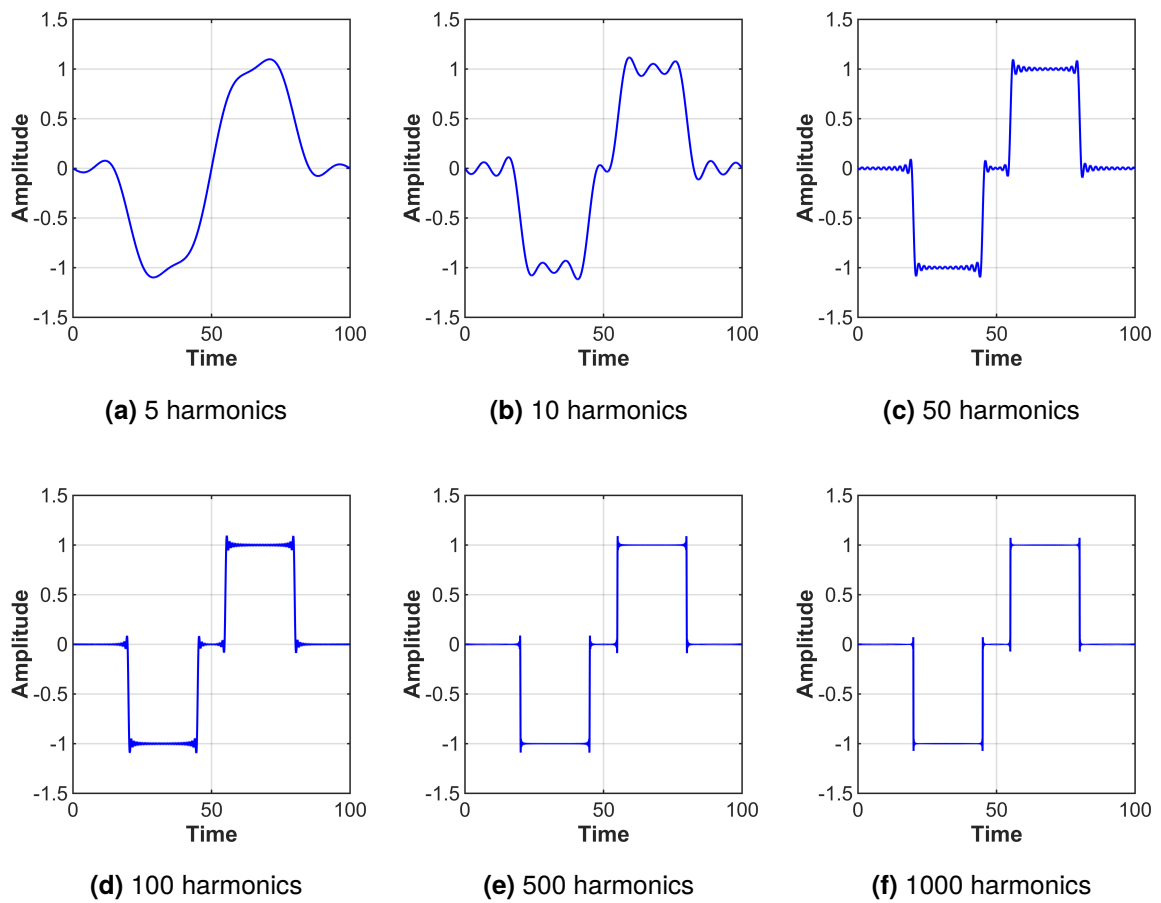


Figure 8.6: Waveform convergence with increasing harmonics for a square-shaped biphasic stimulus with a period of 100 arbitrary time units. The shape of the wave was gradually refined, but the Gibbs phenomenon continued to manifest at the discontinuities even with 5000 harmonics.

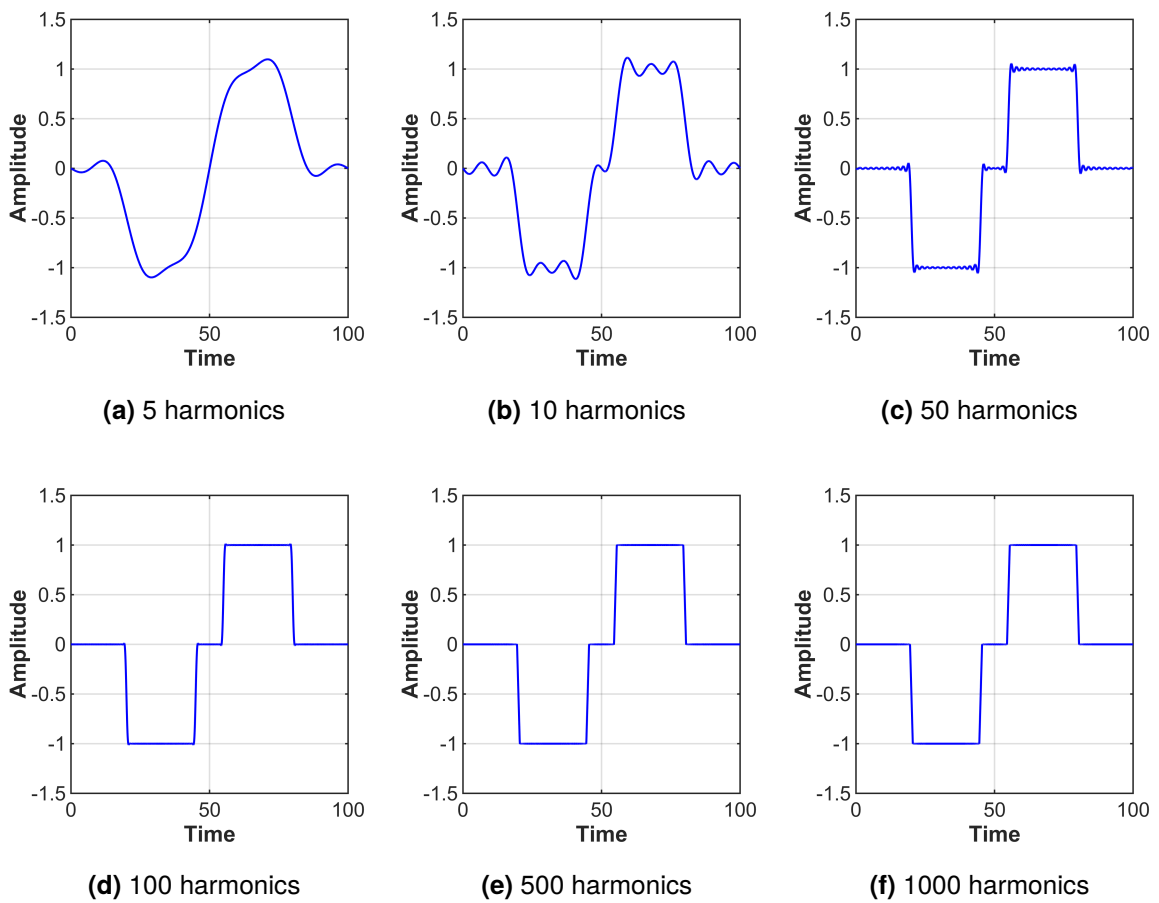


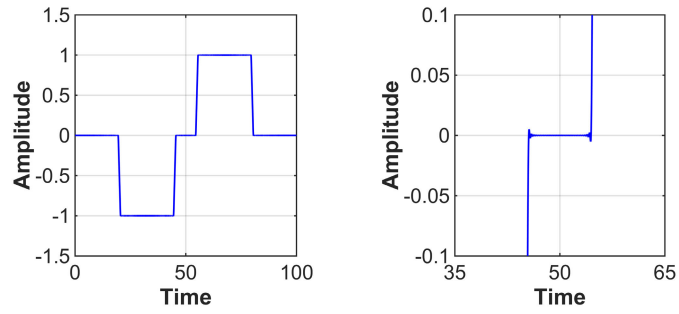
Figure 8.7: Waveform convergence with increasing harmonics for a ramped biphasic stimulus with a period of 100 arbitrary time units. Unlike the unramped counterpart in Figure 8.6, the overshoots are insignificant and the series converged much quicker.

the Fourier transform, but were much smaller. Using 300 harmonics, the overshoot was only 0.5%. Given that the waveform appeared to be well converged at this level, the 300 harmonic ramped waveform was used for further analyses.

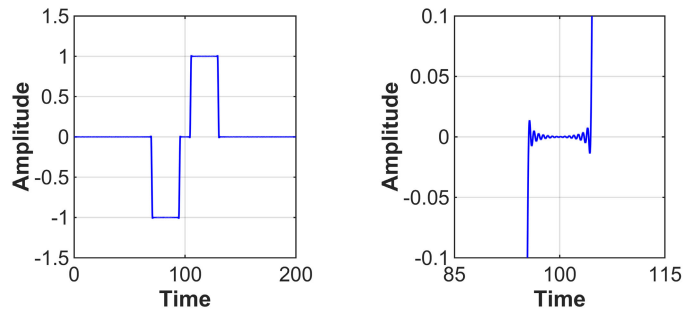
Variation of Pulse Timings

Over the years, many studies have looked into the relationships between speech recognition performance in CI recipients and pulse rate [245–249], pulse width [245, 247, 250], and other timing factors [251]. These studies have found that the stimulus profile affects the psychophysical response. However, it is difficult to ascertain what the optimal settings are because the effect of each factor on performance is highly contextual [247], is often subjective [249], and can involve compromises between competing desires [245]. On a practical level, testing different combinations of parameters is inherently time-consuming. In the Loizou study [247] for instance, only two pulse widths were tested for each pulse rate. Since pulse timings can be easily varied in this model, this represents one area in which time-dependent computational models might be applied to provide additional insight.

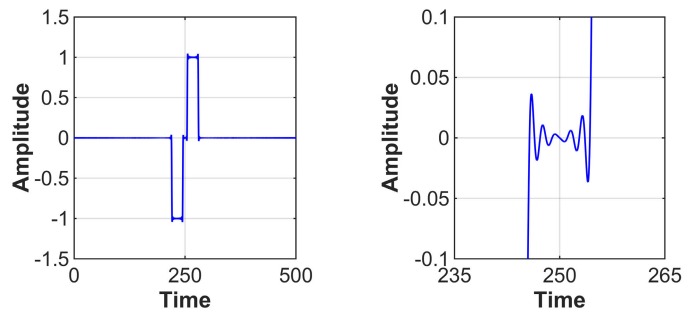
It is important to ensure that the waveform remains converged as the pulse timings are changed. As part of these tests, it was observed that changes in the pulse rate had a particularly strong influence. Figure 8.8 shows what happens to the 300 harmonic ramped waveform as the pulse rate is reduced *ceteris paribus*. Since the period of the stimulus increases, the features of the pulse become proportionately smaller. Simultaneously, the fundamental frequency is lowered, so the highest frequency harmonic is also reduced. These two effects combine to adversely impact the shape of the waveform, with the clean waveform in Figure 8.8a becoming unstable at small features such as the IPG (right panels). This indicates that the number of harmonics needed to study any particular waveform will depend on the ratio between the smallest intrapulse interval and the period.



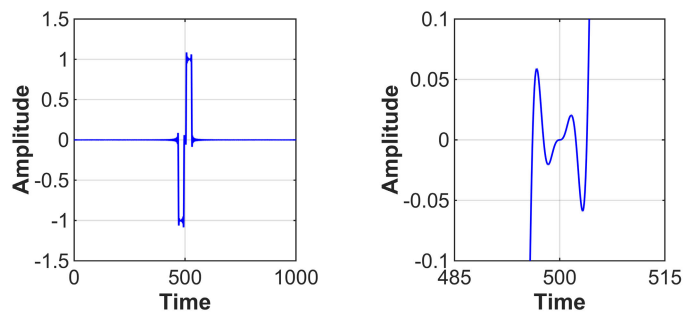
(a) $2L=100$



(b) $2L=200$



(c) $2L=500$



(d) $2L=1000$

Figure 8.8: Changing the pulse rate of the stimulus *ceteris paribus* causes the waveform to become unstable, particularly at small temporal features (in this case, the inter-phase gap as shown to the right.)

8.3.3 Output Reconstructions

Next, output waveforms were reconstructed and visualised in MATLAB. Three different simulation setups were compared: (i) a *stationary* analysis, (ii) a 5000 harmonic *square* stimulus, and (iii) a 300 harmonic *ramped* stimulus.

Voltage and Current Waveforms

Two quantities directly calculated in COMSOL in the frequency domain were converted into the time domain. The first was the voltage along the intracochlear array. Average voltages over the surface of each pad were found, but only those for electrode E5 are shown here for brevity (Figure 8.9). The second was the current exiting the base of the nerve trunk (Figure 8.10). This was measured by integrating the current density flux at the corresponding surface in the model (see Figure 6.1a). It was selected to provide some insight about the current pathways, and exhibited waveforms that served as a good indicator of sufficient convergence.

Under the stationary simulations, the amplitude of the waveforms remained constant during each phase. The magnitudes for both voltage and current differed from the time-dependent predictions at the start of each phase, but were consistent with the values at the end of each phase.

The time-dependent formulations predicted only small increases in electric potential at the scala tympani electrodes over the duration of the pulse, in line with the findings of Spelman *et al.* [98]. This is probably due to the lack of interface capacitance in the model. There was however a relatively large discrepancy in the amount of current flowing through the nerve trunk (>35% drop over the duration of the pulse), possibly because of the low current density at that location. It is clear then that the permittivities of the tissues affects the current distribution. Outputs from the square stimulus exhibited a large overshoot at the leading

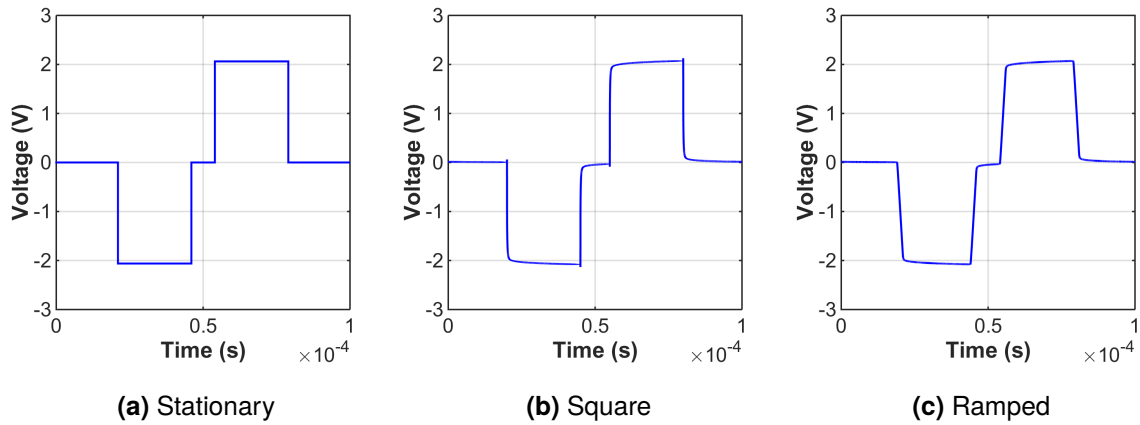


Figure 8.9: Voltage reconstructions at electrode E5 during current injection at E4.

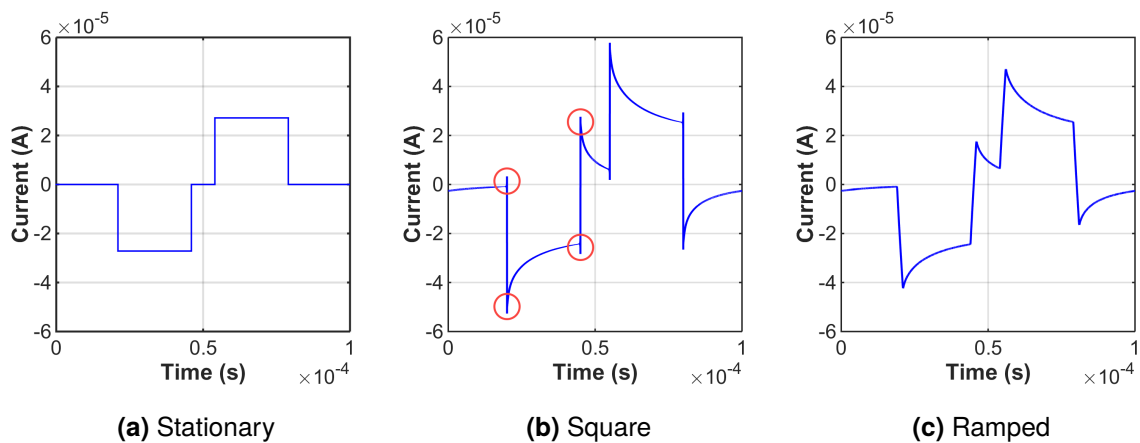


Figure 8.10: Current exiting the nerve trunk during current injection at E4. Overshoots made the true values at the leading and trailing edges difficult to ascertain, as circled for the cathodic phase in (b).

and trailing edges (circled in Figure 8.10b), making it difficult to ascertain the true signal amplitude, while the ramped stimulus provided more definitive results.

It was also observed that the current level did not start and end at zero amplitude in the time-dependent simulations, but rather appeared to have a slight negative offset (see Figures 8.10b and 8.10c). This was simply an artefact of the Fourier transform, which is based on the assumption that the function is periodic for all time, and is not an indicator of a DC bias.

Activating Function

The activating function (AF) along the neural sheet under the ramped stimulus profile was then reconstructed from the voltages at the nodes of Ranvier. Since the simulation was computed in the frequency domain, the voltage at each node was first converted into the time domain. The AF was then calculated using the corresponding voltages for each point in time.

Figures 8.11 and 8.12 show that as per the voltage and current waveforms, the stationary simulations predicted results at the end of each phase better than at the start. In both phases, the stationary simulations substantially overpredicted the level of depolarisation in the early stages. Results over all time points showed that the onset of depolarisation was quick but not instantaneous, and tended to spread as each phase progressed.

To better visualise these dynamic processes, the AF along the neural sheet was rendered as a video (see Appendix E). For the cathodic phase, AF appeared to reach peak values soon after onset at the nodes closest to the stimulating electrode, while the surrounding nodes experienced a more gradual increase over the phase. The spread of depolarisation occurred more slowly during the anodic phase. Further clarification is provided in Figure 8.13, where the AF value for a single fibre is plotted against time as an example of the time-dependent response. Fibre 35 was selected for this because its trajectory passed closest to the stimulating electrode, so it is likely to be one of the first to reach the excitation threshold.

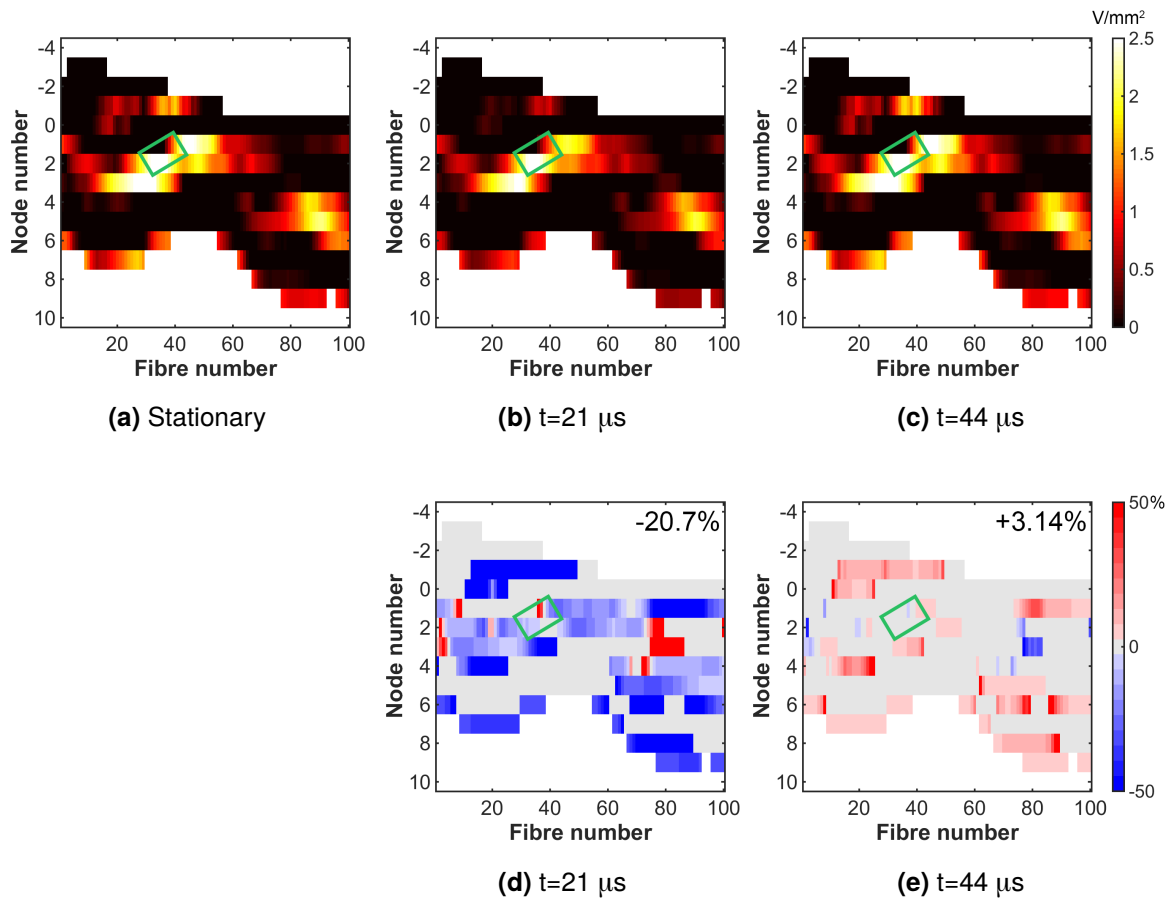


Figure 8.11: Activating function along the neural sheet for cathodic stimulation. The green box marks the approximate location of the stimulating electrode, E4. (a) Stationary simulation result for cathodic current. Times (b) $t=21$ and (c) $t=44$ represent the start and end of the cathodic phase, respectively, and the corresponding deltas relative to the stationary simulation are shown in (d) and (e). The deltas were larger at the start of the phase than at the end, as indicated by the overall root mean square difference in the top right corner of the delta plots.

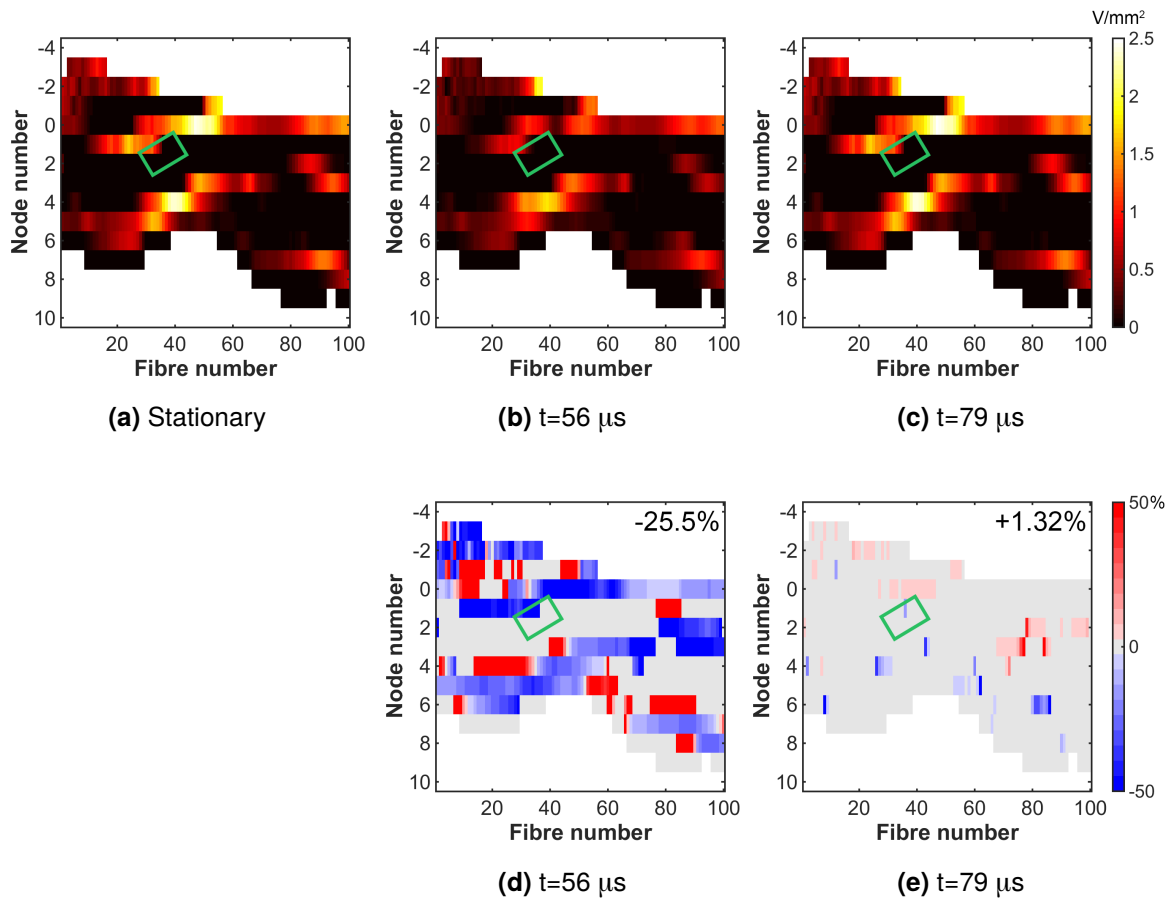
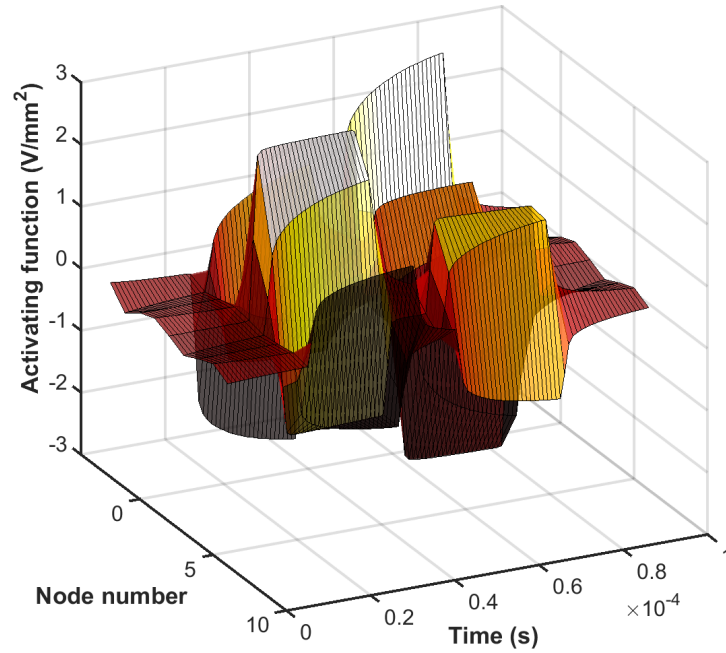
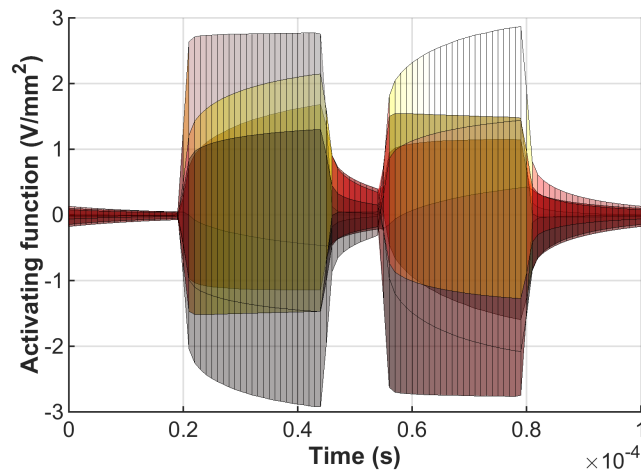


Figure 8.12: Activating function along the neural sheet for anodic stimulation. The green box marks the approximate location of the stimulating electrode, E4. (a) Stationary simulation result for anodic current. Times (b) $t=56$ and (c) $t=79$ represent the start and end of the anodic phase, respectively, and the corresponding deltas relative to the stationary simulation are shown in (d) and (e). Again, the deltas were larger at the start of the phase than at the end. Note that the hotspots appear to complement those in the cathodic case.



(a) 3D view of the response surface



(b) Side view emphasising the response over time

Figure 8.13: Activating function over time for fibre 35.

The video and plots revealed a few trends. Firstly, AF varied with location along the fibre, as expected, but these variations differed depending on the phase. In the cathodic phase, the values were highest at the nodes just below the level of Rosenthal's canal, which are closest to the stimulating electrode, but there was also a secondary peak in the peripheral process. In the anodic phase, the roles were reversed, with a primary peak near the end of the peripheral process. There were also changes at the axonal end of the modelled nerve fibre, but the trends there were less reliable due to the truncated geometry.

Secondly, changes over time not revealed by stationary analyses were also made apparent. In particular, the primary peak in each phase followed a different profile. Figure 8.13b confirms the earlier observation that the cathodic peak reached its maximum value soon after onset, and the nodes on either side showed a somewhat logarithmic increase with time. On the other hand, the peak in the anodic phase only reached its highest point at the end of the phase. This temporal asymmetry arose even though the phases were symmetric, indicating that the permittivity of the tissue played a key role in the neural response.

8.3.4 Comparison with *in vivo* Data

In an attempt to determine whether these time-dependent simulations were reasonable, some preliminary experimental data was sourced from Shefin George at the Bionics Institute in Melbourne, Australia for comparison. Voltage traces were obtained from two guinea pigs with implanted CIs operating in monopolar mode. A 1 mA biphasic pulse was injected at electrode E8, with a 25 μ s pulse width and an 8 μ s IPG. The voltage response at the other electrodes was then measured, with a sampling rate of 500 kHz. However, it was later discovered that the stimulator used in these tests only had a temporal resolution of 10 μ s, hence the mismatched timing in Figures 8.14c and 8.14d. Nevertheless, the following points still hold.

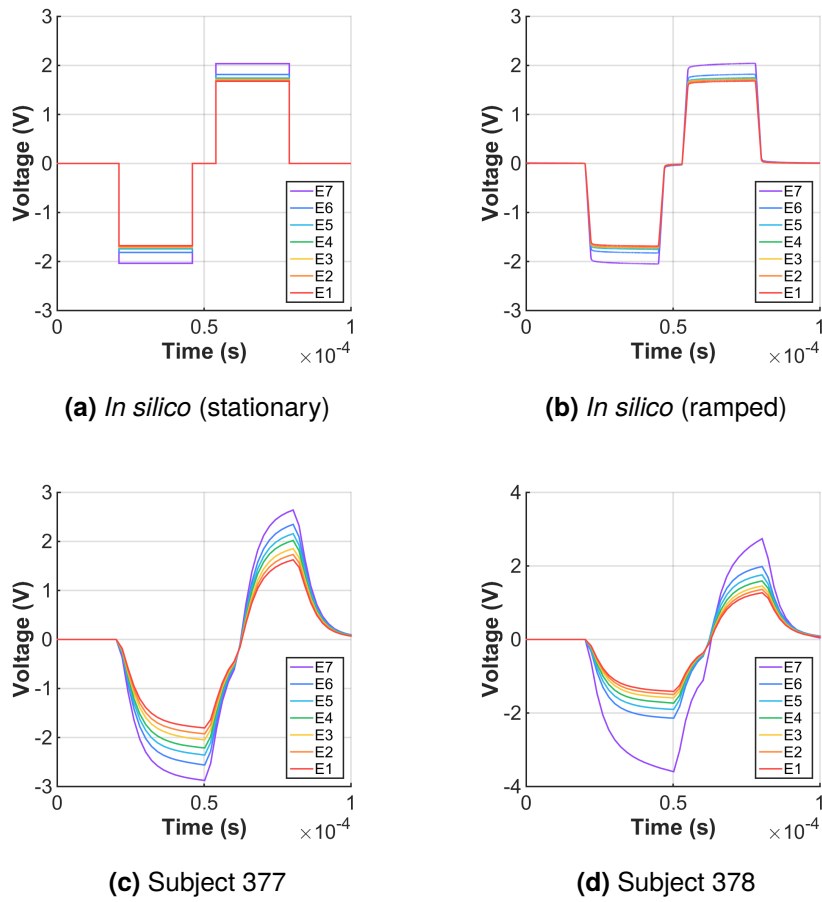


Figure 8.14: Comparison of simulated voltage profiles against *in vivo* data.

Figure 8.14 compares the results of the corresponding simulations with these *in vivo* measurements. It is immediately seen that there are some large differences between the *in silico* and *in vivo* voltage profiles. The most glaring is the difference in shape, from no change over time in the stationary simulation, to a small voltage increase in the ramped simulation, and finally a strong polarisation response in the *in vivo* measurements for both subjects. The lack of polarisation response in the models is expected given that the interface capacitance was not modelled. Peak voltages and the voltage drop along the array were also lower in the simulations.

8.4 Discussion

8.4.1 Modelling Considerations

The results of the study showed that it is indeed feasible to run simulations of volume conduction that incorporate time-dependent effects. Stationary analyses were unable to reveal temporal trends, which may be important to neural excitation, and only predicted values at the end of each phase, which makes sense in that the steady-state equilibrium takes time to reach.

Time-dependent simulations required a significant increase in solution time over their stationary counterparts due to the need to solve for a large number of harmonics. According to the mesh convergence results reported earlier (§6.3.2), linear discretisation may not be sufficient for capturing some of the steeper field gradients in this model, so the time-dependent models should ideally be solved with quadratic elements. This would, of course, need a proportional increase in solution time above the already long times seen in Table 8.2. As a proof of concept study, linear discretisation was considered sufficient. Future studies aiming for numerical accuracy should use higher order shape functions.

The number of harmonics required to produce clean waveforms was seen to vary with a number of factors. With regards to waveform shape, a pure square-shaped wave was not necessary because this would not be seen in practice. Ramping the leading and trailing edges of each phase allowed for faster convergence because fewer harmonics were required to represent the more obtuse corner angles, and removal of the discontinuities reduced the size of the Gibbs overshoot. Ramped stimuli are therefore recommended for future studies. The ramp interval would ideally be based on measurements observed *in vivo*. If this is shorter than the 1 μ s estimate used here, more than 300 harmonics may be required to reach a similar level of convergence due to the presence of sharper corners at the leading and trailing edges. More harmonics would also be required for waveforms with relatively fine temporal features per Figure 8.8. Regardless, Fourier weightings drop rapidly from the fundamental frequency upwards so the impact of the higher frequency harmonics on the overall magnitudes was low; their primary function was merely to reduce rippling in the waveform.

When compared with preliminary *in vivo* data, the simulations predicted noticeably lower voltages. This is probably due to the choice of boundary condition, as explained in §6.4.3—the magnitude of the discrepancy is quite close to the 0.9 V offset suggested therein, especially for subject 377. Discrepancies in the voltage drop along the array are likely due to inaccuracies in the material properties, but could also be due to the presence of fibrous tissue in the animals [156]. These factors may also account for the lower AF results in these simulations compared to the studies in previous chapters. Without complete and accurate material data specific to the cochlear tissues however, it is not possible to perform a more reliable investigation.

The exaggerated polarisation shape seen in these *in vivo* measurements most likely results from the use of standard platinum contacts. The measured potentials include the polarisation voltage across the interface required to overcome the double layer [75, 252], which was not incorporated into this model. Despite the polarisation observed in Figure 8.14, the current

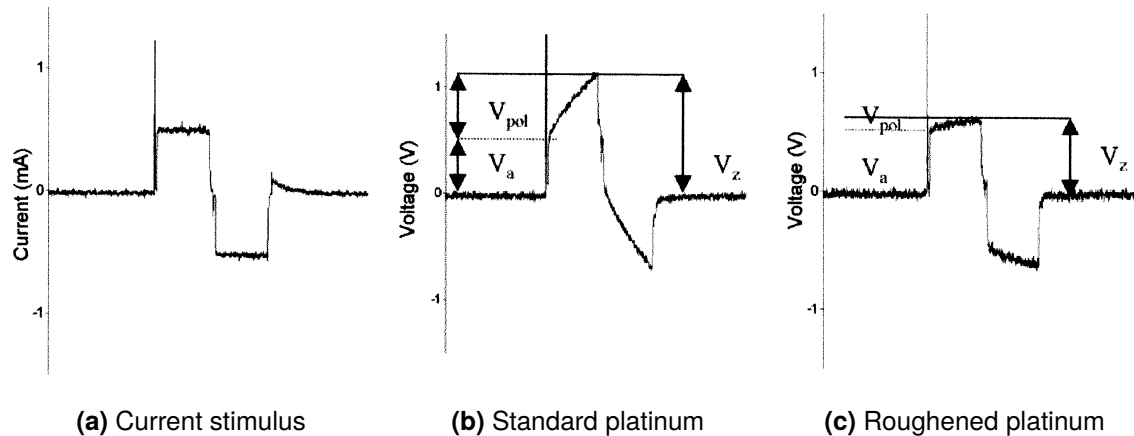


Figure 8.15: Representative voltage waveforms for platinum electrode designs. (a) The current stimulus (0.5 mA, 50 μ s per phase); (b) *in vivo* voltage response for a standard platinum electrode; (c) *in vivo* voltage response for a roughened platinum electrode. The high surface area of roughened platinum significantly reduces polarisation at the interface, and the shape compares favourably to the simulation result shown in Figure 8.14b. (Source: Tykocinski *et al.* [252]. Copyright © 2001, Elsevier B.V.)

actually delivered to the tissues is still that of the constant current input [75]. Measurements using roughened platinum or silver/silver chloride electrodes would therefore serve as a more comparable data point. For instance, voltage measurements in the scala tympani of the cat by Tykocinski *et al.* [252] illustrated that without the interfacial polarisation, the waveforms are quite similar to the time-dependent simulation results (compare Figure 8.15c with Figure 8.14b), lending some credibility to the present methodology. For comparisons with clinical data, where the electrode material cannot be changed, future studies should consider adding a complete model of the electrode-tissue interface.

Lastly, the Fourier transform assumes an infinitely periodic signal. This seemed to be a reasonable assumption for consistent stimulation, and allowed the stimulus waveform and frequency-dependent material properties to be input relatively easily. An alternative method would be the Laplace transform, which is based on the superposition of moments instead of sinusoids. Due to differences in the underlying derivation, it may be better for representing single pulse stimuli. Furthermore, studying more complex stimulus waveforms, such as those with unbalanced or additional phases, or even entire pulse trains, could violate the odd

symmetry condition used in this study to simplify the analysis. Solution using the Fourier method is still possible, but would require additional cosine terms, effectively doubling the computational cost. A method based on the Laplace transform may be more efficient for such analyses. Comparison of the two techniques is beyond the scope of this thesis, but may be worth examining for more complex waveform simulations in the future.

8.4.2 Implications for Neural Excitation

The AF results suggest that the level of depolarisation is sensitive to the small changes in voltage detected in the scala tympani. Put another way, changes in the neural tissue over time can be difficult to detect using intrascalar measurements alone. The relatively high permittivity of nerve tissue changed the impedance over the duration of the pulse, causing a shift in the current flow that worked to increase the AF. Results from stationary simulations tended to predict values at the end of the pulse only, so it is incorrect to extrapolate those values over the entire pulse duration. The quasi-static assumption may therefore be a source of error that contributes to the inconsistencies in neural predictions, such as the psychophysical comparisons attempted by Whiten [22].

Temporal trends in the predicted AF were particularly interesting, especially the asymmetry between the cathodic and anodic phases. A possible explanation for this is the relaxation in neural tissue current during each of the constant current portions of the stimulus (Figure 8.10c). The voltage drop at the trailing edge overcompensates, reversing the polarity of the current flow during the IPG. The net charge delivered to the neural tissue at that point means that the anodic phase does not start from a zero base as per the cathodic phase, leading to the asymmetrical AF response. These reactive components suggest that there are processes occurring during these intervals that stationary models do not predict. Again, whether or not other neural excitation models are sensitive to this remains to be tested. However, these observations provide a potential theoretical framework for explaining why the use of

unbalanced phases appear to improve spatial selectivity in CI recipients [253]. It may also be the case that square-shaped stimuli are suboptimal for electrical stimulation [254, 255]. Stationary models cannot handle such analyses, so the methodology used in this study could provide further insights for improving patient outcomes.

8.5 Conclusions

Time-dependent simulations of CI stimulation are possible using existing data and techniques. They are, however, held back by the lack of complete and reliable tissue property data and the large computational cost. The latter can be reduced significantly by removing discontinuities in the stimulus, such as by including a ramp interval.

The evidence indicates that the quasi-static assumption is not valid. Even though voltage measurements in the scala tympani appear to be primarily resistive, the permittivity of the nerve tissue can lead to differences in the predicted neural response between stationary and time-dependent formulations. Stationary models correspond well with the end of each phase but cannot reveal the changes that occur earlier on. For instance, time-dependent simulations showed that the response is asymmetric between the two phases, and the differences in predicted AF suggest that there is scope for using unbalanced stimuli to improve patient outcomes. Having proven the feasibility of running such analyses, further investigations with a more comprehensive neural excitation model are required before more concrete findings regarding the patient response can be made, but it would appear from these preliminary data that computational analyses of CI systems should take these time-dependent effects into account.

Chapter 9

Conclusions

This chapter addresses the following questions:

- What are the key findings of the thesis?
- How might the study be extended in the future?

9.1 Contributions of the Thesis

To recap, the two main objectives of the thesis were: (i) to develop a realistic computational model of the implanted cochlea for enabling knowledge development, and (ii) to critically evaluate some of the assumptions currently used in volume conduction models of the cochlea. Both of these aims have been achieved and the key findings are summarised below.

Regarding the modelling process, the quality of the image data is key for geometrical accuracy. This may be a challenge in clinical settings due to restrictions in available imaging modalities. A high resolution volumetric image stack is required for reconstructing the fine anatomy, such

as the cochlear membranes and vasculature, accurately. High resolution datasets are, however, a double-edged sword in that the time and computational resources needed to prepare the dataset and compute a solution to the system are significant. Nevertheless, it is possible to do this using contemporary technology.

There is currently no consensus as to which boundary condition assumption is most appropriate. The studies here showed that they are not all equal. Modelling the whole head would be preferred for accuracy but requires additional effort and computation. For standalone models, the best boundary condition to impose depends on the species of animal being modelled. In guinea pigs, the cochlea protrudes into the tympanic bulla so current should exit via the temporal bone only. In humans, a somewhat uniform current spread is expected, so grounding at an infinitely large sphere may be an acceptable compromise. Simply grounding these surfaces is not expected to yield close matches to measured intrascalar voltages because the resistance of the true return path is not accounted for in standalone models. This discrepancy should not be manipulated by changing the resistivity of the surrounding bone domain because this can affect the predicted current distribution. An alternative would be to model it using a voltage offset, representing the effective voltage drop between the model boundary and the monopolar return. This can be determined via comparisons with *in vivo* data, and was found to have minimal effect on nerve fibre depolarisation as predicted by the activating function (AF).

The accuracy of the material properties is another ongoing concern. Although some of the resistivity values are well known, others have not been reliably measured. For instance, some of the cochlear-specific tissue resistivities have been converted from resistances that were fitted to a lumped-element model, while others may only have a single data point in the literature. In addition, there is no data on the permittivities of cochlear tissues, which are important for determining the neural response more accurately.

Of the three models that were created in this thesis, the guinea pig model was the most anatomically accurate. It was found to compare well with *in vivo* data that was obtained independently at the Bionics Institute in Melbourne. As such, this model was used for deeper investigations into two hitherto untested modelling assumptions: the role of the cochlear vasculature in volume conduction, and the validity of the quasi-static assumption.

Modelling the vascular structures required substantial additional effort due to their pervasive and convoluted nature. The distribution of cochlear vessels was clearly illustrated by Microfil-enhanced microCT scans, but even with high resolution sTLIM images, it was not possible to reconstruct the entire vascular tree. The vessels in the modiolus did have an effect on AF predictions, but these were localised to the region nearest to the current source. The vein of the scala tympani (VST) played a particularly noticeable role, so it is recommended that future models include this structure as part of the reconstruction.

It was possible to include time-dependent effects by using Fourier methods to represent the current pulse and permittivity data for some of the tissues in the cochlea. However, there is a very high computational cost due to the large number of harmonics required for a clean signal, especially in simulations using square-shaped stimuli. This can be significantly reduced by ramping the signal at the leading and trailing edges of each phase. The quasi-static criterion did not hold for nerve tissue across the modelled frequency range, so the assumption of quasi-stationarity is not valid. Stationary analyses were shown to only predict field values at the end of each phase. Time-dependent simulations, on the other hand, demonstrated dynamic processes. For example, a relaxation effect during the constant-current portions of the stimulus waveform contributed to an asymmetric AF response between the cathodic and anodic phases, which may help to explain some clinical observations on lead-phase performance differences.

In summary, the project has demonstrated that high fidelity computational modelling of the electrophysiological response during CI stimulation is feasible for research purposes. By

creating this tool for *in silico* investigations, our understanding of the underlying relationships between the anatomy of the inner ear, the current distribution through the tissues, and subsequent neural response has been deepened. This in turn establishes a platform for further studies, such as those in the following section.

9.2 Future Research Directions

“By pointing out some of the gaps in our knowledge, I hope to motivate others to do some of the relevant experiments and theory.”

— James Ranck, 1975 [81]

There are a number of potential avenues for future investigations. First and foremost, further validation of the field quantities should be undertaken to verify that the model predictions are realistic throughout the cochlea, not only in scala tympani. For instance, microelectrodes inserted into the cochlea [256] may be able to provide a more complete electric field map for comparison with the *in silico* voltage distribution, and neural response telemetry techniques [257, 258] could be compared with the predicted activating function along the neural sheet. This data should in turn be used for additional testing of boundary conditions, including more complex boundary conditions such as a distributed resistance to ground or a whole head model (for the guinea pig). Further reducing uncertainties in this manner will help to make the models more clinically relevant.

Secondly, additional measurements of the electric tissue properties should be obtained using modern techniques [220]. These are one of the most crucial inputs for the system but have yet to be determined reliably. The resistivities of cochlear-specific tissues is particularly important as they cannot be sourced from traditional compendiums. Both resistivity and permittivity values across a wide frequency range should also be obtained to enable further

time-dependent simulations. There is substantial potential for a new gold standard to be defined here.

Thirdly, the model may be used to investigate variations in electrode array designs, intrascalar positioning, and other modes of stimulation. For the scope of this thesis, a relatively standard array was inserted in a mid-scalar position, and the focus was on improving simulations of monopolar mode. However, the models can be adapted to allow for the virtual prototyping of more advanced electrode array designs, to observe the effect of insertion trajectories that are closer to or further from the modiolar wall, or to measure reductions in effective current spread by switching to tripolar or phased-array stimulation.

Fourthly, there is scope remaining in this model to improve the nerve fibre trajectories, the spacing of the nodes of Ranvier, and to include non-linear kinetics at each node. Integration of these volume conduction models with more advanced models of neural excitation would enable clinical outcomes such as thresholds to be calculated. The prime candidates for this would be the GSEF model [100] or the NEURON simulation environment [259]. As shown recently by Frijns *et al.*, it is also possible to extend the modelling even further downstream along the hearing pipeline once a comprehensive excitation model has been coupled [260].

Lastly, the methodology used here has highlighted some significant remaining challenges before patient-specific models can be generated easily. Clinical imaging techniques do not provide sufficient resolution for high quality reconstructions, so a level-of-detail study comparing, say, the guinea pig model to less detailed versions would be useful for determining the error differential. Even if high resolution scans become available in the future, the accurate segmentation of such large data sets would require a large time investment due to the lack of reliable automated algorithms. Geometry morphing techniques based on a generic shape may provide a feasible solution [34]. However, the method would need to account for changes in the anatomy due to disease, such as the formation of scar tissue or new bone and the degeneration of neural tissue. The discretisation step also needs to be improved, as the

current iteration, while robust, still requires manual intervention at some stages. Different meshing programs might be sought, or alternatively, the application of meshless methods could be tested [261].

9.3 Closing Remarks

At the start of the twentieth century, the Wright brothers successfully demonstrated that powered flight could be achieved. Over the following decades, aircraft designs were iteratively and continually updated. The ability to fly through the atmosphere revolutionised transport, and commercially viable airlines facilitating intercontinental transport are now commonplace. The next frontier—space—could not however be reached using those same designs because the physics of flight did not transfer well to that environment.

“We humans are wet, salty beasts, and we tend to conduct electricity pretty well.

It not only goes where you want it to go, but also out into the surrounding tissues.”

— Mark Bendett, 2012 [262]

Cochlear implants (CIs) can be thought of as following a similar path. Electrical stimulation of the cochlea has proven itself to be a successful treatment for sensorineural hearing loss. However, evidence from multiple fronts points toward the physics of the cochlea ultimately constraining the ability of contemporary electrode array designs to deliver truly focused stimulation and consistent patient outcomes. This suggests that electrical stimulation may not be the best technique to use in the long run. In order to reach new heights in hearing restoration, more revolutionary designs are required. Research into alternative therapies is already underway, with early test results showing promise in overcoming the limitations

of electrical stimulation [13, 19, 263–265]. This forthcoming paradigm shift in CI designs will take many more years to reach fruition*, but no matter which technology proves most viable, our understanding of the physical relationships underpinning the system will be key to enabling improvements in sound perception and quality of life for affected individuals.

* <https://xkcd.com/678/>

Appendix A

MATLAB Function Licences

interparc.m

```
Copyright (c) 2012, John D'Errico  
All rights reserved.
```

```
Redistribution and use in source and binary forms, with or without  
modification, are permitted provided that the following conditions are  
met:
```

- * Redistributions of source code must retain the above copyright notice, this list of conditions and the following disclaimer.
- * Redistributions in binary form must reproduce the above copyright notice, this list of conditions and the following disclaimer in the documentation and/or other materials provided with the distribution

```
THIS SOFTWARE IS PROVIDED BY THE COPYRIGHT HOLDERS AND CONTRIBUTORS "AS IS"  
AND ANY EXPRESS OR IMPLIED WARRANTIES, INCLUDING, BUT NOT LIMITED TO, THE  
IMPLIED WARRANTIES OF MERCHANTABILITY AND FITNESS FOR A PARTICULAR PURPOSE  
ARE DISCLAIMED. IN NO EVENT SHALL THE COPYRIGHT OWNER OR CONTRIBUTORS BE  
LIABLE FOR ANY DIRECT, INDIRECT, INCIDENTAL, SPECIAL, EXEMPLARY, OR  
CONSEQUENTIAL DAMAGES (INCLUDING, BUT NOT LIMITED TO, PROCUREMENT OF  
SUBSTITUTE GOODS OR SERVICES; LOSS OF USE, DATA, OR PROFITS; OR BUSINESS  
INTERRUPTION) HOWEVER CAUSED AND ON ANY THEORY OF LIABILITY, WHETHER IN  
CONTRACT, STRICT LIABILITY, OR TORT (INCLUDING NEGLIGENCE OR OTHERWISE)  
ARISING IN ANY WAY OUT OF THE USE OF THIS SOFTWARE, EVEN IF ADVISED OF THE  
POSSIBILITY OF SUCH DAMAGE.
```

A. MATLAB FUNCTION LICENCES

arclength.m

```
Copyright (c) 2012, John D'Errico  
All rights reserved.
```

```
Redistribution and use in source and binary forms, with or without  
modification, are permitted provided that the following conditions are  
met:
```

- * Redistributions of source code must retain the above copyright notice, this list of conditions and the following disclaimer.
- * Redistributions in binary form must reproduce the above copyright notice, this list of conditions and the following disclaimer in the documentation and/or other materials provided with the distribution

```
THIS SOFTWARE IS PROVIDED BY THE COPYRIGHT HOLDERS AND CONTRIBUTORS "AS IS"  
AND ANY EXPRESS OR IMPLIED WARRANTIES, INCLUDING, BUT NOT LIMITED TO, THE  
IMPLIED WARRANTIES OF MERCHANTABILITY AND FITNESS FOR A PARTICULAR PURPOSE  
ARE DISCLAIMED. IN NO EVENT SHALL THE COPYRIGHT OWNER OR CONTRIBUTORS BE  
LIABLE FOR ANY DIRECT, INDIRECT, INCIDENTAL, SPECIAL, EXEMPLARY, OR  
CONSEQUENTIAL DAMAGES (INCLUDING, BUT NOT LIMITED TO, PROCUREMENT OF  
SUBSTITUTE GOODS OR SERVICES; LOSS OF USE, DATA, OR PROFITS; OR BUSINESS  
INTERRUPTION) HOWEVER CAUSED AND ON ANY THEORY OF LIABILITY, WHETHER IN  
CONTRACT, STRICT LIABILITY, OR TORT (INCLUDING NEGLIGENCE OR OTHERWISE)  
ARISING IN ANY WAY OUT OF THE USE OF THIS SOFTWARE, EVEN IF ADVISED OF THE  
POSSIBILITY OF SUCH DAMAGE.
```

Appendix B

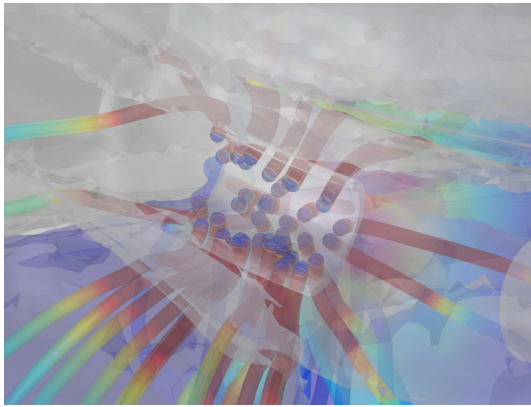
Streamline Seeding

For this thesis, we wanted to know what path injected current follows after it leaves the stimulating electrode. This was in fact one of the earliest questions von Békésy raised in his research [106]. While the technology of his time was limiting, there are now a variety of tools that are able to visualise current pathways in an intuitive and meaningful manner.

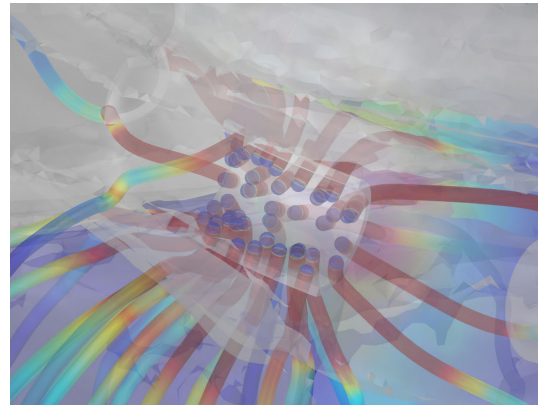
One of the main reasons COMSOL was chosen was because it offers an easy way to generate such streamline plots. These plots trace the path of the vector field through the volume, based on a set of seed points. The streamlines should obviously be seeded on the exposed surface of the active electrode. COMSOL provided several options for streamline seeding. At first, we chose to start the streamlines “on selected boundaries” because that option allowed the number of streamlines desired to be set. However, it soon became apparent that there were some problems with this approach because it did not clearly define how the seed points were distributed spatially over the selected surface.

From our observations, it appeared that the the seeding algorithm was based on the mesh nodes on the selected surface. (Keep in mind that a pre-meshed volume was imported, so COMSOL was unaware of the underlying geometry.) The problems were therefore twofold

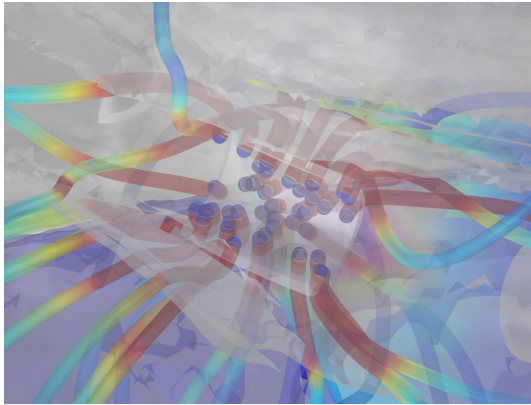
B. STREAMLINE SEEDING



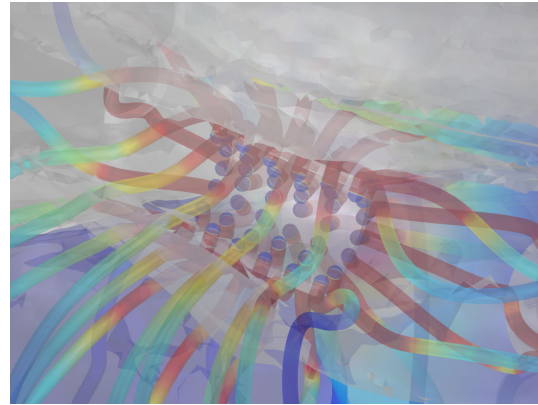
(a) On selected boundaries, attempt 1



(b) On selected boundaries, attempt 2



(c) On selected boundaries, attempt 3



(d) Start point controlled

Figure B.1: The streamline seeding problem. 42 streamlines are plotted in each case, viewed from the lateral aspect. Note the randomised distribution of seed points when plotting on selected boundaries, which resulted in a different distribution of streamlines through the volume.

(see Figure B.1a–B.1c). Since the Octree algorithm used tetrahedral elements, the nodes on the electrode surfaces were not aligned with the edges of the electrode pad, making physical interpretation of the resulting plot difficult. In addition, the nodes appeared to be semi-randomly selected, as replotting the streamlines *ceteris paribus* would result in a different set of selected seed points. This lack of consistency was undesirable because it made direct comparison using different model parameters impossible.

In order to provide a more intuitive visualisation, the seed points should be spaced regularly over the surface of the stimulating electrode. We also wanted to be able to change the set

B. STREAMLINE SEEDING

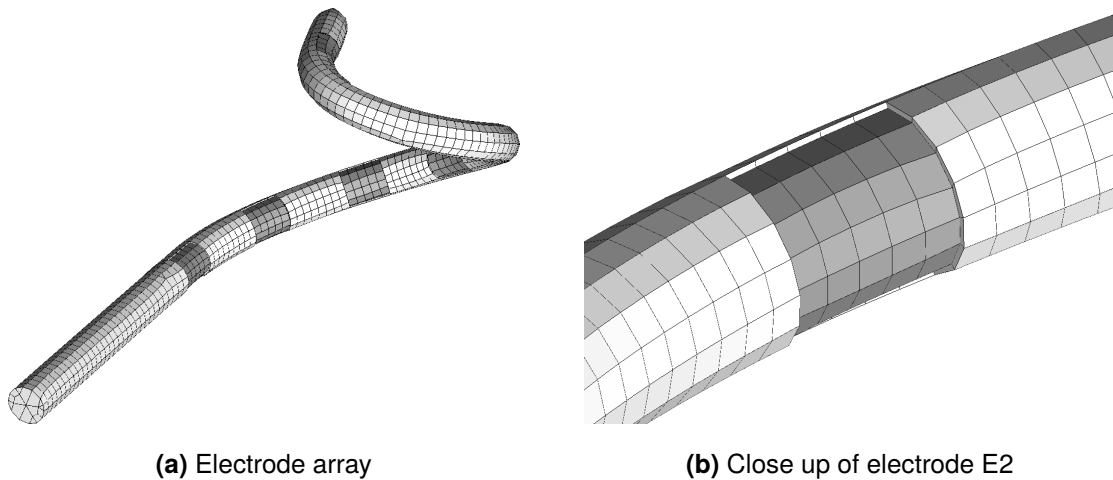


Figure B.2: Quadrilateral mesh of the electrode surface. Here, the silicone carrier is also shown for context.

of seed points programmatically so that the plots could be customised depending on which electrode was active. In my discussions with COMSOL Support, they suggested that the only way to achieve this was to list the coordinates of each seed point manually. As such, a workaround was developed using the ANSYS suite as follows:

1. Import the CAD file for the electrode pads into ICEM CFD.
2. Perform a “Build Topology” operation on the pads to ensure that the edges are recognised by the program.
3. Set the Global Shell Mesh Parameters to generate an “All Quad” mesh using the “Autoblock” method.
4. Set the element mesh size limits using the Part Mesh Setup box to suit the number of streamlines desired. This may require some trial and error. Note that it does not have to match the settings used for the volume mesh.
5. Compute the surface mesh. The result should be similar to that shown in Figure B.2 (but without the carrier). Export the file as a NASTRAN (or STL).
6. Open ANSYS Workbench, add an FE Modeller module, and import the surface mesh file from ICEM CFD. Perform a visual inspection to check that the mesh is correct.

B. STREAMLINE SEEDING

7. Add a Static Structural module in Workbench and link the surface mesh to the model component.
8. Insert a named selection and select the exposed surface of an electrode contact.
9. Insert a second named selection. Using a worksheet, add the named selection from the previous step, then convert to mesh nodes.
10. Ensure that node locations are included when exporting by checking the appropriate option in Workbench. If unsure, see this discussion thread. The relevant comment by Christopher K. Hubley is reproduced below.

```
To grab node locations and displacements from Workbench, you'll have to click "Tools>Options>Simulation>Export>Include Node Locations/Include Node Numbers".
```

```
From there, you can output nodal coordinates by right-clicking on your displacement results and selecting "Export".
```

11. Export the named selection with the nodes as a plain text file. Format the data as comma separated (suggest using Sublime Text for this) and copy into COMSOL as required. Using these coordinates with the “start point controlled” positioning option should result in consistent streamline plots per Figure B.1d.
12. Repeat steps 8–11 for the other electrodes.

Appendix C

Ethics Approval

The guinea pig voltage tomography experiments conducted by Shefin George under the supervision of James Fallon at the Bionics Institute in Melbourne, Australia were approved by the Royal Victorian Eye and Ear Hospital Animal Research and Ethics Committee (project number 12/250AB, granted 28 February 2012). Shefin was added to the project as part of an amendment, as per the Final Report attached.

The author was not directly involved with these experiments, but the data were used for validation of the model as described in Chapter 6.



Eye & Ear Hospital
caring in every sense

March 5, 2012

Dr James Fallon
The Bionics Institute
Mail Box 84, St Vincent's Hospital
Victoria Parade, Fitzroy Vic 3065

The Royal Victorian
Eye & Ear Hospital

32 Gisborne Street
East Melbourne
Victoria 3002 Australia

Locked Bag 8
East Melbourne
Victoria 8002 Australia

Telephone +61 3 9929 8666

TTY +61 3 9929 8052

Facsimile +61 3 9663 7203

Info@rveeh.vic.gov.au

www.rveeh.vic.gov.au

ABN 81 863 814 677

Dear Dr Fallon,

Re: Animal Research & Ethics Committee – NEW PROJECT
Research Project – Focussed current stimulation in the cochlea

The Animal Research & Ethics Committee considered the above project at its 28 February 2012 meeting. I am pleased to inform you that ethical approval was granted.

Project number **12/250AB** was allocated under the BEI SPPL, and this number should be used in all future correspondence. The Committee approved the following animals:

- 32 guinea pigs
- 16 cats

The following Researchers were approved:

- James Fallon
- Sam Irving
- Nicole Critch
- Rob Shepherd
- Alison Neil
- Melanie Gault
- Andrew Wise
- Amy Morley

The Committee requires an annual progress report, and must approve any proposed amendments to the protocol.

The Committee requires you to preserve the confidentiality of information about research subjects, and to ensure the confidentiality of records. Information obtained for your research that is confidential or personal must not be used for purposes other than those specified in the approved protocol.

Ethical approval is valid from the date of this letter until 28 February, 2015. At the end of this period, or at the conclusion of the research, a final report is required along with a copy of any publications.

On behalf of the Committee, I wish you every success with your project.

Yours sincerely

Kerryn Baker
Secretary

Animal Research & Ethics Committee
kerryn.baker@eyeandear.org.au
Telephone +61 3 9929 8525
Facsimile +61 3 9663 7203

cc BRC
AREC file

**THE BIONICS INSTITUTE
ANIMAL RESEARCH & ETHICS COMMITTEE**



One (1) original of the complete final report (plus copies of publications) should be forwarded to

The Secretary, Animal Research & Ethics Committee

FINAL REPORT

1. DETAILS

Project Title	Focussed current stimulation in the cochlea
Project Number	12/250AB
Principal Investigator	Dr James Fallon
Nominated Contact (if applicable)	
Date Original Approval Received	28 th February 2012

2. ANIMAL USE TABLE

	Total		Total
Initial Animals Approved :		Additional Animals Approved:	
Species 1 – Cat	16	Species 1 -	
Species 2 – Guinea Pig	32	Species 2 – Guinea Pig	16
Total Animals Used:			
Species 1 - Cat	13		
Species 2 – Guinea Pig	30		

3. PROJECT PERSONNEL (All persons to have worked on project at any time)

RESEARCHER NAME	POSITION HELD
Dr James Fallon	Senior Research Fellow
Professor Rob Shepherd	Director
Dr. Andrew Wise	Senior Research Fellow
Prof Dexter Irvine	Prof Research Advisor
Dr. Sam Irving	Research Fellow
Ms. Alison Neil	Research Assistant
Ms. Amy Morley	Research Assistant
Ms. Nicole Critch	Technical Officer
Ms. Melanie Gault	International Engineering student
Ms Michelle McPhedran	Research Assistant
Mr Thomas Spencer	Reserch Assistant
Mr Damian Robb	Research Assistant
Ms Emma Johnson	Research Assistant
Dr Philipp Senn	Research Assistant
Ms Shefin George	Research Assistant

4. PLEASE OUTLINE HOW THE PROJECT AIMS WERE ACHIEVED:

The project aimed to evaluate the efficacy of phased array stimulation (PAS) to provide more precise spatial and temporal resolution in cochlear implants in comparison to traditional monopolar (MP) and bipolar (BP) stimulation in controlled animal studies. The experiments were done in guinea pigs and cats of acute, short term and long term deafness. Guinea pigs were in cohorts of 0,1 and 2 months of deafness while cats were in cohorts of 0 and 6 months of deafness. Following assessment of hearing status using auditory brain responses and implantation of the electrode array into the deafened cochlea, each animal had an acute terminal experiment to record neural excitation across the inferior colliculus (IC).

The efficacy of PAS was evaluated by examining whether:

- H1. PAS produces more spatially restricted patterns of neural excitation than bipolar or monopolar stimulation;
- H2. PAS increases the number of temporally independent channels compared with bipolar and monopolar stimulation;
- H3. The advantages of PAS over bipolar and monopolar stimulation are maintained in cochleae with significant neural degeneration;
- H4. PAS efficacy is maintained where the electrode array is positioned distal to the auditory nerves;
- H5. PAS thresholds are negatively correlated with local neural survival;
- H6. PAS does not result in ectopic activation of non-auditory neurones.

Cohort	Species	# animal per group	# animals allocated	Duration of deafness	Hypotheses tested
1	G pig	32	22	0	H1, H2, H3, H5, H6
2	G pig	8	4	1 month	H3, H1, H2, H5, H6
3	G pig	8	4	2 months	H3, H1, H2, H5, H6
4	Cat	8	6	0	H4, H1, H2, H5, H6
5	Cat	8	7	6 months	H4, H3, H2, H1, H5, H6

5. PLEASE DETAIL PROJECT OUTCOMES (e.g. FURTHER RESEARCH PUBLICATIONS):

Preliminary results from this project have been presented at the Australasian Auditory Neuroscience Workshop 2013 & 2014 and published in the Journal of Neural Engineering. An additional two manuscript are current under preparation / review. The experiments showed that PAS results in more restricted supra-threshold stimulation than MP stimulation (Figure 1), in both acutely and long-term deafened animals. However, the improved selectivity comes as the cost of increased thresholds.

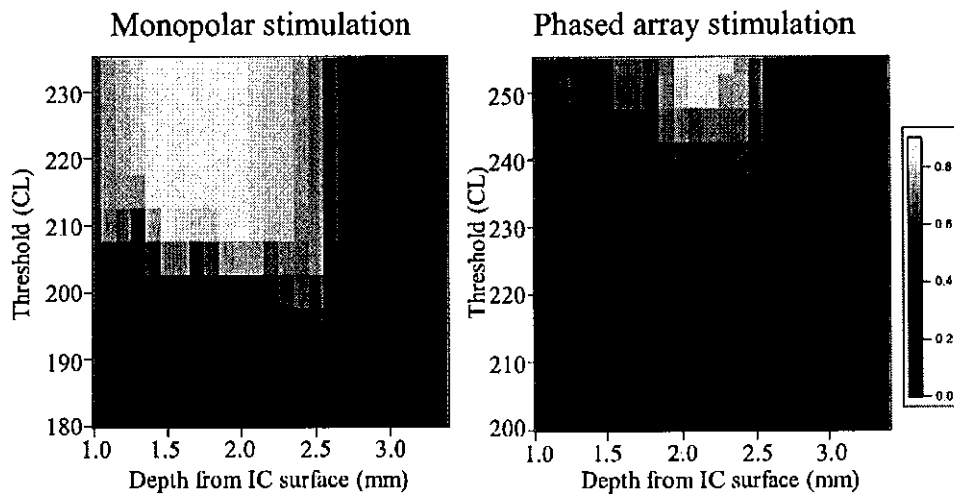


Figure 1. IC response images for MP and PAS at the centre electrode for acutely deafened guinea pig 12_368. The scale represents normalised spike probabilities.

Final Report Publication Listing

Please provide a detailed list of all publications arising from this study.

- George, SS, Fallon, JB & Wise, AK. Evaluation of Focused Multipolar Stimulation for Cochlear Implants in an Animal Model. 3rd International Conference on Medical Bionics 2013. (Presentation)
- George, SS, Fallon, J, Wise, A & Shepherd, R. Evaluation of Focused Multipolar Stimulation for Cochlear Implants in an animal model. SOBR 2013.
- George, SS, Fallon, J, Wise, A & Shepherd, R. Evaluation of Focused Multipolar Stimulation for Cochlear Implants in an animal model. Biomed Link 2013.
- George, SS, Fallon, JB, Wise, AK & Shepherd, RK. INVESTIGATING THE EFFECT OF FOCUSED MULTIPOLAR STIMULATION STRATEGY FOR COCHLEAR IMPLANTS. Australasian Auditory Neuroscience Workshop 2014. (Presentation)
- George, S, Fallon, JB, Wise, AK, Shivdasani, MN & Shepherd, RK. Evaluation of Phased Array Current-Focussing Strategy in Cochlear Implants using Animal Models. Australasian Auditory Neuroscience Workshop 2013. (Presentation)
- George, SS, Wise, AK, Shivdasani, MN, Shepherd, RK & Fallon, JB. 2014. Evaluation of focused multipolar stimulation for cochlear implants in acutely deafened cats. Journal of Neural Engineering 11, 065003.
- George, S, Shepherd, RK, Wise, AK, Shivdasani, MN and Fallon, JB. Focused Multipolar Stimulation for Improved Performance of Cochlear Implants: Preclinical Studies. Australasian Auditory Neuroscience Workshop, Dec 2014. (Presentation)

6. RESEARCH CONCLUSIONS: (May be attached)

PAS offers a potential way to improve hearing fidelity for the next generation of cochlear implant patients, although issues surrounding the increased threshold still need to be addressed. A study to test the chronic safety of this type of stimulation has been funded by the ARC and is currently underway.

PRINCIPAL INVESTIGATOR: *James Fallon*

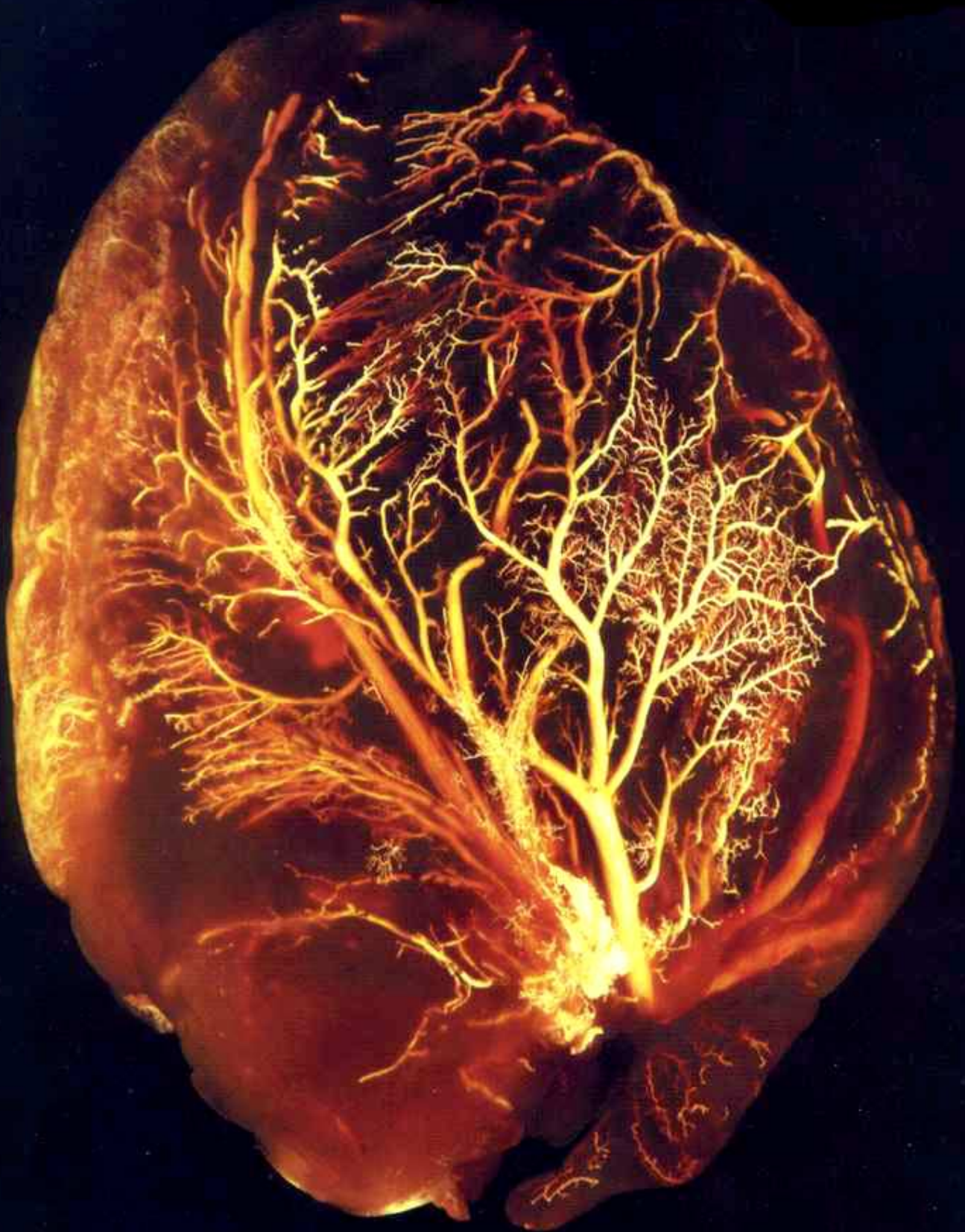
DATE: 27/01/2015

Appendix D

Microfil Specification Sheet

The official documentation for the Microfil compound used in the microCT imaging of the vasculature is provided below.

MICROFIL[®] Injection Compounds



MICROFIL® compounds will fill and opacify microvascular and other spaces of non-surviving animals and postmortem tissue under physiological injection pressure. The continuous, closed vascular system tends itself to flow through injection or perfusion techniques. Following injection, MICROFIL compounds cure to form a three-dimensional cast of the vasculature.

MICROFIL MV-series compounds are available in five radiopaque colors, as well as clear. MV-series compounds require either an alcohol-methyl salicylate or glycerin clearing sequence, whereby the refractive index of the clearing solution is the same as the refractive index of the tissue. This allows for microscopic examination of a selected vascular bed.

MICROFIL CP-101 compound is intended for use in cast-corrosion techniques, and is designed for filling large blood vessels (greater than 100 microns). Although the CP-101 compound will fill capillaries, these vessels fragment when the supporting tissue is removed through exposure to a potassium hydroxide solution. When cured, MICROFIL CP-101 is milky white in color. Casts made using CP-101 will maintain their dimensional accuracy indefinitely.

Advantages offered with MICROFIL compounds over previously available rubber injection materials include:

- Complete filling with minimal shrinkage, to enhance vessel continuity and to produce in cleared preparations a vivid, optically cleared specimen that allows a precise study of the microcirculation.

- Color diversity, to provide delineation within the circulatory tree for microscopic examination and photographic illustration.

Areas of investigation

In physiology, MICROFIL visualization provides a means for establishing the precise vascular architecture of specific organs, allowing comparison between normal and abnormal structure.

In surgery, visualization of the microcirculation and microanatomy is leading to improved surgical techniques in the repair of nerves, tendons, and blood vessels.







In gastrointestinal research, MICROFIL compounds characterize and describe changes in vascular patterns associated with several pathological conditions.

Injected specimens, when preserved in methyl salicylate or glycerin, also serve as a definitive teaching adjunct.

MV-series mixing procedure

To achieve a viscosity level suitable for injection of the microcirculation, it is necessary to blend the MV compound with an equal quantity (by weight) of MV-Diluent. Volume mixing requires 5ml of diluent for every 4ml of compound. The mixture of compound and diluent is catalyzed with 5% (by weight or volume) of MV Curing Agent; Viscosity ranges from 20 to 30 centipoise. Working time is 20 minutes and begins with the addition of curing agent.

Table 1.
Physical properties of MICROFIL compounds

	MV-112	MV-117	MV-120	MV-122	NW-130	MV-132	MV-Diluent	CP-101
Color	 White	 Orange	 Blue	 Yellow	 Red	Clear	Clear	 Milky White
Specific gravity	1.04	1.02	1.00	1.04	1.02	1.00	0.92	0.98
Viscosity, ¹ centipoise	35	25	25	25	30	20	5	25
Gel time, ² minutes	90	90	90	90	90	90	—	45
Useful Shelf life, ³ months	4	4	4	4	4	4	Indefinite	6

Notes

1. Viscosity measured with a Brookfield Model LVF Viscometer, with a No. 2 spindle at 30 RPM.
2. Gel time measured on a blend (by weight) of one part MV compound and one part MV-Diluent followed by addition of 5% MV Curing Agent. Gel time is time required for mixture to cease flowing.
3. Shelf life is in excess of four months. For materials held beyond four months, it is possible to run the following static test to determine acceptability:
 - a. Mix 5 grams of MV compound with 5 grams of MV-Diluent in a vial.
 - b. Add 10 drops (medicine dropper) of MV Curing Agent.
 - c. Cap, shake, and refrigerate overnight.
 - d. The mixture should gel in the vial after this procedure to assure a cure in subsequent animal injections.

Catalyzed mixtures will form an elastomeric gel after 90 minutes at room temperature. Curing takes place with non-exothermic cross-linking and minimal volume change.

It has been possible to refrigerate specimens immediately after injection and still obtain complete cure after overnight aging. This procedure decreases odor level for subsequent sectioning.

Perfusion techniques

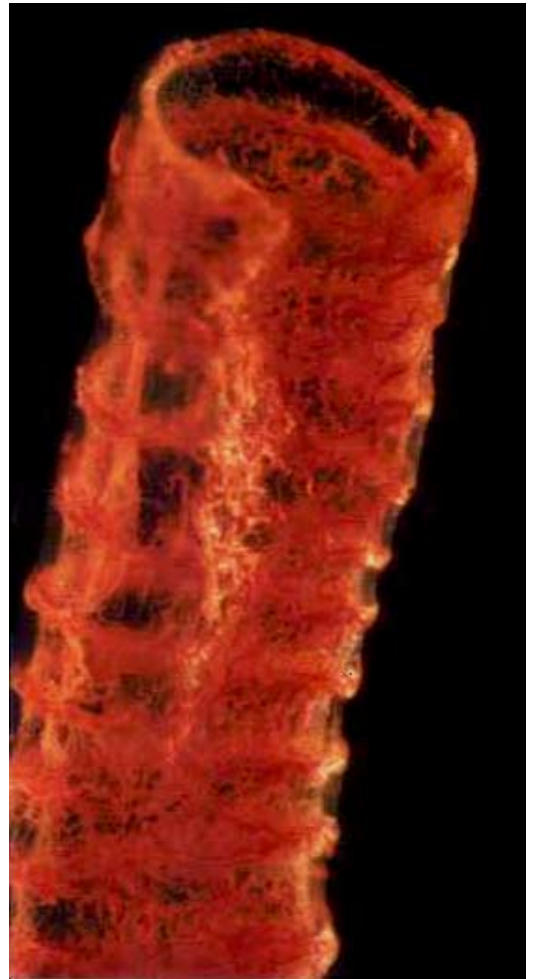
Two techniques of tissue clearing are described below. Alcohol-methyl salicylate clearing produces a stiffer tissue which, from an aesthetic point, provides a pleasing view for gross observation. Glycerin clearing produces a more flexible tissue, allowing easier manipulation for a given vessel.

Alcohol-methyl salicylate clearing

Non-wetting features of MICROFIL compounds prevent any interaction with blood. Therefore, in the non-surviving animal, a selected vascular bed can be readily perfused without prior washout of blood. Heparinization to maintain blood fluidity, however, has been used to realize improved injection preparations.

For the injection of blood vessels from vascular beds removed postmortem, washout of clotted blood with saline is advisable.

Selected vascular beds are perfused through their accessible artery and drained through a similar vein. Infusion pressures will vary with the animal's mean systemic pressure. For organs from the dog, cat, rat,



5 MICROFIL MV-130 (Red) injection of rat trachea.

Courtesy Robert A. Acland, University of Louisville

6 MICROFIL MV-130 (Red) injection of rat kidney.

Courtesy Robert A. Acland, University of Louisville



Table 2
Alcohol-methyl salicylate clearing sequence

First Day	—	Immerse in a 25% solution of ethyl alcohol.
Second Day	—	Immerse in a fresh solution of 50% ethyl alcohol.
Third Day	—	Immerse in a fresh solution of 75% ethyl alcohol.
Fourth Day	—	Immerse in a fresh solution of 95% ethyl alcohol.
Fifth Day	—	Immerse in absolute ethyl alcohol.
Sixth Day	—	Immerse for 12 to 24 hours in methyl salicylate.

If tissue has not cleared, return to 95% ethyl alcohol stage and repeat final steps of clearing procedure.

Notes

1. At the 50% ethyl alcohol concentration, tissue specimens may be bleached with 6% hydrogen peroxide for one day. After bleaching, continue the normal clearing procedure. Peroxide bleaching permits greater depth perception; however, this procedure must be considered against some loss in color contrast.
2. In the final stages of ethyl alcohol-methyl salicylate clearing, the clearing liquid may have a cloudy appearance. Addition of a small amount of 10% ethyl alcohol will alleviate this condition.

and man, a pressure of 150mm. Hg for arterial filling has been used, and 25 to 50mm.Hg for venous fillings.

After the vascular bed is perfused and the MICROFIL injection mass allowed to cure overnight at room temperature, the tissue is subjected to the clearing sequence described in Table 2. Thin tissues may be cleared without sectioning, but thicker organs, such as kidney or brain, should be cut into 1-centimeter slices before immersion. The alcohol-methyl salicylate clearing technique is applicable to all types of tissue with the exception of brain tissue. In the case of brain tissues, it is necessary to allow two days for each step, with an alcohol solution change every day.

Glycerine clearing

The animal is anesthetized with Nembutal, 25 mg/kg i.v., at the same time it is heparinized, to ensure effective removal of its blood volume during perfusion.

A midline incision exposes the abdominal viscera from the sternal notch to symphysis. Following the placement of an abdominal retractor, the thoracic cage is opened rapidly, the thoracic aorta isolated, and a polyethylene cannula inserted distally. The arterial cannula is connected to a sine wave perfusion pump and, prior to instigating perfusion, the right atrium is opened to serve as a drain vent.

The animal is perfused with saline until all of the visceral blood volume is flushed out and the perfusate drained through the arterial vent is essentially free of blood. Adequate perfusion is characterized by severe blanching of all visceral organs.

During perfusion, the curing agent is added to the MICROFIL injection mass. When perfusion is complete, the silicone rubber (e.g., MV-130 Red) is infused through the aortic cannula by syringe. When filling is complete, all organs have a rich, red coloration. MICROFIL compound infusion is continued until the injection mass flows freely from the atrial vent. The atrium and arterial cannula are then clamped and the animal is placed under refrigeration at 4°C overnight, to allow polymerization.

On the following day, specimens are taken by careful dissection, and placed in a 50% mixture of water and glycerin. At successive 24-hour intervals, the glycerin concentration is raised to 75%, then 85%, and finally pure glycerin. This procedure clears the tissue so that microscopic examination readily allows three-dimensional visualization of the vascular bed.



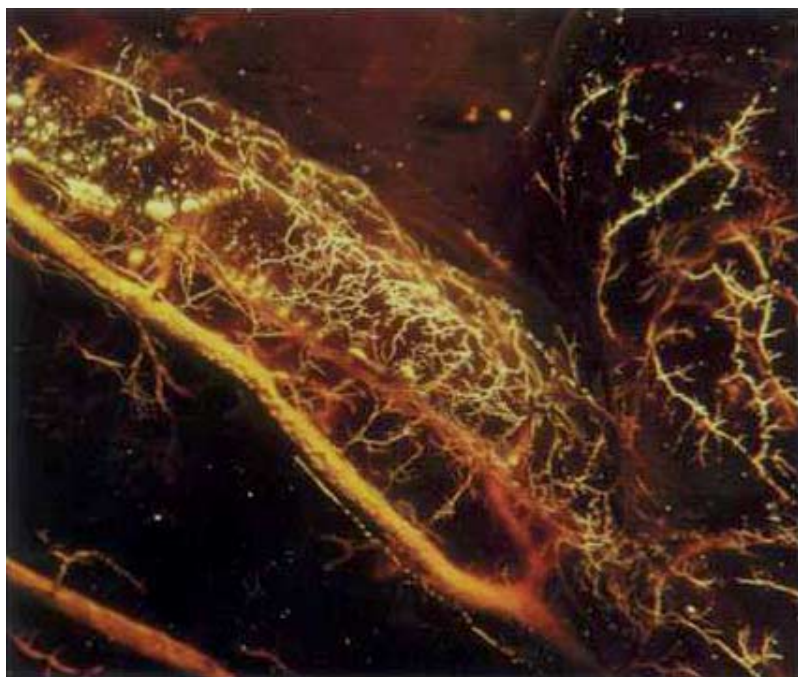
Cross-sectional view of monkey jejunum perfused with MICROFIL MV-118 (Maroon)* followed by MV-122 (Yellow).

Courtesy D. G. Reynolds, Walter Reed Army Institute of Research

*MV-118 (Maroon) is no longer available and has been replaced with MV-130 (Red).

Additional Notes

1. All MV-series compounds are compatible with one another. Therefore, it is possible to mix colors together to suit your needs (e.g., mix MV-120 Blue with MV-122 Yellow to produce a green compound).
2. Faster cure rates are possible by replacing the conventional MV Curing Agent with 2% ethyl silicate and 1% stannous octoate. Using this cross-link and curing agent combination decreases working time to 5 minutes with complete cure in 20 minutes. If you desire this type of cure system, please specify when placing your order. There is no extra charge for substituting this cure system in place of MV Curing Agent.
3. Occasionally it may be necessary to decrease viscosity by changing the mix ratio to either 2 or 3 parts MV-Diluent for each part MV compound. If your study requires such action, the correct level of MV Curing Agent is 10% (by weight) of the amount of MV compound used.
4. One procedure for vessel differentiation is to completely fill a given circulation with conventional MV compound (e.g., MV-130 Red) then, once the circulation is filled, immediately re-inject the artery with a high-viscosity version of MV compound in a different color (e.g., MV-120 Blue). This is accomplished by substituting MV-Diluent, which has a viscosity of 5 cps, with HV-Diluent, which has a viscosity of 1000 cps. With HV-Diluent, the viscosity of MV-130 Red increased to 350-450 cps. Although this procedure stopped penetration at the capillary level, complete success was obscured by shunting



activity. If you desire to replace MV-Diluent with HV-Diluent, please specify when placing your order. There is no extra charge for this substitution.

5. Store MICROFIL kits at room temperature for maximum retention of pigment dispersion. Keep all containers tightly capped. If pigment settling occurs, it is better to lightly shake the MICROFIL compound container and decant this portion. Stirring the container may put an agglomerated pigment particle into the system, which can be detrimental to perfusion.

6. If catalyzed material should spill on clothing, the best available solvent is MV-Diluent. To facilitate removal of cured compound, swelling and softening will occur on contact with an aromatic solvent such as toluene or xylene, and chlorinated solvents such as trichloroethylene.

Arterial injection of a dog kidney using MICROFIL MV-112 (White). Demonstrates filling of glomeruli and peritubular capillaries at 50x magnification.

Courtesy A. C. Berger, Harvard Medical School

≈



∞ Vasa vasorum of the human coronary artery filled with MICROFIL compound.

Courtesy of A. C. Barger, R. Beeuwkes III, L. L. Lainey and K. J. Silverman, Harvard Medical School

Cover Photo:
MICROFIL injection of the left coronary artery of
the human heart.
*Courtesy of A.C. Barger, R. Beeuwkes III, L.L. Lainey and
K.J. Silverman, Harvard Medical School*

Ordering Information

When ordering material, please remember kit weight is based upon the combined weight of MV compound and MV-Diluent (i.e., a 1-pound kit contains 8 ounces of MV compound and 8 ounces of MV-Diluent). In addition, each kit contains enough MV Curing Agent to cure the contents.

Kit Size Specifications	1 lb.	Any one color
	2 lb.	Any one or two colors
	8 lb.	(1 gallon) Any combination of colors

MICROFIL injection kits are available from:

Flow Tech, Inc.
P.O. Box 834
Carver, Massachusetts 02330
Tel: (508) 866-0007
Fax: (508) 866-0090

Terms: Net 30
FOB Carver

A bibliography is available on request.

While the information herein is believed to be reliable, Flow Tech does not guarantee its accuracy. Users are urged to perform their own tests. MICROFIL products are sold without warranty, and various patents may be pertinent to their use and to the use of compositions containing them. The information contained herein is not intended as a recommendation to use MICROFIL products so as to infringe on any patent. Flow Tech assumes no liability for the user's violation of patent or other rights.

©1996, Flow Tech, Inc. All rights reserved.

MICROFIL is a registered trademark of Flow Tech, Inc., Carver, Massachusetts.

Appendix E

Digital Files

Some additional supplementary files can be accessed online at <http://1drv.ms/1S7qigU>.

References

- [1] World Health Organisation, “WHO global estimates on prevalence of hearing loss,” http://www.who.int/pbd/deafness/WHO_GE_HL.pdf, 2012, accessed: 30 November 2014.
- [2] C. Mathers, A. Smith, and M. Concha, “Global burden of hearing loss in the year 2000,” *Global Burden of Disease*, vol. 18, 2000.
- [3] Access Economics, “Listen hear!: The economic impact and cost of hearing loss in Australia,” 2006.
- [4] B. Mo, M. Lindbæk, and S. Harris, “Cochlear implants and quality of life: a prospective study,” *Ear and hearing*, vol. 26, no. 2, pp. 186–194, 2005.
- [5] D. H. Wilson, P. G. Walsh, L. Sanchez, and P. Reed, “Hearing impairment in an Australian population,” 1998, centre for Population Studies in Epidemiology, South Australian Department of Human Services.
- [6] National Institute on Deafness and Other Communication Disorders, “Cochlear implants,” <http://www.nidcd.nih.gov/health/hearing/pages/coch.aspx>, 2014, NIH publication no. 11-4798; accessed: 1 December 2014.
- [7] F. G. Zeng, S. Rebscher, W. Harrison, X. Sun, and H. Feng, “Cochlear implants: system design, integration, and evaluation,” *Biomedical Engineering, IEEE Reviews in*, vol. 1, pp. 115–142, 2008.
- [8] P. Loizou, “Mimicking the human ear,” *Signal Processing Magazine, IEEE*, vol. 15, no. 5, pp. 101–130, 1998.

REFERENCES

- [9] B. S. Wilson, C. C. Finley, D. T. Lawson, R. D. Wolford, D. K. Eddington, and W. M. Rabinowitz, "Better speech recognition with cochlear implants," *Nature*, vol. 352, no. 6332, pp. 236–238, 1991.
- [10] G. Clark, "Electrical stimulation of the auditory nerve: the coding of frequency, the perception of pitch and the development of cochlear implant speech processing strategies for profoundly deaf people," *Clinical and experimental pharmacology and physiology*, vol. 23, no. 9, pp. 766–776, 1996.
- [11] P. Seligman and R. Shepherd, *Neuroprosthetics: Theory and practice*. World Scientific, 2004.
- [12] C. van den Honert and D. C. Kelsall, "Focused intracochlear electric stimulation with phased array channels," *The Journal of the Acoustical Society of America*, vol. 121, no. 6, pp. 3703–3716, 2007.
- [13] J. M. Miller, D. H. Chi, L. J. O’Keeffe, P. Kruszka, Y. Raphael, and R. A. Altschuler, "Neurotrophins can enhance spiral ganglion cell survival after inner hair cell loss," *International Journal of Developmental Neuroscience*, vol. 15, no. 4, pp. 631–643, 1997.
- [14] M. Tykocinski, L. T. Cohen, B. C. Pyman, T. Roland Jr, C. Treaba, J. Palamara, M. C. Dahm, R. K. Shepherd, J. Xu, R. S. Cowan *et al.*, "Comparison of electrode position in the human cochlea using various perimodiolar electrode arrays," *Otology & Neurotology*, vol. 21, no. 2, pp. 205–211, 2000.
- [15] R. Briggs, M. Tykocinski, E. Saunders, W. Hellier, M. Dahm, B. Pyman, and G. Clark, "Surgical implications of perimodiolar cochlear implant electrode design: avoiding intracochlear damage and scala vestibuli insertion," *Cochlear implants international*, vol. 2, no. 2, pp. 135–149, 2001.
- [16] F. van der Beek, P. Boermans, B. Verbist, J. Briaire, and J. Frijns, "Clinical evaluation of the clarion cii hifocus 1 with and without positioner," *Ear and hearing*, vol. 26, no. 6, pp. 577–592, 2005.
- [17] P. Wardrop, D. Whinney, S. J. Rebscher, J. T. Roland, W. Luxford, and P. A. Leake, "A temporal bone study of insertion trauma and intracochlear position of cochlear

REFERENCES

- implant electrodes. i: Comparison of nucleus banded and nucleus contour electrodes,” *Hearing research*, vol. 203, no. 1, pp. 54–67, 2005.
- [18] P. Wardrop, D. Whinney, S. J. Rebscher, W. Luxford, and P. Leake, “A temporal bone study of insertion trauma and intracochlear position of cochlear implant electrodes. ii: comparison of spiral clarion and hifocus ii electrodes,” *Hearing research*, vol. 203, no. 1, pp. 68–79, 2005.
- [19] R. T. Richardson, A. K. Wise, B. C. Thompson, B. O. Flynn, P. J. Atkinson, N. J. Fretwell, J. B. Fallon, G. G. Wallace, R. K. Shepherd, G. M. Clark *et al.*, “Polypyrrole-coated electrodes for the delivery of charge and neurotrophins to cochlear neurons,” *Biomaterials*, vol. 30, no. 13, pp. 2614–2624, 2009.
- [20] G. Girzon, “Investigation of current flow in the inner ear during electrical stimulation of intracochlear electrodes,” Master’s thesis, Massachusetts Institute of Technology, Dept. of Electrical Engineering and Computer Science, 1987.
- [21] A. Micco and C. P. Richter, “Tissue resistivities determine the current flow in the cochlea,” *Current Opinion in Otolaryngology & Head and Neck Surgery*, vol. 14, no. 5, p. 352, 2006.
- [22] D. Whiten, “Electro-anatomical models of the cochlear implant,” Ph.D. dissertation, Massachusetts Institute of Technology, 2007.
- [23] R. V. Shannon, F. G. Zeng, V. Kamath, J. Wygonski, and M. Ekelid, “Speech recognition with primarily temporal cues,” *Science*, vol. 270, no. 5234, pp. 303–304, 1995.
- [24] M. F. Dorman, P. C. Loizou, and D. Rainey, “Speech intelligibility as a function of the number of channels of stimulation for signal processors using sine-wave and noise-band outputs,” *The Journal of the Acoustical Society of America*, vol. 102, no. 4, pp. 2403–2411, 1997.
- [25] G. M. Clark, “Personal reflections on the multichannel cochlear implant and a view of the future,” *J Rehabil Res Dev*, vol. 45, no. 5, pp. 651–693, 2008.
- [26] ———, “The multichannel cochlear implant for severe-to-profound hearing loss,” *Nature medicine*, vol. 19, no. 10, pp. 1236–1239, 2013.
- [27] T. H. Bast and B. J. Anson, *The temporal bone and the ear*. CC Thomas, 1949.

REFERENCES

- [28] P. Dallos, A. N. Popper, and R. R. Fay, *The cochlea*. Springer New York, 1996, vol. 8.
- [29] F. Vanpoucke, A. Zarowski, and S. Peeters, “Identification of the impedance model of an implanted cochlear prosthesis from intracochlear potential measurements,” *Biomedical Engineering, IEEE Transactions on*, vol. 51, no. 12, pp. 2174–2183, 2004.
- [30] A. Kral, R. Hartmann, D. Mortazavi, and R. Klinke, “Spatial resolution of cochlear implants: the electrical field and excitation of auditory afferents,” *Hearing research*, vol. 121, no. 1, pp. 11–28, 1998.
- [31] R. Black and G. M. Clark, “Differential electrical excitation of the auditory nerve,” *The Journal of the Acoustical Society of America*, vol. 67, no. 3, pp. 868–874, 1980.
- [32] A. N. Salt and T. Konishi, *Neurobiology of Hearing: The Cochlea*. Raven Press, 1986, ch. 6. The Cochlear Fluids: Perilymph and Endolymph.
- [33] G. E. Moore, “Cramming more components onto integrated circuits,” *Proceedings of the IEEE*, vol. 86, no. 1, pp. 82–85, 1998.
- [34] T. Hanekom, T. K. Malherbe, L. Gross, R. Baron, R. Asvat, W. Badenhorst, and J. J. Hanekom, “Design and application of user-specific models of cochlear implants,” in *Implantable Auditory Prostheses (CIAP), 2015 Conference on*. ARO, 2015.
- [35] P. Schimpf, J. Haueisen, C. Ramon, and H. Nowak, “Realistic computer modelling of electric and magnetic fields of human head and torso,” *Parallel Computing*, vol. 24, no. 9-10, pp. 1433–1460, 1998.
- [36] P. Hariharan, “Computational modeling in medical devices,” <https://cstools.asme.org/CSCConnect/FileUpload.cfm?View=yes&ID=36699>, 2012, accessed: 16 June 2014.
- [37] R. Saba, “Cochlear implant modelling: stimulation and power consumption,” Ph.D. dissertation, University of Southampton, 2012.
- [38] G. E. Box and N. R. Draper, *Empirical model-building and response surfaces*. John Wiley & Sons, 1987.
- [39] E. Goldstein, *Sensation and perception*. Wadsworth Pub. Co., 2009.
- [40] F. Martini, M. Timmons, and R. Tallitsch, *Human anatomy*. Daryl Fox, 2006.

REFERENCES

- [41] A. Jahn and J. Santos-Sacchi, *Physiology of the Ear*. Singular Publishing Group, 2001.
- [42] P. Wangemann and J. Schacht, “Homeostatic mechanisms in the cochlea,” in *The cochlea*. Springer, 1996, pp. 130–185.
- [43] C. Y. Ota and R. S. Kimura, “Ultrastructural study of the human spiral ganglion,” *Acta oto-laryngologica*, vol. 89, no. 1-2, pp. 53–62, 1980.
- [44] B. M. Verbist, M. W. Skinner, L. T. Cohen, P. A. Leake, C. James, C. Boëx, T. A. Holden, C. C. Finley, P. S. Roland, J. T. Roland Jr *et al.*, “Consensus panel on a cochlear coordinate system applicable in histological, physiological and radiological studies of the human cochlea,” *Otology & neurotology: official publication of the American Otological Society, American Neurotology Society [and] European Academy of Otology and Neurotology*, vol. 31, no. 5, p. 722, 2010.
- [45] P. Tate, *Seeley’s Principles of Anatomy & Physiology*. McGraw-Hill, 2012.
- [46] P. Flint, B. Haughey, V. Lund, J. Niparko, M. Richardson, K. Robbins, and J. Thomas, *Cummings Laryngology: Head and Neck Surgery*. Mosby, 2010.
- [47] E. Erixon, H. Högstorp, K. Wadin, and H. Rask-Andersen, “Variational anatomy of the human cochlea implications for cochlear implantation,” *Otology & Neurotology*, vol. 30, no. 1, p. 14, 2009.
- [48] J. Nadol Jr, “Hearing loss,” *New England Journal of Medicine*, vol. 329, no. 15, pp. 1092–1102, 1993.
- [49] A. Axelsson, “The vascular anatomy of the cochlea in the guinea pig and in man,” *Acta oto-laryngologica*, pp. 5–134, 1968.
- [50] I. Ibsen, “Anatomiske undersøgelser over flörets labyrinth,” *Prof. Panum, Köpenhamn*, 1881.
- [51] G. Schwalbe, “Über die glomeruli arteriosi der gehörschnecke,” *Anat. Anz*, vol. 4, pp. 93–96, 1887.
- [52] O. Eichler, *Anatomische Untersuchungen über die Wege des Blutstromes im menschlichen Ohrlabyrinth*. Hirzel, S., 1892.

REFERENCES

- [53] F. Siebenmann, *Die Blutgefäße im Labyrinth des menschlichen Ohres*. J.F. Bergmann, 1894.
- [54] D. Nabeya, *A study in the comparative anatomy of the blood-vascular system of the internal ear in Mammalia and in Homo (Japanese)*. Universitas Imperialis, 1923.
- [55] R. Scuderi and M. Del Bo, “La vascolarizzazione del labirinto umano,” *Arch. Ital. Otol.*, vol. 63, 1952.
- [56] A. Leblanc, *Atlas of hearing and balance organs: a practical guide for otolaryngologists*. Springer, 1999.
- [57] T. Nakashima, S. Naganawa, M. Sone, M. Tominaga, H. Hayashi, H. Yamamoto, X. Liu, and A. Nuttall, “Disorders of cochlear blood flow,” *Brain research reviews*, vol. 43, no. 1, pp. 17–28, 2003.
- [58] T. Ifukube and R. White, “Current distributions produced inside and outside the cochlea from a scala tympani electrode array,” *Biomedical Engineering, IEEE Transactions on*, no. 11, pp. 883–890, 1987.
- [59] D. D. Greenwood, “A cochlear frequency-position function for several species—29 years later,” *The Journal of the Acoustical Society of America*, vol. 87, no. 6, pp. 2592–2605, 1990.
- [60] F. G. Zeng, A. N. Popper, and R. R. Fay, *Cochlear implants: Auditory prostheses and electric hearing*. Springer Science & Business Media, 2004, vol. 20.
- [61] G. Cooper and A. L. Schiller, *Anatomy of the guinea pig*. Harvard University Press, 1975.
- [62] R. T. Miyamoto, “Electrically evoked potentials in cochlear implant subjects,” *The Laryngoscope*, vol. 96, no. 2, pp. 178–185, 1986.
- [63] J. B. Nadol, “Comparative anatomy of the cochlea and auditory nerve in mammals,” *Hearing research*, vol. 34, no. 3, pp. 253–266, 1988.
- [64] M. Thorne, A. N. Salt, J. E. DeMott, M. M. Henson, O. Henson, and S. L. Gewalt, “Cochlear fluid space dimensions for six species derived from reconstructions of three-dimensional magnetic resonance images,” *The Laryngoscope*, vol. 109, no. 10, pp. 1661–1668, 1999.

REFERENCES

- [65] J. Frijns, J. Briaire, and J. Grote, “The importance of human cochlear anatomy for the results of modiolus-hugging multichannel cochlear implants,” *Otology & neurotology*, vol. 22, no. 3, p. 340, 2001.
- [66] G. von Békésy, *Experiments in hearing*. McGraw Hill, 1960.
- [67] B. E. Pfingst, S. A. Bowling, D. J. Colesa, S. N. Garadat, Y. Raphael, S. B. Shibata, S. B. Strahl, G. L. Su, and N. Zhou, “Cochlear infrastructure for electrical hearing,” *Hearing research*, vol. 281, no. 1, pp. 65–73, 2011.
- [68] J. Nadol Jr and D. Eddington, “Treatment of sensorineural hearing loss by cochlear implantation,” *Annual review of medicine*, vol. 39, no. 1, pp. 491–502, 1988.
- [69] A. Brown, *Nerve cells and nervous systems: An introduction to neuroscience*. Springer Verlag, 2001.
- [70] J. B. Fallon, D. R. Irvine, and R. K. Shepherd, “Cochlear implants and brain plasticity,” *Hearing research*, vol. 238, no. 1, pp. 110–117, 2008.
- [71] J. Webster, *Medical Instrumentation: Application and Design*. John Wiley & Sons, Inc., 1998.
- [72] J. Xu, A. W. Stevenson, D. Gao, M. Tykocinski, D. Lawrence, S. W. Wilkins, G. M. Clark, E. Saunders, and R. S. Cowan, “The role of radiographic phase-contrast imaging in the development of intracochlear electrode arrays,” *Otology & neurotology*, vol. 22, no. 6, pp. 862–868, 2001.
- [73] D. K. Eddington, W. Dobbelle, D. Brackmann, M. Mladejovsky, and J. Parkin, “Auditory prostheses research with multiple channel intracochlear stimulation in man.” *The Annals of otology, rhinology, and laryngology*, vol. 87, no. 6 Pt 2, pp. 1–39, 1977.
- [74] P. Busby, L. Whitford, P. J. Blamey, L. Richardson, and G. M. Clark, “Pitch perception for different modes of stimulation using the cochlear multiple-electrode prosthesis,” *The Journal of the Acoustical Society of America*, vol. 95, no. 5, pp. 2658–2669, 1994.
- [75] S. Grimnes and Ø. Martinsen, *Bioimpedance and bioelectricity basics*. Academic Press, 2000.

REFERENCES

- [76] D. R. Merrill, M. Bikson, and J. G. Jefferys, “Electrical stimulation of excitable tissue: Design of efficacious and safe protocols,” *Journal of neuroscience methods*, vol. 141, no. 2, pp. 171–198, 2005.
- [77] S. Brummer and M. Turner, “Electrochemical considerations for safe electrical stimulation of the nervous system with platinum electrodes,” *Biomedical Engineering, IEEE Transactions on*, no. 1, pp. 59–63, 1977.
- [78] J. C. Lilly, J. R. Hughes, E. C. Alvord Jr, and T. W. Galkin, “Brief, noninjurious electric waveform for stimulation of the brain.” *Science*, 1955.
- [79] R. K. Shepherd, J. Matsushima, R. Millard, and G. M. Clark, “Cochlear pathology following chronic electrical stimulation using non charge balanced stimuli,” *Acta otolaryngologica*, vol. 111, no. 3, pp. 848–860, 1991.
- [80] S. F. Cogan, “Neural stimulation and recording electrodes,” *Annu. Rev. Biomed. Eng.*, vol. 10, pp. 275–309, 2008.
- [81] J. B. Ranck, “Which elements are excited in electrical stimulation of mammalian central nervous system: a review,” *Brain research*, vol. 98, no. 3, pp. 417–440, 1975.
- [82] J. P. Reilly, *Applied bioelectricity: from electrical stimulations to electropathology*. Springer, 1998.
- [83] L. Geddes, “Electrodes and the measurement of bioelectric events,” *Chicester: Interscience*, 1972.
- [84] R. S. Cobbold, *Transducers for biomedical measurements: principles and applications*. John Wiley & Sons, 1974, vol. 15.
- [85] G. M. Clark, “The multiple-channel cochlear implant: the interface between sound and the central nervous system for hearing, speech, and language in deaf people—a personal perspective,” *Philosophical Transactions of the Royal Society B: Biological Sciences*, vol. 361, no. 1469, pp. 791–810, 2006.
- [86] B. H. Bonham and L. M. Litvak, “Current focusing and steering: modeling, physiology, and psychophysics,” *Hearing research*, vol. 242, no. 1, pp. 141–153, 2008.

REFERENCES

- [87] J. Frijns, D. Dekker, and J. Briaire, “Neural excitation patterns induced by phased-array stimulation in the implanted human cochlea,” *Acta oto-laryngologica*, vol. 131, no. 4, pp. 362–370, 2011.
- [88] S. S. George, A. K. Wise, M. N. Shivdasani, R. K. Shepherd, and J. B. Fallon, “Evaluation of focused multipolar stimulation for cochlear implants in acutely deafened cats,” *Journal of neural engineering*, vol. 11, no. 6, p. 065003, 2014.
- [89] G. Stickney, F. Zeng, R. Litovsky, and P. Assmann, “Cochlear implant speech recognition with speech maskers,” *The Journal of the Acoustical Society of America*, vol. 116, p. 1081, 2004.
- [90] K. Gfeller, C. Turner, J. Oleson, X. Zhang, B. Gantz, R. Froman, and C. Olszewski, “Accuracy of cochlear implant recipients on pitch perception, melody recognition, and speech reception in noise,” *Ear and hearing*, vol. 28, no. 3, p. 412, 2007.
- [91] M. Leal, Y. Shin, M. Laborde, M. Calmels, S. Verges, S. Lugaardon, S. Andrieu, O. Deguine, and B. Fraysse, “Music perception in adult cochlear implant recipients,” *Acta oto-laryngologica*, vol. 123, no. 7, pp. 826–835, 2003.
- [92] H. McDermott, “Music perception with cochlear implants: a review,” *Trends in amplification*, vol. 8, no. 2, p. 49, 2004.
- [93] C. M. Sucher and H. J. McDermott, “Pitch ranking of complex tones by normally hearing subjects and cochlear implant users,” *Hearing research*, vol. 230, no. 1, pp. 80–87, 2007.
- [94] V. Ciocca, A. Francis, R. Aisha, and L. Wong, “The perception of cantonese lexical tones by early-deafened cochlear implantees,” *The Journal of the Acoustical Society of America*, vol. 111, p. 2250, 2002.
- [95] L. Xu, Y. Tsai, and B. Pfingst, “Features of stimulation affecting tonal-speech perception: Implications for cochlear prostheses,” *The Journal of the Acoustical Society of America*, vol. 112, p. 247, 2002.
- [96] C. Wei, K. Cao, and F. Zeng, “Mandarin tone recognition in cochlear-implant subjects,” *Hearing research*, vol. 197, no. 1-2, pp. 87–95, 2004.

REFERENCES

- [97] M. W. Skinner, G. M. Clark, L. A. Whitford, P. M. Seligman, S. J. Staller, D. B. Shipp, J. K. Shallop, C. Everingham, C. M. Menapace, P. L. Arndt *et al.*, “Evaluation of a new spectral peak coding strategy for the nucleus 22 channel cochlear implant system.” *Otology & Neurotology*, vol. 15, pp. 15–27, 1994.
- [98] F. Spelman, B. Clopton, and B. Pfingst, “Tissue impedance and current flow in the implanted ear. Implications for the cochlear prosthesis.” *The Annals of otology, rhinology & laryngology. Supplement*, vol. 98, p. 3, 1982.
- [99] M. Suesserman and F. Spelman, “Lumped-parameter model for in vivo cochlear stimulation,” *Biomedical Engineering, IEEE Transactions on*, vol. 40, no. 3, pp. 237–245, 1993.
- [100] J. Frijns, S. De Snoo, and R. Schoonhoven, “Potential distributions and neural excitation patterns in a rotationally symmetric model of the electrically stimulated cochlea,” *Hearing research*, vol. 87, no. 1-2, pp. 170–186, 1995.
- [101] C. Potratz, S. Petersen, A. Grunbaum, and U. van Rienen, “Challenges in bioelectromagnetic modeling,” in *Electromagnetic Theory (EMTS), 2010 URSI International Symposium on Electromagnetic Theory*. IEEE, 2010, pp. 344–347.
- [102] J. Maxwell, “A dynamical theory of the electromagnetic field,” *Philosophical Transactions of the Royal Society of London*, vol. 155, pp. 459–512, 1865.
- [103] L. Baker, “Principles of the impedance technique,” *Engineering in Medicine and Biology Magazine, IEEE*, vol. 8, no. 1, pp. 11–15, 1989.
- [104] G. Machado and C. Toumazou, “An analytical lumped-parameter 3D cochlear model and architecture for cochlear signal processing in VLSI,” in *1996 IEEE International Symposium on Circuits and Systems (ISCAS’96)*, vol. 4. IEEE, 1996, pp. 492–495.
- [105] J. Briaire and J. Frijns, “3D mesh generation to solve the electrical volume conduction problem in the implanted inner ear,” *Simulation Practice and Theory*, vol. 8, no. 1-2, pp. 57–73, 2000.
- [106] G. von Békésy, “The coarse pattern of the electrical resistance in the cochlea of the guinea pig (electroanatomy of the cochlea),” *The Journal of the Acoustical Society of America*, vol. 23, p. 18, 1951.

REFERENCES

- [107] A. Bondeson, T. Rylander, and P. Ingelström, *Computational electromagnetics*. Springer-Verlag New York Inc, 2005, vol. 51.
- [108] Z. Cendes, “Unlocking the magic of Maxwell’s equations,” *Spectrum, IEEE*, vol. 26, no. 4, pp. 29–33, 1989.
- [109] C. Miller and C. Henriquez, “Finite element analysis of bioelectric phenomena,” *Critical reviews in biomedical engineering*, vol. 18, no. 3, pp. 207–233, 1990.
- [110] C. Johnson, *Biomedical Engineering Fundamentals*. Taylor & Francis Group, 2006, ch. 23. Computational Methods and Software for Bioelectric Field Problems.
- [111] J. N. Reddy, *An introduction to the finite element method*. McGraw-Hill New York, 2006, vol. 3.
- [112] P. Tran, A. Sue, P. Wong, Q. Li, and P. Carter, “Development of HEATHER for cochlear implant stimulation using a new modeling workflow,” *Biomedical Engineering, IEEE Transactions on*, vol. 62, no. 2, pp. 728–735, February 2015.
- [113] J. T. Katsikadelis, *Boundary Elements: Theory and Applications*. Elsevier, 2002.
- [114] A. L. Hodgkin and A. F. Huxley, “A quantitative description of membrane current and its application to conduction and excitation in nerve,” *The Journal of physiology*, vol. 117, no. 4, pp. 500–544, 1952.
- [115] B. Frankenhaeuser and A. F. Huxley, “The action potential in the myelinated nerve fibre of xenopus laevis as computed on the basis of voltage clamp data,” *The Journal of Physiology*, vol. 171, no. 2, pp. 302–315, 1964.
- [116] D. Strelhoff, “A computer simulation of the generation and distribution of cochlear potentials,” *The Journal of the Acoustical Society of America*, vol. 54, p. 620, 1973.
- [117] F. Rattay, *Electrical nerve stimulation: theory, experiments and applications*. Springer, 1990.
- [118] M. Åström, E. Diczfalusy, H. Martens, and K. Wardell, “Relationship between neural activation and electric field distribution during deep brain stimulation,” *Biomedical Engineering, IEEE Transactions on*, vol. 62, no. 2, pp. 664–672, 2015.

REFERENCES

- [119] D. McNeal, “Analysis of a model for excitation of myelinated nerve,” *Biomedical Engineering, IEEE Transactions on*, no. 4, pp. 329–337, 1976.
- [120] I. C. Bruce, M. W. White, L. S. Irlicht, S. J. Leary, S. Dynes, E. Javel, and G. M. Clark, “A stochastic model of the electrically stimulated auditory nerve: single-pulse response,” *Biomedical Engineering, IEEE Transactions on*, vol. 46, no. 6, pp. 617–629, 1999.
- [121] J. P. Reilly, V. T. Freeman, and W. D. Larkin, “Sensory effects of transient electrical stimulation-evaluation with a neuroelectric model,” *Biomedical Engineering, IEEE Transactions on*, no. 12, pp. 1001–1011, 1985.
- [122] M. C. Liberman and M. E. Oliver, “Morphometry of intracellularly labeled neurons of the auditory nerve: correlations with functional properties,” *Journal of Comparative Neurology*, vol. 223, no. 2, pp. 163–176, 1984.
- [123] J. Colombo and C. W. Parkins, “A model of electrical excitation of the mammalian auditory-nerve neuron,” *Hearing research*, vol. 31, no. 3, pp. 287–311, 1987.
- [124] F. Rattay, “Analysis of models for external stimulation of axons,” *Biomedical Engineering, IEEE Transactions on*, no. 10, pp. 974–977, 1986.
- [125] —, “The basic mechanism for the electrical stimulation of the nervous system,” *Neuroscience*, vol. 89, no. 2, pp. 335–346, 1999.
- [126] F. Rattay, P. Lutter, and H. Felix, “A model of the electrically excited human cochlear neuron: I. contribution of neural substructures to the generation and propagation of spikes,” *Hearing research*, vol. 153, no. 1, pp. 43–63, 2001.
- [127] J. R. Schwarz and G. Eikhof, “Na currents and action potentials in rat myelinated nerve fibres at 20 and 37 c,” *Pflügers Archiv*, vol. 409, no. 6, pp. 569–577, 1987.
- [128] J. Frijns and J. Ten Kate, “A model of myelinated nerve fibres for electrical prosthesis design,” *Medical and Biological Engineering and Computing*, vol. 32, no. 4, pp. 391–398, 1994.
- [129] H. Meffin, B. Tahayori, D. B. Grayden, and A. N. Burkitt, “Modeling extracellular electrical stimulation: I. derivation and interpretation of neurite equations,” *Journal of neural engineering*, vol. 9, no. 6, p. 065005, 2012.

REFERENCES

- [130] B. Tahayori, H. Meffin, S. Dokos, A. N. Burkitt, and D. B. Grayden, “Modeling extracellular electrical stimulation: Ii. computational validation and numerical results,” *Journal of neural engineering*, vol. 9, no. 6, p. 065006, 2012.
- [131] H. Meffin, B. Tahayori, E. N. Sergeev, I. M. Mareels, D. B. Grayden, and A. N. Burkitt, “Modelling extracellular electrical stimulation: Iii. derivation and interpretation of neural tissue equations,” *Journal of neural engineering*, vol. 11, no. 6, p. 065004, 2014.
- [132] B. Tahayori, H. Meffin, E. N. Sergeev, I. M. Mareels, A. N. Burkitt, and D. B. Grayden, “Modelling extracellular electrical stimulation: Iv. effect of the cellular composition of neural tissue on its spatio-temporal filtering properties,” *Journal of neural engineering*, vol. 11, no. 6, p. 065005, 2014.
- [133] L. Geddes and L. Baker, “The specific resistance of biological material—a compendium of data for the biomedical engineer and physiologist,” *Medical and Biological Engineering and Computing*, vol. 5, no. 3, pp. 271–293, 1967.
- [134] G. Misrahy, K. Hildreth, E. Shinabarger, and W. Gannon, “Electrical properties of wall of endolymphatic space of the cochlea (guinea pig),” *American Journal of Physiology*, vol. 194, no. 2, p. 396, 1958.
- [135] B. Johnstone, J. Johnstone, I. Pugsley *et al.*, “Membrane resistance in endolymphatic walls of the first turn of the guinea-pig cochlea,” *J. Acoust. Soc. Am.*, vol. 40, pp. 1398–1404, 1966.
- [136] R. Black, G. M. Clark, Y. Tong, and J. Patrick, “Current distributions in cochlear stimulation,” *Annals of the New York Academy of Sciences*, vol. 405, no. 1, pp. 137–145, 1983.
- [137] B. Townshend, “Electrical interactions in auditory prostheses,” Ph.D. dissertation, Stanford University, 1987.
- [138] G. Machado and C. Toumazou, “Analytical generation of parameters for in-vivo lumped-parameter models of implanted and normal cochleae,” in *Engineering in Medicine and Biology Society, 1995., IEEE 17th Annual Conference*, vol. 2. IEEE, 1995, pp. 1607–1608.

REFERENCES

- [139] C. Jolly, F. Spelman, and B. Clopton, “Quadrupolar stimulation for cochlear prostheses: modeling and experimental data,” *Biomedical Engineering, IEEE Transactions on*, vol. 43, no. 8, pp. 857–865, 1996.
- [140] F. Vanpoucke, A. Zarowski, J. Casselman, J. Frijns, and S. Peeters, “The facial nerve canal: an important cochlear conduction path revealed by clarion electrical field imaging,” *Otology & Neurotology*, vol. 25, no. 3, pp. 282–289, 2004.
- [141] H. P. Schwan and C. F. Kay, “Capacitive properties of body tissues,” *Circulation Research*, vol. 5, no. 4, pp. 439–443, 1957.
- [142] C. Finley, B. Wilson, and M. White, “A finite-element model of bipolar field patterns in the electrically stimulated cochlea—a two-dimensional approximation,” in *Engineering in Medicine and Biology Society, 1987., Proceedings of the Ninth Annual International Conference of the IEEE Engineering in Medicine and Biology Society*. IEEE, 1987, pp. 1901–1903.
- [143] C. Finley, “A finite-element model of radial bipolar field patterns in the electrically stimulated cochlea—two and three dimensional approximations and tissue parameter sensitivities,” in *Engineering in Medicine and Biology Society, 1989., Proceedings of the Annual International Conference of the IEEE Engineering in Medicine and Biology Society*. IEEE, 1989, pp. 1059–1060.
- [144] C. Finley, B. Wilson, and M. White, “Models of neural responsiveness to electrical stimulation,” *Cochlear implants: models of the electrically stimulated ear*, vol. 56, 1990.
- [145] J. Frijns, J. Briaire, and R. Schoonhoven, “Integrated use of volume conduction and neural models to simulate the response to cochlear implants,” *Simulation Practice and Theory*, vol. 8, no. 1-2, pp. 75–97, 2000.
- [146] J. Briaire and J. Frijns, “Field patterns in a 3D tapered spiral model of the electrically stimulated cochlea,” *Hearing research*, vol. 148, no. 1-2, pp. 18–30, 2000.
- [147] R. K. Kalkman, J. J. Briaire, D. M. Dekker, and J. Frijns, “Place pitch versus electrode location in a realistic computational model of the implanted human cochlea,” *Hearing research*, vol. 315, pp. 10–24, 2014.

REFERENCES

- [148] J. Frijns, S. De Snoo, and J. Ten Kate, “Spatial selectivity in a rotationally symmetric model of the electrically stimulated cochlea,” *Hearing research*, vol. 95, no. 1-2, pp. 33–48, 1996.
- [149] J. Briaire and J. Frijns, “Unraveling the electrically evoked compound action potential,” *Hearing research*, vol. 205, no. 1, pp. 143–156, 2005.
- [150] ———, “The consequences of neural degeneration regarding optimal cochlear implant position in scala tympani: a model approach,” *Hearing research*, vol. 214, no. 1, pp. 17–27, 2006.
- [151] J. Frijns, R. Kalkman, F. Vanpoucke, J. Bongers, and J. Briaire, “Simultaneous and non-simultaneous dual electrode stimulation in cochlear implants: evidence for two neural response modalities,” *Acta oto-laryngologica*, vol. 129, no. 4, pp. 433–439, 2009.
- [152] J. Frijns, R. Kalkman, and J. Briaire, “Stimulation of the facial nerve by intracochlear electrodes in otosclerosis: a computer modeling study,” *Otology & Neurotology*, vol. 30, no. 8, p. 1168, 2009.
- [153] R. K. Kalkman, J. J. Briaire, and J. Frijns, “Current focussing in cochlear implants: An analysis of neural recruitment in a computational model,” *Hearing research*, vol. 322, pp. 89–98, 2015.
- [154] B. Escudé, C. James, O. Deguine, N. Cochard, E. Eter, and B. Fraysse, “The size of the cochlea and predictions of insertion depth angles for cochlear implant electrodes,” *Audiology and Neurotology*, vol. 11, no. 1, pp. 27–33, 2006.
- [155] T. Hanekom, “Three-dimensional spiraling finite element model of the electrically stimulated cochlea,” *Ear and hearing*, vol. 22, no. 4, p. 300, 2001.
- [156] ———, “Modelling encapsulation tissue around cochlear implant electrodes,” *Medical and Biological Engineering and Computing*, vol. 43, no. 1, pp. 47–55, 2005.
- [157] T. K. Malherbe, T. Hanekom, and J. J. Hanekom, “Can subject-specific single-fibre electrically evoked auditory brainstem response data be predicted from a model?” *Medical engineering & physics*, vol. 35, no. 7, pp. 926–936, 2013.

REFERENCES

- [158] ———, “The effect of the resistive properties of bone on neural excitation and electric fields in cochlear implant models,” *Hearing Research*, vol. 327, pp. 126–135, 2015.
- [159] F. Rattay, R. N. Leao, and H. Felix, “A model of the electrically excited human cochlear neuron. ii. influence of the three-dimensional cochlear structure on neural excitability,” *Hearing research*, vol. 153, no. 1, pp. 64–79, 2001.
- [160] C. Choi and C. Hsu, “Conditions for generating virtual channels in cochlear prosthesis systems,” *Annals of biomedical engineering*, vol. 37, no. 3, pp. 614–624, 2009.
- [161] C. Choi, “Shape optimization of cochlear implant electrode array using genetic algorithms,” in *Engineering in Medicine and Biology Society, 2001. Proceedings of the 23rd Annual International Conference of the IEEE*, vol. 2. IEEE, 2001, pp. 1445–1448.
- [162] C. Choi, W. Lai, and S. Lee, “A novel approach to compute the impedance matrix of a cochlear implant system incorporating an electrode-tissue interface based on finite element method,” *Magnetics, IEEE Transactions on*, vol. 42, no. 4, pp. 1375–1378, 2006.
- [163] C. Choi, W. Lai, and Y. Chen, “Optimization of cochlear implant electrode array using genetic algorithms and computational neuroscience models,” *Magnetics, IEEE Transactions on*, vol. 40, no. 2, pp. 639–642, 2004.
- [164] ———, “Comparison of the electrical stimulation performance of four cochlear implant electrodes,” *Magnetics, IEEE Transactions on*, vol. 41, no. 5, pp. 1920–1923, 2005.
- [165] C. Choi and S. P. Wang, “Modeling ECAP in cochlear implants using the fem and equivalent circuits,” *Magnetics, IEEE Transactions on*, vol. 50, no. 2, pp. 49–52, 2014.
- [166] G. Tognola, A. Pesatori, M. Norgia, M. Parazzini, L. Di Rienzo, P. Ravazzani, S. Burdo, F. Grandori, and C. Svelto, “Numerical modeling and experimental measurements of the electric potential generated by cochlear implants in physiological tissues,” *Instrumentation and Measurement, IEEE Transactions on*, vol. 56, no. 1, pp. 187–193, 2007.
- [167] S. Gabriel, R. Lau, and C. Gabriel, “The dielectric properties of biological tissues: II. Measurements in the frequency range 10 Hz to 20 GHz,” *Physics in Medicine and Biology*, vol. 41, p. 2251, 1996.

REFERENCES

- [168] S. Peterson, L. Frishkopff, C. Lechène, C. Oman, and T. Weiss, “Element composition of inner ear lymphs in cats, lizards, and skates determined by electron probe microanalysis of liquid samples,” *Journal of Comparative Physiology A: Neuroethology, Sensory, Neural, and Behavioral Physiology*, vol. 126, no. 1, pp. 1–14, 1978.
- [169] J. Zakis and M. Witte, “Modelling of the cochlea using java 3D,” in *IEEE Engineering in Medicine and Biology Society*, 2001, pp. 1–5.
- [170] R. MacLeod, J. Stinstra, S. Lew, R. Whitaker, D. Swenson, M. Cole, J. Krüger, D. Brooks, and C. Johnson, “Subject-specific, multiscale simulation of electrophysiology: a software pipeline for image-based models and application examples,” *Philosophical Transactions of the Royal Society A: Mathematical, Physical and Engineering Sciences*, vol. 367, no. 1896, pp. 2293–2310, 2009.
- [171] H. Lau, A. Ruys, P. Carter, X. Wang, and Q. Li, “Subject specific modelling of electrical conduction in the body: a case study,” *Journal of Biomimetics, Biomaterials, and Tissue Engineering*, vol. 10, pp. 43–53, 2011.
- [172] D. Beneke, “Home - David Beneke Consulting,” <http://davidbenekeconsulting.com/>, 2014, accessed: 14 December 2014.
- [173] P. Wong, Q. Li, and P. Carter, “Incorporating vascular structure into electric volume conduction models of the cochlea,” in *Biomedical Engineering and Sciences (IECBES), 2012 IEEE EMBS Conference on*. IEEE, 2012, pp. 694–699.
- [174] R. Charachon, *Anatomie de l’artère auditive interne chez l’homme*. Imprimerie Bosc. Frères, 1961.
- [175] W. Mondy, “Data acquisition for modeling and visualization of vascular tree,” Ph.D. dissertation, University of South Florida, 2009.
- [176] A. A. Poznyakovskiy, T. Zahnert, Y. Kalaidzidis, R. Schmidt, B. Fischer, J. Baumgart, and Y. M. Yarin, “The creation of geometric three-dimensional models of the inner ear based on micro computer tomography data,” *Hearing research*, vol. 243, no. 1, pp. 95–104, 2008.
- [177] K. Braun, F. Böhnke, and T. Stark, “Three-dimensional representation of the human cochlea using micro-computed tomography data: presenting an anatomical model for

REFERENCES

- further numerical calculations,” *Acta oto-laryngologica*, vol. 132, no. 6, pp. 603–613, 2012.
- [178] S. B. Johnson, S. Cureoglu, J. T. O’Malley, and P. A. Santi, “Comparison of traditional histology and TSLIM optical sectioning of human temporal bones,” *Otology & Neurotology*, vol. 35, no. 7, pp. 1145–1149, 2014.
- [179] A. Postnov, A. Zarowski, N. De Clerck, F. Vanpoucke, F. Offeciers, D. Van Dyck, and S. Peeters, “High resolution micro-ct scanning as an innovatory tool for evaluation of the surgical positioning of cochlear implant electrodes,” *Acta oto-laryngologica*, vol. 126, no. 5, pp. 467–474, 2006.
- [180] R. D. Silver, H. R. Djalilian, S. C. Levine, and F. L. Rimell, “High-resolution magnetic resonance imaging of human cochlea,” *The Laryngoscope*, vol. 112, no. 10, pp. 1737–1741, 2002.
- [181] R. Hofman, “Three-dimensional guinea pig and pigeon inner ear reconstruction,” Ph.D. dissertation, University of Groningen, 2009.
- [182] S. Connor, D. Bell, R. O’Gorman, and A. Fitzgerald-O’Connor, “CT and MR imaging cochlear distance measurements may predict cochlear implant length required for a 360 insertion,” *American Journal of Neuroradiology*, vol. 30, no. 7, pp. 1425–1430, 2009.
- [183] B. M. Verbist, “Cochlear imaging in the era of cochlear implantation: From silence to sound,” Ph.D. dissertation, Leiden University, 2010.
- [184] P. A. Santi, “Light sheet fluorescence microscopy: A review,” *Journal of Histochemistry & Cytochemistry*, vol. 59, no. 2, pp. 129–138, 2011.
- [185] B. Müller, A. Lareida, F. Beckmann, G. Diakov, F. Kral, F. Schwarm, R. Stoffner, A. Gunkel, R. Glueckert, A. Schrott-Fischer *et al.*, “Anatomy of the murine and human cochlea visualized at the cellular level by synchrotron-radiation-based micro-computed tomography,” in *SPIE Optics+ Photonics*. International Society for Optics and Photonics, 2006, pp. 631 805–631 805.
- [186] A. F. Ghiz, A. N. Salt, J. E. DeMott, M. M. Henson, O. W. Henson, and S. L. Gewalt, “Quantitative anatomy of the round window and cochlear aqueduct in guinea pigs,” *Hearing research*, vol. 162, no. 1, pp. 105–112, 2001.

REFERENCES

- [187] A. H. Voie, “Imaging the intact guinea pig tympanic bulla by orthogonal-plane fluorescence optical sectioning microscopy,” *Hearing research*, vol. 171, no. 1, pp. 119–128, 2002.
- [188] J. Buytaert, E. Descamps, D. Adriaens, and J. Dirckx, “The OPFOS microscopy family: High-resolution optical sectioning of biomedical specimens,” *Anatomy Research International*, vol. 2012, 2011.
- [189] J. Buytaert, S. Johnson, M. Dierick, W. Salih, and P. Santi, “Microct versus stslim 3D imaging of the mouse cochlea,” *Journal of Histochemistry & Cytochemistry*, pp. 382–395, 2013.
- [190] R. Plonsey, *Bioelectric phenomena*. Wiley Online Library, 1969.
- [191] R. Edgerton, “Radial conductivity of arterial walls,” *Medical and Biological Engineering and Computing*, vol. 13, no. 4, pp. 531–534, 1975.
- [192] D. Wyatt, “Blood flow and blood velocity measurement in vivo by electromagnetic induction,” *Medical and Biological Engineering and Computing*, vol. 22, no. 3, pp. 193–211, 1984.
- [193] W. Lee, Z. Deng, T. Kim, A. Laine, S. Lisanby, and A. Peterchev, “Regional electric field induced by electroconvulsive therapy in a realistic finite element head model: Influence of white matter anisotropic conductivity,” *NeuroImage*, 2011.
- [194] C. Gabriel, S. Gabriel, and E. Corthout, “The dielectric properties of biological tissues: I. Literature survey,” *Physics in medicine and biology*, vol. 41, p. 2231, 1996.
- [195] S. Gabriel, R. Lau, and C. Gabriel, “The dielectric properties of biological tissues: III. Parametric models for the dielectric spectrum of tissues,” *Physics in medicine and biology*, vol. 41, p. 2271, 1996.
- [196] J. D. Kosterich, K. R. Foster, and S. R. Pollack, “Dielectric permittivity and electrical conductivity of fluid saturated bone,” *Biomedical Engineering, IEEE Transactions on*, no. 2, pp. 81–86, 1983.
- [197] M. W. Cannon, “Electrical impedances, current pathways and voltage sources in the guinea pig cochlea,” Ph.D. dissertation, Syracuse University, 1976.

REFERENCES

- [198] C. Inguva, P. Wong, A. Sue, A. McEwan, and P. Carter, "Frequency-dependent simulation of volume conduction in a linear model of the implanted cochlea," in *Neural Engineering (NER), 2015 7th International IEEE/EMBS Conference on*. IEEE, 2015, pp. 426–429.
- [199] H. Donkelaar and K. Kaga, "The auditory system," *Clinical Neuroanatomy*, pp. 305–329, 2011.
- [200] P. Wong, S. George, P. Tran, A. Sue, P. Carter, and Q. Li, "Development and validation of a high-fidelity finite-element model of monopolar stimulation in the implanted guinea pig cochlea," *Biomedical Engineering, IEEE Transactions on*, vol. 63, no. 1, pp. 188–198, 2016.
- [201] P. Wong, A. Sue, P. Tran, Q. Li, and P. Carter, "Effect of petrous bone resistivities on volume conduction in the cochlea," in *Medical Bionics, 3rd International Conference on*. The Bionics Institute, 2013.
- [202] P. Wong, P. Tran, A. Sue, Q. Li, and P. Carter, "Sensitivity of cochlear volume conduction models to boundary conditions," in *Implantable Auditory Prostheses (CIAP), 2013 Conference on*. ARO, 2013.
- [203] M. Bishop, P. Boyle, G. Plank, D. Welsh, and E. Vigmond, "Modeling the role of the coronary vasculature during external field stimulation," *Biomedical Engineering, IEEE Transactions on*, vol. 57, no. 10, pp. 2335–2345, 2010.
- [204] M. F. Suesserman, "Noninvasive microelectrode measurement technique for performing quantitative, in vivo measurements of inner ear tissue impedances," Ph.D. dissertation, University of Washington, 1992.
- [205] G. Bredberg, H. Engstrom, and H. W. Ades, "Cellular pattern and nerve supply of the human organ of corti: a preliminary report," *Archives of Otolaryngology*, vol. 82, no. 5, pp. 462–469, 1965.
- [206] H. Spoendlin, "Anatomy of cochlear innervation," *American journal of otolaryngology*, vol. 6, no. 6, pp. 453–467, 1985.
- [207] C. G. Wright and P. S. Roland, "Temporal bone microdissection for anatomic study of cochlear implant electrodes," *Cochlear Implants International*, vol. 6, no. 4, pp. 159–168, 2005.

REFERENCES

- [208] C. Q. Huang and R. K. Shepherd, “Reduction in excitability of the auditory nerve following electrical stimulation at high stimulus rates. iv. effects of stimulus intensity,” *Hearing research*, vol. 132, no. 1, pp. 60–68, 1999.
- [209] L. H. Mens, G. Huiskamp, T. Oostendorp, and P. v. d. Broek, “Modelling surface potentials from intracochlear electrical stimulation,” *Scandinavian audiology*, vol. 28, no. 4, pp. 249–255, 1999.
- [210] P. Tran, Q. Li, and P. Carter, “Finite element modeling of current flow from cochlear implant stimulation,” in *Modelling, simulation, identification, 2011 IASTED International Conference on*. IASTED, 2011, pp. 436–442.
- [211] P. Tran, P. Wong, A. Sue, Q. Li, and P. Carter, “Determining the boundary conditions for cochlear implant models,” in *Implantable Auditory Protheses (CIAP), 2013 Conference on*. ARO, 2013.
- [212] ———, “A multi-scale model of cochlear implant stimulation,” in *Implantable Auditory Protheses (CIAP), 2015 Conference on*. ARO, 2015.
- [213] M. J. Ackerman, “The visible human project: a resource for anatomical visualization.” *Studies in health technology and informatics*, vol. 52, pp. 1030–1032, 1997.
- [214] F. Spelman, B. Clopton, and M. Suesserman, “Measurements of the resistivity of bony tissues of the cochlea,” in *Proceedings of the IEEE/EMBS*, vol. 4, 1987, pp. 191–192.
- [215] J. Haueisen, C. Ramon, M. Eiselt, H. Brauer, and H. Nowak, “Influence of tissue resistivities on neuromagnetic fields and electric potentials studied with a finite element model of the head,” *Biomedical Engineering, IEEE Transactions on*, vol. 44, no. 8, pp. 727–735, 1997.
- [216] P. A. Williams and S. Saha, “The electrical and dielectric properties of human bone tissue and their relationship with density and bone mineral content,” *Annals of biomedical engineering*, vol. 24, no. 2, pp. 222–233, 1996.
- [217] C. Gabriel, A. Peyman, and E. Grant, “Electrical conductivity of tissue at frequencies below 1 mhz,” *Physics in medicine and biology*, vol. 54, no. 16, p. 4863, 2009.
- [218] W. M. Grill and J. T. Mortimer, “Electrical properties of implant encapsulation tissue,” *Annals of biomedical engineering*, vol. 22, no. 1, pp. 23–33, 1994.

REFERENCES

- [219] N. B. Slepecky, "Structure of the mammalian cochlea," in *The cochlea*. Springer, 1996, pp. 44–129.
- [220] F. A. Spelman, "Determination of tissue impedances of the inner ear: models and measurements," in *Cochlear Implants*. Springer, 1990, pp. 35–53.
- [221] C. A. Smith, "Capillary areas of the cochlea in the guinea pig," *The Laryngoscope*, vol. 61, no. 11, pp. 1073–1095, 1951.
- [222] P. Roland and C. Wright, "Surgical aspects of cochlear implantation: mechanisms of insertional trauma," *Advanced Otorhinolaryngology*, vol. 64, pp. 11–30, 2006.
- [223] C. G. Wright and P. S. Roland, "Vascular trauma during cochlear implantation: a contributor to residual hearing loss?" *Otology & Neurotology*, vol. 34, no. 3, pp. 402–407, 2013.
- [224] P. Tran, P. Wong, A. Sue, Q. Li, and P. Carter, "Influence of blood vessel conductivity in cochlear implant stimulation using an finite element head model," in *Engineering in Medicine and Biology Society (EMBC), 35th Annual International Conference of the IEEE*. IEEE, 2013.
- [225] R. Johnson, H. Hu, S. Haworth, P. Cho, C. Dawson, and J. Linehan, "Feldkamp and circle-and-line cone-beam reconstruction for 3d micro-ct of vascular networks," *Physics in medicine and biology*, vol. 43, p. 929, 1998.
- [226] T. Ross, H. Handels, U. Breuer, and K. Szabo, "3d visualization of microvascular blood vessel networks," *Computers & graphics*, vol. 19, no. 1, pp. 89–96, 1995.
- [227] B. Müller, J. Fischer, U. Dietz, P. J. Thurner, and F. Beckmann, "Blood vessel staining in the myocardium for 3D visualization down to the smallest capillaries," *Nuclear Instruments and Methods in Physics Research Section B: Beam Interactions with Materials and Atoms*, vol. 246, no. 1, pp. 254–261, 2006.
- [228] R. Wagner, D. Van Loo, F. Hossler, K. Czymmek, E. Pauwels, and L. Van Hoorebeke, "High-resolution imaging of kidney vascular corrosion casts with nano-ct," *Microscopy and Microanalysis*, vol. 17, no. 02, pp. 215–219, 2011.

REFERENCES

- [229] T. Shatari, Y. Hosoda, and J. Kanzaki, "A study on the vasculature of the internal auditory artery in humans by casts," *Acta Oto-Laryngologica*, vol. 114, no. S514, pp. 101–107, 1994.
- [230] A. Mudry and R. Tange, "The vascularization of the human cochlea: its historical background," *Acta Oto-Laryngologica*, vol. 129, no. S561, pp. 3–16, 2009.
- [231] F. E. Hossler and J. E. Douglas, "Vascular corrosion casting: review of advantages and limitations in the application of some simple quantitative methods," *Microscopy and microanalysis*, vol. 7, no. 03, pp. 253–264, 2001.
- [232] W. Mondy, D. Cameron, J. Timmermans, N. De Clerck, A. Sasov, C. Casteleyn, and L. Piegler, "Micro-ct of corrosion casts for use in the computer-aided design of microvasculature," *Tissue Engineering Part C: Methods*, vol. 15, no. 4, pp. 729–738, 2009.
- [233] M. Anniko and P.-G. Lundquist, "The influence of different fixatives and osmolality on the ultrastructure of the cochlear neuroepithelium," *European Archives of Oto-Rhino-Laryngology*, vol. 218, no. 1, pp. 67–78, 1977.
- [234] P. Schneider, T. Krucker, E. Meyer, A. Ulmann-Schuler, B. Weber, M. Stampanoni, and R. Müller, "Simultaneous 3D visualization and quantification of murine bone and bone vasculature using micro-computed tomography and vascular replica," *Microscopy research and technique*, vol. 72, no. 9, pp. 690–701, 2009.
- [235] C. C. Wong, I. S. Curthoys, S. J. O'Leary, and A. S. Jones, "Heavy metal staining, a comparative assessment of gadolinium chloride and osmium tetroxide for inner ear labyrinthine contrast enhancement using x-ray microtomography," *Acta otolaryngologica*, vol. 133, no. 1, pp. 22–27, 2013.
- [236] P. Franz, S. Aharinejad, P. Böck, and W. Firbas, "The cochlear glomeruli in the modiolus of the guinea pig," *European archives of oto-rhino-laryngology*, vol. 250, no. 1, pp. 44–50, 1993.
- [237] T. Guenther, N. H. Lovell, and G. J. Suaning, "Bionic vision: system architectures—a review," *Expert review of medical devices*, vol. 9, no. 1, pp. 33–48, 2012.

REFERENCES

- [238] R. Plonsey and D. B. Heppner, “Considerations of quasi-stationarity in electrophysiological systems,” *The Bulletin of mathematical biophysics*, vol. 29, no. 4, pp. 657–664, 1967.
- [239] H. P. Schwan and C. F. Kay, “The conductivity of living tissues,” *Annals of the New York Academy of Sciences*, vol. 65, no. 6, pp. 1007–1013, 1957.
- [240] P. Hasgall, F. Di Gennaro, C. Baumgartner, E. Neufeld, M. Gosselin, D. Payne, A. Klöngböck, and N. Kuster, “IT’IS database for thermal and electromagnetic parameters of biological tissues,” <http://www.itis.ethz.ch/virtual-population/tissue-properties/database/tissue-frequency-chart/>, version 2.6, 13 January 2015, accessed: 31 March 2015.
- [241] D. Andreuccetti and R. Fossi, “Dielectric properties of human tissues: Definitions, parametric model, computing codes,” TR/ICEMM/13.00, Tech. Rep., 2000.
- [242] E. Kreyszig, *Advanced engineering mathematics*. John Wiley & Sons, 1988.
- [243] C. R. Butson and C. C. McIntyre, “Tissue and electrode capacitance reduce neural activation volumes during deep brain stimulation,” *Clinical neurophysiology*, vol. 116, no. 10, pp. 2490–2500, 2005.
- [244] C. A. Bossetti, M. J. Birdno, and W. M. Grill, “Analysis of the quasi-static approximation for calculating potentials generated by neural stimulation,” *Journal of neural engineering*, vol. 5, no. 1, p. 44, 2008.
- [245] B. S. Wilson, D. T. Lawson, and M. Zerbi, “Speech processors for auditory prostheses,” *NIH Contract*, no. NOI-DC-9-2401, 1991.
- [246] A. E. Vandali, L. A. Whitford, K. L. Plant, G. M. Clark *et al.*, “Speech perception as a function of electrical stimulation rate: using the nucleus 24 cochlear implant system,” *Ear and hearing*, vol. 21, no. 6, pp. 608–624, 2000.
- [247] P. C. Loizou, O. Poroy, and M. Dorman, “The effect of parametric variations of cochlear implant processors on speech understanding,” *The Journal of the Acoustical Society of America*, vol. 108, no. 2, pp. 790–802, 2000.

REFERENCES

- [248] L. M. Friesen, R. V. Shannon, and R. J. Cruz, “Effects of stimulation rate on speech recognition with cochlear implants,” *Audiology and Neurotology*, vol. 10, no. 3, pp. 169–184, 2005.
- [249] R. V. Shannon, R. J. Cruz, and J. J. Galvin, “Effect of stimulation rate on cochlear implant users’ phoneme, word and sentence recognition in quiet and in noise,” *Audiology and Neurotology*, vol. 16, no. 2, pp. 113–123, 2010.
- [250] R. Shannon, “Psychophysics,” pp. 357–388, 1993.
- [251] J. C. Middlebrooks, “Effects of cochlear-implant pulse rate and inter-channel timing on channel interactions and thresholds,” *The Journal of the Acoustical Society of America*, vol. 116, no. 1, pp. 452–468, 2004.
- [252] M. Tykocinski, Y. Duan, B. Tabor, and R. S. Cowan, “Chronic electrical stimulation of the auditory nerve using high surface area (hiq) platinum electrodes,” *Hearing research*, vol. 159, no. 1, pp. 53–68, 2001.
- [253] R. P. Carlyon, O. Macherey, S. Cosentino, and J. M. Deeks, “Spatial selectivity: How to measure and (maybe) improve it,” in *Implantable Auditory Prostheses (CIAP), 2015 Conference on*. ARO, 2015.
- [254] B. Tahayori and S. Dokos, “Challenging the optimality of rectangular pulse stimulation for neuroprosthetic devices,” in *Neural Engineering (NER), 2013 6th International IEEE/EMBS Conference on*. IEEE, 2013, pp. 1131–1134.
- [255] ———, “Optimal stimulus profiles for neuroprosthetic devices: Monophasic versus biphasic stimulation,” in *Engineering in Medicine and Biology Society (EMBC), 2013 35th Annual International Conference of the IEEE*. IEEE, 2013, pp. 5978–5981.
- [256] P. R. Thorne, D. J. Muñoz, and G. D. Housley, “Purinergic modulation of cochlear partition resistance and its effect on the endocochlear potential in the guinea pig,” *Journal of the Association for Research in Otolaryngology*, vol. 5, no. 1, pp. 58–65, 2004.
- [257] P. J. Abbas, C. J. Brown, J. K. Shallop, J. B. Firszt, M. L. Hughes, S. H. Hong, and S. J. Staller, “Summary of results using the nucleus ci24m implant to record the electrically evoked compound action potential,” *Ear and Hearing*, vol. 20, no. 1, pp. 45–59, 1999.

REFERENCES

- [258] L. T. Cohen, L. M. Richardson, E. Saunders, and R. S. Cowan, “Spatial spread of neural excitation in cochlear implant recipients: comparison of improved ecap method and psychophysical forward masking,” *Hearing research*, vol. 179, no. 1, pp. 72–87, 2003.
- [259] M. L. Hines and N. T. Carnevale, “The NEURON simulation environment,” *Neural computation*, vol. 9, no. 6, pp. 1179–1209, 1997.
- [260] J. H. Frijns, M. van Gendt, R. K. Kalkman, and J. J. Briaire, “Modeled neural response patterns from various speech coding strategies,” in *Implantable Auditory Prostheses (CIAP), 2015 Conference on*. ARO, 2015.
- [261] A. Horton, A. Wittek, and K. Miller, “Towards meshless methods for surgical simulation,” in *MICCAI Workshop*, 2006.
- [262] R. Boyle, “How it works: A laser-powered ear implant to boost hearing,” <http://www.popsci.com.au/tech/how-it-works-a-laserpowered-ear-implant-to-boost-hearing>, 377491, 2012, accessed: 7 March 2014.
- [263] A. D. Izzo, C.-P. Richter, E. D. Jansen, J. T. Walsh *et al.*, “Laser stimulation of the auditory nerve,” *Lasers in surgery and medicine*, vol. 38, no. 8, pp. 745–753, 2006.
- [264] A. D. Izzo, E. Suh, J. Pathria, J. T. Walsh, D. S. Whitlon, and C.-P. Richter, “Selectivity of neural stimulation in the auditory system: a comparison of optic and electric stimuli,” *Journal of biomedical optics*, vol. 12, no. 2, pp. 021 008–021 008, 2007.
- [265] M. Jeschke and T. Moser, “Considering optogenetic stimulation for cochlear implants,” *Hearing research*, vol. 322, pp. 224–234, 2015.